HOKKAIDO UNIVERSITY

Title	Construction of Molecule-based Multi-electron/proton Transfer Systems based on Non-precious Metal Complexes with Electron/proton Pooling Ligands
Author(s)	脇坂, 聖憲
Degree Grantor	北海道大学
Degree Name	博士(理学)
Dissertation Number	甲第12330号
Issue Date	2016-03-24
DOI	https://doi.org/10.14943/doctoral.k12330
Doc URL	https://hdl.handle.net/2115/61805
Type	doctoral thesis
File Information	Masanori_Wakisaka.pdf



Hokkaido University Collection of Scholarly and Academic Papers : HUSCAP

Construction of Molecule-based Multi-electron/proton Transfer Systems based on Non-precious Metal Complexes with Electron/proton Pooling Ligands

Masanori Wakizaka

Graduate School of Chemical Sciences and Engineering,

Hokkaido University

March 2016

Contents

Acknowledgements

Chapter 1 General Introduction 1

1-1. Energy Problems - Research Opportunities 1

1-2. Electron and Proton Transfer Reactions at Molecular Level 12

1-3. Redox-active Ligands 25

1-4. Electron and Proton Transfer Reactions of Group 8 Metal Complexes 39

1-5. Metalloligands 43

1-6. Objectives of This Study 56

1-7. Survey of This Thesis 61

1-8. References 65

Chapter 2 Coordination Site–dependent Cation Binding and Multi–responsible Redox Properties of Janus–head Metalloligand $[Mo^{V}(2\text{-mercaptophenolato})_3]^-$ 73

2-1. Introduction 74

2-2. Experimental Section 76

2-3. Results and Discussion 83

2-4. Conclusions 105

2-5. References 106

Chapter 3 Interactions Between the Trianionic Ligand-centered Redox-active Metalloligand $[Cr^{III}(perfluorocatecholato)_3]^{3-}$ and Guest Metal Ions 111

3-1. Introduction 112

3-2. Experimental Section 115

3-3. Results and Discussion 117

3-4. Conclusions 146

3-5. Notes and References 147

Chapter 4 **Guest Metal Ion Binding of Ligand-centered Redox-active $[Cr^{III}(2\text{-mercaptophenolato})_3]^{3-}$ Metalloligand with Heteroleptic Coordination Site** 151
4-1. Introduction 152
4-2. Experimental Section 154
4-3. Results and Discussion 158
4-4. Conclusions 173
4-5. References 174

Chapter 5 **Nonprecious-Metal-Assisted Photochemical Hydrogen Production from *ortho*-Phenylenediamine** 177
5-1. Introduction 178
5-2. Experimental Section 180
5-3. Results and Discussion 189
5-4. Conclusions 212
5-5. Notes and References 213

Chapter 6 **Photocatalytic Hydrogen Evolution from MeOH by *o*-Aminophenol, *o*-Aminophenolate, and Its Fe(II) Complex at Room Temperature** 219
6-1. Introduction 220
6-2. Experimental Section 224
6-3. Results and Discussion 231
6-4. Conclusions 252
6-5. Notes and References 253

Future Perspectives 257

List of Publications 260

Other Publications 261

List of Presentations 262

Acknowledgements

The study presented in this thesis was carried out under the supervision of Prof. Masako Kato and Prof. Ho-Chol Chang at the Department of Chemistry, Faculty of Science, Hokkaido University (April 2010-March 2016), as well as at the Department of Applied Chemistry, Faculty of Science and Engineering, Chuo University (April 2013-March 2016).

The author would like to express his most profound gratitude to Prof. Masako Kato (Hokkaido University) for the countless valuable comments and for the continuous warm encouragement, as well as for providing the author with the opportunity to carry out his research in the laboratory of Prof. Chang. Furthermore, the author would like to express his sincerest gratitude to Prof. Ho-Chol Chang (Chuo University) for all his invaluable guidance, the fruitful discussions, for his encouragement, and for inviting the author in his laboratory. The author is also greatly indebted to Associate Prof. Atsushi Kobayashi (Hokkaido University) for numerous helpful discussions and his encouragement. The author would also like to gratefully acknowledge Assistant Prof. Takeshi Matsumoto (Chuo University) for his invaluable experimental guidance, the discussions, and the encouragement. The author would also like to use this opportunity to thank Assistant Prof. Masaki Yoshida (Hokkaido University) for the helpful discussions.

Moreover, the author would like to express his gratitude to Prof. Yoichi Sasaki, Prof. Kohei Uosaki, as well as Prof. Yasuchika Hasegawa and Prof. Kei Murakoshi (both Hokkaido University) for their helpful guidance. The author is also grateful to Prof. Yukio Hinatsu, Associate Prof. Makoto Wakeshima, Prof. Takayoshi Nakamura, and Associate Prof. Shin-ichiro Noro (all Hokkaido Univ.) for their support with and discussions on the magnetic measurements carried out in this study. The author also gratefully acknowledges to Prof. Noboru Kitamura (Hokkaido University) and Associate Prof. Eri Sakuda (Nagasaki University), as well as Prof. Tamejiro Hiyama and Assistant Prof. Yasunori Minami (both Chuo University) for their support with ESI-MS measurements. The author would like to acknowledge to Prof. Youichi Ishii and

Assistant Prof. Shintaro Kodama for their support with elemental analyses. The author would also like to acknowledge to Prof. Masa-aki Haga and Assistant Prof. Hiroaki Ozawa for their support with emission measurements. The author would like to thank Prof. Yutaka Hitomi (Doshisha University) for his support with UV-vis titration experiments, and Mr. Koichi Shiomi (Shimadzu Analytical & Measuring Center Inc.) for his support and discussions on D_2/HD/H_2 detection by GC. The author would moreover like to thank Mr. Hirokazu Yano for his invaluable experimental guidance, the discussions, and the encouragement. The author would also like to thank Mr. Sho Ueno, Ms. Akane Usui, and Mr. Ryota Tanaka for their great deal of experimental efforts. Last but not least, the author would like to extend his deep appreciation and gratitude to all members of the laboratories of Prof. Kato and Prof. Chang for their warm and kind hospitality.

This work was supported by the *Elements Science and Technology Project* "Nano-hybridized Precious-metal-free Catalysts for Chemical Energy Conversion", a grant-in-aid for scientific research for the priority area "Coordination Programming" (area no. 2107), a grant-in-aid for scientific research (26620050 and 25288024), and a grant-in-aid for scientific research (B) (23350025) from the Japanese ministry of education, culture, sports, science and technology (MEXT), as well as by a KAKENHI grant from the JSPS (grant no. 26·2494).

The author would also like to express his deep appreciation for his family, Dr. Kazuyori Wakizaka, Mrs. Yoshiko Wakizaka, Dr. Kazuki Wakizaka, and Ms. Tamaki Wakizaka for their constant financial support and their affectionate encouragement.

Masanori Wakizaka

Graduate School of Chemical Science and Engineering

Hokkaido University

March 2016

Chapter 1

General Introduction

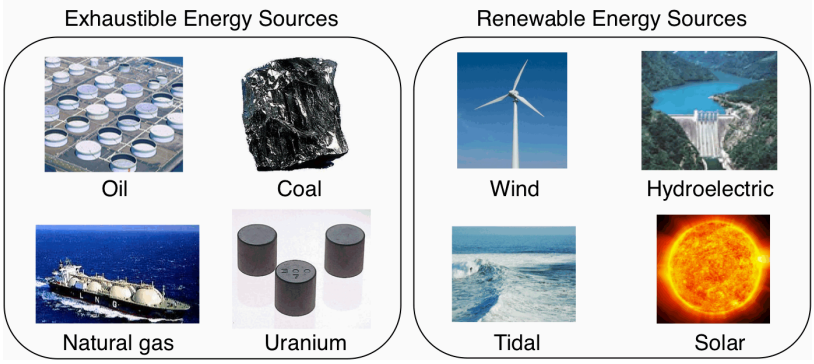
1-1. Energy Problems - Research Opportunities

1-1-1. Renewable Energy Sources

While the world population reached 1.6 billion at the beginning of the 20th century, it has meanwhile increased to 7 billion.[1] Considering current social, economical, and technological developments, the global energy resources will soon be unable to meet the demand *per capita*.[2] For example, the global energy consumption in 2013 was ~5.3 × 10^{20} J,[3] then this energy consumption corresponds approximately to the annual energy output of 17,000 nuclear power plants of 1 GW.[4] Most of the energy carries are still based on so-called fossil fuels such as oil, coal, and natural gas (Chart 1), which are derived from carbon recycling on a geological timescale.[2] Fossil fuel reservoirs continuously decreases, and reserves-to-production ratios of 2060 (oil), 2070 (neutral gas), and 2120 (coal) have been estimated.[3] Another energy source that has been exploited since the 1950s is nuclear energy, but the handling of radioactive substances, as well as the storage of the associated waste products is relatively risky.[3]

In contrast to exhaustible energy sources, *i.e*. the fossil fuels and nuclear fuels (*e.g*. uranium), other primary energy sources such as wind, hydroelectric, tidal, and solar power, are called renewable energy sources, as they are semi-permanently available.[3] Great expectations are placed upon these renewable energy sources as alternatives for exhaustible energy carriers.

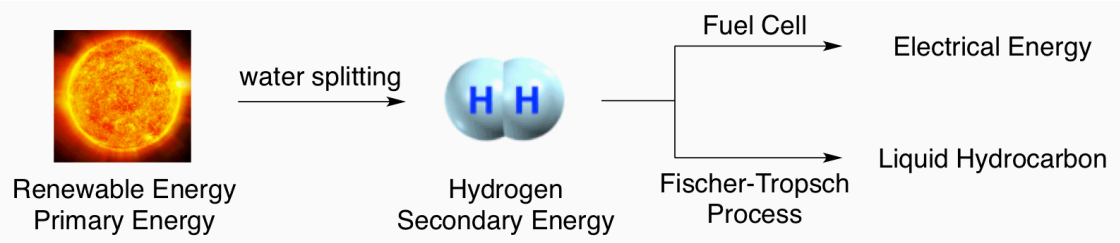
Chart 1. Classification for energy sources.



1-1-2. The Development of Catalysts for the Generation of Secondary Energy

The use of renewable energy sources represented by solar power, is expected to help to solve the energy problems.[2] However, such renewable energy is difficult to store in its original form, and therefore it must be converted into a secondary energy form, *e.g.* chemical energy.[5] One of the most attractive carrier for such chemical energy is hydrogen, and it has established a track record as an energy source that is used *e.g.* in fuel cells[6] and the Fischer-Tropsch process (Chart 2).[7]

Chart 2. Diagram for energy conversion.



Fuel cells are electric generators for the conversion of chemical energy to electrical energy. For example, hydrogen or methanol (MeOH) is oxidized at the anode, and electrical energy is harvested at the cathode from the reduction of oxygen (eqs. 1-3). Fuel cells are a relatively efficient, as they convert chemical energy to electrical energy directly, without an intermediate conversion into thermal and/or kinetic energy.[6]

$$H_2 \xrightarrow{-2e^-} 2H^+ \qquad \text{eq. 1}$$

$$CH_3OH + H_2O \xrightarrow{-6e^-} 6H^+ + CO_2 \qquad \text{eq. 2}$$

$$O_2 + 4H^+ \xrightarrow{+4e^-} 2H_2O \qquad \text{eq. 3}$$

The Fischer-Tropsch process combines a series of reactions for the synthesis of liquid hydrocarbon compounds from carbon monoxide and hydrogen (eq. 4), and it has been used for industrial production of artificial fuels.[7]

$$n\text{CO} + (2n+1)\text{H}_2 \xrightarrow{\Delta} \text{C}_n\text{H}_{2n+2} + n\text{H}_2\text{O} \qquad \text{eq. 4}$$

A strong advantage of hydrogen as a secondary energy carrier is that it can be generated from a variety of hydrogen sources. One of the most promising methods for the generation of hydrogen is the splitting of water (eq. 5) by using a photocatalyst (Cat.).[8]

$$2H_2O \xrightarrow[\text{Cat.}]{h\nu} H_2 + O_2 \qquad \text{eq. 5}$$

Water is an attractive starting material for the generation of hydrogen, as the only byproduct of this photoreaction, mediated by heterogeneous photocatalysts, is non-polluting oxygen. As photocatalysts, inorganic semiconductors such as *e.g.* TiO_2 have been used, as they are able to split water stoichiometrically based on the Honda-Fujishima effect. (Table 1).[8] Recently, Domen *et al*. reported that the photocatalyst $LaMg_{0.33}Ta_{0.67}O_2N$, which absorbs light at 410-470 nm, also promotes the splitting of water.[8c] However, in order to use natural sun light, whose spectrum contains significant contributions in the visible/NIR region, the development of new photocatalysts that absorb light at longer wavelengths is highly desirable.[9]

Table 1. Inorganic semiconductor catalysts for the splitting of water in refs. 8b and 8c

Photocatalyst	Crystal structure	Co-catalyst	Activity / μmol h^{-1}		Quantum yield (%)
			H_2	O_2	
TiO_2	Anatase	Rh	449		29 (Hg lamp)
$Rb_2La_2Ti_3O_{10}$	Layered perovskite	NiO_x	869	430	5 (at 330 nm)
$Y_2Ti_2O_7$	Cubic pyrochlore	NiO_x	850	420	6 (at 313 nm)
$K_4Nb_6O_{17}$	Layered structure	NiO_x	1837	850	5 (at 330 nm)
$Rb_4Nb_6O_{17}$	Layered structure	NiO_x	936	451	10 (at 330 nm)
$Cs_2Nb_4O_{11}$	Pyrochlore like	NiO_x	1700	800	3 (at 270 nm)
$K_3Ta_3B_2O_{12}$	Tungsten bronze		2390	1210	6.5 (at 254 nm)
$NaTaO_3$	Perovskite	NiO	2180	1100	20 (at 270 nm)
$NaTaO_3$:La	Perovskite	NiO	19800	9700	56 (at 270 nm)
$SrTa_2O_6$	$CaTa_2O_6$ (orth.)	NiO	960	490	7 (at 270 nm)
$Sr_2Ta_2O_7$	Layered perovskite	NiO	1000	480	12 (at 270 nm)
Ge_3N_4		RuO_2	1400	700	9 (at 300 nm)
$Ga_{0.88}Zn_{0.12}O_{0.12}N_{0.88}$		$Rh_{2-x}Cr_xO_3$	800	400	5.9 (420–440 nm)
$LaMg_{0.33}Ta_{0.67}O_2N$	Complex perovskite	$RhCrO_x$	40	20	0.03 (410-470 nm)

Homogeneous molecular catalysts can also be used in this context, and especially transition metal complexes represent an attractive alternative.[10] Transition metal complexes have been reported to catalyze the generation of hydrogen using a reductant (Red)[10a], as well as the generation of oxygen using an oxidant (Ox);[10b] both of these reactions are constitutional parts of the water splitting process (eqs. 6 and 7). As these reactions consume sacrificial reagents, the aforementioned stoichiometric water splitting using semiconductor-based catalysts is still more desirable. Moreover, the metal centers in theses homogeneous catalysts usually consist of precious metal such as Pt, Ru, or Ir (Tables 2 and 3), which are expensive and limited in terms of availability. Therefore, the development of homogeneous water splitting photocatalysts based on non-precious metals represents a desirable research target.[11]

$$2H^+ + Red \xrightarrow{Cat.} H_2 + Red' \qquad \text{eq. 6}$$

$$2H_2O + Ox \xrightarrow{Cat.} O_2 + 4H^+ + Ox' \qquad \text{eq. 7}$$

Table 2. Pt complexes for the catalytic evolution of hydrogen in ref. 10a

Complex	Quantum yield (%)
$[Pt^{II}_2(NH_3)_4(\mu\text{-acetamidate})_2]^{2+}$ (**1**$^{2+}$)	31
$[Pt^{II}_2(NH_3)_4(\mu\text{-2-fluoroacetamidate})_2]^{2+}$	25
$[Pt^{II}_2(NH_3)_4(\mu\text{-}\alpha\text{-pyrrolidinonato})_2]^{2+}$	10
$[Pt^{II}_2(NH_3)_4(\mu\text{-}\alpha\text{-pyridonato})_2]^{2+}$	23
$[Pt^{II}_2(NH_3)_4(\mu\text{-5-carboxy-}\alpha\text{-pyridonato}]^{2+}$	20
$[Pt^{II}_2(bpy)_2(\mu\text{-OH})_2]^{2+}$	14
$[Pt^{II}(NH_3)_4]^{2+}$	1
cis-$[Pt^{II}(Cl)_2(NH_3)_2]$	20
$[Pt^{II}(Cl)_2$(ethylenediamine)]	24
$[Pt^{II}(Cl)_2$(4-methylpyridine)$_2$]	22
$[Pt^{II}(Cl)_2$(4,4'-dicarboxy-2,2'-bipyridine)]	2.9
$[Pt^{II}(Cl)_2$(2,2':6',2"-terpiridine)]$^+$	2.4

[a] Hydrogen production from an aqueous buffer solution (pH 5.0) containing ethylenediaminetetraacetic acid, $[Ru^{II}$(2,2'-bipyridine$)_3]^{2+}$, methyl viologen, and Pt complex, irradiated with a 350 W Xe lamp.

Table 3. Ru and Ir complexes for the catalytic evolution of oxygen in ref. 10b

Complex	TON	TOF / s^{-1}
$[Ru^{II}(tpy)(2,2'\text{-bibyrazine})(H_2O)]^{2+}$ (**3**$^{2+}$)	7.5	0.031
$[Ru^{II}(tpy)(bpy)(H_2O)]^{2+}$	320	0.00051
$[Ru^{II}(tpy)(4\text{-methyl-pyridine})_2(H_2O)]^{2+}$	450	0.092
$[Ru^{II}(tpy)(2,9\text{-dimethyl-1,10-phenanthroline})_2(H_2O)]^{2+}$	60	0.005
$[Ru^{II}(Cl)\{1\text{-methyl-4-(2-pyridyl)triazole}\}(p\text{-cymene})]^{+}$	18	0.055
$[Ru^{II}(6,6'\text{-dicarboxy-bpy})(isoquinoline)_2]$	8360	303
cis-cis-$[Ru^{II}_2(\mu\text{-O})(bpy)_4(H_2O)_2]^{4+}$	13.2	0.0042
$[Ru^{II}_2(pdp)(tpy)_2(H_2O)_2]^{3+}$	512	0.014
trans,fac-$[Ru^{III}_2(pdp)(OH)_2(bpea)]^{3+}$	11.1	0.0033
trans,fac-$[Ru^{II}_2(pdp)(H_2O)_2\{tris(2\text{-pyridyl})methane\}]^{3+}$	9.6	0.031
$[Ru^{II}_2(Cl)(bbnp)(4\text{-methoxypyridine})_4]^{3+}$	601	0.07
$[Ru^{II}_2(Cl)(bbnp)(4\text{-methylpyridine})_4]^{3+}$	459	0.041
$[Ir^{III}(ppy)_2(H_2O)_2]^{+}$	2490	0.0041
$[Ir^{III}(\eta_5\text{-1,2,3,4,5-pentamethylcyclopentadiene})(ppy)(Cl)]$	1500	0.91

[a] Hydrogen production from an aqueous solution containing cerium ammonium nitrate and Ru complex. tpy = 2,2':6',2"-terpiridine, bpy = 2,2'-bipyridine, pdp = pyrazole-3,5-diyl) dipyridine, bpea = N,N-bis(pyridine-2-ylmethyl)ethanamine, ppy = cyclometalated phenylpyridine, bbnp = 3.6-bis[6'-(benzo[*b*]-1",8"-naphthyrid-2"-yl)pyrid-2'-yl]pyridazine.

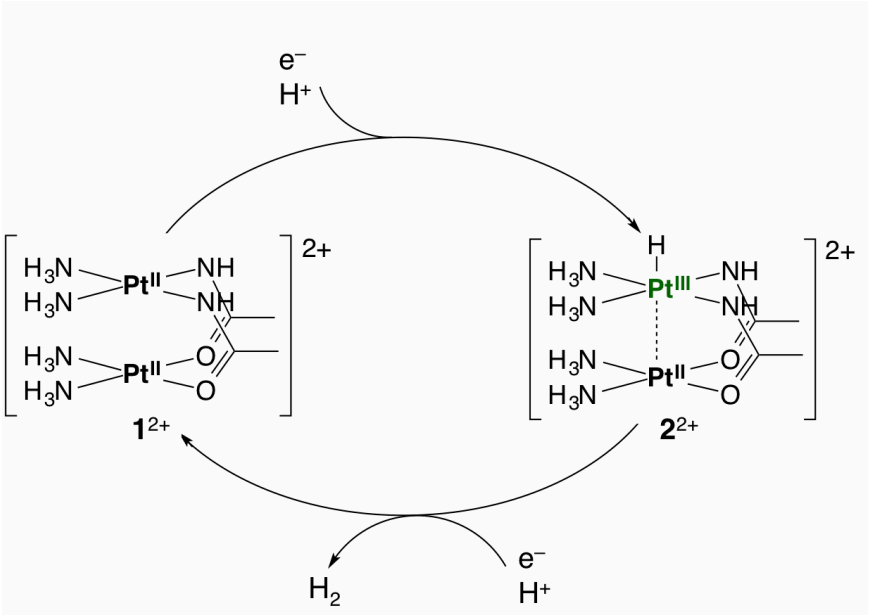
The elementary reactions of the water splitting process are redox reactions, which are accompanied by multi-proton transfer reactions. Essentially, the water splitting reaction generates hydrogen from the addition of two electrons to two water molecules under the concomitant formation of hydroxide ions (eq. 8). Conversely, oxygen is produced from two water molecules by the abstraction of four electrons (eq. 9). Accordingly, the design of suitable multi-electron and proton transfer reactions is one of the most important tasks in order to develop effective molecular catalysts.

$$2H_2O \xrightarrow{+2e^-} H_2 + 2OH^- \qquad \text{eq. 8}$$

$$2H_2O \xrightarrow{-4e^-} O_2 + 4H^+ \qquad \text{eq. 9}$$

For example, Sakai *et al*. reported $[Pt^{II}_2(NH_3)_4(\mu\text{-acetamidate})_2]^{2+}$ ($\mathbf{1}^{2+}$), which reduces water to generate hydrogen in the presence of a sacrificial reagent (Scheme 1).[12] In this reaction, the resting state of $\mathbf{1}^{2+}$ accepts one electron from the sacrificial reagent, before donating two electrons to protons under the formation of $\mathbf{2}^{2+}$. Subsequently, $\mathbf{2}^{2+}$ reacts with water-derived protons and electrons from the sacrificial reagent to afford hydrogen under regeneration of $\mathbf{1}^{2+}$. In this hydrogen evolution reaction, the transfer and binding of two electrons and two protons occurs on Pt center, while the supporting ligands do not engage in the electron and proton transfer reactions.

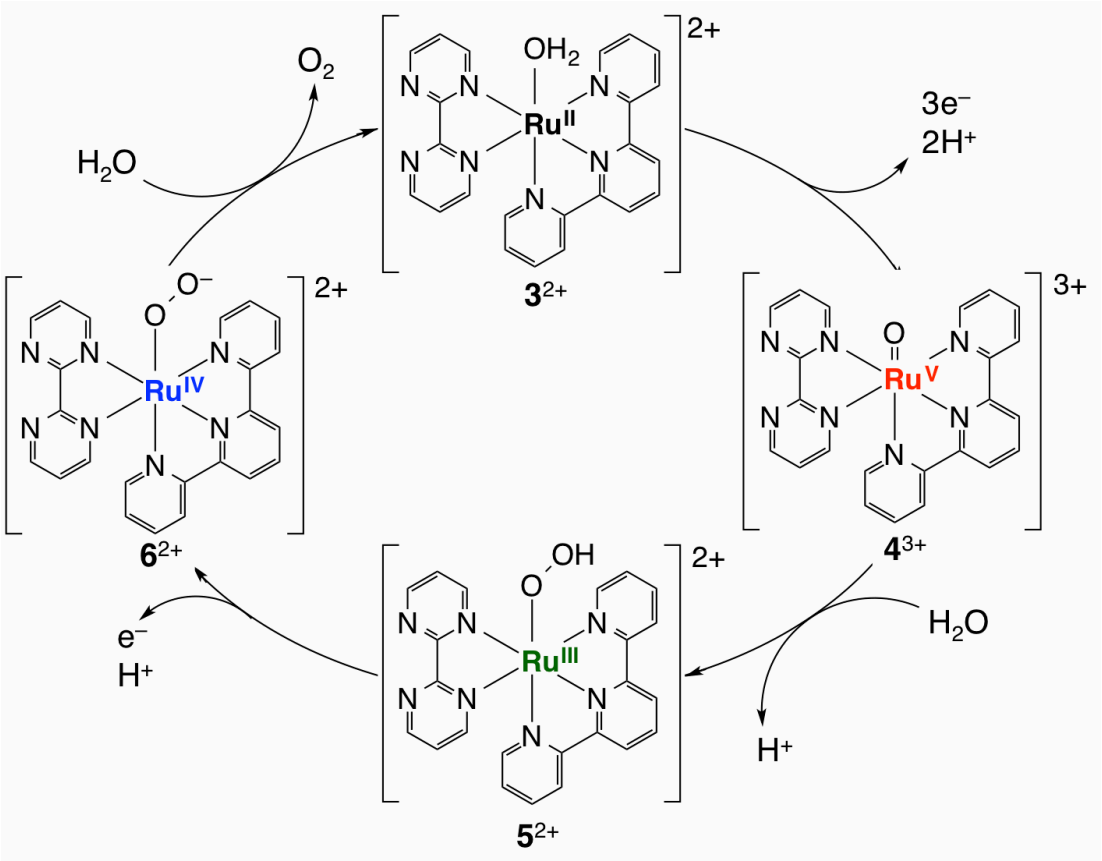
Scheme 1. Proposed mechanism for the evolution of hydrogen catalyzed by $\mathbf{1}^{2+}$ in ref. 12.



Meyer *et al*. reported that $[Ru^{II}(tpy)(bpz)(H_2O)]^{2+}$ ($\mathbf{3}^{2+}$) (tpy = 2,2':6',2"-terpyridine; bpz = 2,2'-bibyrazine) is able to catalytically oxidized water under acidic conditions (Scheme 2).[13] Complex $\mathbf{3}^{2+}$, which is a resting state, is oxidized under concomitant elimination of a proton from an aquo ligand by using a sacrificial reagent to produce the corresponding oxidized species $\mathbf{4}^{3+}$, which is considered the active species for the oxidation of water. As $\mathbf{4}^{3+}$ is extremely electron-deficient, it accepts two electrons from the oxo ligand and water to produce $\mathbf{5}^{2+}$. In this electron transfer process, the water molecule is considered to form an O–O bond with the oxo ligand *via* an acid-base mechanism. In a subsequent reaction, $\mathbf{5}^{2+}$ is oxidized on the

expense of a sacrificial reagent to generate $\mathbf{6}^{2+}$. The Ru(IV) center in $\mathbf{6}^{2+}$ extracts two electrons from the peroxo ligand, and $\mathbf{1}^{2+}$ is regenerated under the generation of oxygen. It should be noted that in this four-electron oxidation of water, Ru plays the role of an electron transfer site, and that although the tpy and bpz ligands protect the active Ru center, they are not directly involved in electron transfer reactions.

Scheme 2. Proposed mechanism for the oxidation of water catalyzed by $\mathbf{3}^{2+}$ in ref. 13.



1-1-3. Development of Materials for the Storage of Secondary Energy Carriers

The generation of hydrogen from, for instance, water splitting is a highly useful method to create a secondary energy carrier. However, as hydrogen is a gas under ambient conditions and explosive in the presence of atmospheric oxygen, it is not easy to store.[14] Currently, the prevalent method for physical storage of hydrogen is compression or liquefaction in gas cylinders. As these systems require high pressure (200-700 atom) or very low temperature

Table 4. Dehydrogenation catalysts for methylcyclohexane in ref. 19

Catalyst	Temperature / °C	Activity / $mmol_{H2}\ g_{metal}^{-1}\ min^{-1}$
3.82 wt% Pt/Alumina	300	1700
10 wt% Pt/AC cloth	298	520
0.1 wt% K^+ 0.6 wt% Pt/Al_2O_3	320	744 (mmol L_{cat} min)
44 wt% Mo-SiO_2	400	0.9
61 wt% Mo-SiO_2	400	3.6

AC = activated carbon.

Table 5. Heterogeneous dehydrogenation catalysts for methanol in ref. 20

Catalyst	Preparation method	Temperature / °C	Activity / $\mu mol_{H2}\ g_{cat}^{-1}\ s^{-1}$
Cu/ZrO_2	IMP	260	3
	OGCP	260	90
Cu/ZnO	CP	250	51
$Cu/ZnO/Al_2O_3$	HP	250	109
Cu-Mn	OGCP	260	51
Cu-Mn spinel	SRG	260	79
Cu/Zn/Zr/Al	WT	260	159
	CP	260	261

IMP = impregnation, CP = co-precipitation, OGCP = oxalate gel co-precipitation, HP = homogeneous precipitation, SRG = soft reactive grinding technique, WT = wet impregnation.

(–253 ºC), some problems, *e.g.* leaks, and losses, are unavoidable.[15]

In contrast, chemical hydrogen storage, which uses chemical bonds between hydrogen and a material, is able to store hydrogen more stably compared to the aforementioned physical methods. For example, metal-organic frameworks (MOFs),[16] metal hydrides,[17] and clathlates[18] have been investigated with respect to their potential as chemical hydrogen storage materials. In addition, organic compounds such as *e.g.* cyclic hydrocarbons and alcohols are also expected to be useful as hydrogen carriers, as they may potentially incorporate hydrogen in their structures.[19] Especially, methylcyclohexane (MCH) and MeOH are interesting in this context, as they are liquid under ambient conditions, and exhibit a relatively high hydrogen storage rate, *i.e.* 6.2 wt% for MCH/toluene[19] and 12 wt% for MeOH /water (mol/mol = 1/1)/carbon dioxide (CO_2)[20] (Scheme 3). However, the dehydrogenation of MCH requires precious metal catalysts

and high temperature-conditions (~300 ºC) in order to achieve high activity (Table 4).[19] The dehydrogenation of MeOH can be catalyzed by either Cu-based heterogeneous catalysts at high temperatures (~200-300 ºC) (Table 5),[20] or at lower temperatures (64-150 ºC) by homogeneous transition metal catalysts based on Pd,[21] Ir,[22] Rh[21, 23], Ru[24-31], or Fe[32] (Table 6). Accordingly, catalysts based on non-precious metals are required for evolution of hydrogen from hydrogen carriers.

Scheme 3. Hydrogen evolution reaction from a) MCH and b) MeOH with water.

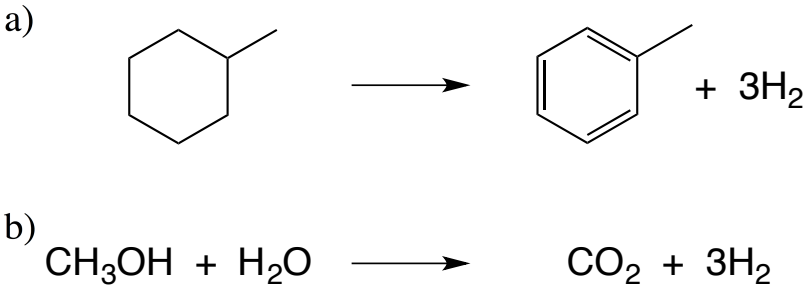


Figure 6. Homogeneous dehydrogenation catalysts for MeOH

Catalyst	Condition	TON	Ref.
$[Pd^{I}_{2}Cl_{2}(dpm)_{2}]$	64 °C, *hv*	156	21
$(Et_4N)_3[Ir^{IV}H(Sn^{II}Cl_3)_5]$	65 °C, *hv*	> 1.1	22
$[Rh^{I}(bpy)_2]Cl$	120 °C		23
$[Rh^{I}_{2}Cl_{2}(CO)(dpm)_{2}]$	64 °C, *hv*	130	21
$[Ru^{II}_{2}(OAc)_4Cl]/PEtPh_2$	65 °C	34	24
$[Ru^{II}_{2}(OAc)_4Cl]PPh_3$	65 °C	30	25
$[Ru^{II}(H)_2(N_2)(PPh_3)_3]$	150 °C, *hv*	> 1000	23
$[Ru^{II}(Sn^{II}Cl_3)_5]/PPh_3]$	65 °C	16	26
$Ru^{III}Cl_3/AgBF_4$	79 °C	> 1.1	27
$Ru^{III}Cl_3/Sn^{II}Cl_2$	140 °C	> 100	28
$[Ru^{II}Cl_2(PPh_3)_3]$	64 °C	> 9	29
$K[Ru^{I}(H)(top_2dad)]$	90 °C		30
$[Ru^{II}(H)(Cl)(CO)\{HN(CH_2CH_2PiPr_2)_2\}]$	91 °C	350000	31
$[Fe^{II}(H)(BH_4)(CO)\{HN(CH_2CH_2PiPr_2)_2\}]$	120 °C	6270	32

top_2dad = 1,4-bis(5*H*-dibenzo[*a*,*d*]cyclohepten-5-yl)-1,4-diazabuta-1,3-diene.

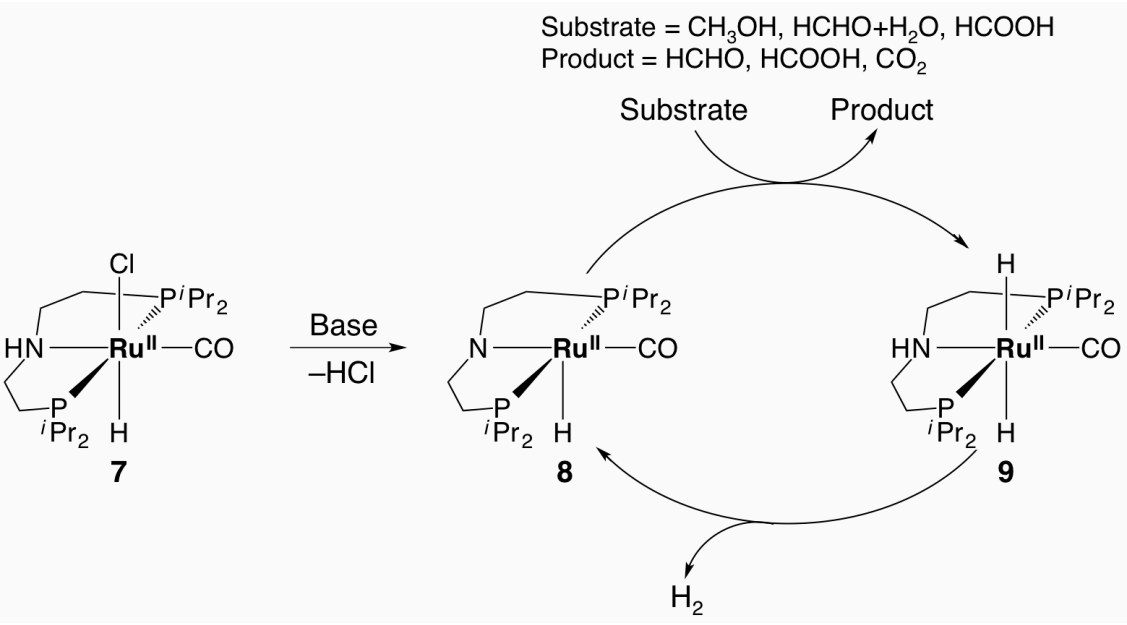
The elementary reactions of chemical hydrogen storage and release involve redox reactions. Hydrogen is split homolytically into two hydrogen radicals, or heterolytically into a hydride and a proton (eqs. 10 and 11). Hydrogen radicals, hydrides, and protons form chemical bonds with the storage material, and these bond-forming and cleavage processes have to be chemically reversible. Therefore, the judicious design of multi-electron and proton transfer is very important for the development of hydrogen storage materials.

$$H_2 \rightleftharpoons 2H\cdot \qquad \text{eq. 10}$$

$$H_2 \rightleftharpoons H^- + H^+ \qquad \text{eq. 11}$$

Beller *et al*. reported that $[Ru^{II}(H)(Cl)(CO)\{HN(CH_2CH_2PiPr_2)_2\}]$ (**7**) is able to catalytically dehydrogenate MeOH to produce hydrogen and CO_2 (Scheme 4).[31] Complex **7** is dissolved in MeOH/water under basic conditions, which leads to the formation of **8** under elimination of HCl. Complex **8**, which is the active species for the alcohol oxidation, incorporates a hydride and a proton from MeOH on the Ru center and ligand, respectively, to form **9** and formaldehyde (HCHO). Subsequently, hydrogen is released from in **9** to regenerate **8**. In this catalytic

Scheme 4. Proposed mechanism for dehydrogenation of MeOH catalyzed by **7** in ref. 31.



hydrogen evolution cycle, HCHO is oxidized to formic acid (HCO_2H) in the presence of water, and HCO_2H is oxidized to CO_2. In this system, the central Ru acts as a hydride-transfer site, while the ligand serves as a proton transfer site.

1-1-4. Limitations and Research Opportunities

Previous studies succeeded in producing oxygen or hydrogen, capitalizing on the multi-electron and proton transfer properties of molecular catalysts. However, these electron and proton transfer reactions usually require the presence of precious metal centers. Although the studies on these precious metal complexes have afforded a valuable stock knowledge regarding the generation, chemical storage, and release of hydrogen, the development of non-precious metal-based catalysts and materials is desirable on account of the aforementioned limitations of precious metals (*e.g.* high cost and limited availability). Moreover, the question of how exactly ligands coordinated to the metal center act as an electron and proton transfer sites is still not fully understood. Accordingly, the design and synthesis of new multi-electron and proton transfer systems is necessary.

1-2. Electron and Proton Transfer Reactions at Molecular Level

1-2-1. Theoretical Background for the Transfer of Electrons and Protons

Thermodynamical electron transfer reactions depend on the redox potential (E) of the electron donor and acceptor. E is usually expressed by the Nernst equation (eqs. 12 and 13):[33]

$$\mathrm{Red} \underset{+ne^-}{\overset{-ne^-}{\rightleftharpoons}} \mathrm{Ox}^{n+} \qquad \text{eq. 12}$$

$$E = E^\circ + \frac{RT}{nF} \ln \frac{[\mathrm{Ox}^{n+}]}{[\mathrm{Red}]} \qquad \text{eq. 13}$$

wherein Red, Ox, $E°$, n, F, R, T, [Red], and [Ox] refer to the reduced species, oxidized species, standard redox potential, number of electrons, Faraday constant, gas constant, temperature, concentration of the reduced species, and concentration of the oxidized species, respectively. Then, the change in Gibbs free energy (ΔG) between the redox potential of the electron donor (E_D) and that of the electron acceptor (E_A) may then be quantified by eq. 14.[33]

$$\Delta G = -nF(E_A - E_D) \qquad \text{eq. 14}$$

Eq. 14 indicates that E_D must be lower than E_A for thermodynamical electron transfer reactions to occur. In the case of oxygen evolution from the oxidation of water, for example, the use of an electron acceptor with a higher redox potential than that of water ($E°$ = 1.23 V vs. SHE) is necessary.[33] Conversely, in the case of the generation of hydrogen from the reduction of protons, the redox potential of the electron acceptor has to be lower than 0 V, for the electron transfer reactions to proceed thermodynamically.[33] Therefore, the design of molecular catalysts and materials, especially with respect to controlling their redox potentials is very important.

A kinetic theory of electron transfer reactions has been established by Marcus,[35] and the outer-sphere electron transfer reaction between the electron donor (D) and the acceptor (A) in solution is shown in eq. 15.

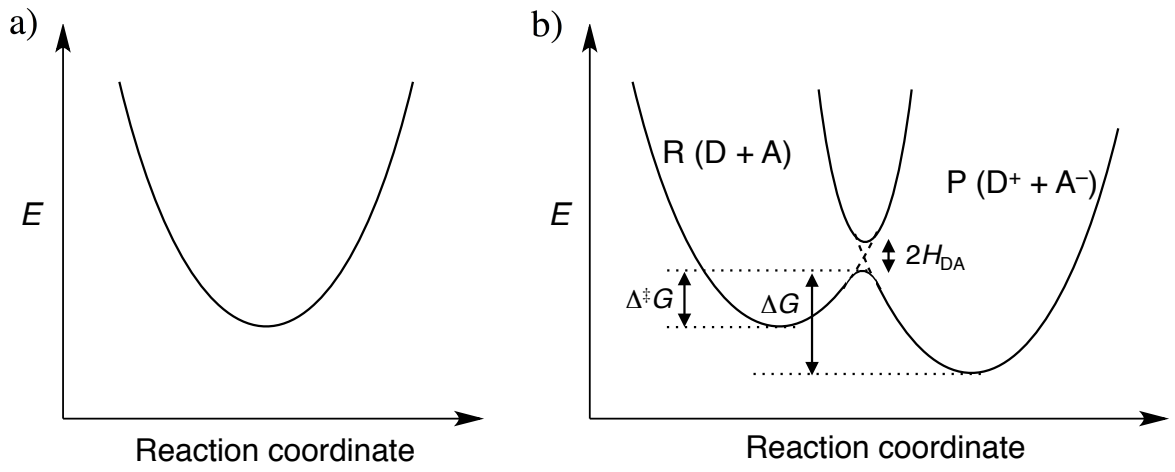


Figure 1. Potential curves for a) solvated species and b) electron transfer reactions from the R to the P state.

$$D + A \rightleftharpoons [D\cdots A] \rightleftharpoons [D^{+}\cdots A^{-}] \rightleftharpoons D^{+} + A^{-} \qquad \text{eq. 15}$$

In this theory, species D and A are solvated in solution, and the potential energy of the solvated molecules changes with the orientation of the solvent molecules according to the potential curve shown in Figure 1a. Solvated D and A approach each other by diffusion, and form an activated complex [D···A] *via* solvent reorientation and intramolecular nuclear displacement. Subsequently, electron transfer occurs from D to A in [D···A] to generate [$D^{+}\cdots A^{-}$], followed by relaxation and dissociation of [$D^{+}\cdots A^{-}$] to afford D^{+} and A^{-} as products (eq. 15).

For electron transfer reactions to occur in an activated complex, the potential energy of [D···A] and [$D^{+}\cdots A^{-}$] must be equal, as atoms cannot move accordingly to the Franck-Condon principle if the electron transfer rate is too high. Accordingly, identical potential energies are given for an activated complex between the solvated state before the reaction, *i.e.* R (D + A), and after the reaction P (A^{+} + D^{-}) (Figure 1b). In this context, it should be noted that, the potential energy gap between the ground and the excited state is given the electron coupling energy ($2H_{DA}$).

Usually, formation of the activated complex is assumed to be the rate-determining step in such electron transfer reactions; it can be described quantitatively by eqs. 16-20:

$$k_{et} = \kappa A \exp \frac{-\Delta^{\ddagger}G}{RT} \qquad \text{eq. 16}$$

$$\Delta^{\ddagger}G = w_R + \frac{\lambda}{4}\left(1 + \frac{\Delta G'}{\lambda}\right)^2 \qquad \text{eq. 17}$$

$$\Delta G' = \Delta G + w_R - w_P \qquad \text{eq. 18}$$

$$w_R = \frac{Z_D Z_A}{\varepsilon r_{DA}} \qquad \text{eq. 19}$$

$$w_P = \frac{Z_{D+} Z_{A-}}{\varepsilon r_{DA}} \qquad \text{eq. 20}$$

wherein, k_{et} κ, A, $\Delta^{\ddagger}G$, λ, w_R, w_P, Z, ε, and r_{DA} refer to the electron transfer rate, probability for the electron transfer to proceed (insulation coefficient), frequency factor, activation energy, reorientation energy, electrostatic work to ascertain the average distance for the activated complex between D and A, electrostatic work to remove D from A from the average distance of the activated complex to infinity, charge of chemical species, electrostatic permittivity, and the distance between D and A when the electron transfer occurs, respectively. The correlation between k_{et} and $\Delta G'$ can then be expressed by eq. 21:

$$\ln k_{et} = -\frac{\lambda}{4RT}\left(1 + \frac{\Delta G'}{\lambda}\right)^2 - \frac{w_R}{RT} + \ln \kappa A \qquad \text{eq. 21}$$

Figure 2 shows the parabola based on the relationship between $\ln k_{et}$ and $-\Delta G'$, exhibits a maximum value at $-\Delta G' = \lambda$. In the region $-\Delta G' < \lambda$, the so-called normal region, k_{et} increases

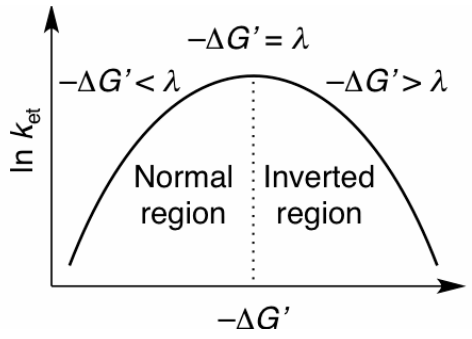


Figure 2. Relationship between ln k_{et} and $-\Delta G'$ based on eq. 21.

with an increase of $-\Delta G$, while k_{et} decreases with an increase of $-\Delta G'$ in the region $-\Delta G' > \lambda$, which is called inverted region. Marcus theory stipulates that electron transfer reactions are kinetically suppressed if ΔG is too large, even if the process is thermodynamically advantageous.

The index for proton transfer is generally defined by the acid dissociation constant (pK_a) described by eqs. 22 and 23,[33] wherein AH and A^- refer to the protonated and deprotonated species, respectively. Proton transfer occurs from the proton donor, with a small p*K*a value, to the proton acceptor with a large p*K*a value.

$$\mathrm{AH} \underset{+\mathrm{H}^-}{\overset{-\mathrm{H}^+}{\rightleftharpoons}} \mathrm{A}^- \qquad \text{eq. 22}$$

$$pK_a = -\log \frac{[\mathrm{H}^+][\mathrm{A}^-]}{[\mathrm{AH}]} \qquad \text{eq. 23}$$

Moreover, the proton transfer may be accompanied by an electron transfer, and the simultaneous transfer of protons and electrons is called proton-coupled electron transfer (eqs. 24-26),[33,34] wherein $RedH_m$ and m refer to the protonated reduced species and the number of protons, respectively. In transfer reactions that involved one electron and one proton, E increases linearly by 59 mV with an increase of the pH value. Accordingly, the water splitting reaction requires potentially 0.82 V for the evolution of oxygen, and of –0.41 V for the evolution of hydrogen at pH = 7.

$$\mathrm{RedH}_m \underset{+m\mathrm{H}^+}{\overset{-n\mathrm{e}^-}{\overset{-m\mathrm{H}^+}{\rightleftharpoons}}} \mathrm{Ox}^{n+} \qquad \text{eq. 24}$$

$$E = E^\circ + \frac{RT}{nF} \ln \frac{[\mathrm{Ox}^{n+}][\mathrm{H}^+]^m}{[\mathrm{RedH}_m]} \qquad \text{eq. 25}$$

$$E = E^\circ + \frac{2.3mRT}{nF} \mathrm{pH} + \frac{RT}{nF} \ln \frac{[\mathrm{Ox}^{n+}]}{[\mathrm{RedH}_m]} \qquad \text{eq. 26}$$

1-2-2. Multi-electron Transfer Reactions on Metal Centers

Several types of molecular compounds that exhibit multi-electron transfer activity on their metal centers have been developed,[36-45] and a representative selection of these is described below.

Multi-nuclear Transition Metal Complexes

The electrochemical properties of trinuclear Ru complexes such as $[Ru^{III}{}_3O(CH_3CO_2)_6(H_2O)_3]^+$, which has been synthesized by Wilkinson *et al*., are well documented.[36] For example, Meyer *et al*. reported that $[Ru^{III}{}_3O(CH_3CO_2)_6(py)_2(bpe)]^+$ (**10**$^+$) (py = pyridine, bpe = *trans*-1,2-bis (4-pyridyl)4-ethylene) exhibits a reversible five-step one-electron transfer process in acetonitrile (MeCN) (eq. 27),[37] and that all these electron transfers occur on the Ru centers.

$$[Ru^{III}Ru^{IV}{}_2]^{2-} \underset{+e^-}{\overset{-e^-}{\rightleftharpoons}} [Ru^{III}{}_2Ru^{IV}]^{-} \underset{+e^-}{\overset{-e^-}{\rightleftharpoons}} \underset{\mathbf{10}^+}{[Ru^{III}{}_3]^{+}} \underset{+e^-}{\overset{-e^-}{\rightleftharpoons}} [Ru^{II}Ru^{III}{}_2]^{0} \underset{+e^-}{\overset{-e^-}{\rightleftharpoons}} [Ru^{II}{}_2Ru^{III}]^{2+} \underset{+e^-}{\overset{-e^-}{\rightleftharpoons}} [Ru^{II}{}_3]^{3+} \qquad \text{eq. 27}$$

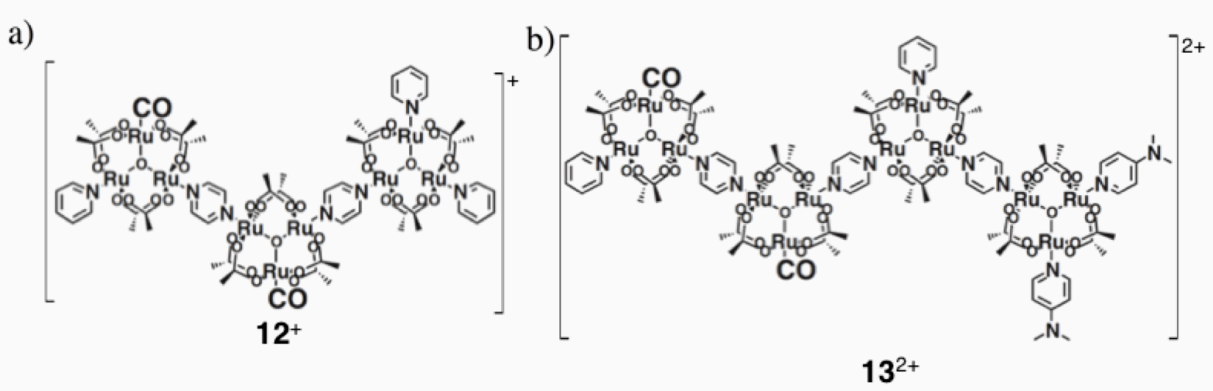
$$[Ru^{II}{}_2Ru^{III}\text{–}Ru^{II}{}_2Ru^{III}]^{2-} \underset{+e^-}{\overset{-e^-}{\rightleftharpoons}} [Ru^{II}{}_2Ru^{III}\text{–}Ru^{II}Ru^{III}{}_2]^{-} \underset{+e^-}{\overset{-e^-}{\rightleftharpoons}} \underset{\mathbf{11}}{[Ru^{II}Ru^{III}{}_2\text{–}Ru^{II}Ru^{III}{}_2]^{0}} \underset{+2e^-}{\overset{-2e^-}{\rightleftharpoons}} [Ru^{III}{}_3\text{–}Ru^{III}{}_3]^{2+} \underset{+2e^-}{\overset{-2e^-}{\rightleftharpoons}} [Ru^{III}{}_2Ru^{IV}\text{–}Ru^{III}{}_2Ru^{IV}]^{4+} \qquad \text{eq. 28}$$

Ito and Kubiak *et al*. synthesized dimers of trinuclear Ru complexes such as $[\{Ru^{II}Ru^{III}{}_2O(CH_3CO_2)_6(CO)(py)\}_2(\mu\text{-pz})]$ (**11**), by introduction of a bridging pyrazine (pz) ligand.[38] They discovered that complex **11** shows a reversible metal-centered two-step one-electron reduction, as well as a reversible two-step two-electron oxidation (eq. 28). The one-electron reduction suggests a step-wise electron transfer for the two trinuclear units in **11**, whereas the two-electron oxidation is indicative of a synchronized electron transfer on the units. Accordingly, the electronic interactions between the two trinuclear units depend on the

oxidation states of the metals.

Moreover, Ito and Yamaguchi *et al*. reported that trimers (**12**$^{+}$) and tetramers (**13**$^{2+}$) of this trinuclear complex show reversible metal-centered eleven-step twelve-electron transfer reactions, as well as reversible 14-step 15-electron transfer reactions (Chart 3).[39]

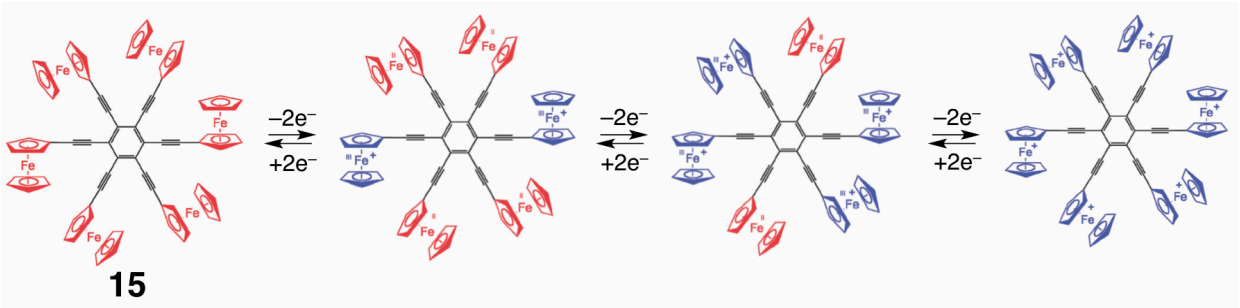
Chart 3. Structures of a) **12**$^{+}$ and b) **13**$^{2+}$ in ref. 39.



Ferrocenyldendrimers

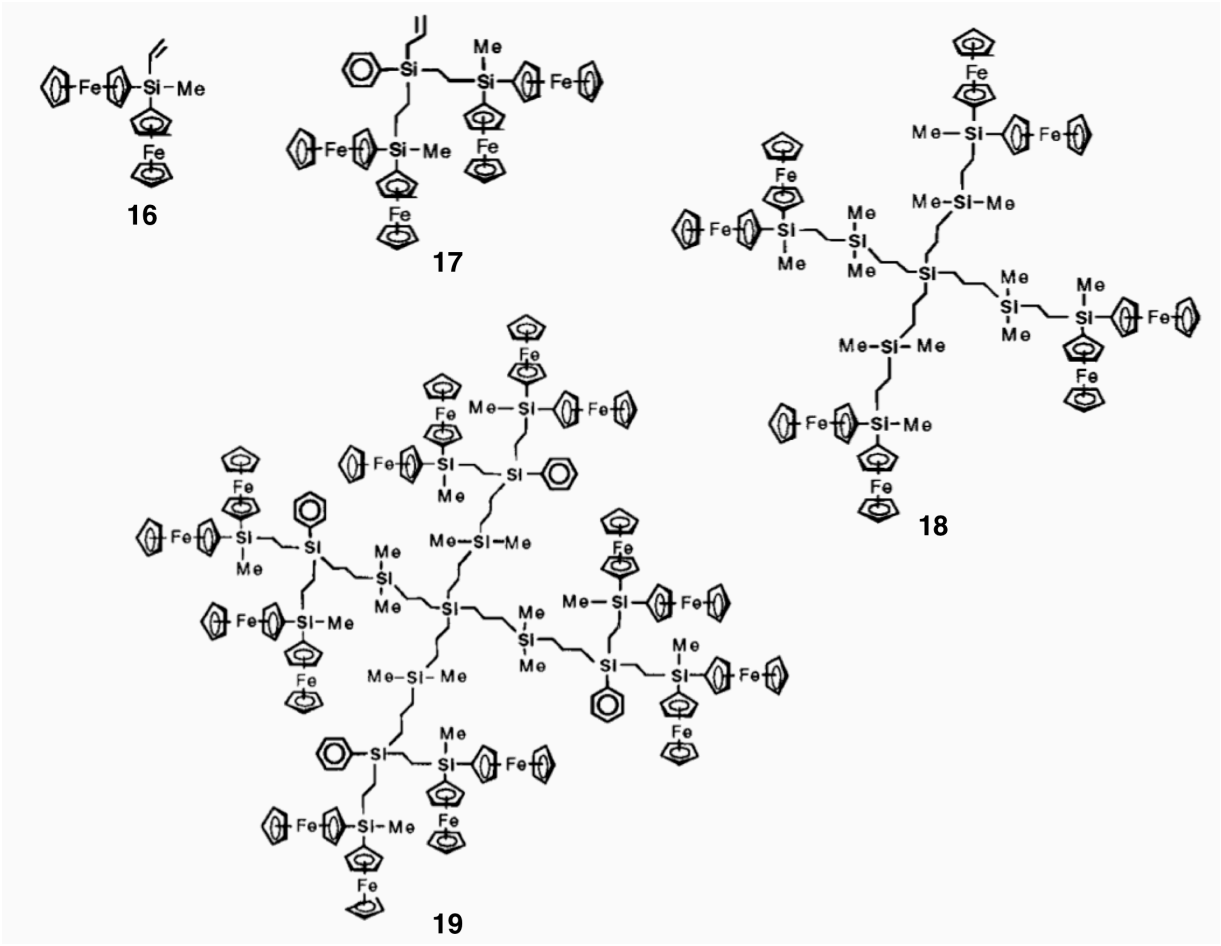
Ferrocene (Fc) and ferrocenium cation (Fc^{+}) are well known for their reversible Fe^{II}/Fe^{III} redox couple,[33,35] and Astruc *et al*. reported the multi-electron transfer properties of ferrocrnyldendrimers such as 1,3,5-tris(ferrocenylethynyl)benzene (**14**) and hexa (ferrocenylethynyl)benzene (**15**).[40] While the former contains three ferrocenyl units, and shows reversible three-step one-electron oxidations in dichloromethane (CH_2Cl_2), the latter contains six ferrocenyl units, and displays reversible three-step two-electron oxidations (Scheme 5). It was suggested that the ferrocenyldendrimers transfer electrons onto metal centers, and that the electronic interactions between the ferrocenyl moieties proceed *via* the central benzene ring.

Scheme 5. Reversible three-step two-electron redox scheme for **15** in ref. 40.



Cuadrado *et al*. reported another ferrocenyldendrimer, based on an organosilicon frameworks (**16**-**19**) (Chart 4).[41] For example, ferrocenyldendrimer **16** exhibits two-step one-electron redox properties in solution, due to the interactions between the ferrocenyl units. For the corresponding dimer (**17**), tetramer (**18**), and octamer (**19**), two-step two-, four-, and eight-electron transfer properties were observed, respectively.

Chart 4. Structures of **16**-**19** in ref. 41.



Polyoxometalates

Polyoxometalates (POMs), established by Pope and Müller, also show interesting multi-electron transfer reactions. For example, Kegging-type α-$[PMo^{VI}_{12}O_{40}]^{3-}$ ($\mathbf{20}^{3-}$) was reported to show reversible five-step two-electron reductions in 0.1 M aqueous HCl (eq. 29).[42] Since the four-electrons reduced species of $\mathbf{20}^{3-}$ ($\mathbf{20}^{+}$) contains inter-valence charge transfer (IVCT) bands based on the Mo centers, metal-centered processes should be involved in the

$$[PMo_{12}O_{40}]^{7+} \underset{+2e^-}{\overset{-2e^-}{\rightleftarrows}} [PMo_{12}O_{40}]^{5+} \underset{+2e^-}{\overset{-2e^-}{\rightleftarrows}} [PMo_{12}O_{40}]^{3+}$$
$$\underset{+2e^-}{\overset{-2e^-}{\rightleftarrows}} [PMo_{12}O_{40}]^{+} \underset{+2e^-}{\overset{-2e^-}{\rightleftarrows}} [PMo_{12}O_{40}]^{-} \underset{+2e^-}{\overset{-2e^-}{\rightleftarrows}} [PMo^{VI}_{12}O_{40}]^{3-} \quad \text{eq. 29}$$
$$\mathbf{20}^{+} \qquad\qquad \mathbf{20}^{3-}$$

electron transfer reactions.[43]

Keita *et al*. reported that α-$[P_2W^{VI}_{18}O_{62}]^{6-}$ ($\mathbf{21}^{6-}$) shows two-step one-electron reductions, and subsequent two-step two-electron reductions in 1 M aqueous HCl (eq. 30).[44] Conversely, in 12.4 M aqueous HCl, three-step two-electron transfers accompanied by positive shifts of the redox potentials were observed (eq. 31). The change of redox properties was rationalized in terms of a change of electronic interactions between the Mo atoms, on account of accepting a proton on the oxo ligands.

$$[P_2W_{18}O_{62}]^{0} \underset{+2e^-}{\overset{-2e^-}{\rightleftarrows}} [P_2W_{18}O_{62}]^{2-} \underset{+2e^-}{\overset{-2e^-}{\rightleftarrows}} [P_2W_{18}O_{62}]^{4-}$$
$$\underset{+e^-}{\overset{-e^-}{\rightleftarrows}} [P_2W_{18}O_{62}]^{5-} \underset{+e^-}{\overset{-e^-}{\rightleftarrows}} [P_2W^{VI}_{18}O_{62}]^{6-} \quad \text{eq. 30}$$
$$\mathbf{21}^{6-}$$

$$[P_2W_{18}O_{62}]^{0} \underset{+2e^-}{\overset{-2e^-}{\rightleftarrows}} [P_2W_{18}O_{62}]^{2-} \underset{+2e^-}{\overset{-2e^-}{\rightleftarrows}} [P_2W_{18}O_{62}]^{4-} \underset{+2e^-}{\overset{-2e^-}{\rightleftarrows}} [P_2W^{VI}_{18}O_{62}]^{6-} \quad \text{eq. 31}$$
$$\mathbf{21}^{6-}$$

Hill *et al*. reported reversible two-step one-electron reductions, as well as four-step one-electron oxidations on the Ru centers of $[\{Ru^{IV}_4O_4(OH)_2(H_2O)_4\}(\gamma\text{-}SiW^{VI}_{10}O_{36})_2]^{10-}$ ($\mathbf{22}^{10-}$) (eq. 32).[45] Interestingly, the reversible reduction of the W moiety was confirmed to proceed after the four-step reductions on the Ru centers.

$$[Ru^{III}_2Ru^{IV}_2]^{12-} \underset{+e^-}{\overset{-e^-}{\rightleftarrows}} [Ru^{III}Ru^{IV}_3]^{11-} \underset{+e^-}{\overset{-e^-}{\rightleftarrows}} [Ru^{IV}_4]^{10-} \underset{+e^-}{\overset{-e^-}{\rightleftarrows}} [Ru^{IV}_3Ru^{V}]^{9-}$$
$$\underset{+e^-}{\overset{-e^-}{\rightleftarrows}} [Ru^{IV}_2Ru^{V}_2]^{8-} \underset{+e^-}{\overset{-e^-}{\rightleftarrows}} [Ru^{IV}Ru^{V}_3]^{7-} \underset{+e^-}{\overset{-e^-}{\rightleftarrows}} [Ru^{V}_4]^{6-} \quad \text{eq. 32}$$
$$\mathbf{22}^{10-}$$

1-2-3. Multi-electron and Proton Transfer Reactions on Metal Centers

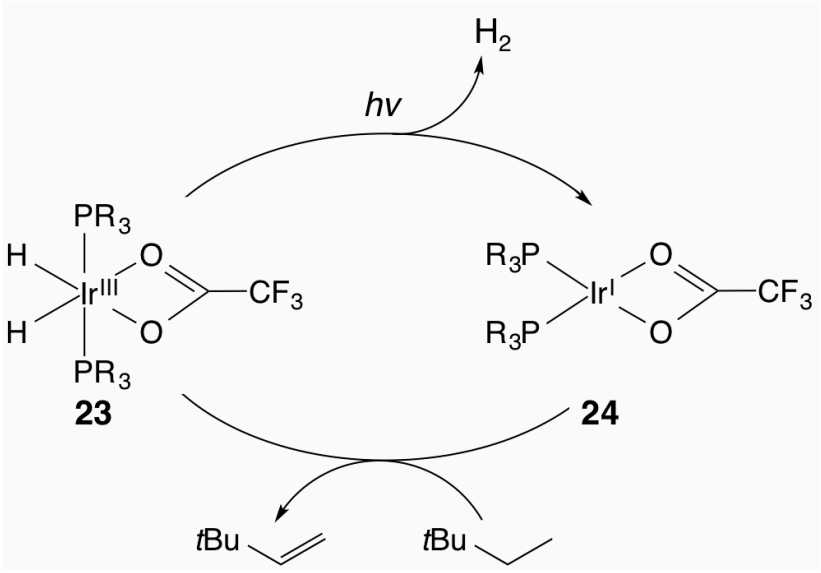
The abovementioned molecules with multi-electron transfer properties require the presence of multiple metal sites. On another hand, molecules with mono- or dinuclear precious metal

centers have been reported to exhibit metal-centered electron and proton transfer properties.[46-51] A representative selection of such complexes is discussed in the following section.

Ir Complexes

Crabtree *et al*. demonstrated that $[Ir^{III}(H)_2\{P(C_6H_{11})_3\}_2]$ (**23**) is able to catalyze the photochemical dehydrogenation of 2,2-dimethylbutane to generate 2,2-dimethyl-3-butene (Scheme 6).[46] The photochemical excitation of **23** affords hydrogen from the reductive elimination of two coordinated hydrides under concomitant formation of the Ir(I) species (**24**). The subsequent oxidative addition of 2,2-dimethylbutane furnishes 2,2-dimethyl-3-butene under regeneration of **23**. As this thermal dehydrogenation reaction proceeds *via* the oxidative addition reaction of 2,2-dimethylbutane, the Ir center acts as an electron and proton transfer site in this catalytic dehydrogenation.

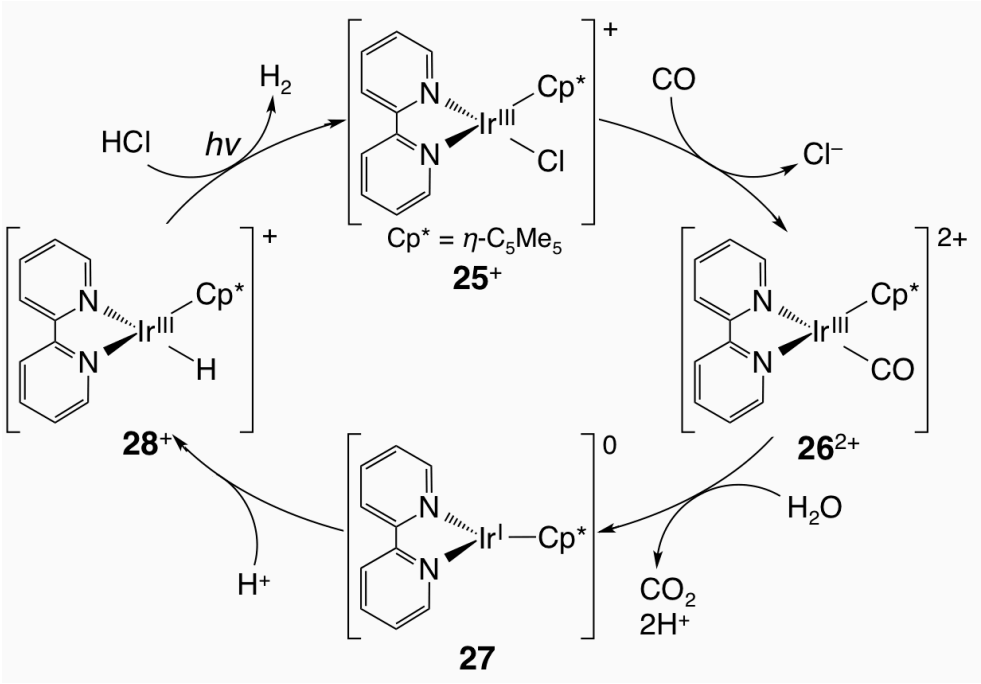
Scheme 6. Proposed electron and proton transfer mechanism of **23** in ref. 46.



$[Ir^{III}(\eta^5\text{-}C_5Me_5)(bpy)(Cl)]^+$ (**25**$^+$), reported by Ziessel, catalyzes the so-called water-gas shift reaction, which generates hydrogen and CO_2 from water and CO (Scheme 7).[47] Initially, a Cl^- ligand on the Ir center in **25**$^+$ is replaced with CO, resulting in the formation of **26**$^{2+}$. Subsequently, the reaction between water and **26**$^{2+}$ produces CO_2, protons, and Ir(I) species **27**.

This oxidation of CO proceeds by a two-electron reduction of the Ir(III) center, followed by an oxidative protonation of the Ir center in **27** to afford hydride species $\mathbf{28}^{+}$. Subsequently, the photochemical reaction of $\mathbf{28}^{+}$ generates hydrogen under simultaneous recovery of $\mathbf{25}^{+}$.

Scheme 7. Proposed electron and proton transfer mechanism of $\mathbf{25}^{+}$ in ref. 47.



Rh Complexes

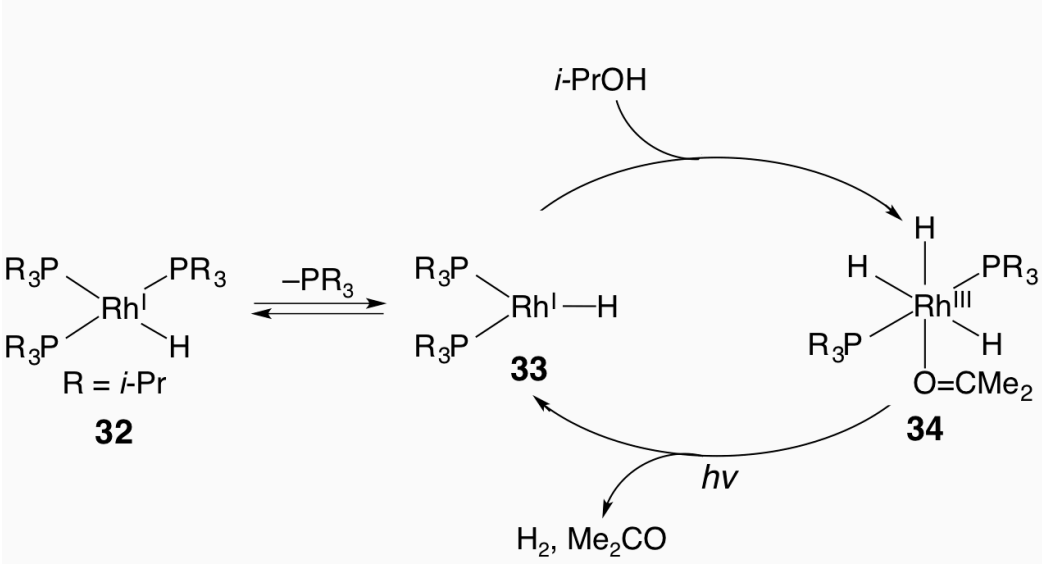
$[Rh^{I}(Cl)(PMe_3)_2(CO)]$ (**29**), reported by Goldman *et al*., was found to be susceptible to photochemical elimination of CO from the Rh center to afford **30** (eq. 33).[48] Complex **30** serves as the active species for the dehydrogenation of cycloalkanes (*cyclo*-C_nH_{2n}, n = 6-8) to furnish the corresponding cycloalkenes and the Rh (III) di-hydride **31** (eq. 34). As part of the dehydrogenation process, the cycloalkanes oxidatively add onto Rh center, is thermally promoted by a two-electron reduction of the Rh center together with the acceptance of two protons.

$$\underset{\mathbf{29}}{[Rh^{I}(Cl)(PMe_3)_2(CO)]} \xrightarrow{h\nu} \underset{\mathbf{30}}{[Rh^{I}(Cl)(PMe_3)_2]} + CO \qquad \text{eq. 33}$$

$$[Rh^{I}(Cl)(PMe_3)_2] + c\text{-}CH_2CH_2R \rightleftharpoons \underset{\mathbf{31}}{[Rh^{III}(H)_2(Cl)(PMe_3)_2]} + c\text{-}CH{=}CHR \qquad \text{eq. 34}$$

Cole-Hamilton *et al*. reported that the photochemical dehydrogenation of 2-propanol catalyzed by $[Rh^{I}(H)\{P(i\text{-}Pr)_3\}_3]$ (**32**) proceeds *via* electron and proton transfer on the Rh center (Scheme 8).[49] The active species for the photochemical dehydrogenation is **33**, which is obtained from **32** *via* elimination of a phosphine ligand. Complex **33** forms oxidative addition product **34** upon incorporation of two electrons and two protons from 2-propanol. Subsequently, photolytically induced excitation of **34** results in the generation of hydrogen and acetone, as well as in the regeneration of **33**.

Scheme 8. Proposed electron and proton transfer mechanism of **32** in ref. 49.



Ru Complexes

Bäckvall *et al*. reported the racemization of (*S*)-2-phenylpropanol with $[Ru^{II}(Cl)_2(PPh_3)_3]$ (**35**).[50] Complex **35** reacts with (*S*)-2-phenylpropanol in the presence of base (B) to afford di-hydride **36** and acetophenone (eq. 35). An ensuring reductive elimination from **36** generates Ru^0 species **37** and (*rac*)-2-phenylpropanol (eq. 36). Subsequently, complex **37** accepts two electrons and two protons from (*S*)-2-phenylpropanol to generate **36** under concomitant formation of acetophenone (eq. 37). The racemization reaction catalyzed by **36** is promoted by alternating oxidative addition and reductive elimination reactions on the Ru center.

$$[Ru^{II}(Cl)_2(PPh_3)_3] + 2(S)\text{-PhMeCHOH} \xrightarrow[-2BH^+]{2B} [Ru^{II}(H)_2(PPh_3)_3] + 2PhMeC{=}O \quad \text{eq. 35}$$
35 **36**

$$[Ru^{II}(H)_2(PPh_3)_3] + PhMeC{=}O \longrightarrow [Ru^{0}(PPh_3)_3] + (rac)\text{-PhMeCHOH} \quad \text{eq. 36}$$
37

$$[Ru^{0}(PPh_3)_3] + 2(S)\text{-PhMeCHOH} \longrightarrow [Ru^{II}(H)_2(PPh_3)_3] + PhMeC{=}O \quad \text{eq. 37}$$

Pt Complexes

The photochemical abstraction of hydrogen radicals from 2-propanol by $[Pt^{II}_2(POP)_4]^{4-}$ (**38**$^{4-}$) (POP = $P_2O_5H_2^{2-}$) was independently reported by Roundhill *et al.*,[51a] and Gray *et al.*[51b] Complex **38**$^{4-}$ forms a Pt–Pt bond, and is converted to the excited biradical state (^{3}dσ*-pσ) by photochemical excitation (eq. 38). The excited state of **38**$^{4-}$ abstracts a hydrogen radical from the α-carbon atom of 2-propanol to afford hydride species **39**$^{4-}$ and the corresponding radical (eq. 39). The photochemical abstraction of H radicals from **38**$^{4-}$ represents an electron and proton transfer reaction on the metal center, generating a Pt(III) hydride from the corresponding Pt(II) precursor.

$$[Pt^{II}_2(POP)_4]^{4-} \xrightarrow{h\nu} [Pt^{II}_2(POP)_4]^{4-*} \quad \text{eq. 38}$$
38^{4-}

$$[Pt^{II}_2(POP)_4]^{4-*} + (CH_3)_2CHOH \longrightarrow [Pt^{II}Pt^{III}(POP)_4(H)]^{4-} + (CH_3)_2COH\cdot \quad \text{eq. 39}$$
39^{4-}

1-2-4. Limitations and Perspectives

On one hand, multi-nuclear metal molecules, such as metal complexes, ferrocenyldendrimers, and polyoxometalates usually include a number of redox-active transition metal centers and thus represent molecules with multi-electron transfer properties. Even though multiple nucleation of is a powerful method to construct such multi-electron transfer molecules, the electron transfer activity depends predominantly on the nature of the metals, and regardless of the nature of the metal, a considerable amount of metals is required.

On the other hand, mono- or dinuclear precious metal complexes are well documented, especially regarding their electron and proton transfer properties. The key reactions for the

electron and proton transfer are the oxidative addition and reductive elimination of protons and/or hydrogen radicals on the metal centers, as well as hydride transfers from the metal center to the substrate. However, the electron and proton transfer activity largely depends on the nature of the precious metals, which are usually expensive and scarce.

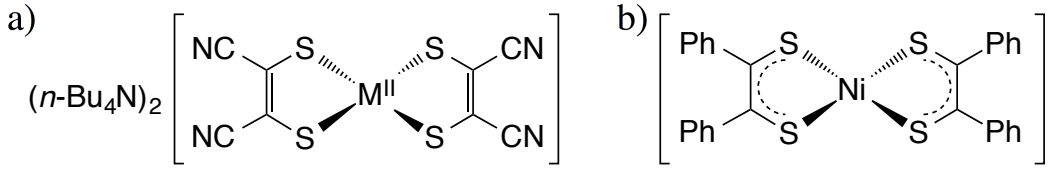
The new design and synthesis of new multi-electron and proton transfer systems, which do not depend on the potential activity of the metals, are therefore strongly desirable, especially from an economic perspective, but also with respect to a demand for advanced catalytic systems and materials. In many electron and proton transfer systems, ligands merely occupy the coordination sphere of the central metal, without getting significantly involved electron and proton transfer processes. If ligands effectively participate in electron and proton transfer reactions, multi-electron and proton transfer systems that are independent from the nature of the metals should be expected.

1-3. Redox-active Ligands

1-3-1. History of Redox-active Ligands

In the early 1960s, Gray *et al*.[52] and Schauzer *et al*.[53] reported metal complexes containing dithiolene ligands, which potentially have redox-active properties (Chart 5). Gray *et al*. discussed the magnetic properties of the square-planar bis-type complexes, $(n\text{-}Bu_4N)_2[M^{II}\{S_2C_2(CN)_2\}_2]$ (M = Co (**40**), Ni (**41**), Pt (**42**)) and proposed a dianionic state for theses ligands. Conversely, Schauzer *et al*. proposed a monoanionic radical state for the ligands in $[Ni(S_2C_2Ph_2)_2]$ (**43**). Since only few examples for ligands with a radical state had been known compared to ligands with a dianionic state, the redox activity of such ligands as well as their potential radical states became the subject of intensive investigation. Theses studies thus opened the research area for metal complexes with redox-active ligands, which has since become a widely studied field.

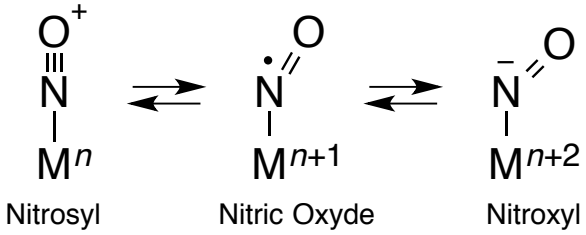
Chart 5. Structures of dithiolene complexes reported by a) Gray *et al*. and b) Schauzer *et al*. in refs. 52 and 53.



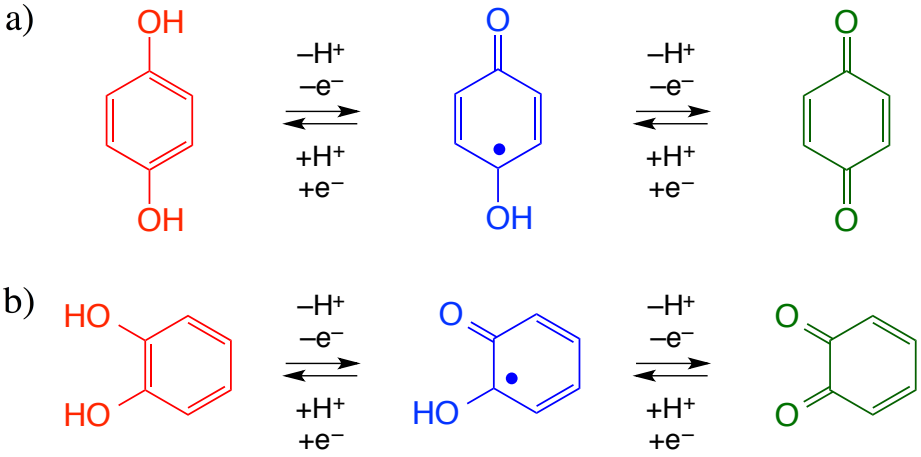
M = Co (**40**), Ni (**41**), Pt (**42**) **43**

In the early phase of research on redox-active ligands, Jørgensen pointed out that transition metal-coordinated NO ligands can adopt three electronically different states ($NO^+/NO^{\cdot}/NO^-$) (Scheme 9).[54] In his paper from 1966, he proposed to label ligands "innocent", if they allow oxidation states of the central atom to be defined unambiguously. Accordingly, ligands such as H_2O, NH_3, and Cl^- should be considered innocent. In contrast, the NO ligand is not innocent, as its charge distribution changes with the coordination geometry and environment in the complex. The importance of the Jørgensen's definition was recognized later, and the word "non-innocent" is still used for transition metal complexes with redox-active ligands, for which the electronic state cannot be defined unambiguously.[55]

Scheme 9. Three different electronical state of the non-innocent NO ligand in refs. 54 and 55.



Scheme 10. Schemes for the redox processes involving a) HQ and b) $CatH_2$ in ref. 56.



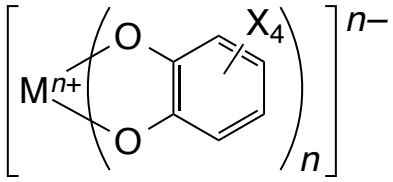
In the areas of organic chemistry and biochemistry, it is well documented that aromatic diols such as hydroquinone (HQ) and catechol ($CatH_2$) exhibit redox-activity.[56] HQ, for example, can be oxidized to *p*-semiquinone and *p*-quinone *via* consecutive one-electron transfer (Scheme 10a), while for $CatH_2$, semiquinone (SQH), and benzoquinone (BQ) are obtained (Scheme 10b).

In 1964, Eaton reported that SQ, which was generated from $CatH_2$ in aqueous solution by oxygen-induced *in-situ* oxidation, coordinates with several metal ions such as Na^+, Mg^{2+}, Ca^{2+}, Sr^{2+}, Ba^{2+}, Zn^{2+}, Cd^{2+}, La^{3+}, and Y^{3+}.[57] In 1966, Holm *et al*. reported the synthesis of several di- and trimeric Cat complexes (**44**-**54**) as well as Cat or SQ complexes (**55**-**57**), for which the electronic distribution states were not assigned (Chart 6).[58] Further details of the complexes were not reveled at this point.

In 1971, Balch *et al*. reported the generation of $[Pd^{II}(Cl_4Cat)(PPh_3)_2]$ (**58**) from the oxidative complexation of $Pd(PPh_3)_3$ and *o*-tetrachlorobenzoquinone (Cl_4BQ),[59a] and in 1975, Pierpont *et al*. reported a detailed structure for **58** (Figure 3).[59b] The single-crystal X-ray diffraction analysis of **58** revealed a square-planar coordination geometry for the Pd center, which is

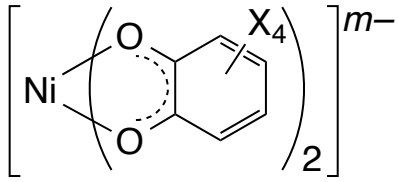
Chart 6. Structures of a) Cat and b) Cat/SQ metal complexes reported by Holm *et al*. in ref. 58.

a)



X = H; *n* = 2; M = Mg (**44**), Ni (**45**), Cu (**46**), Zn (**47**)
X = H; *n* = 3; M = Al (**48**)
X = Cl; *n* = 2; M = Co (**49**), Ni (**50**), Cu (**51**), Zn (**52**), Cd (**53**)
X = Cl; *n* = 3; M = Fe (**54**)

b)



X = H, *m* = 0 (**55**)
X = Cl, *m* = 0 (**56**)
X = Cl, *m* = 1 (**57**)

coordinated by Cl_4Cat and two molecules of PPh_3. Cl_4Cat exhibited a bidentate binding mode to the Pd center *via* the lone pairs of electrons on the oxygen atoms. The observed bond distances of 1.342(10) and 1.345(10) Å for the C–O bonds, and 1.366-1.407(12) Å for the C–C bonds in the $Cl_4C_6O_2$ ligand indicate a single bond and aromatic character, respectively, suggesting a fully reduced state of Cl_4Cat. In addition, the square-planar coordination geometry of the Pd-center indicates a d^8 electron configuration for Pd(II). Interestingly, complex **58** was the first Cat complex to be registered in the Cambridge Crystallographic Data Centre (CCDC).

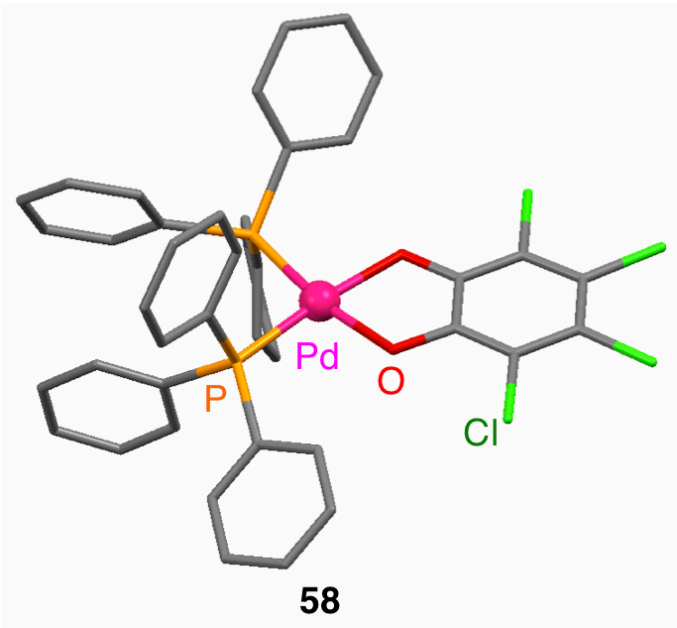
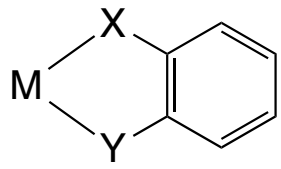


Figure 3. Molecular structure of **58** reported by Pierpont *et al*. in ref. 59b.

Since the 1970s, aforementioned Pierpont *et al*., Lever *et al*.,[60] Raymond *et al*.,[61] Wieghardt *et al*.,[62] and many other research groups have reported numerous metal complexes with redox-active ligands based on homo- or heterolytically *ortho*-disubstituted benzenes (Chart 7).[63] These ligands, which exhibit the substitution patterns X = Y = O; X = Y = S; X = Y = NH_2; X = O and Y = S; X = O and Y = NH_2; or X = S and Y = NH_2, are called Cat[64], 2-benzenedithiolato (Bdt),[65] *o*-phenylenediamine (Opda),[66] 2-mercaptophenolato (Mp),[67] 2-aminophenolato (ApH_2),[68] or 2-aminothiophenolato ($AtpH_2$),[69] respectively, and molecular structures, magnetic properties, spectroscopic and electrochemical properties of their transition metal complexes have been revealed.

Chart 7. Representative structures of transition metal complexes with redox-active homo- or heterolytically *ortho*-disubstituted benzene ligands.



X = Y = O (Cat) X = O, Y = S (Mp)
X = Y = S (Bdt) X = O, Y = NH_2 (ApH_2)
X = Y = NH_2 (Opda) X = S, Y = NH_2 ($AtpH_2$)

1-3-2. Electron and Proton Transfer Reactions of Metal Complexes with Redox-active Ligands

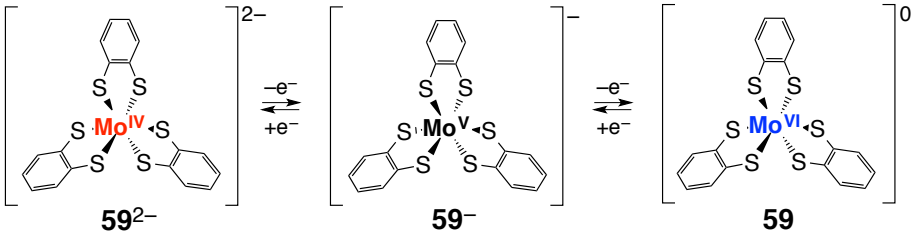
Metal complexes with redox-active ligands are able to transfer electrons and protons not only at the metal center but also at their ligands.[70-79] Previously reported studies in this area are discussed bellow.

Metal-centered Electron transfer

Mo complexes of Bdt represent a typical example for multi-electron transfer reactions at a metal center (Scheme 11).[70] Bennett *et al*. reported a trigonal prism structure for [$Mo^{VI}(Bdt)_3$]

(**59**), which was synthesized from $MoCl_5$ and Bdt^{2-} in the presence of oxygen.[70a] Subsequently, Cervilla *et al*. reported that complex **59** shows a reversible two-step one-electron reduction.[70b] Moreover, they reported $[Mo^{V}(Bdt)_3]^{-}$ (**59**$^{-}$) as the one-electron reduced species of **59**, which suggests a metal-centered reduction. Furthermore, Hahn reported the Mo(IV) complex $[Mo^{IV}(Bdt)_3]^{2-}$ (**59**$^{2-}$), whose HOMO, SOMO, and LUMO are located on the d-orbitals of Mo, thus facilitating metal-centered electron transfer reactions.

Scheme 11. Metal-centered redox processes of **59** in ref. 70.

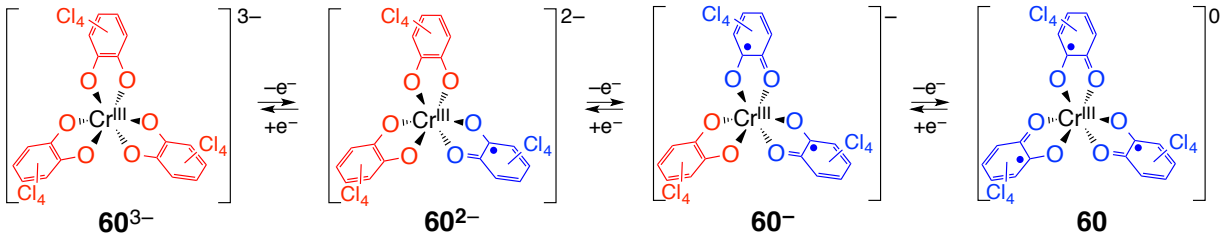


Ligand-centered Electron Transfer

While complex **59** shows metal-centered electron transfer reactions, $[Cr^{III}(Cl_4SQ)_3]$ (**60**), consisting of Cr(III) and tetrachlorosemiquinonato (Cl_4SQ) ligands, exhibits ligand-centered electron transfer reactions (Scheme 12).[71] Pierpont *et al*. reported the synthesis of **60** from the oxidative complexation between $Cr(CO)_6$ and Cl_4BQ.[71a] The observed C–O bond distances of 1.265-1.293(9) Å in **60** are indicative of an SQ character for the ligands. The reported redox properties of **60** revealed a reversible three-step one-electron reduction in CH_2Cl_2.[71b] Subsequently, Chang and Kitagawa *et al*. synthesized and characterized one- and two-electron reduced species of **60**.[71c] The one-electron reduced species $[Cr^{III}(Cl_4Cat)(Cl_4SQ)_2]^{-}$ (**60**$^{-}$), was prepared from **60** by addition of the oxidant Fc^{+}. The solid state and the spectroscopic behavior of **60**$^{-}$ in CH_2Cl_2 revealed the presence of IVCT bands in the NIR region, indicating a mixed-valence state of the ligands. The corresponding two-electron reduced species $[Cr^{III}(Cl_4Cat)_2(Cl_4SQ)]^{2-}$ (**60**$^{2-}$) was obtained from **60** by treatment with cobaltocenium cation, which is a stronger reductant than Fc^{+}. Complex **60**$^{2-}$ also showed IVCT bands, albeit at longer wavelengths region than **60**$^{-}$. These characteristics clearly demonstrate ligand-centered

electron transfer reactions for **60**. It should be noted that even though the corresponding three-electron reduced species $[Cr^{III}(Cl_4Cat)_3]^{3-}$ (**60**$^{3-}$) could not be isolated, an estimate of its properties could be obtained by extrapolation. The ligand-centered redox property were attributed to the frontier orbitals, *i.e.* π and π* ligand orbitals, because Cr(III) is a thermodynamically stable state in this coordination environment.

Scheme 12. Ligand-centered redox processes of **60** in ref 71.



Electron Transfer on Complexes with Delocalized Charge Distribution

For the Ru complex $[Ru(3,5\text{-}DTBQ)_3]$ (**61**) (3,5-DTB = 3,5-di-*tert*-butyl, Q means a quinoid-type ligand) reported by Pierpont *et al*., the charge distribution could not be assigned unambiguously, due to interactions between the d-orbitals of Ru the π-orbital of the ligands (Chart 8).[72] When the d-orbitals of the metal lie energetically higher than the π-orbital of the ligands, the frontier orbitals are located on the metal and *vice versa*. An example for the former case is **59**, while an example for the latter case is **60**. In **61**, however, metal d- and ligand π-orbital levels overlap, and therefore, the frontier orbitals are delocalized over the metal and the ligands. Accordingly, complex **61** exhibited a reversible one-electron oxidation as well as a two-step one-electron reduction (Scheme 13), and the intramolecular charge distribution in the redox isomers of **61** could not be defined.

Scheme 13. Redox processes of **61** in ref. 72.

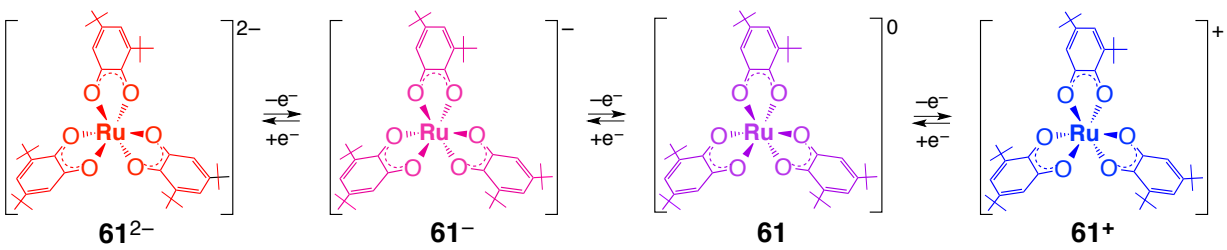
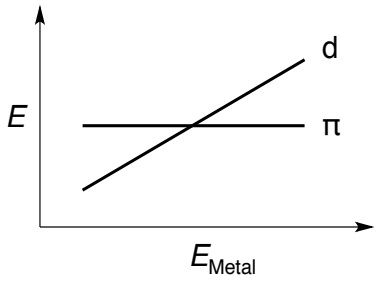


Chart 8. Diagram for the energy of the frontier orbitals of metal complexes with redox-active ligands in ref. 72.



Intramolecular Electron Transfer Induced by External Stimuli

The intramolecular charge distribution of metal complexes with redox-active ligands can be modulated by external stimuli. For example, Pierpont *et al*. reported that *ls*-[Co^{III}(3,5-DTBCat)(3,5-DTBSQ)(bpy)] (*ls*-**62**a) was reversibly converts to *hs*-[Co^{II}(3,5-DTBSQ)$_2$(bpy)] (*hs*-**62**b) upon heating (eq. 40).[73] This conversion was rationalized in terms of a valence tautomerization (VT), which is driven by the entropy change (ΔS) (eqs. 41 and 42) and involves an electron transfer from DTBCat to Co(III), resulting in the formation of DTBSQ and Cu(II), accompanied by a spin crossover reaction on the metal-center;[74]

$$\underset{ls\text{-}\mathbf{62}\text{a}}{ls\text{-}[Co^{III}(3,5\text{-DTBCat})(3,5\text{-DTBSQ})(bpy)]} \overset{\Delta}{\rightleftharpoons} \underset{hs\text{-}\mathbf{62}\text{b}}{hs\text{-}[Co^{II}(3,5\text{-DTBSQ})_2(bpy)]} \qquad \text{eq. 40}$$

$$\Delta G = \Delta H - T\Delta S_{total} \qquad \text{eq. 41}$$

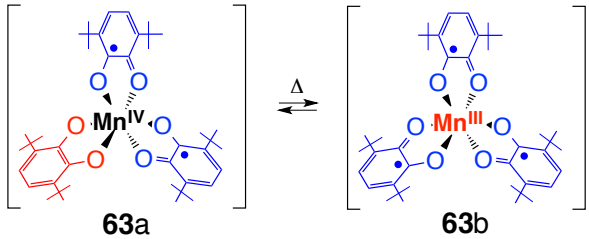
$$\Delta S_{total} \approx \Delta S_{vib} + \Delta S_{elect} \qquad \text{eq. 42}$$

where ΔH, T, ΔS_{total}, ΔS_{vib}, and ΔS_{elect} refer to the enthalpy change, temperature, total entropy change, entropy change of the vibrational mode, and the entropy change of the spin multiplicity in the reaction, respectively. The electron configuration of *ls*-**62**a, which exhibits an octahedral geometry, was assigned as $(d\pi)^6(d\sigma*)^0(\pi)^2(\pi)^1$, whereas that of *hs*-**62**b was assigned as $(d\pi)^5(d\sigma*)^2(\pi)^1(\pi)^1$. As two electrons reside in the $d\sigma*$ orbital of *hs*-**62**b, which is the antibonding orbital between Co and the ligands, the bond strength around the Co center decreases, resulting in an increase of ΔS_{vib} as well as ΔS_{elect}. The increased temperature induces a more negative value for ΔG, thus driving the VT reaction. Alternatively, the VT reaction

also proceeds when using light[75] or pressure[76] as external stimuli.

It is noteworthy that not only Co complexes exhibit such VT reactions, but also complexes of Mn, Fe, and Cu.[77] For example, Pierpont *et al*. reported that [Mn^{IV}(3,6-DTBCat)(3,6-DTBSq)$_2$] (**63**a) (3,6-DTBCat = 3,6-di-*tert*-butylcatecholato, 3,6-DTBSQ = 3,6-di-*tert*-butylsemiquinonato) afforded the valence tautomer [Mn^{III}(3,6-DTBSq)$_3$] (**63**b) from a thermally induced intramolecular electron transfer from DTBCat to Mn(IV) (Scheme 14).[78] This VT equilibrium is driven by the increase of ΔS_{vib} and ΔS_{elect} as a result of changing the electron configuration from $(d\pi)^3(d\sigma*)^0(\pi)^2(\pi)^1(\pi)^1$ to $(d\pi)^3(d\sigma*)^1(\pi)^1(\pi)^1(\pi)^1$.

Scheme 14. VT equilibrium of **63**a in ref. 78.



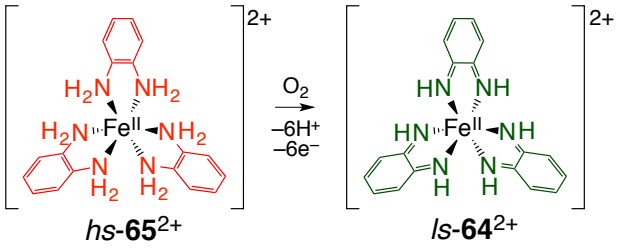
63a **63**b

Ligand-centered Electron and Proton Transfer

As redox-active ligands such as Opda contain protons on their coordinating nitrogen atoms, they are able to transfer these in addition to electrons. For example, Peng *et al*. reported that the mixture of Fe^{2+} and three equivalents of Opda afforded *ls*-[Fe^{II}(Bqdi)$_3$]$^{2+}$ (*ls*-**64**$^{2+}$) (Bqdi = *o*-benzoquinodiimine) in the presence of oxygen in anhydrous CH_2Cl_2 (Scheme 15).[79] Despite the reduced form of *ls*-**64**$^{2+}$ has not been reported so far, it was isolated and characterized *hs*-[Fe^{II}(Opda)$_3$] (*hs*-**65**$^{2+}$), which will be presented in Chapter 5. During this reaction, the oxidation state of the Fe center remained unaffected, but the Opda ligand was oxidized to Bqdi which is the by two electrons and two protons oxidized Opda analogue. In this context, it should be noted that Bqdi is able to accommodate strongly back-donation from the *ls*-Fe(II) center, which has a $(d\pi)^6$ electron configuration. Therefore, the preferential oxidation of Opda in this reaction was rationalized in terms of a higher level of the Opda π-orbital with respect to the d-orbital of the metal center on one hand, as well as in terms of a stabilization of the *ls*-Fe(II)

center from the Bqdi ligand on the other.

Scheme 15. Multi-electron and proton transfer of *hs*-**65**$^{2+}$ in ref. 79.



hs-**65**$^{2+}$ *ls*-**64**$^{2+}$

1-3-3. Catalytic Activity of Metal Complexes with Redox-active Ligands

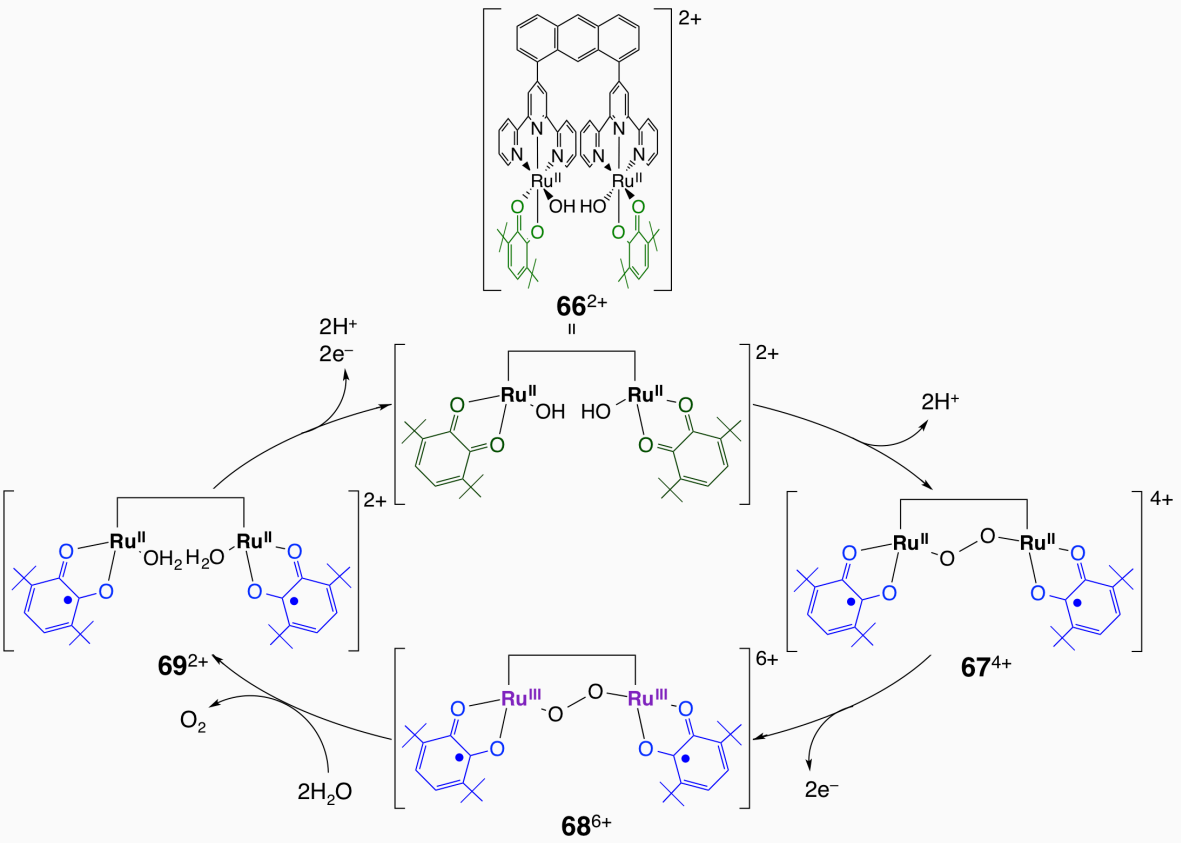
In the 1990s, the first reports on the catalytic activity of metal complexes with redox-active ligands started emerge,[80-83] and since then, the electron transfer properties of the ligands have been identified as key features for the catalytic activity. The following section describes a representative selection of such studies.

Oxidation of Water

Tanaka *et al*. reported that a dinuclear Ru complex of BQ (**66**$^{2+}$) can act as a catalyst for the generation of oxygen from water.[84a] In this reaction, the redox-active ligands serve as electron- and hole-pooling sites (Scheme 16).[84b] The proposed reaction mechanism is initiated by the deprotonation of the two hydroxo ligands in **66**$^{2+}$, which affords the corresponding peroxo complex (**67**$^{4+}$) with a O–O bond. Upon formation of the O–O bond, each BQ ligand accepts one electron from the peroxo ligand, and a subsequent electrochemical oxidation removes one electron from each Ru canter to afford **68**$^{6+}$. Then, in the presence of water, each electron-deficient Ru(III)-center in **68**$^{6+}$ accepts one electron from the peroxo ligand to furnish **69**$^{2+}$ under concomitant extrusion of oxygen. Complex **66**$^{2+}$ is then recovered from a ligand-centered electrochemical oxidation of **69**$^{2+}$. Interestingly, both the Ru centers, as well as the redox-active ligands, act as electron-accepting sites for water. Although this catalytic oxidation of water depends on the non-innocent behavior between Ru and BQ, the use of redox-active ligands as electron- and hole-pooling sites afforded a new design guide, which is

different from the electron transfer systems based on metal centers.

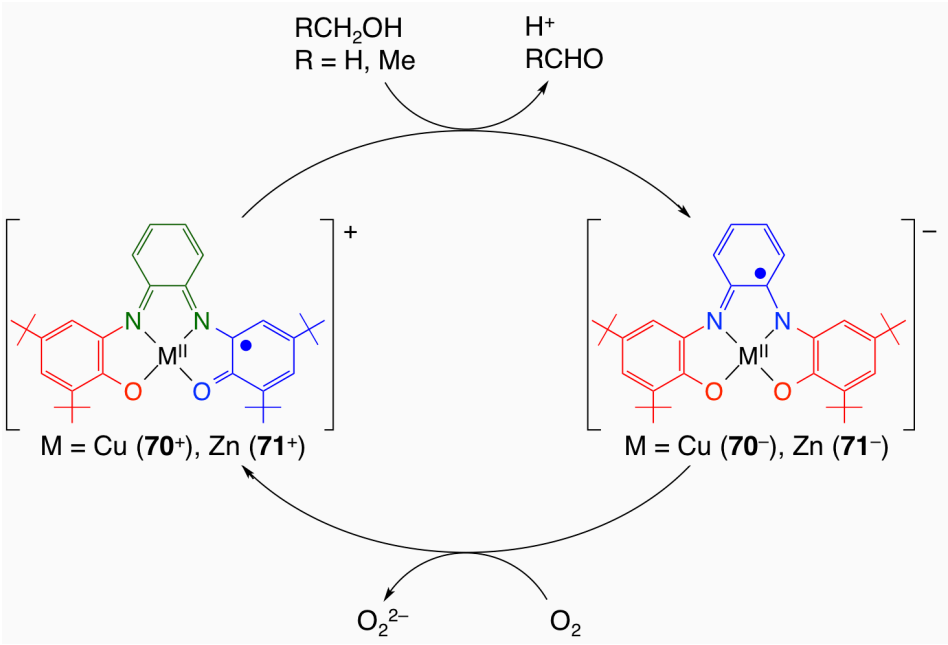
Scheme 16. Proposed mechanism for the oxidation of water catalyzed by $\mathbf{66}^{2+}$ in ref. 84.



Oxidation of Alcohols

Chaudhuri and Wieghardt *et al*. reported that primary alcohols, *e.g*. MeOH and ethanol (EtOH), are susceptible to oxidation in the presence of catalysts based on Zn or Cu complexes of a Bqdi derivative with Ap and iminosemiquinonato (ISQ) functionality ($\mathbf{70}^{+}$ and $\mathbf{71}^{+}$) (scheme 17).[85a] Dissolving $\mathbf{70}^{+}$ and $\mathbf{71}^{+}$ in alcohol affords the two electron-reduced species $\mathbf{70}^{-}$ and $\mathbf{71}^{-}$ under simultaneous generation of the corresponding aldehyde. During this reaction, the oxidation state of the metal center remains unchanged, while the ligand is subject to a two-electron reduction. A subsequent oxidation using oxygen regenerates $\mathbf{70}^{+}$ and $\mathbf{71}^{+}$ and affords hydrogen peroxide. It should be noted that all electron transfer processes in this reaction are ligand-centered and that similar reactions using redox-active ligands were reported by Chaudhuri *et al*.,[85b,85c] as well as by Safaei and Storr *et al*.[85d]

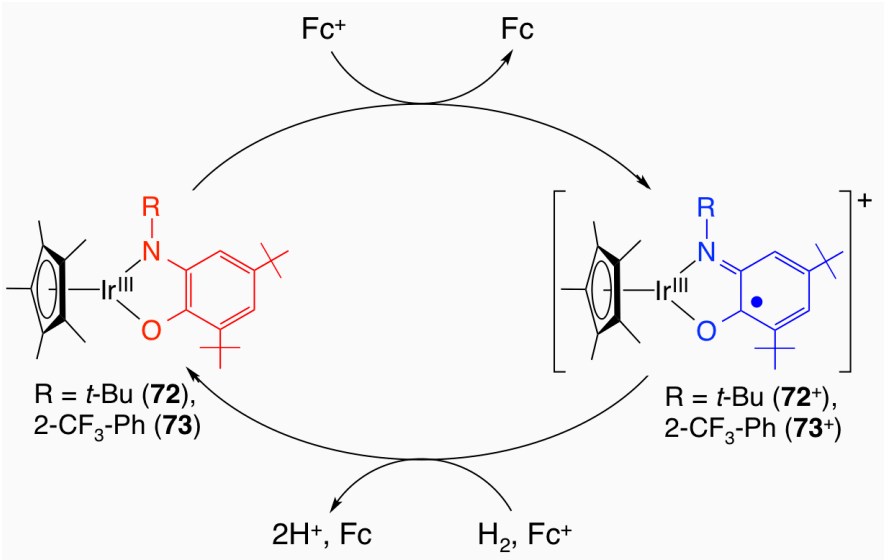
Scheme 17. Proposed mechanism for the oxidation of alcohols catalyzed by **70**$^+$ and **71**$^+$ in ref. 85a.



Oxidation of Hydrogen

Rauchfuss *et al*. reported that Ir complexes of Ap derivatives, containing additional substituents on the nitrogen atom (**72** and **73**), are able to catalyze the oxidation of hydrogen in the presence of sacrificial Fc^+ oxidants (Scheme 18).[86] Initially, **72** and **73** are subjected to the ligand-centered oxidation by Fc^+ to afford the corresponding one-electron oxidized species **72**$^+$ and **73**$^+$, which contain ISQ moieties. Subsequently, hydrogen is oxidized by **72**$^+$ and **73**$^+$ in

Scheme 18. Proposed mechanism for the oxidation of hydrogen catalyzed by **72** and **73** in ref. 86.

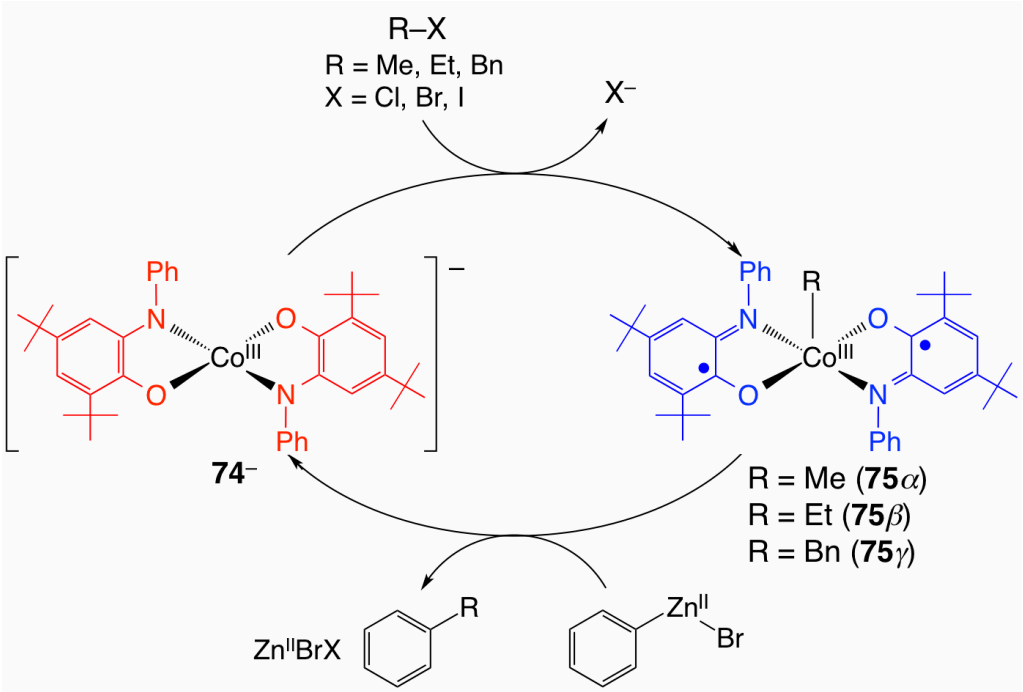


the presence of Fc^+, furnishing Fc, protons, as well as **72** and **73**. In this oxidation of hydrogen, each $\mathbf{72}^+$ and $\mathbf{73}^+$ accepts one electron from hydrogen on the ligand, while the other electron is accepted by Fc^+.

Cross-coupling Reactions

Sorper *et al*. reported that a square-planer Co complex with an Ap-type ligand ($\mathbf{74}^-$) was able to act as a catalyst for C–C cross-coupling reaction (Scheme 19).[87] Alkyl halides are added onto the Co center of $\mathbf{74}^-$ to afford **75**, in which the coordinated carbanion occupies the apical position. The oxidation state of the Co(III) was maintained, whereas each Ap ligand was subjected to a one-electron oxidation, resulting in the formation of the corresponding ISQ derivative. Accordingly, the Ap ligands perform the role of an electron donor during the oxidative addition. The subsequent nucleophilic addition of phenylzincbromide onto **75** furnished the cross-coupling product (R–Ph) *via* a reductive elimination under simultaneous regeneration of $\mathbf{74}^-$. It should be noted that during the reductive elimination, each ISQ ligand acts as a one-electron acceptor.

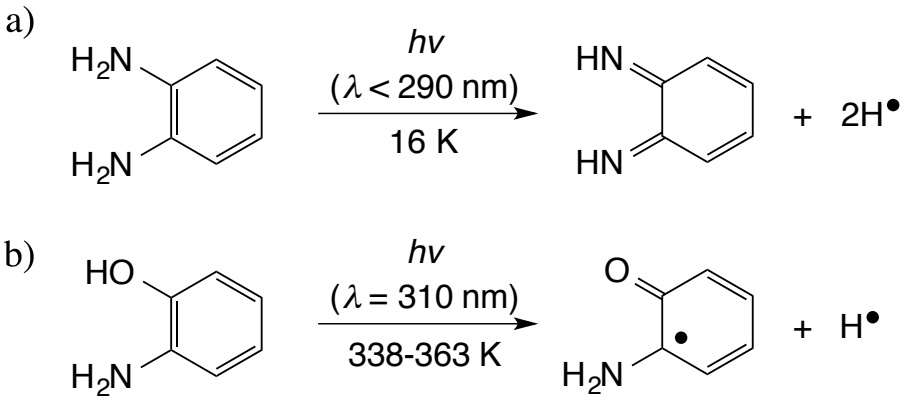
Scheme 19. Proposed mechanism for cross-coupling reactions catalyzed by $\mathbf{74}^-$ in ref. 87.



1-3-4. Photochemical Reactions of Aromatic Amines and Alcohols

Aromatic amines and alcohols represented by Opda and ApH_2, are known to show interesting photochemical reactivity.[88-90] In 2004, Nakata *et al*. reported that Opda generated Bqdi and two H radicals *via* a photochemical excitation, generated by UV light absorption in an argon matrix (Scheme 20a).[88] During the photochemical reaction, the N–H bonds in the amino groups were homolytically cleaved in the excited state.

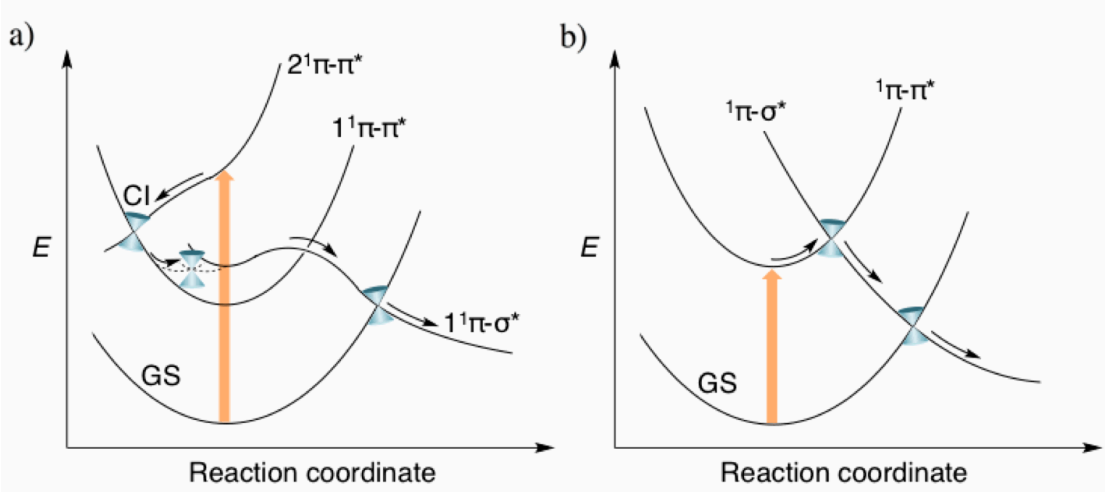
Scheme 20. Photochemical hydrogen atom transfer processes of a) Opda and b) ApH_2 in refs. 88 and 90.



A photochemical mechanism of the cleavage of the N–H bonds in aniline, which exhibits a similar framework to Opda, was reported by Stavros *et al*. in 2012 (Chart 9a).[89] The three excited states of aniline, *i.e*. $1^1\pi$-π^*, $1^1\pi$-σ^*, (the antibonding orbital of the N–H bond), and $2^1\pi$-π^*, were located at 4.22 (294 nm), 4.61 (269.5 nm), and 5.10 eV (240 nm) relative to the ground state. The π-π^* transition was allowed, whereas the π-σ^* transition represents a forbidden process. In the $2^1\pi$-π^* excited state, an internal conversion leads to afford a $1^1\pi$-π^* excited state *via* conical intersection (CI) during the relaxation process, and this excited state was further transferred to a $1^1\pi$-σ^* excited state *via* another CI. In the $1^1\pi$-σ^* excited state, an N-H bond is activated, and H and anilino radicals are generated from the homolytic cleavage of the N–H bonds. Conversely, in the case of a lower energy level, *e.g*. for the $1^1\pi$-π^* transition, an N–H bond cannot be photochemically activated, because the CI level between the $1^1\pi$-π^* and the $1^1\pi$-σ^* state is considerably higher than that of the initially formed $1^1\pi$-π^* excited state.

In 2014, Pino *et al*. reported a mechanism for the photochemical generation of H radicals from ApH_2, which contains aromatic amine as well as alcohol functionality (Scheme 20b, Chart 9b).[90] The two excited states of ApH_2, *i.e*. $^1\pi$-π^* and $^1\pi$-σ^* (an antibonding orbital of the O–H bond), were located at 4.54 (273 nm) and 4.64 eV (267 nm) relative to the ground state. The activation barrier between the $^1\pi$-π^* and $^1\pi$-σ^* excited states was found to be relatively small (0.2 eV), as they were mixed at the CI *via* their out-of-plane vibration modes. Accordingly, the H radical and ISQ were produced from the homolytic cleavage of the activated O–H bond after the $^1\pi$-π^* excited state was converted to $^1\pi$-σ^* excited state.

Chart 9. Energy diagrams for the photochemical reactions of a) aniline and b) ApH_2 in refs. 89 and 90.



1-4. Electron and Proton Transfer Reactions of Group 8 Metal Complexes

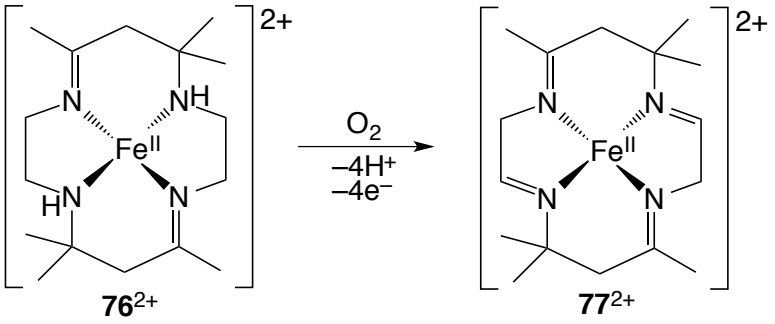
1-4-1. The Conversion of Amines to Imines

Metal complexes of group 8 (Fe, Ru, and Os) with amine ligands can be oxidized to produce the corresponding imine complexes,[91] and a selection of representative studies is discussed bellow.

Fe Complexes

In 1972, Busch *et al*. reported that $[Fe^{II}(htd)]^{2+}$ (**76**$^{2+}$), a Fe complex containing the tetradentate planar amine ligand 5,7,7,12,14-hexamethyl-1,4,8,11-tetraazacyclotetradeca-4,11-diene (htd), can be oxidized by oxygen (Scheme 21).[92] This oxidation generates $[Fe^{II}(htt)]^{2+}$ (**77**$^{2+}$) (htt = 5,7,7,12,14-hexamethyl-1,4,8,11-tetraazacyclotetradeca-1,4,8,11-tetraene), which is the by four electrons and four protons oxidized form of htd. Most importantly, the oxidation state of the Fe center does not change during this reaction, whereas each of the two amino moieties is oxidized to the corresponding imines.

Scheme 21. Ligand-centered oxidation of **76**$^{2+}$ under concomitant proton transfer in ref. 92.



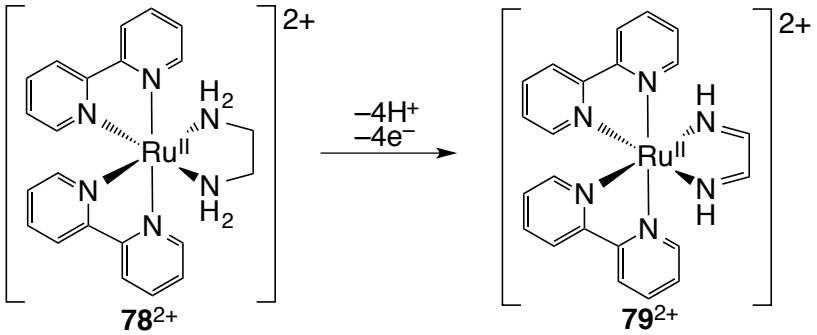
76^{2+} **77**$^{2+}$

Ru Complexes

In 1976, Meyer *et al*. reported the electrochemical oxidation reaction of $[Ru^{II}(bpy)_2(en)]^{2+}$ (**78**$^{2+}$) (en = ethylenediamine) to afford **79**$^{2+}$ with an oxidized en ligand (Scheme 22).[93] For this oxidation. $[Ru^{III}(bpy)_2(en)]^{3+}$ was proposed as the active species, and it was suggested that Ru(III) could extract one electron from the en ligand, prior to furnishing **79**$^{2+}$ in a subsequent

electrochemical oxidation.

Scheme 22. Electrochemical ligand-centered oxidation of **78**$^{2+}$ accompanied by proton transfer in ref. 93.

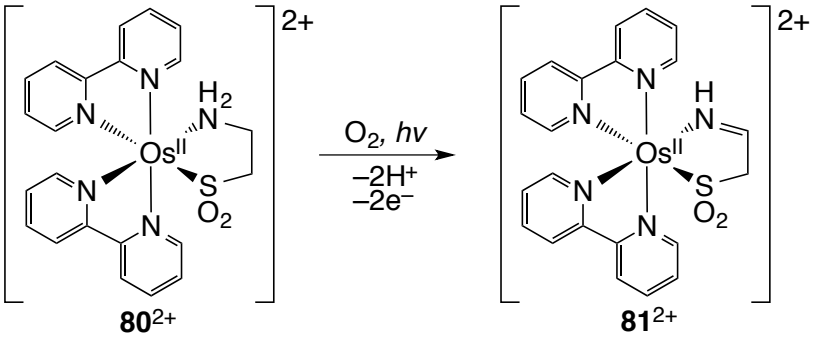


78^{2+} **79**$^{2+}$

Os Complexes

In 2011, Konno *et al*. reported that the photochemical oxidation of [Os^{II}(bpy)$_2$(2-aminoethanesulfinate)]$^{2+}$ (**80**$^{2+}$) is induced by a metal-to-ligand charge transfer excitation in **80**$^{2+}$, which generates an Os(III) excited state (Scheme 23).[94] Subsequently, this excited state is able to oxidize the amine moiety of the ligand in the presence of oxygen to generate [Os^{II}(bpy)$_2$(2-iminoethanesulfinate)]$^{2+}$ (**81**$^{2+}$) *via* the transfer of two electrons and two protons. Here, it should be noted that the oxidation state of Os center is identical before and after the reaction, but changes in the intermediate state.

Scheme 23. Photochemical ligand-centered oxidation of **80**$^{2+}$ under simultaneous proton transfer in ref. 94.



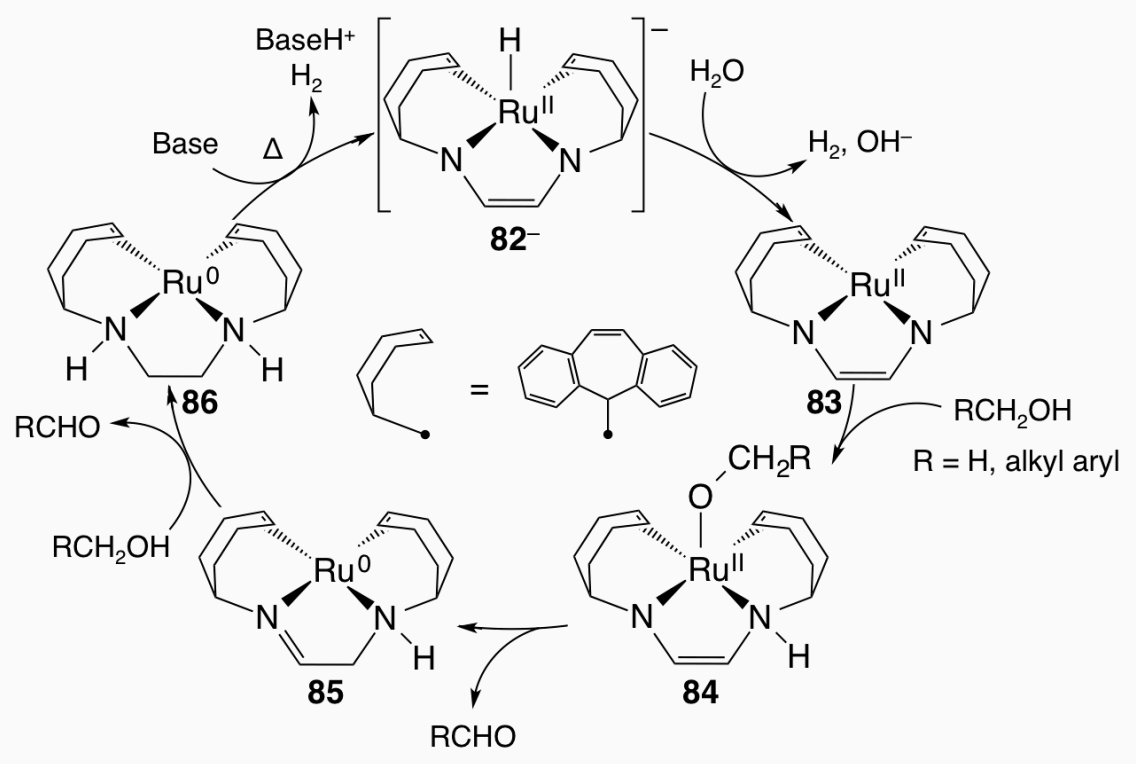
80^{2+} **81**$^{2+}$

1-4-2. Hydrogen Evolution Reactions based on Amine/imine Conversions

In 2013, Grützmacher *et al*. reported that Ru complex **82**$^{-}$ catalyzes the thermal evolution of hydrogen from alcohols including MeOH upon addition of water to afford **83** (Scheme 24).[30]

The evolved hydrogen originates from the Ru-bound hydride in **82**$^-$ and a water-derived proton. Moreover, the alcohol O–H bond is activated and the corresponding alkoxide coordinated onto the Ru-center in **83**, while the proton is transferred to the amine moiety of **83**, thus affording **84**. Subsequently, the Ru(II) center accepts two electrons from the alkoxide, and the α-carbone of the amino group accepts a proton from the alkoxide to afford **85** and the corresponding aldehyde. By accepting two more electrons and two protons from another alcohol molecule, **86** is generated, before a subsequent thermal reaction in the presence of base liberates hydrogen as well as proton from the ligand to regenerate **82**$^-$. Remarkably, during this alcohol dehydrogenation, the ligand performs the role of an electron- and proton-pooling site. In the reaction from **83** to **84**, the ligand acts as a two-proton acceptor, whereas it accepts two electrons and two protons in the reaction from **84** to **85**. Furthermore, it converts its two electrons and two protons into hydrogen in the reaction from **86** to **82**$^-$.

Scheme 24. Alcohol dehydrogenation catalyzed by **82**$^-$ in ref. 30.



1-4-3. Limitations and Perspective

Group 8 transition metal complexes with amine ligands may show activity for the conversion of amines to imines by aerobic, electrochemical, or photochemical oxidation.[91-94] Additionally, in the case of **82**$^{-}$, a ligand-centered conversion of electrons and protons into hydrogen was successfully accomplished.[30] However, this alcohol dehydrogenation still requires the presence of the relatively rare transition metal Ru, as well as substantial amounts of thermal energy. Therefore, the development of non-precious metal catalysts that operate at low temperatures remains an attractive research target. Considering the previous discussion, the use of ligands that act as electron- and proton-pooling and exhibit photochemical functionality represents a promising strategy.

1-5. Metalloligands

1-5-1. The Discovery of Metalloligands

In 1966, Cohen and Hoard *et al*. reported the synthesis and structural characterization of $[Ca\{Fe^{III}(dcta)(H_2O)\}_2(H_2O)_5]$ (**87**) (dcta = 1,2-diaminocyclohexane-N,N'-tetraacetato), a seven-coordinate Fe complex (Figure 4).[95] In this complex, the hexadentate dcta ligand does not adopt its sterically preferred octahedral coordination; instead a distorted trigonal prism geometry is imposed on the Fe-center. The distortion position at the Fe center is occupied by a water molecule, resulting in the formation of $[Fe^{III}(dcta)(H_2O)]^-$, which exhibits a trigonal prismatic, square face-monocapped structure. Conversely, Ca^{2+} counter cation is coordinated by five water molecules in a planar pentagonal geometry, as well as by oxygen atoms of $[Fe^{III}(dcta)(H_2O)]^-$ carboxylates at the apical positions, generating a distorted pentagonal bipyramidal structure. The distance of 2.380(1) Å, which was observed between Ca^{2+} and the dcta oxygen atoms is shorter than the sum of ionic radius of Ca^{2+} (1.00 Å)[96] and the van der waals radius of the oxygen atom (1.52 Å),[97] thus unambiguously confirming the formation of a $Ca–O_{dcta}$ coordination bond. Two molecules of $[Fe^{III}(dcta)(H_2O)]^-$ bind to Ca^{2+} and thus form a discrete complex in **87**. Thereafter, transition metal complexes with the ability to coordinate other metals *via* peripheral coordination sites in their ligands are called metalloligands (MLs).[98]

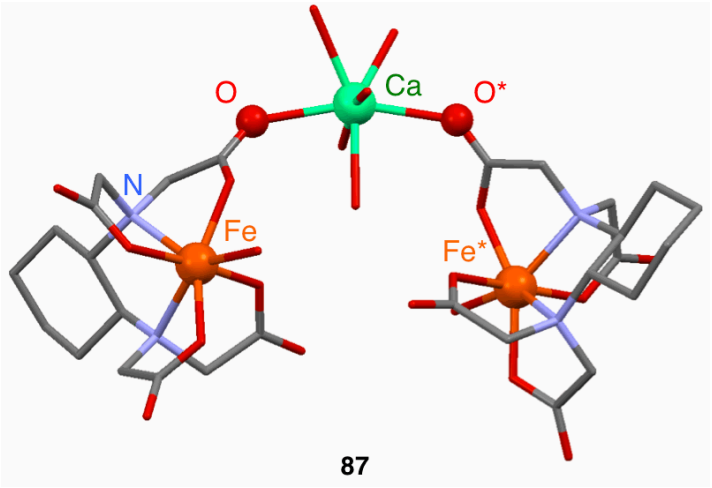


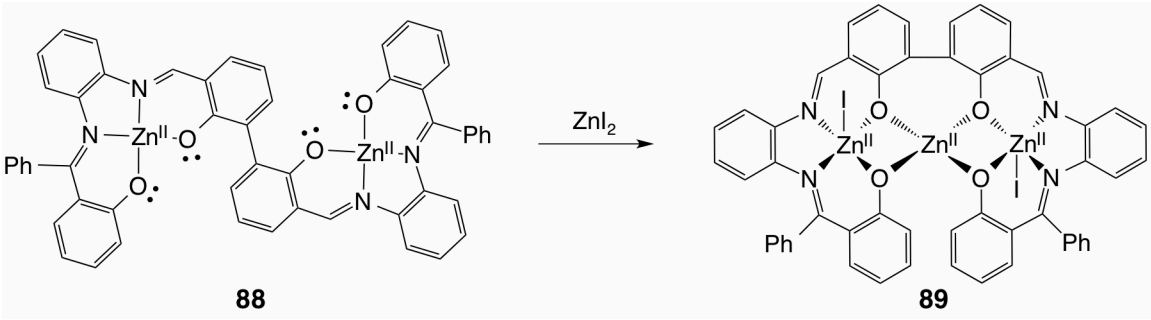
Figure 4. Molecular Structure of **87** in ref. 95.

1-5-2. Catalytic Activity of Multi-nuclear Metal Complexes based on MLs

Recently, several reactions that use multi-nuclear complexes with MLs as molecular catalysts have been reported.[99-102] For example, Kleiji *et al*. reported that the dinuclear Zn complex **88** reacts with ZnI_2 to furnish the trinuclear complex **89**, in which Zn^{2+} is coordinated by the lone pairs of the ligand oxygen atoms (Scheme 25).[99] Subsequently, this trinuclear complex **89** is able to catalyze the insertion of CO_2 into epoxy moieties in (methoxymethyl)oxirane to furnish propylene carbonate derivatives (eq. 43). While this catalytic reaction progresses efficiently (conversion rate = 100%), mechanistic details of this reaction, *e.g*. the activation site of the substrates, or the role of the ML, still remain to be determined.

$$CH_3OCH_2CH_2CH_2O \xrightarrow[CO_2]{\textbf{89}} CH_3OCH_2CH_2CH_2O_2CO \qquad \text{eq. 43}$$
18 h, 85 ºC

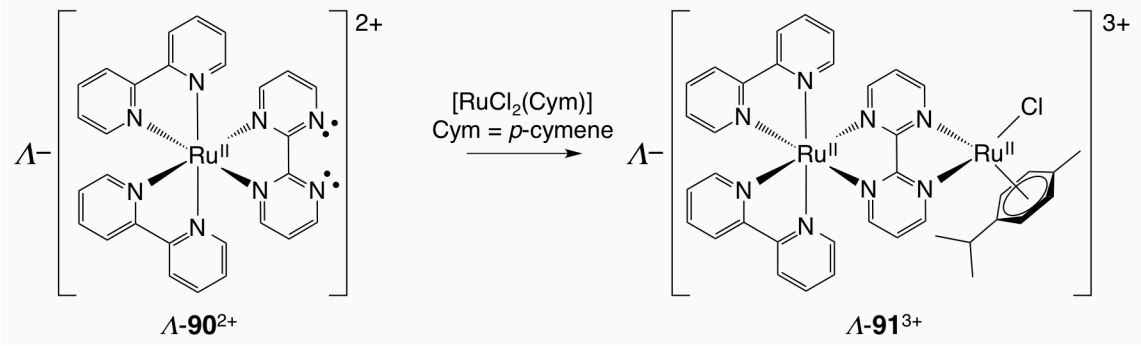
Scheme 25. Coordination of **88** to Zn^{2+} in ref. 99.



Hamelin *et al*. reported that optically active *Λ*-Ru complex *Λ*-**90**$^{2+}$ can act as an ML to form dinuclear Ru complex *Λ*-**91**$^{3+}$, which accommodates a guest metal (Ru^{2+}) *via* the lone pairs on the nitrogen atoms of the 2,2'-bipyrimidine ligand (Scheme 26).[100] Complex *Λ*-**91**$^{3+}$ serves as a moderately selective catalyst (26%ee) for the reduction of phenylmethylketone to (*S*)-1-methyl-2-phenylethanol (eq. 44). Even though the optical selectivity in this catalytic reaction was attributed to the chirality of the ML, the detals of the reaction mechanism ware not discussed.

$$C_6H_5COCH_3 \xrightarrow[\substack{HCO_2Na \\ 24\ h,\ 80\ ^\circ C}]{\Lambda\text{-}\mathbf{91}^{3+}} (S)\text{-}C_6H_5CHOHCH_3 \qquad \text{eq. 44}$$

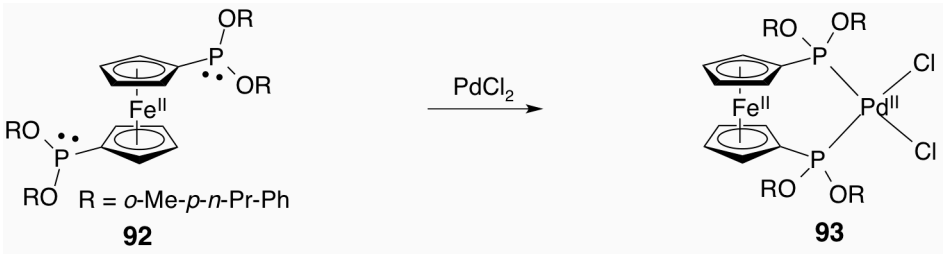
Scheme 26. Coordination of Λ-$\mathbf{90}^{2+}$ to Ru^{2+} in ref. 100.



A complexation reaction using Fc derivative **92** as an ML was reported by Balakrishna *et al*.[101] Complex **92** binds Pd^{2+} *via* the lone pairs on the phosphorus atoms to afford heterobimetallic dinuclear complex **93** (Scheme 27), which showed catalytic activity (TON = 150,000) in a cross-coupling reaction (eq. 45).

$$p\text{-}CN\text{-}C_6H_4Br + C_6H_5B(OH)_2 \xrightarrow[\substack{K_2CO_3 \\ 60\ ^\circ C}]{\mathbf{93}} 4\text{-}CN\text{-}1\text{-}C_6H_5\text{-}C_6H_4 \qquad \text{eq. 45}$$

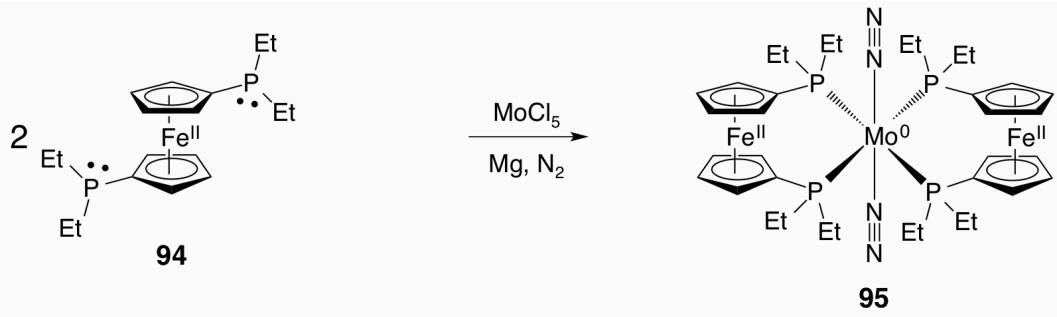
Scheme 27. Coordination of **92** to Pd^{2+} in ref. 101.



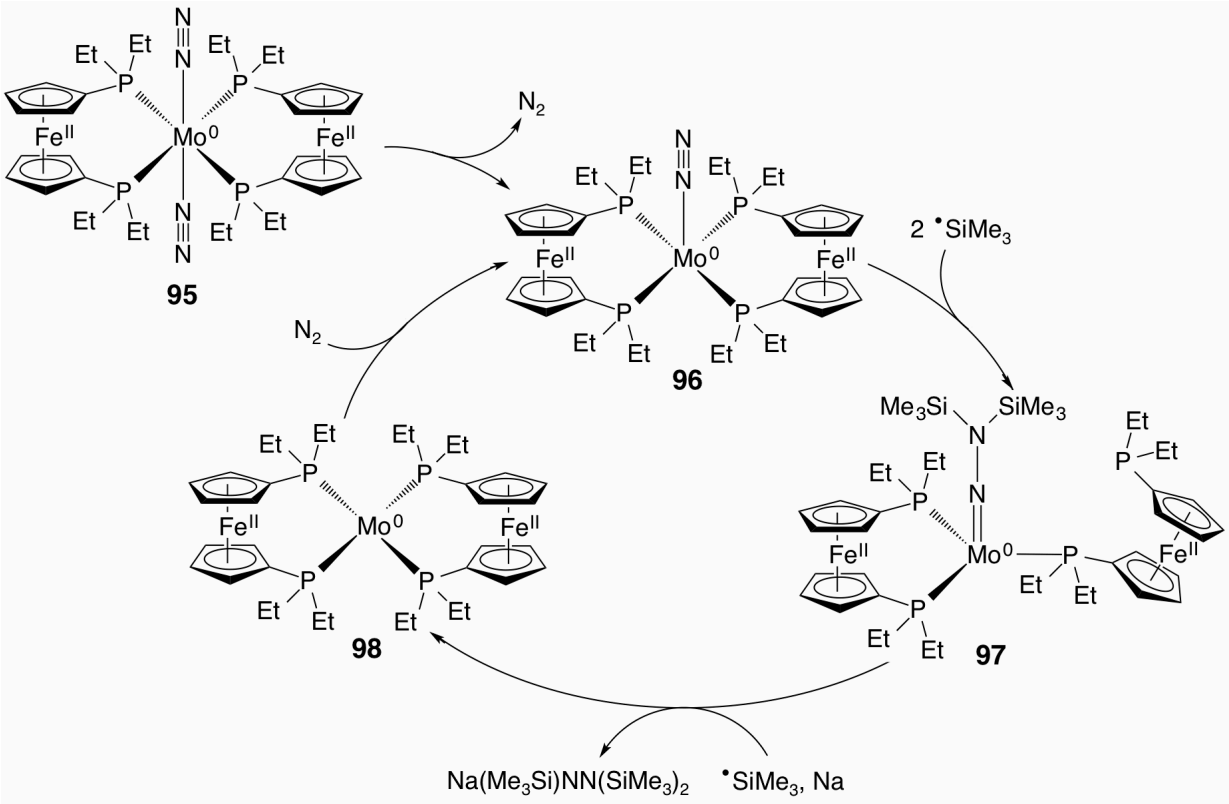
Nishhibayashi and Yoshizawa *et al*. synthesized Fc derivative **94** and **95**, which is a discrete complex of **94** and $MoCl_5$, in the presence of Mg under an atmosphere of N_2 (Scheme 28).[102a] Complex **95** can catalyze the reduction of N_2 with sodium metal using Me_3SiCl as a sacrificial reagents (Scheme 29).[102b] During the first step of the catalytic reaction, the elimination of one N_2 molecule from the Mo-center affords coordinatively unsaturated **96**. Subsequently, two

·$SiMe_3$ radicals attack the coordinated N_2 to form **97**, before further addition of a ·$SiMe_3$ radical furnishes $Na(Me_3Si)NN(SiMe_3)_2$ under formation of **98**, from which **96** is regenerated by addition of a molecule of N_2. It should be noted that the fully reduced nitrogen species, $N(SiMe_3)_3$, may be obtained from $Na(Me_3Si)NN(SiMe_3)_2$ in a subsequent reaction. In this catalytic reaction, the MLs serve as electron-donating groups to promote the reaction on the Mo-center.

Scheme 28. Coordination of **94** and N_2 to Mo^0 in ref. 102a.



Scheme 29. Proposed mechanism for the catalytic reduction of N_2 by **95** in ref. 102b.



1-5-3. Redox-active Metalloligands

Redox-active metalloligands (RMLs) represent a subgroup of MLs. RMLs have been reported to generate multi-nuclear complexes by binding guest metals, to form *e.g.* discrete structure or coordination polymers, that display metal-centered, ligand-centered, or guest metal-centered redox properties (Table 7). Details on representative studies that investigated RMLs are discussed bellow.

Table. 7. Multi-nuclear complexes containing RMLs and associated redox properties

Multi-nuclear Complex	Redox centres	Ref.
100^{+}	Metal	103
101^{+}	Metal	103
103^{2+}	Metal, Ligand	104
104^{2+}	Ligand, Guest metal	104
$[Fe^{II}\{Ni^{II}(bme\text{-}daco)\}(NO)_2]$	Metal, Guest metal	105
$[Ag^{I}\{Ti^{IV}{}_2Cp_4(\mu\text{-}SC_3H_6S)_2\}]^{+}$	Metal	106
$[Cu^{I}\{Mo^{0}(CO)_3(\kappa^3\text{-}N\text{-}Si(3,5\text{-}dmpz)_3)\}Cl]^{-}$	Metal	107
$[Ir^{I}\{Ru^{II}(Cp)(\kappa^3\text{-}N\text{-}C(pz)_3(CNH))\}(Cl)_2(cod)]^{+}$	Metal	108
$[Cu^{I}\{Ru^{II}(Cp)(\kappa^3\text{-}N\text{-}C(pz)_3)\}(SiMe_3)]$	Metal, Guest metal	109
$[Zr^{IV}\{Ni^{II}(tenb)\}_2]$	Metal	110
$[M^{I}(dme)_2\{Ru^{III}{}_2(3,5\text{-}DTBCat)_4\}]$ (M = Li, K, Rb)	Metal	111
$[Zn^{II}\{Ru^{III}(acac)_2(pz)_2\}_2]$	Metal	112
$[Ru^{II}\{Ru^{III}(acac)_2(pz)_2\}_2(CO)]$	Metal, Guest metal	112
$[Fe^{III}\{Fe^{III}(thpa)_3\}]^{3+}$	Metal	113
$[Cu^{I}\{5\text{-}Fc\text{-}2,2'\text{-}5'\text{-}Me\text{-}bpy\}(6,6'\text{-}dmes\text{-}bpy)]^{+}$	Metal, Guest metal	114
$[Pd^{II}{}_3\{Ru^{II}(pytpy)_2\}_3(Cl)_6]^{6+}$	Metal, Ligand, Guest metal	115

bme-daco = bismercaptoethanediazacyclooctane, 3,5-dmpz = 3,5-dimethylpyrazolyl, pz = pyrazolyl, cod = 1,5-cyclooctadiene, tenb = 3,3'-[(1,1,2,2-tetramethyl-1,2-ethanediyl)-bis-(nitrilomethylidyne)]-bis-1,2-benzenediolato, thpa = tris(6-hydroxymethyl-2-pyridylmethyl) amine), dmes = dimesityl, pytpy = 4-(3-pyridyl)-tpy.

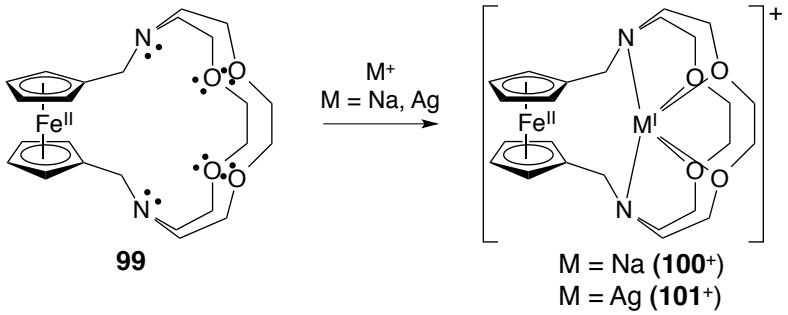
Metal-centered Electron transfers of Redox-active Metalloligands

In 1991 and 1992, Lynn, Kaifer, and Gokel *et al*. reported that a Fc derivative with a cryptand moiety (**99**) can coordinate Na^{+} and Ag^{+} cations *via* the lone pairs on nitrogen and oxygen to

form the dinuclear heterobimetallic complexes **100**$^+$ and **101**$^+$ (Scheme 30).[103] In MeCN, **100**$^+$ and **101**$^+$ exhibited reversible one-electron oxidation processes at the Fe center (eq. 46), and in the equilibrium, **100**$^+$ and **101**$^+$ is partly dissociate from the RML (**99**). Coordination of **99** to Na^+ or Ag^+ led to positive shift of the redox potential of the RML by 0.19 or 0.28 V, respectively, and this shift suggests that the metal-centered redox properties of the RML is significantly perturbed by the positive charge of the guest metal ions.

$$\begin{array}{ccc} [\{Fe^{II}\}\text{–}M^{I}]^{+} & \underset{+e^-}{\overset{-e^-}{\rightleftharpoons}} & [\{Fe^{III}\}\text{–}M^{I}]^{2+} \\ \updownarrow & & \updownarrow \\ [Fe^{II}] + M^{+} & \underset{+e^-}{\overset{-e^-}{\rightleftharpoons}} & [Fe^{III}]^{+} + M^{+} \\ \textbf{99} & & \end{array} \qquad \text{eq. 46}$$

Scheme 30. Coordination of **99** to Na^+ or Ag^+ in ref. 103.



99

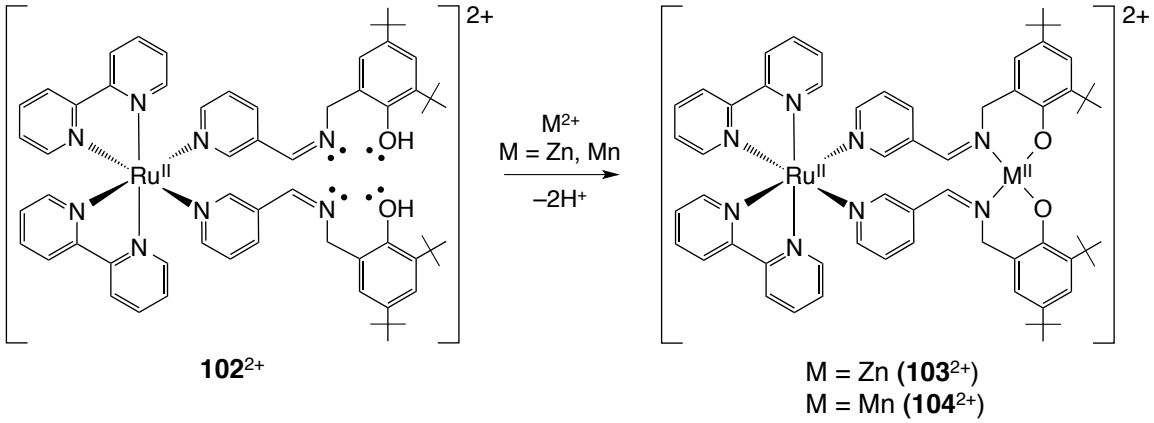
M = Na (**100**$^+$)
M = Ag (**101**$^+$)

Ligand-centered Electron Transfers of Redox-active Metalloligands

In 2010, Hamelin *et al*. reported that Ru complex **102**$^{2+}$ produces heterobimetallic dinuclear complex **103**$^{2+}$ to bind Zn^{2+} *via* the lone pairs on the oxygen and nitrogen atoms (Scheme 31).[104] Complex **102**$^{2+}$ showed reversible two-step one-electron reductions on the bpy ligand, in addition to an electrochemically irreversible one-electron oxidation on the Ru center. Moreover, a similar reversible bpy-centered redox process was observed for **103**$^{2+}$, even though the Ru-centered oxidation is reversible in this case (eq. 47), which indicates that the corresponding one-electron oxidized species (**103**$^{2+}$) is stabilized by the interaction with Zn^{2+}.

$$\begin{array}{l} [\{Ru^{II}(bpy^{\cdot-})_2\}\text{–}Zn^{II}] \underset{+e^-}{\overset{-e^-}{\rightleftharpoons}} [\{Ru^{II}(bpy^{\cdot-})(bpy)\}\text{–}Zn^{II}]^{+} \\ \underset{+e^-}{\overset{-e^-}{\rightleftharpoons}} [\{Ru^{II}(bpy)_2\}\text{–}Zn^{II}]^{2+} \underset{+e^-}{\overset{-e^-}{\rightleftharpoons}} [\{Ru^{III}(bpy)_2\}\text{–}Zn^{II}]^{3+} \\ \qquad\qquad \textbf{103}^{2+} \end{array} \qquad \text{eq. 47}$$

Scheme 31. Coordination of $\mathbf{102}^{2+}$ to Zn^{2+} or Mn^{2+} in ref. 104.



$\mathbf{102}^{2+}$

Guest Metal-centered Electron transfers of Redox-active Metalloligands

Hamelin *et al*. reported that $\mathbf{102}^{2+}$ affords another heterobimetallic dinuclear complex ($\mathbf{104}^{2+}$) upon complexation of Mn^{2+} on the same coordination site as in the case of $\mathbf{103}^{2+}$ (Scheme 31).[104] Complex $\mathbf{104}^{2+}$ also showed bpy-centered redox properties, in addition to a reversible one-electron oxidation on the Mn center (eq. 48). In this case, the interaction between the RML and the guest metal ion affected the redox properties of the multi-nuclear RML complexes, *i.e*. the redox potentials, the reversibility of redox processes, and the redox centers.

$$[\{Ru^{II}(bpy^{\cdot-})_2\}\text{–}Mn^{II}] \underset{+e^-}{\overset{-e^-}{\rightleftharpoons}} [\{Ru^{II}(bpy^{\cdot-})(bpy)\}\text{–}Mn^{II}]^{+}$$
$$\underset{+e^-}{\overset{-e^-}{\rightleftharpoons}} \underset{\mathbf{104}^{2+}}{[\{Ru^{II}(bpy)_2\}\text{–}Mn^{II}]^{2+}} \underset{+e^-}{\overset{-e^-}{\rightleftharpoons}} [\{Ru^{II}(bpy)_2\}\text{–}Mn^{III}]^{3+} \qquad \text{eq. 48}$$

1-5-4. RMLs based on *Ortho*-disubstituted Benzenes

Metal centers, which have a preference for octahedral coordination geometry, may accommodate up to three molecules of *o*-disubstituted benzene ligands. Such tris (*o*-disubstituted benzene) complexes potentially contain multi-electron transfer sites at the central metal and up to three ligands, as well as guest metals (Chart 10).[60-69] Among the previously discussed ligands, Cat, Bdt, Mp, ApH_2, and $AtpH_2$ complexes contain lone pairs on oxygen and/or sulfur atoms that them to serve as RMLs. While Cat and Bdt contain homoleptic guest metal binding sites based on oxygen or sulfur, respectively. Mp contains a

heteroleptic (O/S) guest metal binding site, and ApH_2 and $AtpH_2$ contain a heteroleptic guest metal binding site based on oxygen. In this context, it is important to note that the homogeneity of the RML binding sites is considered to control the supramolecular assembly structure (Table 8).

Chart 10. Schematic structure of a tris-RML coordinating to a guest metal ion M'.

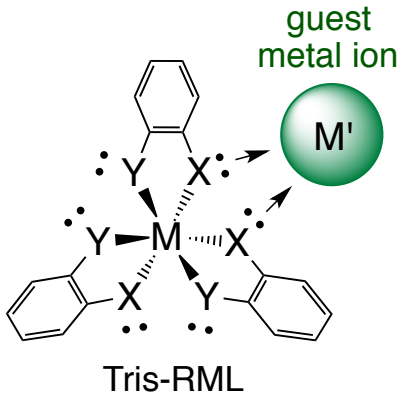


Table 8. Assembly structures for multi-nuclear tris-RMLs

Multi-nuclear complex	Binding Sites	ML/guest M	Structure	Ref.
$[K_3\{Cr^{III}(Cat)_3\}(H_2O)_{1.5}]_n$ (**105**)	Homo	1/3	Polymer	116
$[K_2\{Mn^{IV}(3,5\text{-DTBCat})\}(MeCN)_6]$ (**106**)	Homo	1/2	Discrete	117
$[Na_2\{Mn^{IV}(3,5\text{-DTBCat})\}(MeCN)_6]$	Homo	1/2	Discrete	118
$[Li_2\{Mn^{III}(Br_4Cat)_3\}(thf)_4]^-$	Homo	1/2	Discrete	119
$[K_3\{V^{III}(Cat)_3\}]_n$	Homo	1/3	Polymer	120
$[Co^{II}\{V^{IV}(Mp)_3\}(py)_2(MeCN)]$ (**107**)[a]	Hetero	1/1	Discrete	121
$[V^{III}\{V^{IV}(Mp)_3\}_2]^-$ (**108**$^-$)[a]	Hetero	2/1	Discrete	122
$[Mo_2\{Mo(Mp)_3\}(CO)_7]^{2-}$,[b]	Hetero	1/2	Discrete	123
$[Co^{III}\{Co^{III}(AtpH)_3\}]^{3+}$	Hetero (*s*)[c]	2/1	Discrete	124
$[Cu^{I}\{Mo^{V}(Bdt)_3\}]_n$ (**109**)	Homo	1/1	Polymer	125
$[Ag^{I}\{Mo^{V}(Bdt)_3\}]_n$ (**110**)	Homo	1/1	Polymer	125
$[Mo\{Mo(Mp)_3\}(CO)_3]^{2-}$ (**111**$^{2-}$)[a]	Hetero	1/2	Discrete	126

[a] Oxygen atoms binding mode. [b] Oxygen and sulfur atoms binding mode. [c] Single site.

Homoleptic Redox-active Metalloligands with Guest Metal Ions

Raymond *et al*. reported the synthesis and structural analysis of $[K_3(H_2O)_{1.5}\{Cr^{III}(Cat)_3\}]_n$ (**105**) (Figure 5a).[116] The single-crystal X-ray diffraction analysis of **105** revealed the

coordination of three K^+ ions *via* the homoleptic oxygen sites of $[Cr^{III}(Cat)_3]^{3-}$, resulting in the formation of a one-dimensional coordination polymer.

In addition, Cooper *et al*. reported the structural characterization of $[K_2(MeCN)_6\{Mn^{IV}(3,5\text{-DTBCat})\}]$ (**106**). In contrast to **105**, complex **106** was observed to be a discrete molecule, accommodating two K^+ ions on its oxygen sites (Figure 5b).[117] As 3,5-DTB is a relatively bulky substituent, the lack of further supramolecular assembly was attributed to steric repulsion. These examples suggest that the supramolecular assembly structure, *e.g*. discrete *vs*. oligomeric/polymeric, may be controlled by the substituents on the RMLs.

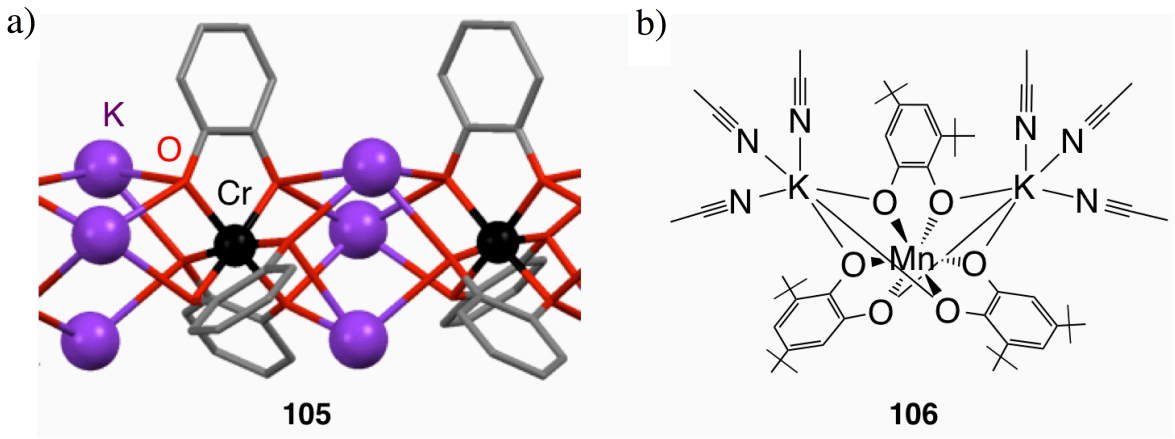


Figure 5. a) Assembled structure of **105** and b) structure of **106** in refs. 116 and 117.

Heteroleptic Redox-active Metalloligands with Guest Metal Ions

Usually, Mp complexes adopt *facial* coordination geometry, due to the *trans*-effect of oxygen and sulfur atoms at the metal center. Accordingly, Mp complexes contain heteroleptic binding sites, and a site-selective coordination of guest metal ions by these heteroleptic sites should be expected.[59] Kang *et al*. revealed that $[V^{IV}(Mp)_3]^{2-}$ selectively incorporates Co^{2+} on its oxygen sites in a tridentate fashion, resulting in the formation of $[Co^{II}\{V^{IV}(Mp)_3\}(py)_2(MeCN)]$ (**107**) (Figure 6a).[121] Complex **107** adopts a discrete 1:1 complex, most likely due to the steric constraints imposed by the py and MeCN ligands on Co^{2+}, which prevent the coordination of another RML.

Moreover, V^{3+} is selectively bound *via* the oxygen sites on two molecules of $[V^{IV}(Mp)_3]^{2-}$ to generate $[V^{III}\{V^{IV}(Mp)_3\}_2]$ (**108**$^-$), which is a discrete complex (Figure 6b).[122] These site-selective metal binding properties should be explained in terms of the HSAB principles defined by Pearson.[127] Accordingly, relatively hard acid metals such as Co^{2+} and V^{3+} can be expected to be coordinated by the relatively hard Lewis base oxygen. Thus, the site-selective metal binding of heteroleptic RMLs is a simple yet effective design principle to control the supramolecular assembly of RMLs and guest metals.

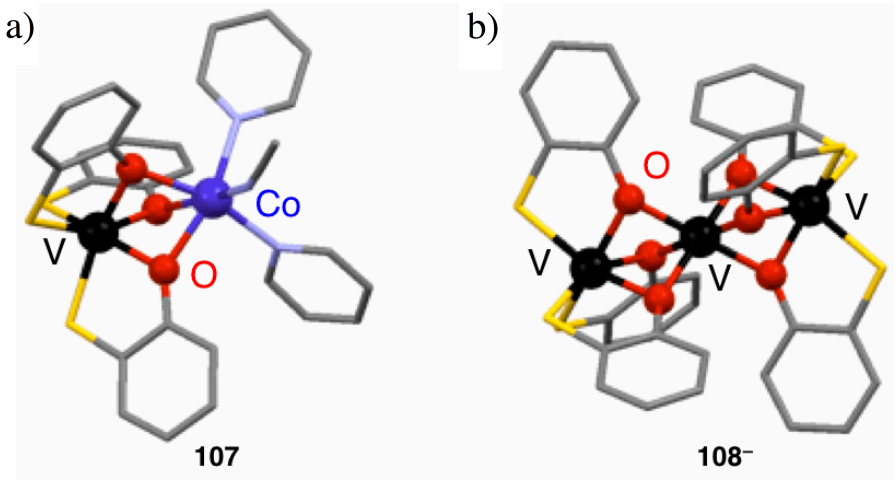


Figure 6. Molecular structures of a) **107** and b) **108**$^-$ in refs. 121 and 122.

Metal-centered Electron Transfer of Homoleptic RMLs

In 2011, Matsumoto, Chang, and Kato *et al*. reported the coordination behavior and the redox properties of $[Mo^{V}(Bdt)_3]^-$ (**59**$^-$).[125] The homoleptic RML **59**$^-$ contains six sulfur atoms as guest metal binding sites, and these are able to coordinate soft metal ions such as Cu^+ and Ag^+, which led to the formation of the 1–D coordination polymers $[Cu^{I}\{Mo^{V}(Bdt)_3\}]_n$ (**109**) and $[Ag^{I}\{Mo^{V}(Bdt)_3\}]_n$ (**110**) in the solid state (Figure 7).

In MeCN, complex **59**$^-$ showed a reversible metal-centered one-electron reduction and a one-electron oxidation at –0.68 and 0.00 V vs. Ag/Ag^+, respectively (Figure 8a), while **109**, which formed oligomers in MeCN, exhibited a positive shift of its reduction potential to 0.30 V (Figure 8b). This shift suggests that the coordinative interaction between RML and Cu^+ increase the electron accepting properties of the RML.

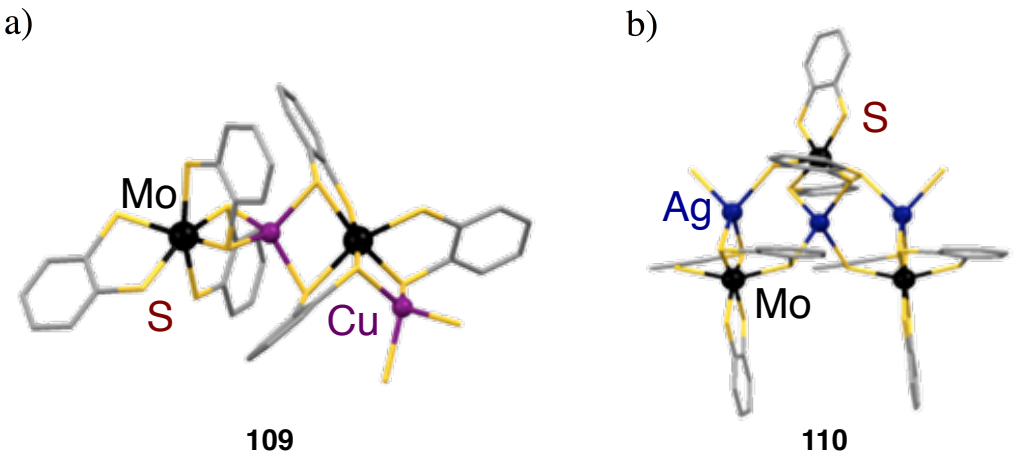


Figure 7. Assembled structures of a) **109** and b) **110** in ref. 125.

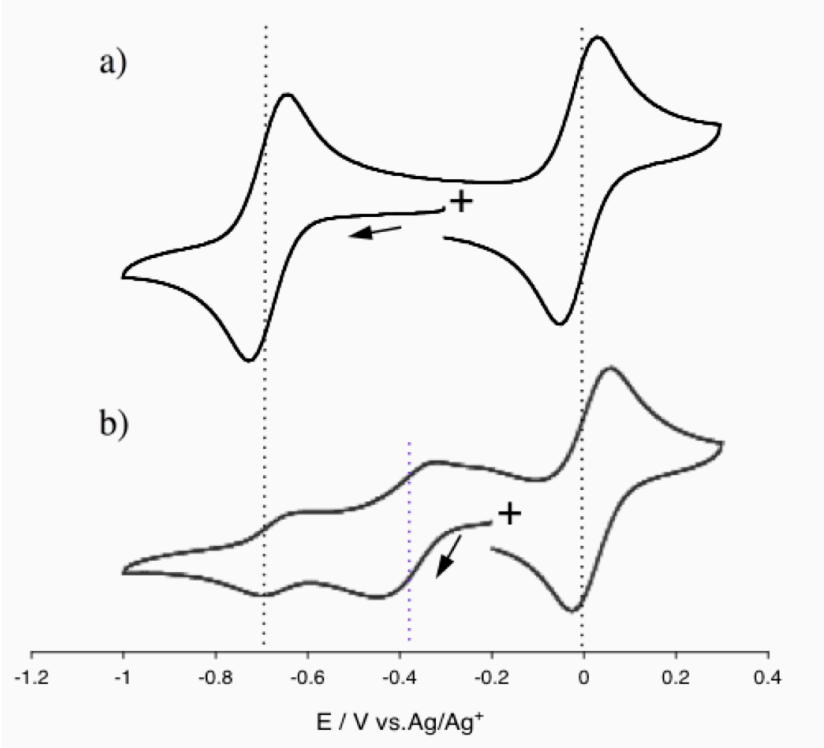


Figure 8. Cyclic voltammogram of 1 mM a) $\mathbf{59}^{-}$ and b) **109** recorded in MeCN at 500 mV s^{-1} under an atmosphere of Ar using 0.1 M *n*-Bu_4NPF_6 as the supporting electrolyte in ref. 125.

Electron Transfer of Heteroleptic Redox-active Metalloligands

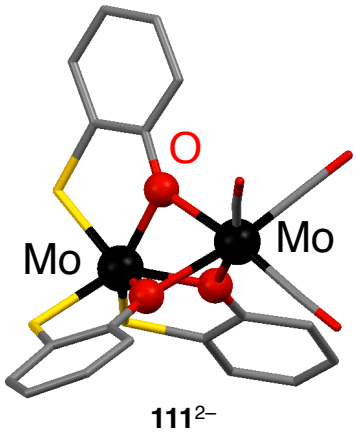
In 1991, Zhuang *et al*. reported the structure and redox properties of the dinuclear complex, $[Mo^{n}\{Mo^{m}(Mp)_3\}(CO)_3]^{2-}$ ($\mathbf{111}^{2-}$) ($n + m = 4$, $1 \leqq n \leqq 3$, $1 \leqq m \leqq 3$),[126] which selectively binds Mo *via* there oxygen atoms (Figure 9). Subsequently, three molecules of CO coordinate to the

guest Mo center, thus forming a discrete 1:1 complex. The oxidation state of the two Mo atoms in **111**$^{2-}$ was not determined, but the absence of Mo^0 centers was confirmed.

In MeCN, complex **111**$^{2-}$ exist in an equilibrium state, which involves $[Mo^0(CO)_3(MeCN)_3]$ and $[Mo^{IV}(Mp)_3]^{2-}$ species (eq. 49). Complex **111**$^{2-}$ exhibited a reversible two-electron reduction as well as a one-electron oxidation. It is worth pointing out that these redox processes present the first example for the redox properties of heteroleptic RMLs. It was speculated that the redox centers might be located on the Mo atoms, although this hypothesis was not validated.

$$[Mo_2^{n+m-1}]^{3-} \underset{+e^-}{\overset{-e^-}{\rightleftharpoons}} [Mo_2^{n+m}]^{2-} \underset{+e^-}{\overset{-e^-}{\rightleftharpoons}} [Mo_2^{n+m+1}]^{-} \underset{+e^-}{\overset{-e^-}{\rightleftharpoons}} [Mo_2^{n+m+2}]$$

$$[Mo_2^{n+m}]^{2-} \; \mathbf{111}^{2-} \rightleftharpoons [Mo^{IV}]^{2-} + Mo^0 \qquad \text{eq. 49}$$



111^{2-}

Figure 9. Molecular structure of **111**$^{2-}$ in ref. 126.

1-5-5. Research Opportunities

Even though homo- and heteroleptic RMLs are able to create various supramolecular assemblies by coordination of guest metal ions, systematic studies on such binding reactions and the interactions between the RMLs and the guest metal ions still remain scarce.[116-126] In addition, a lot of questions, regarding the redox properties of assemblies composed of RMLs and guest metal ions require answering.[125,126] For example, systematic investigations on how

the modulation of the redox properties of the RML/guest metal assemblies might be exerted are necessary, as not only the redox properties of the RML and those of the guest metal ions are influenced by the interactions between RML and guest metal ions, but as the RMLs also influence each other. Moreover, ligand-centered redox properties may afford different effects than metal-centered one. The thorough elucidation of the electronic interactions operative in the supramolecular assemblies of RMLs and guest metal ions is therefore highly important, not only with respect to controlling the redox potentials, but also for developing advanced multi-electron transfer reactions.

1-6. Objectives of This Study

1-6-1. Development of Multi-electron Transfer Systems based on RMLs

Tris(*o*-disubstituted benzene)-type RMLs can be subdivided into four groups according to the homogeneity of their guest metal binding sites and redox centers: i) homoleptic metal-centered RMLs, ii) heteroleptic metal-centered RMLs, iii) homoleptic ligand-centered RMLs, and iv) heteroleptic ligand-centered RMLs (Chart 11).

Chart 11. Classification of tris(*o*-disubstituted benzene)-type RMLs.



i) Homoleptic *Metal*-centered RML
M = Mo *etc.*, X = Y = O or S

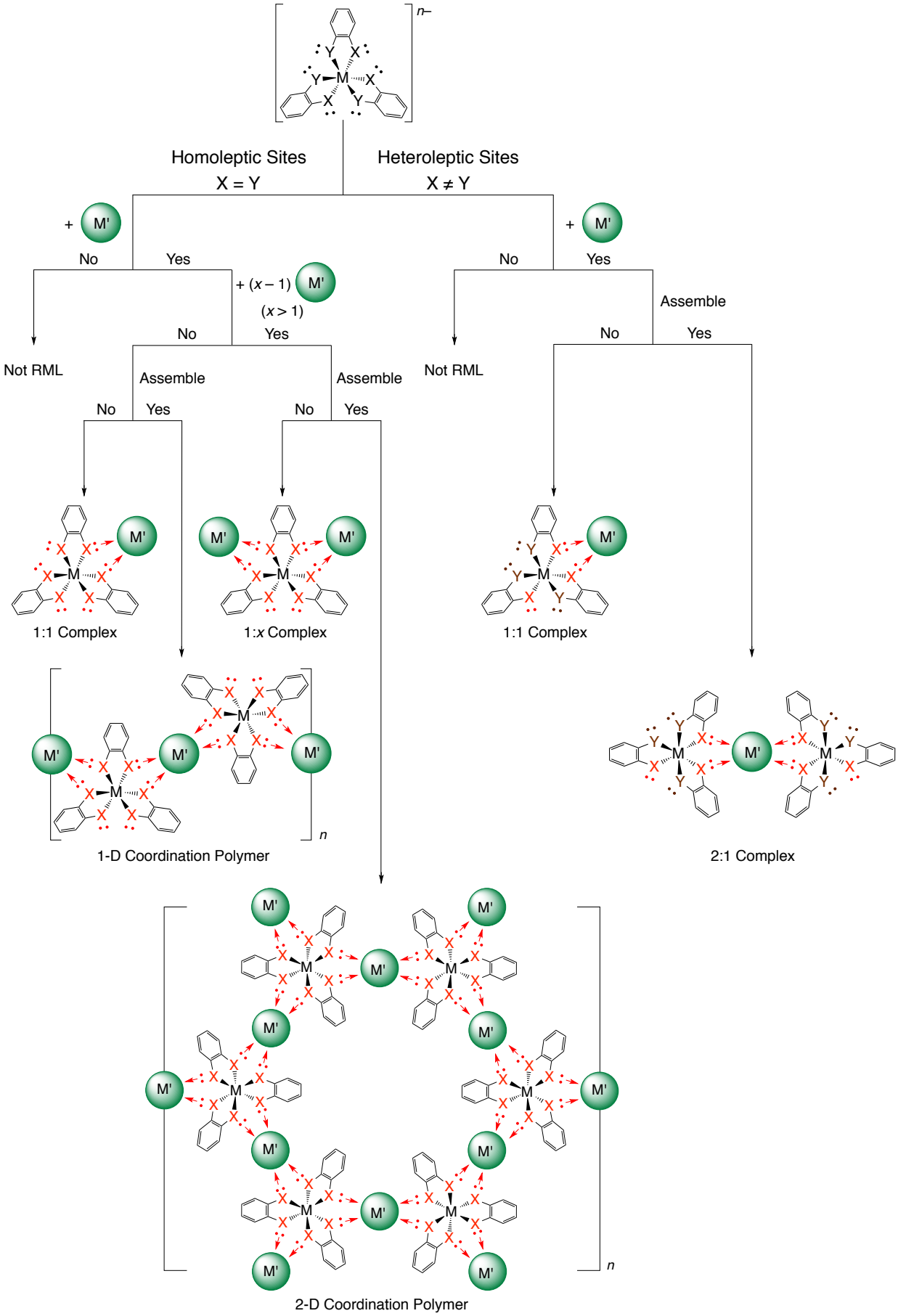
ii) Heteroleptic *Metal*-centered RML
M = Mo *etc.*, X = O, Y = S

iii) Homoleptic *Ligand*-centered RML
M = Cr *etc.*, X = Y = O or S

iv) Heteroleptic *Ligand*-centered RML
M = Cr *etc.*, X = O, Y = S

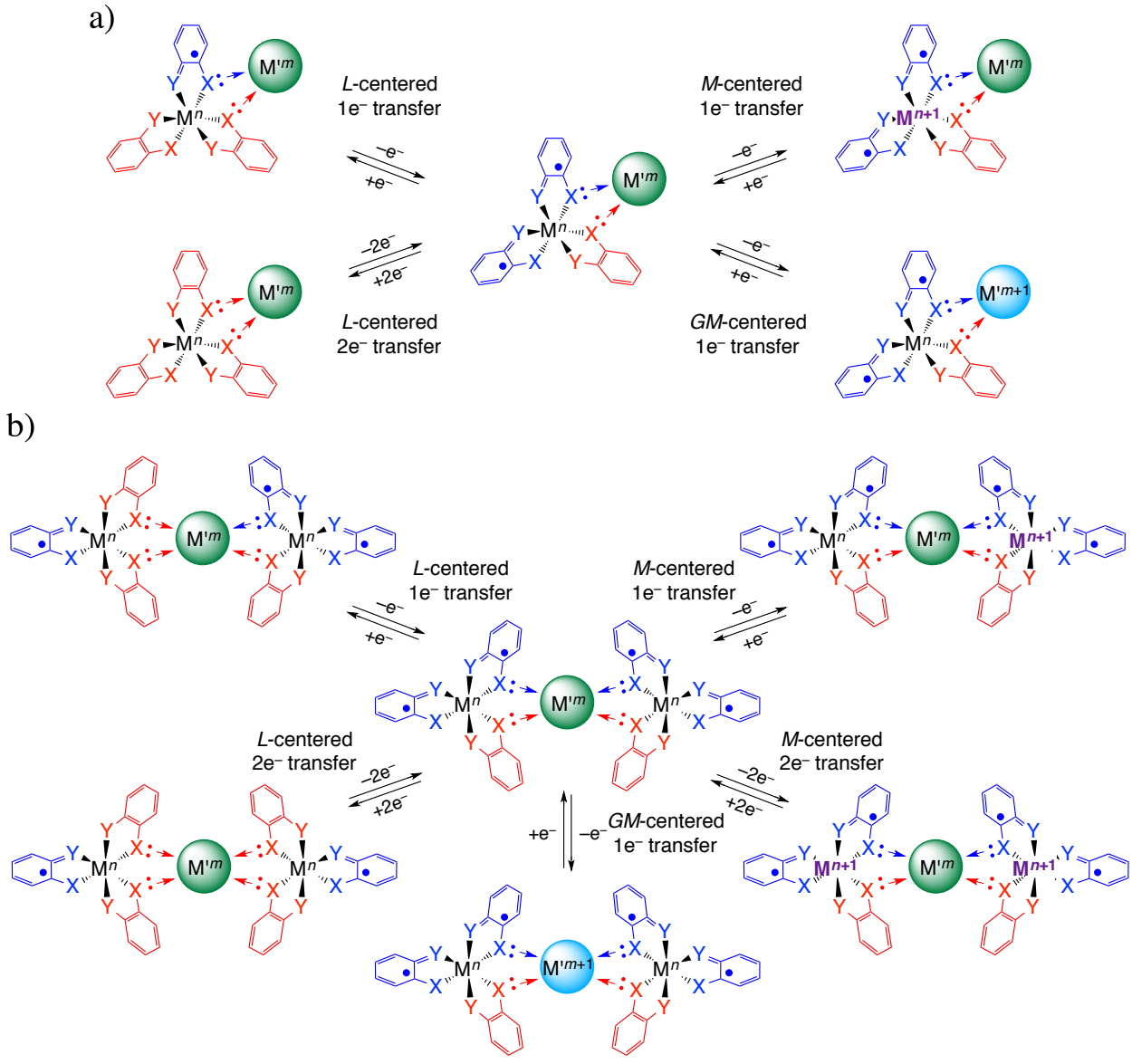
Chart 12 shows a flow diagram for the systematic investigations undertaken during the course of this study. Initially, the non-site-selective coordination of homoleptic RMLs (X = Y) to guest metal ions was investigated. Moreover the site-selective coordination of heteroleptic RMLs (X ≠ Y) to guest metal ion on one site was evaluated. Subsequently, the stoichiometry between the guest metal ions and the RMLs, as well as the binding constants between RMLs and the guest metal ions were examined in order to control the formation of either 1:1 or 1:*x* complexes ($x > 1$). When the steric congestion of the RMLs is sufficiently low, the coordinated guest metal ions may bind an additional RML molecule. The reduced steric repulsion between RMLs may thus lead to the formation of 1- or 2-D coordination polymers for homoleptic RMLs, or to 2:1 discrete complexes for heteroleptic RMLs. Therefore, the first task of this study was to achieve control over the supramolecular assembly structures *via* the homogeneity of the binding sites and the steric bulk of the RMLs by using a bottom-up method.

Chart 12. Flow chart for the coordination of homo- and heteroleptic RMLs to guest metal ions.



The RML metal-, ligand-, and, guest meta-centered, electron transfer activities can be affected by the interactions between the RMLs and the guest metal ions (Chart 13). In this context, it should be expected that such interactions cause different perturbations for the central metal and the ligands of the RMLs. For example, ligand-centered two-electron transfers may arise from the modulation of electronic interactions between the ligands. Furthermore, the electronic interactions between RMLs should change the redox properties of the RMLs within supramolecular assemblies. Therefore, the second task of this study was to elucidate details on the interactions between the RMLs and the guest metal ions, as well as to establish design

Chart 13. Metal (M)-, ligand (L)-, or guest metal (GM)-centered redox schemes for a) 1:1 complexes and b) 2:1 discrete complex of RMLs with guest metal ions.



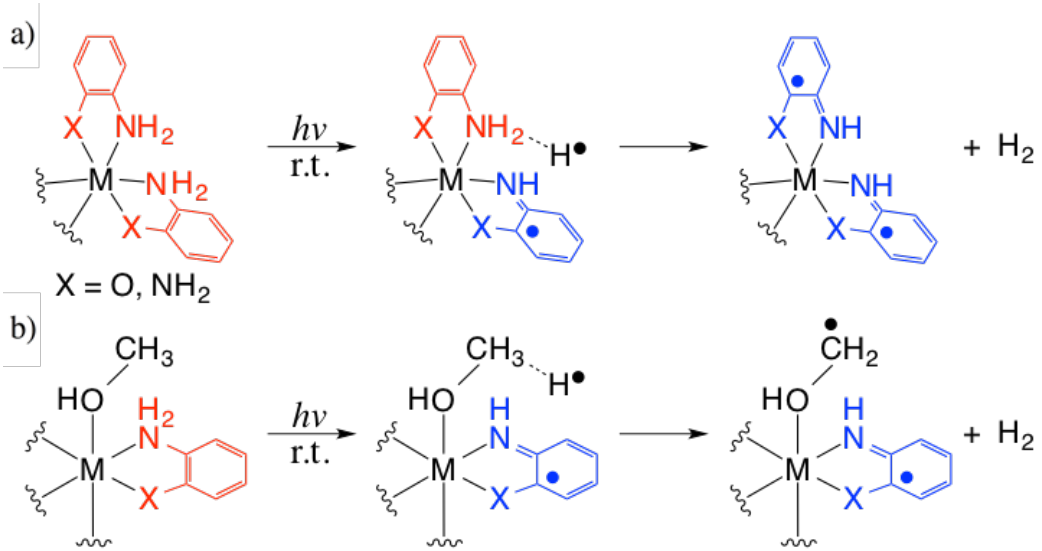
principles that provide control over redox potentials, as well as over the number of transferred electrons and redox centers in RML complexes and supramolecular assemblies.

A previous report from our group revealed the guest metal binding and metal-centered redox properties for the homoleptic RML **59**$^{-}$.[125] In order to expand and establish this study, guest metal bindings and redox properties of a heteroleptic metal-centered RML, as well as those of homo- and heteroleptic ligand-centered RML should be investigated.

1-6-2. Development of Photochemical Hydrogen Evolution Reaction Systems based on the Electron- and Proton-pooling Activity on Ligands

Among the previously discussed redox-active ligands, Opda, ApH_2, and $AtpH_2$, which contain coordinating nitrogen atoms, are able to simultaneously transfer electrons and protons.[79] Subsequently, H radicals can be generated on account of the abovementioned photochemical functionality of the aromatic amine ligands (Scheme 32). In such reactions, the generation of hydrogen is expected to occur *via* the abstraction of H radicals from neighboring amino groups on the ligands or from substrates. Thus, the task of this study is to create photochemical hydrogen evolution reaction (PHER) systems that are operated at ambient temperatures by using electron and proton transfer-active ligands as electron- and proton-pooling sites. The

Scheme 32. Schematic PHERs from a) ligands or b) MeOH using the electron and proton transfer ability of the ligands.



objectives for PHER systems were defined in the context of this study: i) the development of non-precious metal-based materials which perform PHERs under ambient-temperature based on ligand-centered reactions, and ii) the development of non-precious metal-based catalysts which can drive PHERs from hydrogen carrier such as MeOH under ambient-temperature.

In order to create the PHER systems, molecular structures, as well as photochemical properties and reactivities of complexes composed of non-precious metals, *e.g.* Fe(II), and the electron and proton transfer-active ligands, *e.g.* Opda and ApH_2, should be investigated.

1-7. Survey of This Thesis

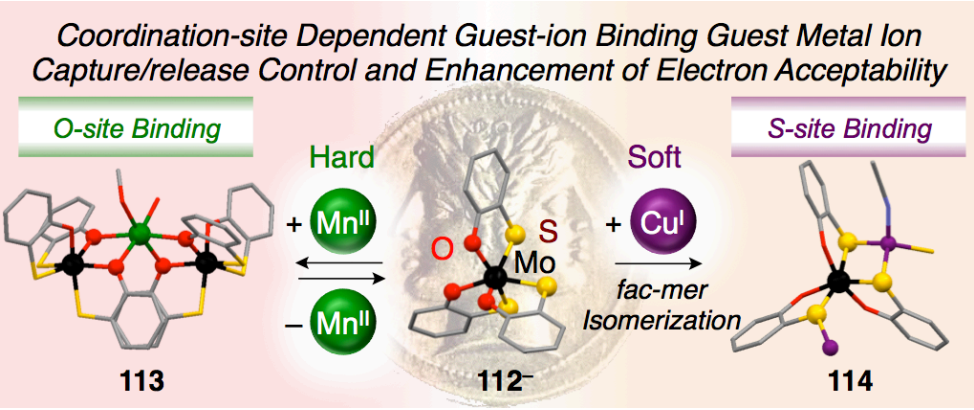
Chapter 1. General Introduction

Chapter 1 describes: 1) Energy Problems - Research Opportunities, 2) Electron and Proton Transfer Reactions at Molecular Level, 3) Redox-active Ligands, 4) Electron and Proton Transfer Reactions of Group 8 Metal Complexes, 5) Metalloligands, and 6) Objectives of This Study. Natural energy that is not obtained from fossil or nuclear carriers is called renewable energy, and these alternatives are expected to offer solutions to the currently problematic energy situation. Renewable energy can be stored in secondary energy carriers such as hydrogen, and accordingly, the development of catalysts that evolved hydrogen, preferably from benign sources such as water, as well as development of hydrogen storage materials is required. In this study, multi-electron and proton systems, which are necessary for water splitting and hydrogen absorption/adsorption processes, are created by metal complexes with electron and proton transfer-active ligands.

Chapter 2. Coordination Site–dependent Cation Binding and Multi–responsible Redox Properties of Janus–head Metalloligand $[Mo^{V}(2\text{-mercaptophenolato})_3]^-$

Chapter 2 describes the site-selective binding of guest metal ions, the structures of the corresponding supramolecular assemblies, control over guest metal capture/release properties by external stimuli, and metal-centered redox properties for the heteroleptic RML, *fac*-$[Mo^{V}(Mp)_3]^-$ (**112**$^-$) (Chart 14). Whereas **112**$^-$ selectively binds Mn^{2+} *via* its oxygen sites to generate the 2:1 discrete complex, $[Mn^{II}\{Mo^{V}(Mp)_3\}(H_2O)(MeOH)]$ (**113**), Cu^+ is selectively bound *via* the sulfur sites, furnishing the 1-D coordination polymer $[Cu^{I}\{mer\text{-}Mo^{V}(Mp)_3\}(MeCN)]_n$ (**114**). The electron-accepting properties of **113** are enhanced upon complexation of Mn^{2+}, which suggests stepwise metal-centered two-electron redox behavior for the complex. Thus, the O/S site-selective coordination to guest metal ions, as well as metal-centered multi-electron transfer properties for **112**$^-$ are discussed.

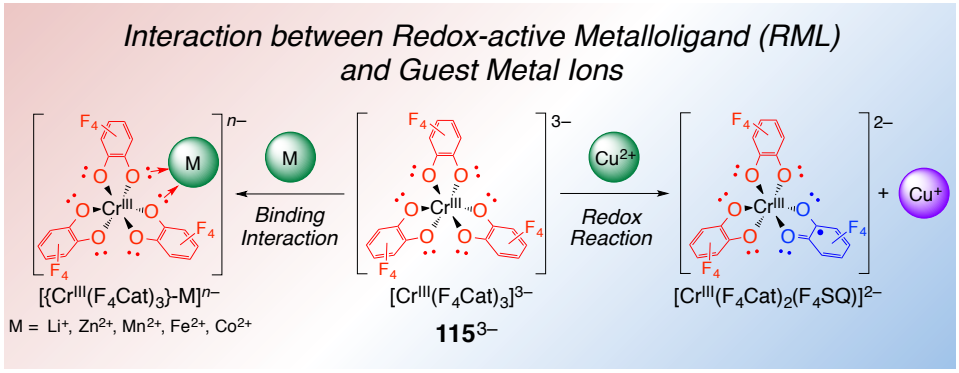
Chart 14. Survey for Chapter 2.



Chapter 3. Interactions Between the Trianionic Ligand-centred Redox-active Metalloligand $[Cr^{III}(perfluorocatecholato)_3]^{3-}$ and Guest Metal Ions

Chapter 3 describes the synthesis of the homoleptic RML $[Cr^{III}(F_4Cat)_3]^{3-}$ (**115**$^{3-}$), the interactions between **115**$^{3-}$ and guest metal ions, as well as ligand-centered redox properties (Chart 15). In CH_2Cl_2 and MeCN, complex **115**$^{3-}$ showed reversible ligand-centered three-step one-electron oxidation reactions. Addition of Cu^{2+} to a MeCN solution of **115**$^{3-}$ resulted in the formation of $[Cr^{III}(F_4Cat)_2(F_4SQ)]^{2-}$ and Cu^{+}. Mn^{2+}, Fe^{2+}, Co^{2+}, and Zn^{2+} guest metal ions are bound *via* oxygen sites to form a 1:1 complex in MeCN. Interactions between **115**$^{3-}$ and the guest metal ions, modulate the ligand-centered redox properties of the RML. This study represents the first example of RML activity for **115**$^{3-}$ in solution.

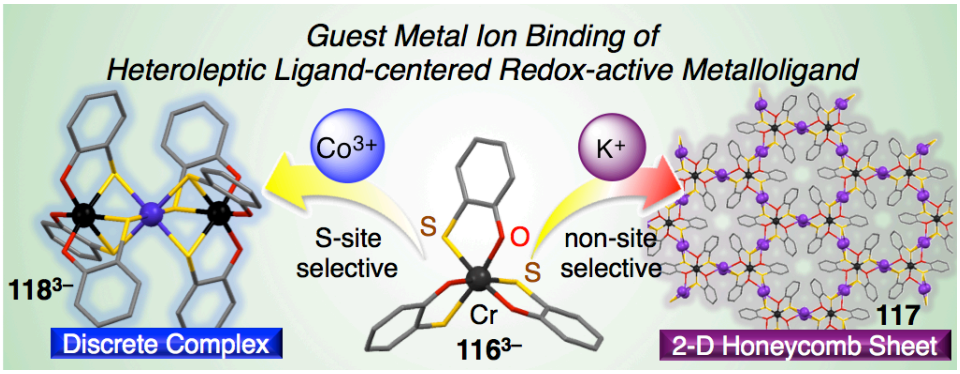
Chart 15. Survey for Chapter 3.



Chapter 4. Guest Metal Ion Binding of Ligand-centered Redox-active $[Cr^{III}(2\text{-mercaptophenolato})_3]^{3-}$ Metalloligand with Heteroleptic Coordination Site

Chapter 4 describes the coordination of guest metal ions, the corresponding structures of the supramolecular assemblies, and the ligand-centered redox properties of the heteroleptic RML $[Cr^{III}(Mp)_3]^{3-}$ (**116**$^{3-}$) (Chart 16). Complex **116**$^{3-}$ exhibited a reversible one-electron oxidation, and the corresponding one-electron oxidized species exhibited IVCT bands in the NIR region, suggesting the occurance of ligand-centered oxidation process. Moreover, complex **116**$^{3-}$ is able to bind K^+ guest cations non-site-selectively, which resulted in the formation of the honeycomb-like 2-D coordination polymer $[K_3\{fac\text{-}Cr^{III}(Mp)_3\}]_n \cdot 6H_2O$ (**117**). Conversely, Co^{3+} is site-selectively bound on the sulfur sites, resulting in the formation of the 2:1 discrete complex $[Co^{III}\{fac\text{-}Cr^{III}(Mp)_3\}_2]^{3-}$ (**118**$^{3-}$).

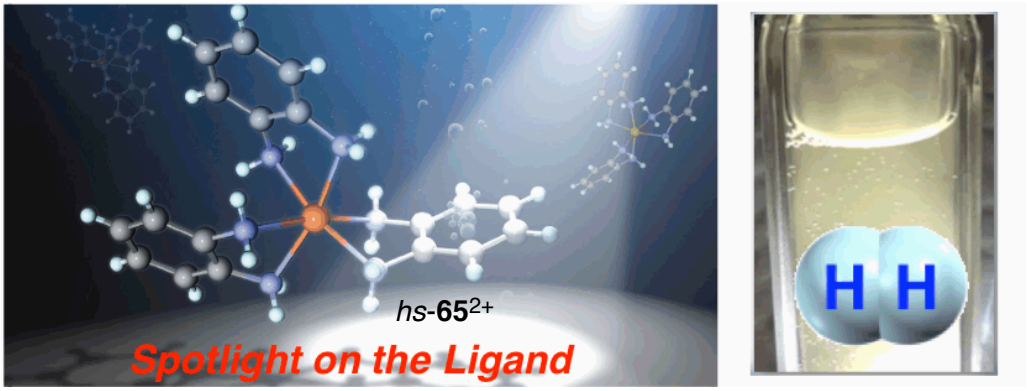
Chart 16. Survey for Chapter 4.



Chapter 5. Nonprecious-Metal-Assisted Photochemical Hydrogen Production from *ortho*-Phenylenediamine

Chapter 5 describes the structure, PHER performance, and mechanistic PHER details for *hs*-**65**$^{2+}$ (Chart 17). In the presence of Fe^{2+} in tetrahydrofuran Opda indicates PHERs by π-π* excitation (300 nm), whereas such photoreactivity is not observed in the absence of Fe^{2+}. The active species in these PHERs is *hs*-**65**$^{2+}$, in which Opda acts as an electron and proton source for the generation of hydrogen. Theses PHERs proceed catalytically upon the addition of HQ as a hydrogen reservoir. This study demonstrated for the first time PHER activity at ambient temperature for the non-precious metal complex *hs*-**65**$^{2+}$, which is based on its ligand-centered electron and proton transfer activity.

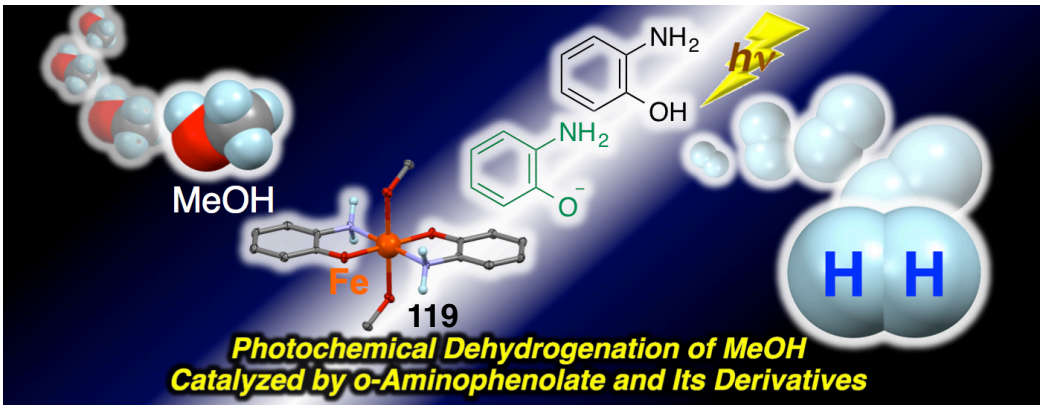
Chart 17. Survey for Chapter 5.



Chapter 6. Photocatalytic Hydrogen Evolution from MeOH by 2-Aminophenol, 2-Aminophenolate, and Its Fe(II) Complex at Room Temperature

Chapter 6 demonstrates the PHER performances using MeOH, and the PHER mechanism for ApH_2, ApH^-, and $[Fe^{II}(ApH_2)_2(MeOH)_2]$ (**119**) (Chart 18). At ambient temperature, ApH_2, ApH^-, and **119** were able to induce a PHER with MeOH under π-π* excitation (289 nm). In addition, complex **119** was able to induce a PHER with MeOH under CT excitation (350 nm), while ApH_2 and ApH^- did not show any activity under these conditions. This study delivers the first example of an ambient temperature PHER with MeOH using the organophotocatalysts and non-precious metal complex **119**.

Chart 18. Survey for Chapter 6.



1-8. References

1. State of world population 2014, United Nations Population Fund.
2. G. A. Olah, A. Goeppert, G. K. S. Parakash, *Beyond Oil and Gas: The Methanol Economy,* 2009, WILEY-VCH.
3. Japan's Energy White Paper 2015, Ministry of Economy, Trade and Industry.
4. International Energy Out look 2007, U. S. Energy Information Administration.
5. C.-J. Winter, *Int. J. Hydrog. Energy,* **2009**, *34*, S1.
6. a) O. Z. Sharaf, M. F. Orhan, *Renew. Sust. Energy Rev.,* **2014**, *32*, 810; b) A. Rabis, P. Rodriguez, T. J. Schmidt, ACS *Catal.,* **2012**, *2*, 864.
7. M. E. Dry, *Catal. Today,* **2002***, 71*, 227.
8. a) D. Lu, T. Takata, N. Saito, Y. Inoue, K. Domen, *Nature*, **2006**, *440*, 295; b) A. Kudo, Y. Miseki, *Chem. Soc. Rev.,* **2009***, 38*, 253; c) C. Pan, T. Takata, M. Nakabayashi, T. Matsumoto, N. Shibata, Y. Ikuhara, K. Domen, *Angew. Chem. Int. Ed.,* **2015**, *54*, 2955.
9. R. Abe, *J. Photoch. Photobio. C,* **2010**, *11*, 179.
10. a) M. D. Märkäs, O. Verho, E. V. Johnston, B. Akermark, *Chem. Rev.,* **2014**, *114*, 11863; b) K. Sakai, H. Ozawa, *Coord. Chem. Rev.,* **2007**, *251*, 2753.
11. P. Du, R. Eisenberg, *Energy Environ. Sci.,* **2012**, *5*, 6012.
12. K. Yamauchi, S. Masaoka, K. Sakai, *J. Am. Chem. Soc.,* **2009***, 131*, 8404.
13. J. J. Concepcion, J. W. Jurss, J. L. Templeton, T. J. Meyer, *J. Am. Chem. Soc.,* **2008**, *130*, 16462.
14. U. Eberle, M. Felderhoff, E. Schüth, *Angew. Chem. Int. Ed.,* **2009**, *48*, 6608.
15. A. F. Dalebrook, W. Gan, M. Grasemann, S. Moret, G. Laurenczy, *Chem. Commun.,* **2013**, *49*, 8735.
16. M. P. Suh, H. J. Park, T. K. Prasad, D.-W. Lim, *Chem. Rev,* **2012**, *112*, 782.
17. B. Sakintuna, F. L -Darkrim, M. Hirscher, *Int. J. Hydrog. Energy,* **2007**, *32*, 1121.
18. H. Lee, J.-W. Lee, D. Y. Kim, J. Park, Y.-T. Seo, H. Zeng, I. L. Moudrakovski, C. I.

Ratcliffe, J. A. Ripmeester, *Nature,* **2005**, *434*, 743.

19. a) R. B. Biniwale, S. Rayalu, S. Devotta, M. Ichikawa, *Int. J. Hydrog. Energy,* **2008**, *33*, 360; b) N. Boufaden, R. Akkari, B. Pawelec, J. L. G. Fierro, M. S. Zina, A. Ghorbel, *Appl. Catal. A-Gen.,* **2015**, *502*, 329.
20. S. Sá, H. Silva, L. Brandao, J. M. Sousa, A. Mendes, *Appl. Chem. B Environ.,* **2010**, *99*, 43.
21. H. Yamamoto, S. Shinoda, Y. Saito, *J. Mole. Catal.,* **1985**, *30*, 259.
22. K. Makita, K. Nomura, Y. Saito, *J. Mole. Catal.,* **1994**, *89*, 143.
23. D. Morton, D. J. Cole-Hamilton, *J. Chem. Soc., Chem. Commun.,* **1988**, 1154.
24. S. Shinoda, H. Itagaki, Y. Saito, *J. Chem. Soc. Chem. Commun.,* **1985**, 860.
25. H. Itagaki, S. Shinoda, Y. Saito, *Bill. Chem. Soc. Jpn.,* **1988**, *61*, 2291.
26. S. Shinoda, T. Yamakawa, *J. Chem. Soc. Chem. Commun.,* **1990**, 1511.
27. T. Fujii, Y. Saito, *J. Mole. Catal.,* **1991**, *67*, 185.
28. L.-C. Yang. T. Yamakawa, S. Shinoda, *J. Mole. Catal. A,* **1998**, *130*, 249.
29. L.-C. Yang, T. Ishida, T. Yamakawa, S. Shinoda, *J. Mole., Catal. A,* **1996**, *108*, 87.
30. R. E. Rodríguez-Lugo, M. Trincado, M. Vogt, F. Tewes, G. santiso-Quinones, H. Grützmacher, *Nature Chem.,* **2013**, *5*, 342.
31. M. Nielsen, E. Alberico, W. Baumann, H. J. Drexler, H. Junge, S. Gladiali, M. Beller, *Nature,* **2013**, *495*, 85.
32. E. Alberico, P. Sponholz, C. Cordes, M. Nielsen, H. -J. Drexler, W. Baumann, H. Junge, M. Beller, *Angew. Chem. Int. Ed.,* **2013**, *52*, 14162.
33. P. Atkins, T. Overton, J. Rourke, M. Weller, F. Armstrong, *Inorganic Chemistry, Fourth Edition*, 2006, Oxford University Press.
34. M. H. V. Huynh, T. J. Meyer, *Chem. Rev.,* **2007**, *107*, 5004.
35. R. A. Marcus, *J. Chem. Phys.,* **1956**, *24*, 966.
36. A. Spencer, G. Wilkinson, *J. Chem. Soc. Dalton Trans.,* **1972**, 1577.
37. J. A. Baumann, D. J. Salmon, S. T. Wilson, T. J. Meyer, *Inorg. Chem.,* **1978**, *17*, 3342.
38. T. Ito, T. Hamaguchi, H. Nagino, T. Yamaguchi, J. Washington, C. P. Kubiak, *Science,*

1997, *277*, 660.

39. T. Hamaguchi, H. Nagino, K. Hoki, H. Kido, T. Yamaguchi, B. K. Breedlove, T. Ito, *Bull. Chem. Soc. Jpn.,* **2005**, *78*, 591.
40. A. K. Diallo, J.-C. Daran, F. Varret, J. Ruiz, D. Astruc, *Angew. Chem. Int. Ed.,* **2009**, *48*, 3141.
41. I. Cuadrado, C. M. Casado, B. Alonso, M. Morán, J. Losada, V. Belsky, *J. Am. Chem. Soc.,* **1997**, *119*, 7613.
42. M. T. Pope, A. Müller, *Angew. Chem. Int. Ed.,* **1991**, *30*, 34.
43. J. N. Barrows, G. B. Jameson, M. T. Pope, *J. Am. Chem. Soc.,* **1985**, *107*, 1771.
44. B. Keita, L. Nadjo, *J. Electroanal. Chem.,* **1987**, *227*, 77.
45. S.-X. Guo, C.-Y Lee, J. Zhang, A. M. Bond, Y. V. Geletii, C. L. Hill, *Inorg. Chem.,* **2014**, *53*, 7561.
46. M. J. Burk, R. H. Crabtree, *J. Am. Chem. Soc.,* **1987**, *109*, 8025.
47. R. Ziessel, *J. Am. Chem. Soc.,* **1993**, *115*, 118.
48. J. A. Maguire, A. S. Goldman, *J. Am. Chem. Soc.,* **1991**, *113*, 6706.
49. E. Delgado-Lieta, M. A. Luke, R. F. Jones, D. J. Cole-Hamilton, *Polyhedron,* **1982**, *1*, 839.
50. O. Pàmies, J.-E. Bäckvall, *Chem. Eur. J.,* **2001**, *7*, 5052.
51. a) D. M. Roundhill, S. J. Atherton, Z.-P. Shen, *J. Am. Chem. Soc.,* **1987**, *109*, 6076; b) E. L. Harvey, A. E. Stiegman, A. Vl´cek Jr., H. B. Gray, *J. Am. Chem. Soc.,* **1987**, *109*, 5233.
52. H. B. Gray, R. Willams, I. Bernal, E. Billig, *J. Am. Chem. Soc.,* **1962**, *84*, 3596.
53. G. N. Shrauzer, V. Mayweg, *J. Am. Chem. Soc.,* **1962**, *84*, 3221.
54. C. K. Jørgensen, *Coor. Chem. Rev.,* **1966**, *1*, 164.
55. a) M. D. Ward, J. A. McCleverty, *J. Chem. Soc. Dalton. Trans.,* **2002**, 275; b) W. Kaim, B. Schwederski, *Coord. Chem. Rev.,* **2010**, *254*, 1580.
56. a) L. Fiester, M. Tishler, W. L. Sampson, *J. Biol. Chem.,* **1941**, *137*, 659; b) J. E. Luvalle, A. Weissberger, *J. Am. Che, Soc.,* **1947**, *69*, 1567; c) G. Stein, J. Weiss, *J. Chem. Soc.,* **1951**, 3265.

57. D. R. Eaton, *Inorg. Chem.,* **1964**, *9*, 1268.

58. F. Röhrscheid, A. L. Balch, R. H. Holm, *Inorg. Chem.,* **1966**, *9*, 1542.

59. a) Y. S. Sohn, A. L. Balch, *J. Am. Chem. Soc.,* **1971**, *93*, 1290; b) C. G. Pierpont, H. H. Downs, *Inorg. Chem.,* **1975**, *14*, 343.

60. M. Haga, E. S. Dodworth, A. B. P. Lever, *Inorg. Chem.,* **1986**, *25*, 447.

61. S. R. Cooper, Y. B. Koh, K. N. Raymond, *J. Am. Chem. Soc.,* **1982**, *104*, 5092.

62. K. Ray, T. Weyhermüller, F. Neese, K. Wieghardt, *Inorg. Chem.,* **2005**, *44*, 5345.

63. a) C. G. Pierpont, R. M. Buchanan, *Coord. Chem. Rev.,* **1981**, *38*, 45; b) B.-S Kang, M.-C Hong, T.-B Wen, H.-Q. Liu, J.-X. Lu, *J. Clust. Sci.,* **1995**, *6*, 379, c) P. Zanello, M. Corsini, *Coord. Chem. Rev.,* **2006**, *250*, 2000; d) A. I. Poddel'sky, V. K. Cherkasov, G. A. Abakumov, *Coord. Chem. Rev.,* **2009**, *253*, 291.

64. R. M. Buchanan, C. G. Pierpont, *J. Am. Chem. Soc.,* **1980**, *102*, 4951.

65. G. A. N. Felton, A. K. Vannucci, J. Chen, L. T. Lockett, N. Okumura, B. J. Petro, U. I. Zakai, D. H. Devans, R. S. Glass, S. Richard, D. L. Lichtenberger, *J. Am. Chem. Soc.,* **2007**, *129*, 12521.

66. E. Bill, E. Bothe, P. Chaudhuri, K. Chlopek, D. Herebian, S. Kokatam, K. Ray, T. Weyhermüller, F. Neese, K. Wieghardt, *Chem. Eur. J.,* **2005**, *11*, 204.

67. P. R. Klich, A. T. Daniher, P. R. Challen, D. B. McConville, *Inorg. Chem.,* **1996**, *35*, 347.

68. H. Kang, S. Liu, S. N. Shaikh, T. Nicholson, J. Zubieta, *Inorg. Chem.,* **1989**, *28*, 920.

69. M. Ebadi, A. B. P. Lever, *Inorg. Chem.,* **1999**, *38*, 467.

70. a) M. Cowie, M. Bennett, *Inorg. Chem.,* **1976**, *7*, 1584; b) A. Cervilla, E. Llopis, D. Marco, F. Pérez, *Inorg. Chem.,* **2001**, *40*, 6525; c) C. S. Isfort, T. Pape, F. E. Hahn, *J. Inorg. Chem.,* **2005**, 2607.

71. a) C. G. Pierpont, H. H. Downs, *J. Am. Chem. Soc.,* **1976**, *98*, 4834; b) H. H. Downs, R. M. Buchanan, C. G. Pierpont, *Inorg. Chem.,* **1979**, *18*, 1736; c) H.-C. Chang, H. Miyasaka, S. Kitagawa, *Inorg. Chem.,* **2001**, *40*, 146.

72. S. Bhattacharya, S. R. Boone, G. A. Fox, C. G. Pierpont, *J. Am. Chem. Soc.,* **1990**, *112*,

1088.

73. R. M. Buchanan, C. G. Pierpont, *J. Am. Chem. Soc.,* **1980**, *102*, 4951.
74. C. G. Pierpont, O. -S. Jung, *Inorg. Chem.,* **1995**, *34*, 4281.
75. C. Roux, D. M. Adams, J. P. Itié, A. Poolian, D. N. Hendrickson, M. Verdaguer, *Inorg. Chem.,* **1996**, *35*, 2846.
76. D. M. Adams, B. Li, J. D. Simon, D. N. Hendrickson, *Angew. Chem. Int. Ed.,* **1995**, *34*, 1481.
77. C. G. Pierpont, *Cood. Chem. Rev.,* **2001**, *216-217*, 99.
78. A. S. Attia, C. G. Pierpont, *Inorg. Chem.,* **1998**, *37*, 3051.
79. S.-M. Peng, C.-T. Chen, D.-S. Liaw, C.-I. Chen, Y. Wang, *Inorg. Chim. Acta,* **1985***, 101*, L31.
80. R. F. Munhá, R. A. Zarkesh, A. F. Heyduk, *Dalton Trans.,* **2013**, *42*, 3751.
81. O. R. Luca, R. H. Crabtree, *Chem. Soc. Rev.,* **2013**, *42*, 1440.
82. V. K. K. Praneeth, M. R. Ringenberg, T. R. Ward, *Angew. Chem. Int. Ed.,* **2012**, *51*, 10228.
83. D. L. J. Broere, R. Plessius, J. I. van der Vlugt, *Chem. Soc. Rev.,* **2015**, *44*, 6886.
84. a) T. Wada, K. Tsuge, K. Tanaka, *Inorg. Chem.,* **2001**, *40*, 329; b) K. Tanaka, H. Isobe, S. Yamanaka, K. Yamaguchi, *P. Natl. Acad. Sci. U. S. A.,* **2012***, 109*, 15600.
85. a) P. Chaudhuri, M. Hess, J. Müller, K. Hildenbrand, E. Bill, T. Weyhermüller, K. Wieghardt, *J. Am. Chem. Soc.,* **1999**, *121*, 9599; b) C. Mukherjee, U. Pieper, E. Bothe, V. Bachler, E. Bill, T. Weyhermüller, P. Chaudhuri, *Inorg. Chem.,* **2008**, *47*, 8943; c) C. Mukherjee, T. Weyhermüller, E. Bothe, P. Chaudhuri, *Inorg. Chem.,* **2008**, *47*, 11620; d) S. E. Balaghi, E. Safaei, L. Chiang, E. W. Y. Wong, D. Savard, R. M. Clarke, T. Storr, *Dalton Trans.,* **2013**, *42*, 6829.
86. a) M. R. Ringenberg, S. L. Kokatam, Z. M. Heiden, T. B. Rauchfuss, *J. Am. Chem. Soc.,* **2008**, *130*, 788; b) M. R. Ringenberg, M. J. Nilges, T. B. Rauchfuss, S. R. Wilson, *Organometallics,* **2010**, *29*, 1956.
87. A. L. Smith, K. I. Hardcastle, J. D. Soper, *J. Am. Chem. Soc.,* **2010**, *132*, 14358.

88. a) K. Ujike, S. Kudoh, M. Nakata, *Chem. Phys. Lett.,* **2004**, *396*, 288; b) K. Ujike, N. Akai, S. Kudoh, M. Nakata, *J. Mol. Struct.,* **2005**, *735-736*, 335.

89. G. M. Roberts, C. A. Williams, J. D. Young, S. Ullrich, M. J. Paterson, *J. Am. Chem. Soc.,* **2012**, *134*, 12578.

90. M. C. Capello, M. Broquier, S. Ishiuchi, W. Y. Sohn, M. Fujii, C. Dedonder-Lardeux, C. Jouvet, G. A. Pino, *J. Phys. Chem. A,* **2014**, *118*, 2056.

91. F. R. Keene, *Coor. Chem. Rev.,* **1999**, *187*, 121.

92. V. L. Goedken, D. H. Busch, *J. Am. Chem. Soc.,* **1972**, *94*, 7355.

93. G. M. Brown, T. R. Weaver, F. R. Keene, T. J. Meyer, *Inorg. Chem.,* **1976**, *15*, 190.

94. M. Tamura, K. Tsuge, A. Igashira-Kamiyama, T. Konno, *Chem. Comm.,* **2011**, *47*, 12464.

95. G. H. Cohen, J. L. Hoard, *J. Am. Chem. Soc.,* **1966**, *88*, 2338.

96. J. C. Slater, *J. Chem. Phys.,* **1964**, *41*, 3199.

97. A. Bondi, *J. Phys. Chem.,* **1964**, *68*, 441.

98. a) L. Gelmini, D. W. Stephan, *Inorg. Chim. Acta,* **1986**, *111*, L17; b) S. Kitagawa, R. Kitaura, S. Noro, *Angew. Chem. Int. Ed.,* **2004**, *43*, 2334; c) S. R. Halper, L. Do, J. R. Stork, S. M. Cohen, *J. Am. Chem. Soc.,* **2006**, *128*, 15255; d) B. Chen, S. Xiang, G. Qian, *Accounts Chem. Res.,* **2010**, *43*, 1115.

99. M. V. Escárcega-Bobadilla, M. M. Belmonte, E. Martin, E. C. Escudero-Adán, A. W. Kleij, *Chem. Eur. J.,* **2013**, *19*, 2641.

100. O. Hamelin, M. Rimboud, J. Pécaut, M. Fontecave, *Inorg. Chem.,* **2007**, *46*, 5354.

101. A. Rao, J. T. Mague, M. S. Balakrishna, *Dalton Trans.,* **2013**, *42*, 11695.

102. a) M. Yuki, Y. Miyake, Y. Nishibayashi, *Organometallics,* **2008**, *27*, 3947; b) H. Tanaka, A. Sasada, T. Kouno, M. Yuki, Y. Miyake, H. Nakanishi, Y. Nishibayashi, K. Yoshizawa, *J. Am. Chem. Soc.,* **2011**, *133*, 3498.

103. a) J. C. Medina, T. T. Goodnow, M. S. Bott, J. L. Atwood, A. E. Kaifer, G. W. Gokel, *J. Chem. Soc. Chem. Commun.,* **1991**, 290; b) J. C. Medina, T. T. Goodnow, M. T. Rojas, J. L. Atwood, B. C. Lynn, A. E. Kaifer, G. W. Gokel, *J. Am. Chem. Soc.,* **1992**, *114*, 10583.

104. P. Guillo, O. Hamelin, F. Loiseau, J. Pécaut, S. Ménage, *Dalton Trans.,* **2010**, *39*, 5650.

105. T. A. Pinder, S. K. Montalvo, C. -H. Hsieh, A. M. Lunsford, R. D. Bethel, B. S. Pierce, M. Y. Darensbourg, *Inorg. Chem.,* **2014**, *53*, 9095.

106. T. T. Nadasdi, D. W. Stephan, *Organometallics,* **1992**, *11*, 116.

107. S. Styra, S. González-Gallardo, F. Armbruster, P. Ona-Burgos, E. Moos, M. Vonderach, P. Weis, O. Hampe, A. Grün, Y. Schmitt, M. Gerhards, F. Menges, M. Gaffga, G. Niedner-Schatteburg, F. Breher, *Chem. Eur. J.,* **2013**, *19*, 8436.

108. I. Trapp, S. González-Gallardo, S. Hohnstein, D. Garnier, P. Ona-Burgos, F. Breher, *Dalton Trans.,* **2014**, *43*, 4313.

109. S. González-Gallardo, I. Kuzu, P. Ona-Burgos, T. Wolfer, C. Wang, K. W. Klinkhammer, W. Klopper, S. Brase, F. Brefer, *Organometallics,* **2014**, *33*, 941.

110. S. Fritzsche, P. Lönnecke, T. Höcher, E. Hey-Hawkins, *Z. Anorg. Allg. Chem.,* **2006**, 2256.

111. H.-C. Chang, K. Mochizuki, S. Kitagawa, *Inorg. Chem.,* **2005**, *44*, 3810.

112. J. Yohida, K. Sugawara, H. Yuge, J. Okabayahsi, *Dalton Trans.,* **2014**, *43*, 16066.

113. G. Guisado-Barrios, Y. Li, A. M. Z. Slawin, D. T. Richens, I. A. Gass, P. R. Murray, L. J. Yellowless, E. K. Brechin, *Dalton Trans.,* **2008**, 551.

114. S. Ø. Scottwell, K. J. Shaffer, C. J. McAdam, J. D. Crowley, *RSC Adv.,* **2014**, *4*, 35726.

115. A. K. Pal, B. Laramée-Milette, G. S. Hanan, *RSC Adv.,* **2014**, *4*, 21262.

116. K. N. Raymond, S. S. Isied, L. D. Brown, F. R. Fronczek, J. H. Nibert, *J. Am. Chem. Soc.,* **1976**, *98*, 1767.

117. J. R. Hartman, B. M. Foxman, S. R. Cooper, *Inorg. Chem.,* **1984**, *23*, 1381.

118. D.-H. Chin, D. T. Sawyer, W. P. Schaefer, C. J. Simmons, *Inorg. Chem.,* **1983**, *22*, 752.

119. C. J. Rolle III, K. I. Hardcastle, J. D. Soper, *Inorg. Chem.,* **2008**, *47*, 1892.

120. S. R. Cooper, Y. B. Koh, K. N. Raymond, *J. Am. Chem. Soc.,* **1982**, *104*, 5092.

121. B.-S. Kang, X.-J. Wang, C.-Y. Su, H.-Q. Liu, *Transit. Metal Chem.,* **1999**, *24*, 712.

122. B. Kang, L. Weng, H. Liu, D. Wu, L. Huang, C. Lu, J. Cai, X. Chen, J. Lu, *Inorg. Chem.,* **1990**, *29*, 4873.

123. B. Zhuang, L. Huang, A. Lan, L. He, X. Zhao, J. Lu, *Polyhedron,* **1992**, *11*, 2557.

124. A. Panja, C. E. Moore, D. M. Eichhorn, *J. Coord. Chem.,* **2013**, *66*, 3037.

125. T. Matsumoto, H.-C. Chang, A. Kobayashi, K. Uosaki, M. Kato, *Inorg. Chem.,* **2011**, *50*, 2859.

126. B. Zhuang, L. Huang, L. He, P. Yu, A. Lan, J. Lu, *Inorg. Chim. Acta,* **1991**, *179*, 179.

127. R. G. Pearson, *J. Am. Chem. Soc.,* **1962***, 84*, 3533.

Chapter 2

Coordination Site–dependent Cation Binding and Multi–responsible Redox Properties of Janus–head Metalloligand $[Mo^{V}(2\text{-mercaptophenolato})_3]^-$

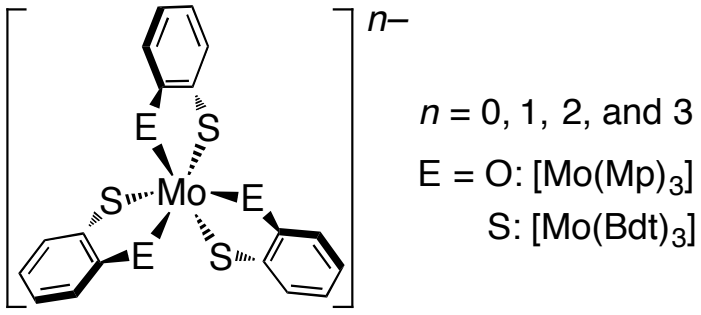
Abstract

The redox-active metalloligand (RML) *fac*-$[Mo^{V}(Mp)_3]^-$ (Mp = 2-mercaptophenolato) bearing asymmetric O- and S-cation binding sites can bind with several kinds of metal ions such as Na^+, Mn^{2+}, Fe^{2+}, Co^{2+}, Ni^{2+}, and Cu^+. The *fac*-$[Mo^{V}(Mp)_3]^-$ coordinates to Na^+ to form contact ion pair $[Na^+(THF)_3\{fac\text{-}Mo^{V}(Mp)_3\}]$ (**1**), while a separated ion pair, *fac*-(*n*-Bu_4N)$[Mo^{V}(Mp)_3]$ (**2**), is obtained by exchanging Na^+ with *n*-Bu_4N^+. In the presence of asymmetric binding-sites, the RML reacts with $MnCl_2{\cdot}4H_2O$, $FeCl_2{\cdot}4H_2O$, $CoCl_2{\cdot}6H_2O$, and $NiCl_2{\cdot}6H_2O$ to afford UV-vis-NIR spectra, indicating binding of these guest metal cations. Especially, for the cases of the Mn^{II} and Co^{II} products, trinuclear complexes, $[M(H_2O)(MeOH)\{fac\text{-}Mo^{V}(Mp)_3\}_2]{\cdot}1.5CH_2Cl_2$ (**3**$\cdot 1.5CH_2Cl_2$ (M = Mn^{II}), **4**$\cdot 1.5CH_2Cl_2$ (M = Co^{II})), are successfully isolated and structurally characterized where the M are selectively bound to the hard O-binding sites of the *fac*-$[Mo^{V}(Mp)_3]^-$. On the other hand, a coordination polymer, $[Cu^{I}(CH_3CN)\{mer\text{-}Mo^{V}(Mp)_3\}]_n$ (**5**), is obtained by the reaction of *fac*-$[Mo^{V}(Mp)]^-$ with $[Cu^{I}(CH_3CN)_4]ClO_4$. In sharp contrast to the cases of **1**, **3**$\cdot 1.5CH_2Cl_2$, and **4**$\cdot 1.5CH_2Cl_2$, the Cu^+ in **5** are selectively bound to the soft S-binding sites, where each Cu^+ is shared by two $[Mo^{V}(Mp)_3]^-$ with bidentate or monodentate coordination modes. The second notable feature of **5** is found in the geometric change of the $[Mo^{V}(Mp)_3]^-$, where the original *fac*-form of **1** is isomerized to the *mer*-$[Mo^{V}(Mp)_3]^-$ in **5**, which was structurally and spectroscopically characterized for the first time. Such isomerization demonstrates the structural flexibility of the $[Mo^{V}(Mp)_3]^-$. Spectroscopic studies strongly indicate that the association/dissociation between the guest metal ions and RML can be modulated by solvent polarity. Furthermore, it was also found that such association/dissociation features are significantly influenced by coexisting anions such as ClO_4^- or $B(C_6F_5)_4^-$. This suggests that coordination bonds between the guest metal ions and RML are not too static, but are sufficiently moderate to be responsive to external environments. Moreover, electrochemical data of **1** and **3**$\cdot 1.5CH_2Cl_2$ demonstrated that guest metal ion binding led to enhance electron-accepting properties of the RML. Our results illustrate the use of a redox-active chalcogenolato complex with a simple mononuclear structure as a multifunctional RML that is responsive to chemical and electrochemical stimuli.

2-1. Introduction

The redox functions of coordination complexes are fundamentally important in biochemistry and materials chemistry.[1] The past half-century has witnessed increasing of interest in the chemistry of redox-active transition metal complexes, and lately their use has been expanded for the creation of electron transfer systems possessing multiple redox processes by assembling these redox-active complexes as building modules.[2] In this regard, the chemistry of dithiolene-[3] and dioxolene-complexes[4] can be cited as a representative example of complexes having remarkable redox activities, they have played a leading role in this research area. Such remarkable redox features inspired us to use these chalcogenolato-complexes as building modules of assemblies possessing tunable electron transfer ability. Very recently, the use of the $[Mo^{V}(Bdt)_3]^{-}$ (Bdt = 2-benzenedithiolato) complex was reported as a "redox-active metalloligand (RML)" that leads to new type of redox-active assemblies.[5] The selective binding ability for soft Cu^{+} and Ag^{+}, together with strong redox-dependence on metal ion binding, prompted us to expand this chemistry. It may be applicable to a wider range of metal ions, and enable the creation of molecular systems with multiple responsive functions. In this regard, the chalcogenolato complex has good design ability, based on the types of central metal ions, coordinating atoms, and terminal substituents. Therefore, the first aim of this expanding study was to introduce asymmetric coordination-sites into RMLs, because this would create more intelligent RMLs that capture several types of metal ions under controlled chemical and physical conditions. Moreover, the electrochemical properties of the RMLs could be

Chart 1. Schematic structure of a tris-RML.



significantly affected by cation binding.[6] Accordingly, we modified the symmetric S_6 coordination sphere of the aforementioned $[Mo^{V}(Bdt)_3]^-$ into an asymmetric O_3S_3 sphere by using *fac*-$[Mo^{V}(Mp)_3]^-$ (Mp = 2-mercaptophenolato).[7] This Janus-head-type[8] complex is able to show stepwise redox behavior similar to the $[Mo^{V}(Bdt)_3]^-$ RML (Chart 1). In this chapter, the intriguing coordination site-dependent binding ability of the *fac*-$[Mo^{V}(Mp)_3]^-$, depending on the types of guest metal ions, Na^+, Mn^{2+}, Fe^{2+}, Co^{2+}, Ni^{2+}, and Cu^+, are detailed. Interestingly, the association of guest metal ions enhances electron acceptability of the RMLs, and moreover, the association/dissociation behavior can be controlled not only by solvents polarity but also coexisting anions.

2-2. Experimental Section

General Procedures. All synthetic operations and measurements were performed under Ar atmosphere using Schlenk-line techniques. $MoCl_5$ and NaOMe were purchased from Wako Pure Chemical Industries. $MnCl_2{\cdot}4H_2O$, $FeCl_2{\cdot}4H_2O$, $CoCl_2{\cdot}6H_2O$, $NiCl_2{\cdot}6H_2O$ were purchased from Kanto Chemical Co. Inc. 2-Mercaptophenol (MpH_2), *n*-Bu_4NCl, and *n*-Bu_4NClO_4 were purchased from Tokyo Kasei Kogyo Co. Ltd. $[Cu^{I}(CH_3CN)_4]ClO_4$[9] and *n*-$Bu_4NB(C_6F_5)_4$[10] were synthesized using reported procedures. *n*-Hexane, and tetrahydrofuran (THF) were distilled from Na metal under an Ar atmosphere. Acetonitrile (CH_3CN), dichloromethane (CH_2Cl_2), methanol (MeOH), and *o*-dichlorobenzene (*o*-$Cl_2C_6H_4$) were distilled from CaH_2 under an Ar atmosphere. All the solvents were finally degassed in three freeze-pump-thaw cycles at least just prior to use. **Caution!** Although we experienced no difficulties with the perchlorate salt, it should be regarded as potentially explosive, and therefore handled with care.

$[Na(THF)_3\{fac\text{-}Mo^{V}(Mp)_3\}]$ (1). A greenish-blue MeOH (14 mL) solution of Na_2Mp, which was prepared by the treatment of MpH_2 (510 mg, 4.04 mmol) and NaOMe (440 mg, 8.15 mmol) in MeOH, was added to a green mixture of $MoCl_5$ (370 mg, 1.35 mmol) and MeOH (4 mL). The appearance of the reaction mixture then changed to a reddish-brown suspension. After boiling under reflux for 20 h, a brown suspension formed. The reaction mixture was cooled to room temperature, MeOH was removed, and the product extracted with THF (8 mL). A white by-product was filtered off to afford a brown THF solution. *n*-Hexane (16 mL) was layered onto this solution, and, after storage for 3 d at room temperature, reddish-brown crystals of **1**, suitable for X-ray crystallographic analysis, were obtained. The crystals were finally isolated by filtration and washing with *n*-hexane (3 mL × 3) and drying *in vacuo*. Yield 83%. Anal. Found: C, 50.19; H, 4.72. Calc. for $C_{28}H_{32}MoNaO_{5.5}S_3$ (**1**–0.5THF): C, 50.07; H, 4.80%. $\chi_M T_{300K} = 0.340$ emu·K·mol^{-1}.

***fac*-(n-Bu_4N)[$Mo^V(Mp)_3$] (2).** A reddish-brown MeOH (7 mL) solution of **1** (100 mg, 0.157 mmol) was added to a colorless MeOH (4 mL) solution of n-Bu_4NCl (175 mg, 0.63 mmol). After stirring for 1 h at room temperature, a brown precipitate formed. A brown powder was obtained after filtration, washing with H_2O (3 mL × 2) and MeOH (1 mL × 2), and drying *in vacuo*. This powder was then dissolved in THF (10 mL), and *n*-hexane (15 mL) was layered onto this THF solution. Storage of this mixture for 5 d at room temperature afforded brown crystals suitable for X-ray crystallographic analysis. After filtration and washing with *n*-hexane (3 mL × 3) and drying *in vacuo*, afforded **2** as brown crystals in 40% yield. Anal. Found: C, 57.44; H, 6.89; N, 2.09. Calc. for $C_{34}H_{48}MoNO_3S_3$ (**2**): C, 57.44; H, 6.81; N, 1.97%. $\chi_M T_{300K} = 0.337$ emu·K·mol^{-1}.

[$Mn^{II}(H_2O)(MeOH)$\{*fac*-$Mo^V(Mp)_3$\}$_2$]·1.5CH_2Cl_2 (3·1.5CH_2Cl_2). A dark brown MeOH (5 mL) solution of **1** (200 mg, 0.315 mmol) was added to a pink MeOH (1 mL) solution of $Mn^{II}Cl_2·4H_2O$ (125 mg, 0.632 mmol). After stirring for 1 h, a reddish-brown precipitate was obtained. This was filtered, and washed with H_2O (3 mL × 2) and MeOH (1 mL × 2). The resulting reddish-brown powder was dried in vacuo and used for UV-vis-NIR measurements as Mn^{II}-powder sample. For synthesis of crystal sample suitable for X-ray crystallographic analysis, this powder sample was dissolved in CH_2Cl_2 (20 mL), then *n*-hexane (20 mL) was layered onto this solution. After storage of this solution for 5 d at room temperature, reddish-brown crystals were obtained. After filtration and washing with *n*-hexane (2 mL × 3), followed by drying *in vacuo*, complex **3**·1.5CH_2Cl_2 was isolated as reddish-brown crystals in 23% yield. Anal. Found: C, 39.42; H, 3.04. Calc. for $C_{38.5}H_{33}Cl_3MnMoO_8S_6$ (**3**·1.5CH_2Cl_2): C, 39.55; H, 2.84%. $\chi_M T_{300K} = 4.471$ emu·K·mol^{-1}.

Fe^{II}-powder sample. A dark brown MeOH (0.7 mL) solution of **1** (25 mg, 0.039 mmol) was added to a pink MeOH (0.3 mL) solution of $Fe^{II}Cl_2·4H_2O$ (15.5 mg, 0.078 mmol). After stirring for 1 h, a reddish-brown precipitate was obtained. This was filtered, and washed with

H_2O (0.5 mL × 2) and MeOH (0.3 mL × 2). The resulting reddish-brown powder was dried *in vacuo* and used for UV-vis-NIR measurements as Fe^{II}-powder sample.

$[Co^{II}(H_2O)(MeOH)\{fac\text{-}Mo^{V}(Mp)_3\}_2]\cdot 1.5CH_2Cl_2$ ($4\cdot 1.5CH_2Cl_2$). A dark brown MeOH (5 mL) solution of **1** (200 mg, 0.315 mmol) was added to a pink MeOH (1 mL) solution of $Co^{II}Cl_2\cdot 4H_2O$ (125 mg, 0.632 mmol). After stirring for 1 h, a reddish-brown precipitate was obtained. This was filtered, and washed with H_2O (3 mL × 2) and MeOH (1 mL × 2). The resulting reddish-brown powder was dried *in vacuo* and used for UV-vis-NIR measurements as Co^{II}-powder sample. For synthesis of crystal sample suitable for X-ray crystallographic analysis, this powder sample was dissolved in CH_2Cl_2 (20 mL), then *n*-hexane (20 mL) was layered onto this solution. After storage of this solution for 5 d at room temperature, reddish-brown crystals were obtained. After filtration and washing with *n*-hexane (2 mL × 3), followed by drying *in vacuo*, complex $\mathbf{4}\cdot 1.5CH_2Cl_2$ was isolated as reddish-brown crystals in 10% yield. Anal. Found: C, 39.21; H, 2.86. Calc. for $C_{38.5}H_{33}Cl_3CoMoO_8S_6$ ($\mathbf{4}\cdot 1.5CH_2Cl_2$): C, 39.41; H, 2.86%. $\chi_M T_{300K} = 4.515$ emu·K·mol^{-1}.

Ni^{II}-powder sample. A dark brown MeOH (0.7 mL) solution of **1** (25 mg, 0.039 mmol) was added to a pink MeOH (0.3 mL) solution of $Ni^{II}Cl_2\cdot 4H_2O$ (18.5 mg, 0.078 mmol). After stirring for 1 h, a reddish-brown precipitate was obtained. This was filtered, and washed with H_2O (0.5 mL × 2) and MeOH (0.3 mL × 2). The resulting reddish-brown powder was dried *in vacuo* and used for UV-vis-NIR measurements as Ni^{II}-powder sample.

$[Cu^{I}(CH_3CN)\{mer\text{-}Mo^{V}(Mp)_3\}]_n$ (5). A dark-brown MeOH (5 mL) solution of **1** (100 mg, 0.14 mmol) was added to a MeOH (1 mL) suspension of $[Cu^{I}(CH_3CN)_4]ClO_4$ (52 mg, 0.14 mmol). After stirring for 3 h, a brown precipitate formed. This was filtered, and washed with H_2O (2 mL × 2) and MeOH (1 mL × 2) and dried *in vacuo* to give brown powder. For synthesis of crystal sample suitable for X-ray crystallographic analysis, this powder sample was dissolved in CH_3CN (3 mL) to afford a brown solution. This solution was layered onto H_2O (6

mL) and reddish-brown crystals, suitable for X-ray crystallographic analysis, were obtained after storage of this solution for 5 d at room temperature. After filtration and washing with CH_3CN (2 mL × 7) and diethyl ether (2 mL × 3), followed by drying *in vacuo*, complex **5** was isolated as brown crystals in 40% yield. Anal. Found: C, 41.95; H, 2.81; N, 2.73. Calc. for $C_{20}H_{15}CuMoNO_3S_6$ (**5**): C, 41.92; H, 2.64; N, 2.44%. $\chi_M T_{300K} = 0.368$ emu·K·mol^{-1}.

Physical Measurements. Elemental analyses were performed at the analysis center at Hokkaido University. Cyclic voltammetry measurements were recorded with a BAS model 650A electrochemical analyzer, using a glassy carbon working electrode and a platinum auxiliary electrode. The reference electrode was made from a silver wire, inserted into a small glass tube fitted with a porous Vycor frit at the tip, and filled with a CH_3CN solution containing 0.1 M *n*-Bu_4NClO_4 and 0.01 M $AgNO_3$. All three electrodes were immersed in 2 mL of an *o*-$Cl_2C_6H_4$ or CH_3CN solution containing 0.05 M *n*-$Bu_4NB(C_6F_5)_4$ or 0.05 M *n*-Bu_4NClO_4 as a support electrolyte, and analytes. Crystalline samples of **1**, **2**, and **3**·1.5CH_2Cl_2 were used for these measurements. In all cases, redox potentials were measured with respect to the Ag/Ag^+ redox couple. UV-Vis-NIR spectra in solution were recorded on a Hitachi U-4100 spectrophotometer over the range 200–3300 nm at 296 K using crystalline samples of **1**, **2**, and **3**·1.5CH_2Cl_2. UV-Vis-NIR spectra in the solid state were recorded on a Hitachi U-4100 spectrophotometer over the range 200–3300 nm at 296 K using KBr pellets using crystalline samples of **1**, **2**, **3**·1.5CH_2Cl_2, and **5**, and Mn^{II}-, Fe^{II}-, Co^{II}-, and Ni^{II}-powder samples. The IR spectra were recorded on a Nicolet 6700 ET-IR spectrometer equipped with a Smart-Orbit (Diamond) ATR accessory. Magnetic susceptibility of the crystalline samples was measured using a Quantum Design MPMS-XL SQUID magnetometer in a magnetic field of 1 T. Diamagnetic correlation were made based on the Pascal's constants.[11]

Crystallographic Data Collection and Refinement of Structures. Crystallographic measurements were performed on a Rigaku AFC-7R diffractometer equipped with a Mercury

CCD area detector, and graphite-monochromated Mo-Kα radiation (λ = 0.71069 Å). Specimens of suitable size and quality were selected under paraffin oil and mounted in a nylon loop (for **1** and **2**) or onto a glass fiber (for **3**·1.5CH_2Cl_2, **4**·1.5CH_2Cl_2, and **5**). The structures were solved by direct methods (SIR2004),[12] which successfully located non-hydrogen atoms. All calculations were performed using the CrystalStructure crystallographic software package,[13] except for refinement calculations, which were performed using SHELXL-97.[14] A summary of the crystallographic data for **1**, **2**, **3**·1.5CH_2Cl_2, **4**·1.5CH_2Cl_2 and **5** are summarized in Tables 1 and 2. Full crystallographic details have been deposited with the Cambridge Crystallographic Data Centre as a supplementary publication No. CCDC-823173 for **1**, -823174 for **2**, -823175 for **3**·1.5CH_2Cl_2, -823176 for **4**·1.5CH_2Cl_2, and -823177 for **5.**

Table 1. Crystallographic data of **1** and **2**

	1	**2**
Formula	$C_{30}H_{36}MoNaO_6S_3$	$C_{34}H_{48}MoNO_3S_3$
fw	707.72	710.88
Crystal size (mm^3)	0.40×0.40×0.10	0.30×0.24×0.18
Crystal system	trigonal	monoclinic
Space group	*R*-3(No. 148)	$P2_1/c$(No. 14)
a (Å)	13.334(3)	9.600(3)
b (Å)	13.334(3)	18.538(5)
c (Å)	31.203(6)	19.720(6)
α (°)	90	90
β (°)	90	97.4835(11)
γ (°)	120	90
V ($Å^3$)	4804.5(18)	3479.4(17)
T (K)	223	223
Z	6	4
D_{calc} (g cm^{-3})	1.468	1.357
F (000)	2190	1492
μ(Mo Kα) (cm^{-1})	6.578	5.895
Measured	10397	27972
Unique reflections	2449	7962
Refined parameters	125	380
GOF on F^2	1.113	0.842
R_{int}	0.034	0.036
R_1 [a]	0.0688	0.0467
wR_2 [b] (all data)	0.2264	0.1432

[a] $R_1 = \Sigma||F_o| - |F_c||/\Sigma|F_o|$. [b] $wR_2 = \{[\Sigma w(F_o^2 - F_c^2)^2]/[\Sigma w(F_o^2)^2]\}^{1/2}$.

Table 2. Crystallographic data of **3**·1.5CH_2Cl_2, **4**·1.5CH_2Cl_2, and **5**

	3·1.5CH_2Cl_2	**4**·1.5CH_2Cl_2	**5**
Formula	$C_{38.5}H_{33}Cl_3MnMo_2O$	$C_{38.5}H_{33}Cl_3CoMo_2O$	$C_{20}H_{15}CuMoNO_3S_3$
fw	1169.22	1173.21	573.01
Crystal size	0.20×0.20×0.05	0.05×0.05×0.05	0.20×0.10×0.05
Crystal system	triclinic	triclinic	monoclinic
Space group	*P*-1(No. 2)	*P*-1(No. 2)	$P2_1/n$(No. 14)
a (Å)	11.298(3)	11.356(2)	10.3274(15)
b (Å)	13.113(4)	13.024(2)	11.2089(19)
c (Å)	15.057(4)	14.982(3)	17.151(2)
α (°)	96.392(3)	96.542(3)	90
β (°)	105.830(4)	106.062(3)	92.542(7)
γ (°)	96.331(3)	95.802(3)	90
V (Å^3)	2109.6(10)	2095.0(6)	1983.4(5)
T (K)	163	163	163
Z	2	2	4
D_{calc} (g cm^{-3})	1.841	1.860	1.919
F (000)	1168	1172	1140
μ(Mo Kα) (cm^{-1})	14.176	15.223	20.423
Measured	17023	14583	33664
Unique	9469	9140	5665
Refined	533	533	263
GOF on F^2	1.015	1.014	1.109
R_{int}	0.040	0.025	0.086
R_1 [a]	0.0536	0.0534	0.0652
wR_2 [b] (all data)	0.1696	0.1418	0.1518

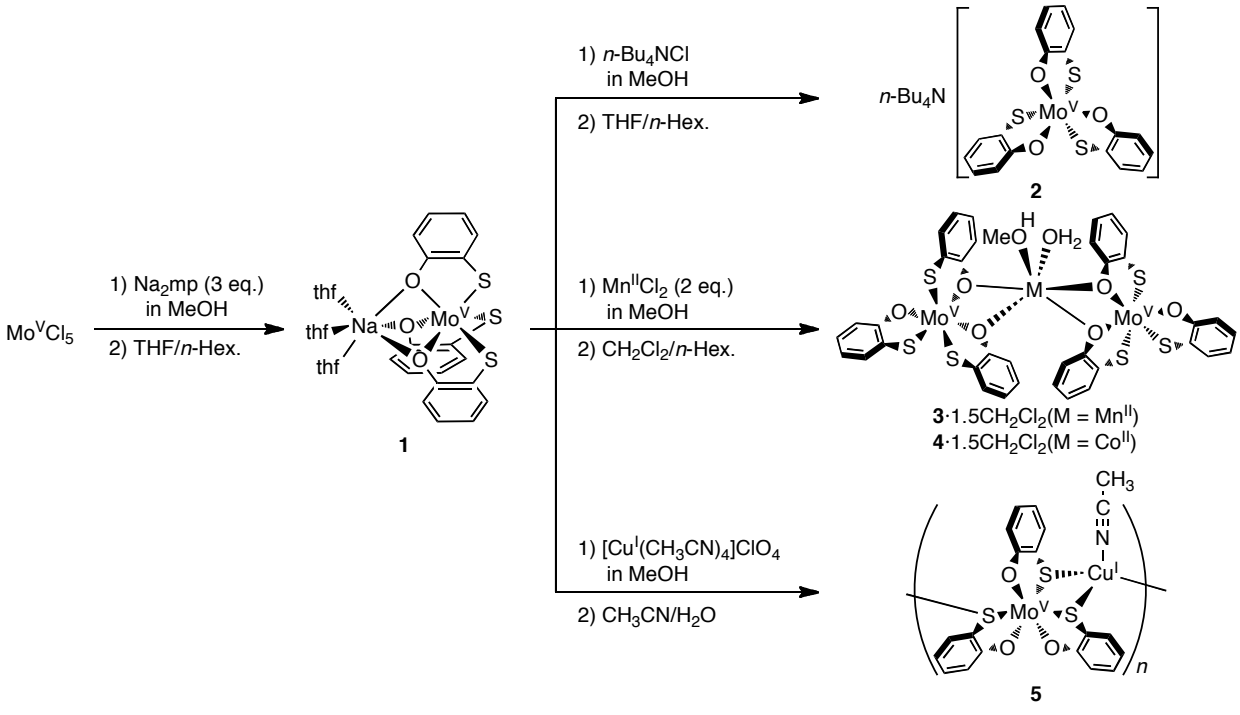
[a] $R_1 = \Sigma||F_o| - |F_c||/\Sigma|F_o|$. [b] $wR_2 = \{[\Sigma w(F_o^2 - F_c^2)^2]/[\Sigma w(F_o^2)^2]\}^{1/2}$.

2-3. Results and Discussion

2-3-1. Cation Binding Behavior of 1

The starting material **1**, the Na^+ salt of *fac*-$[Mo^V(Mp)_3]^-$, was prepared by the treatment of Na_2Mp with $MoCl_5$ in MeOH solution as reddish-brown crystals, which were grown from *n*-hexane/THF (Scheme 1). On the other hand, the Na^+ in **1** could be easily exchanged by treatment with *n*-Bu_4NCl to afford the *n*-Bu_4N^+ salt of *fac*-$[Mo^V(Mp)_3]^-$ (**2**) in MeOH solution, implying the lability of the Na^+ in **1** in MeOH. By the treatments of **1** with two equivalents of MCl_2 (M = Mn^{2+}, Fe^{2+}, Co^{2+}, and Ni^{2+}) in MeOH, brown-colored precipitations were commonly obtained. Especially for Mn^{II}- and Co^{II}-samples, reddish-brown crystals were obtained from *n*-hexane/CH_2Cl_2, and which were structurally characterized as **3**·1.5CH_2Cl_2 (M = Mn^{II}) and **4**·1.5CH_2Cl_2 (M = Co^{II}) (*vide infra*). On the other hand, a similar reaction of **1** with $[Cu^I(CH_3CN)_4]ClO_4$ in MeOH resulted in the formation of precipitation having quite lower solubility rather than those of Mn^{II}- and Co^{II}-samples. Complex **5** was finally crystallized from CH_3CN/H_2O as brown colored crystals.

Scheme 1. Synthetic schemes for **1**, **2**, **3**·1.5CH_2Cl_2, **4**·1.5CH_2Cl_2, and **5**.



2-3-2. Crystal Structures of 1 and 2

The asymmetric units of **1** and **2** are shown in Figure 1. A dinuclear structure of **1** comprises a contact ion pair, including a Na^+ and *fac*-$[Mo(C_6H_4OS)_3]^-$,[15] unit, in the ratio of 1:1 (Figure 1a). The Na^+ and Mo atoms lie on the same threefold axis. Three THF molecules coordinate to the Na^+ with a distorted octahedral geometry. The Na^+ can be removed by treatment with *n*-Bu_4NCl, to afford **2** (Figure 1b). In complex **2**, no direct interaction is found between the *n*-Bu_4N^+ and the *fac*-$[Mo(C_6H_4OS)_3]^-$. It is noteworthy that the *fac*-$[Mo(C_6H_4OS)_3]^-$ units persist in the *fac*-form in **1** and **2**, independently from the type of countercations. They can be considered predominant, based on the *trans*-effect between the O- and S-atoms[16] in *fac*-$[Mo(C_6H_4OS)_3]^-$. Notably, the Na^+ in **1** is coordinated selectively from the O-atoms of the *fac*-$[Mo(C_6H_4OS)_3]^-$, demonstrating the coordination site-selectivity of the RML with asymmetric coordinating atoms.

The Mo–O and Mo–S bond distances of **1**-**5** are listed in Table 3. The Mo–O distance in **1** is slightly longer than those in **2**, while the Mo–S distance in **1** is shorter than those in **2**. Such elongation found in the Mo–O bonds of **1** can be understood by the weakened coordination bond from the O-atoms to the Mo center by connection with the Na^+, resulting further elongation of the Mo–S distances.[5,17] According to similar complexes such as $[Mo(C_6H_4S_2)_3]^{n-}$ (n = 0, 1, and 2), bond distances in the $C_6H_4S_2$ moieties also correlate to the oxidation states of the Mo center.[18]

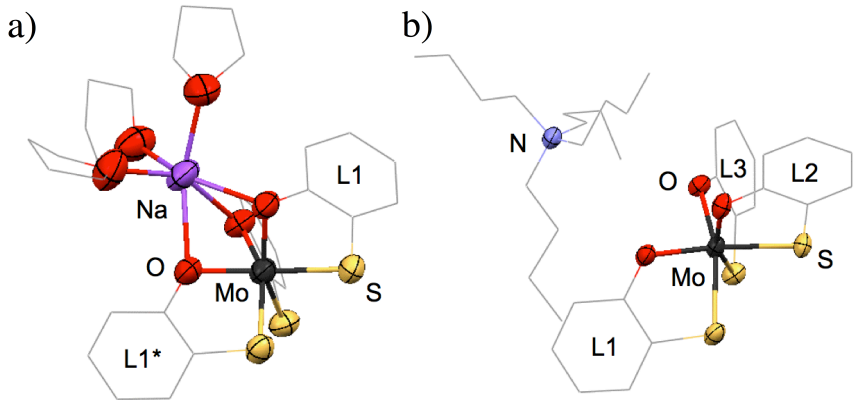


Figure 1. Crystal structures of a) **1** and b) **2** with thermal ellipsoid plots for Mo (black), O (red), S (yellow), Na (light purple), and N (light blue) (50% probability). Hydrogen atoms are omitted, and carbon atoms are depicted as wireframe for clarity.

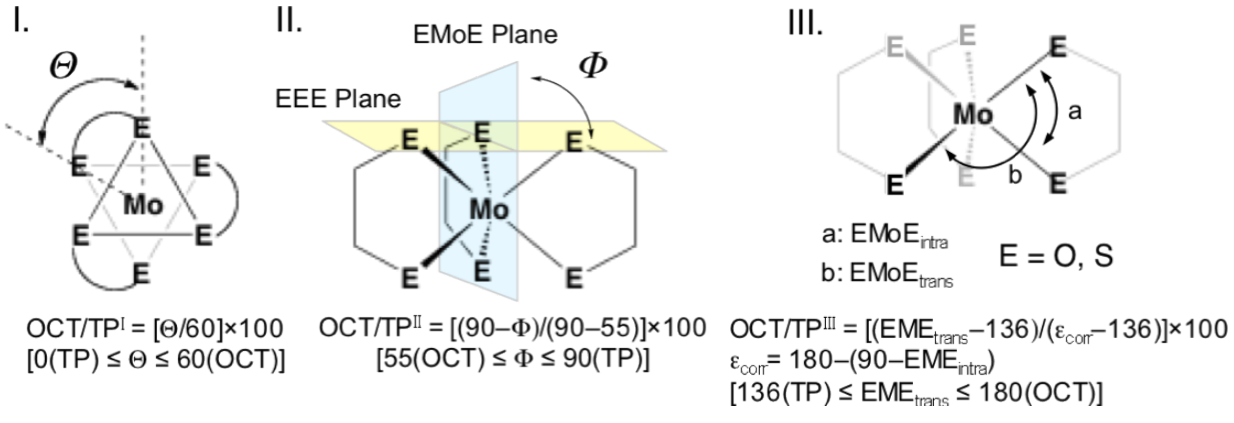
Table 3. Selected bond distances (Å) of **1**-**5**

	1	**2**	**3**·1.5CH_2Cl_2	**4**·1.5CH_2Cl_2	**5**
Mo(1)-O(1) [L1]	2.022(3)*	1.992(2)	2.071(4)*	2.065(4)*	1.980(3)
Mo(1)-O(2) [L2]		1.992(2)	2.053(3)*	2.072(3)*	1.984(3)
Mo(1)-O(3) [L3]		1.990(2)	2.026(3)	2.021(3)	1.972(3)
Mo(2)-O(4) [L4]			2.067(3)*	2.063(3)*	
Mo(2)-O(5) [L5]			2.057(3)*	2.068(3)*	
Mo(2)-O(6) [L6]			2.023(3)	2.017(3)	
Mo(1)-S(1) [L1]	2.3618(14)	2.3787(8)	2.3266(16)	2.3224(15)	2.4274(13)*
Mo(1)-S(2) [L2]		2.3858(8)	2.3208(13)	2.3190(12)	2.3905(12)*
Mo(1)-S(3) [L3]		2.3619(8)	2.3499(16)	2.3490(15)	2.4373(14)*
Mo(2)-S(4) [L4]			2.3299(15)	2.3297(14)	
Mo(2)-S(5) [L5]			2.3080(12)	2.3033(12)	
Mo(2)-S(6) [L6]			2.3515(15)	2.3559(15)	

*Distances between the Mo and chalcogen atoms directly attached to Na (**1**), Mn (**3**·1.5CH_2Cl_2), Co (**4**·1.5CH_2Cl_2), or Cu (**5**) atoms.

The C–O and C–S bond distances of **1**-**5** are listed in Table 4 and definitions of octahedral (OCT) /trigonal prism (TP) criteria, geometrical parameters for **1**-**5**, and bending angles in Mp^{2-} of **1**-**5** are shown in Chart 2, Tables 5 and 6. The C–O distances of **1** and **2** are all slightly longer than those of the previously reported benzoquinone (BQ^0) (1.28-1.34 Å)[19] or semiquinonato ($SQ^{\cdot-}$) (1.301-1.323 Å)[20] type ligands coordinating to a Mo atom. The C–S distances for **1** and **2** are greater than those of dithiobenzoquinone (DTBQ) or

Chart 2. Definitions of OCT/TP(%) criteria.



OCT/TP^{I} = [Θ/60]×100
[0(TP) ≤ Θ ≤ 60(OCT)]

OCT/TP^{II} = [(90–Φ)/(90–55)]×100
[55(OCT) ≤ Φ ≤ 90(TP)]

OCT/TP^{III} = [(EME$_{trans}$–136)/(ε_{corr}–136)]×100
ε_{corr}= 180–(90–EME$_{intra}$)
[136(TP) ≤ EME$_{trans}$ ≤ 180(OCT)]

dithiosemiquinonato (DTSQ) in $[Mo(C_6H_4S_2)_3]^0$.[18] These characters suggest that the C–O and C–S bonds in **1** and **2** are both single bonds. Furthermore, these estimations are also supported by comparisons of the C–C bond distances of the C_6H_4OS ring in **1** and **2**. In the case of DTBQ or DSTQ in $[Mo(C_6H_4S_2)_3]^0$, six-membered ring in the $C_6H_4S_2$ moiety partially has cyclohexa-3,5-diene like character, canonical structures of DTBQ or DTSQ. However, in the

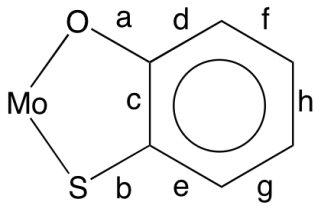


Table 4. Bond distances (Å) of the Mp^{2-} in **1**-**5**

		Å							
		a	b	c	d	e	f	g	h
1	L1*	1.361(4)	1.749(4)	1.375(6)	1.396(6)	1.429(5)	1.406(6)	1.384(8)	1.402(8)
2	L1	1.336(3)	1.746(3)	1.399(4)	1.393(4)	1.400(4)	1.384(5)	1.377(5)	1.387(6)
	L2	1.337(3)	1.748(3)	1.394(4)	1.399(4)	1.387(4)	1.378(5)	1.385(5)	1.382(6)
	L3	1.343(3)	1.751(3)	1.393(4)	1.397(4)	1.395(4)	1.378(4)	1.388(4)	1.385(5)
	Av.	1.339(3)	1.748(3)	1.395(4)	1.396(4)	1.394(4)	1.380(5)	1.383(5)	1.385(6)
3·1.5CH_2Cl_2	L1*	1.367(7)	1.748(6)	1.395(7)	1.386(8)	1.397(9)	1.391(9)	1.374(9)	1.390(8)
	L2*	1.374(6)	1.751(5)	1.396(6)	1.395(8)	1.400(7)	1.378(8)	1.373(9)	1.386(7)
	L3	1.347(7)	1.749(5)	1.406(7)	1.396(7)	1.393(9)	1.395(9)	1.387(7)	1.390(8)
	L4*	1.363(6)	1.755(6)	1.409(8)	1.390(8)	1.399(9)	1.386(8)	1.381(10)	1.389(10)
	L5*	1.374(5)	1.740(5)	1.405(7)	1.377(7)	1.406(6)	1.387(6)	1.367(9)	1.394(8)
	L6	1.344(7)	1.740(5)	1.401(7)	1.389(7)	1.406(8)	1.380(9)	1.380(8)	1.396(8)
	Av.	1.362(6)	1.747(5)	1.402(7)	1.389(8)	1.400(8)	1.386(8)	1.378(9)	1.391(8)
4·1.5CH_2Cl_2	L1*	1.361(7)	1.755(6)	1.401(6)	1.393(8)	1.388(8)	1.400(8)	1.370(8)	1.388(7)
	L2*	1.375(6)	1.749(5)	1.386(6)	1.395(7)	1.397(7)	1.376(8)	1.377(8)	1.396(7)
	L3	1.341(7)	1.748(5)	1.419(6)	1.387(7)	1.395(8)	1.390(9)	1.388(7)	1.388(7)
	L4*	1.364(6)	1.750(6)	1.397(7)	1.382(7)	1.411(8)	1.384(8)	1.372(9)	1.388(9)
	L5*	1.363(4)	1.746(5)	1.411(7)	1.386(7)	1.389(6)	1.379(6)	1.396(8)	1.396(8)
	L6	1.360(7)	1.752(5)	1.376(7)	1.398(7)	1.401(8)	1.375(8)	1.371(8)	1.398(8)
	Av.	1.361(6)	1.750(5)	1.398(7)	1.390(7)	1.397(8)	1.384(8)	1.379(8)	1.392(8)
5	L1*	1.352(6)	1.765(5)	1.395(7)	1.402(7)	1.386(7)	1.381(8)	1.383(8)	1.387(9)
	L2*	1.338(5)	1.754(5)	1.413(7)	1.400(7)	1.393(7)	1.396(8)	1.378(8)	1.363(9)
	L3*	1.349(5)	1.748(4)	1.396(7)	1.382(6)	1.402(7)	1.382(7)	1.396(7)	1.379(8)
	Av.	1.346(5)	1.756(5)	1.401(7)	1.395(7)	1.394(7)	1.386(8)	1.386(8)	1.376(9)

* Ligands directly attached to Na (**1**), Mn (**3**·1.5CH_2Cl_2), Co (**4**·1.5CH_2Cl_2), or Cu (**5**) atoms.

cases of **1** and **2**, C_6H_4OS ring does not show such cyclohexa-3,5-diene but aromatic character. Therefore, it is concluded that the C_6H_4OS moieties in **1** and **2** can be best described as Mp^{2-}. On consideration of the monoanionic charge distributions of *fac*-$[Mo(C_6H_4OS)_3]^-$ in **1** and **2**, the oxidation states of the Mo center are reasonably assigned as Mo^V, leading to the electronic structures of *fac*-$[Mo(C_6H_4OS)_3]^-$ moieties as *fac*-$[Mo^V(Mp)_3]^-$.

Furthermore, the absence of absorption peaks in these complexes arises from an intervalence

Table 5. Geometrical parameters of **1**-**5**

		OCT/TP^{I}	OCT/TP^{II}	OCT/TP^{III}
1		43.4	45.3	50.7
2		50.5	54.0	49.5
3·1.5CH_2Cl_2	Mo1	38.2	39.6	45.0
	Mo2	44.6	46.7	51.6
4·1.5CH_2Cl_2	Mo1	36.4	37.7	41.3
	Mo2	43.5	45.3	50.1
5		63.5	68.8	76.2

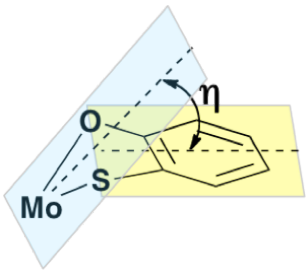


Table 6. Bending angles (η) in Mp^{2-} of **1**-**5**

	η / °				
	1	**2**	**3**·1.5CH_2Cl_2	**4**·1.5CH_2Cl_2	**5**
L1	9.27*	7.60	4.48*	4.43*	11.32*
L2	9.27*	6.60	18.92*	20.55*	9.26*
L3	9.27*	18.0	10.99	10.60	3.35*
L4			3.19*	2.81*	
L5			16.57*	18.34*	
L6			9.58	9.47	
Av.	9.27	10.73	10.62	11.03	7.98

* Ligands directly attached to Na (**1**), Mn (**3**·1.5CH_2Cl_2), Co (**4**·1.5CH_2Cl_2), or Cu (**5**) atoms.

charge transfer, which can be observed in similar complexes having electronically unequivalent ligands such as catecholato, SQ, and BQ; this also supports the characterization of the electronic structure and charge valence between three Mp^{2-} ligands.[21]

2-3-3. Crystal Structures of $3\cdot1.5CH_2Cl_2$ and $4\cdot1.5CH_2Cl_2$

In contrast to **1** and **2**, the reaction of *fac*-$[Mo^{V}(Mp)_3]^{-}$ with Mn^{2+} afforded the trinuclear complex $\mathbf{3}\cdot1.5CH_2Cl_2$, which consists of Mn and *fac*-$[Mo(C_6H_4OS)_3]$ in the ratio of 1:2 (Figure 2a). In this complex, as in the case of **1**, each $[Mo(C_6H_4OS)_3]$ unit has a *fac*-form, independently from the type of guest cation, which is selectively coordinated from the O-atoms of *fac*-$[Mo(C_6H_4OS)_3]$. Despite the presence of two equivalents of guest Mn^{2+} under the synthetic conditions used, assemblies having additional binding to extra Mn from the S-atoms were not obtained, suggesting that the S-sites are inert. The central Mn atom has octahedral geometry; it is surrounded by four O-atoms from two *fac*-$[Mo(C_6H_4OS)_3]$ with the bidentate coordination mode, and two O-atoms from H_2O and MeOH at the *cis* position.

The Mn–O bond distances (2.173(4) and 2.167(3) Å for $\mathbf{3}\cdot1.5CH_2Cl_2$) are in the range for the well-defined Mn^{II}–OH_2[22] and Mn^{II}–OHMe,[23] while the distance are longer than those of Mn=O,[24] Mn^{II}–OH,[25] and Mn^{II}–OMe,[25d,26] suggesting a best formulation around a Mn moiety as $[Mn^{II}(H_2O)(MeOH)]^{2+}$. On the other hand, as shown in Table 3, remarkably elongated Mo–O bond distances are found for $\mathbf{3}\cdot1.5CH_2Cl_2$, compared with those of **2**, together with shortened Mo–S distances. These deviations of Mo–O and Mo–S distances can be understood by similar manner with the case of **1** derived from Mn^{II} on O-atom. However, its larger magnitude of deviation in $\mathbf{3}\cdot1.5CH_2Cl_2$ than **1** can be explained based on the higher oxidation number of Mn^{II} and electronegativity (χ_{spec} = 1.74), compared with those of Na^{+} (χ_{spec} = 0.979).[27] As shown in Table 4, the C–O (1.376(5)-1.342(8) Å) and C–S (1.757(7)-1.741(5) Å) bond distances suggest that both are single bonds. Furthermore, taking into consideration the absence of partial oxidation in the C_6H_4OS ring, C_6H_4OS moieties can be suitably described as Mp^{2-}, naturally leading to the representation of RMLs as *fac*-$[Mo^{V}(Mp)_3]^{-}$. From detailed considerations of the

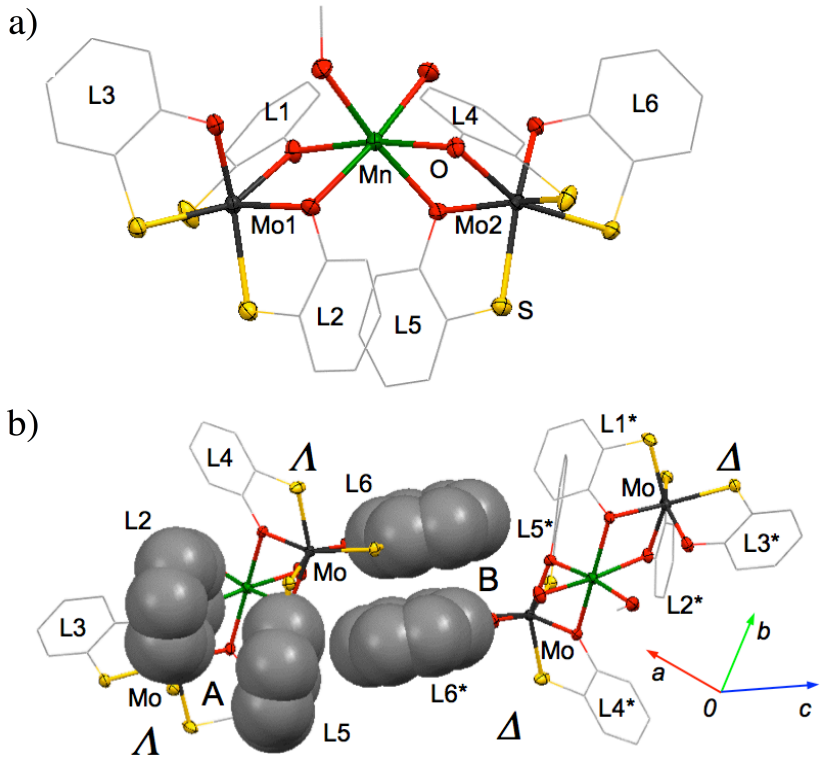


Figure 2. a) Asymmetric unit of **3**·1.5CH_2Cl_2 and b) Intramolecular (A) and intermolecular π–π interaction (B), with thermal ellipsoid plots for Mo (black), O (red), S (yellow), and Mn (green) (50% probability). Hydrogen atoms and solvent molecules are omitted, and carbon atoms are depicted as wireframe for clarity.

structural properties, **3**·1.5CH_2Cl_2 can be best described as $[Mn^{II}(H_2O)(MeOH)\{fac\text{-}Mo^{V}(Mp)_3\}_2]\cdot 1.5CH_2Cl_2$.

ΔΛ-Chirality around the pseudo-octahedral Mo^{V} centers is unified in trinuclear units (Figure 2b). The intramolecular π-π interaction with the shortest carbon atom distances among the aromatic rings are 3.450 Å (denoted as A) is found between neighboring *fac*-$[Mo(Mp)_3]^-$ units through L2 and L5, both of which are involved in coordination to additional metal (Mn^{II}). Furthermore, the optically isomeric trinuclear units are alternately stacked between layers through intermolecular π–π interaction between L6 and L6* (denoted as B), which are free from additional metal binding, with the closest carbon atom distances 3.480 Å. Since the other Mp^{2-} rings such as L1, L3, and L4 are not related with any intermolecular interaction, it is finally revealed that structures of trinuclear units through intermolecular π–π interaction are formed in crystals of **3**·1.5CH_2Cl_2.

The similar structural and spectroscopic properties were obtained also in the structurally characterized **4**·1.5CH_2Cl_2, which is isomorphous with **3**·1.5CH_2Cl_2 and described in Figure 3. Furthermore, The characteristic absorption maxima around 390, 470, and 590 nm are commonly observed for Mn^{II}-crystal sample (**3**·1.5CH_2Cl_2) and powder samples of Mn^{II}, Fe^{II}, Co^{II}, and Ni^{II}, and these spectral features indicate that these divalent metal cations interact with RML

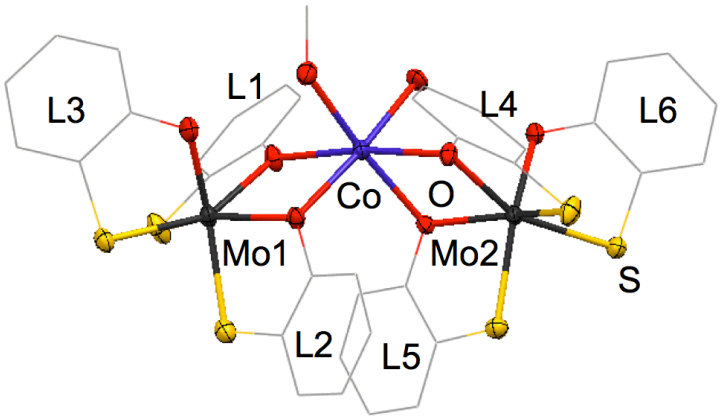


Figure 3. Asymmetric unit of **4**·1.5CH_2Cl_2 with thermal ellipsoid plots for Mo (black), O (red), S (yellow), and Co (blue) (50% probability). Hydrogen atoms and solvent molecules are omitted, and carbon atoms are depicted as wireframe for clarity.

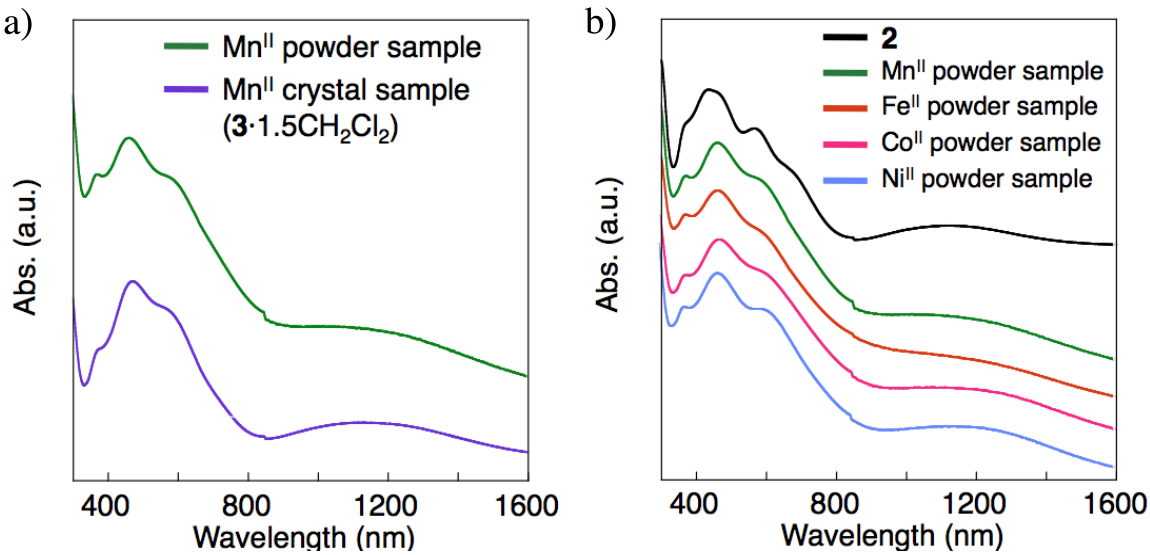


Figure 4. a) UV-Vis-NIR spectra of Mn^{II} powder sample (green line) and Mn^{II} crystal sample (purple line), and b) **2** (black line), Mn^{II} powder sample (green line), Fe^{II} powder sample (orange line), Co^{II} powder sample (pink line), and Ni^{II} powder sample (right blue line) in the solid states using KBr pellets.

$[Mo^{V}(Mp)_3]^-$ by similar manner (Figure 4b). Moreover, IR spectra of all these species which are alike in shapes also support these considerations (Figure 5).

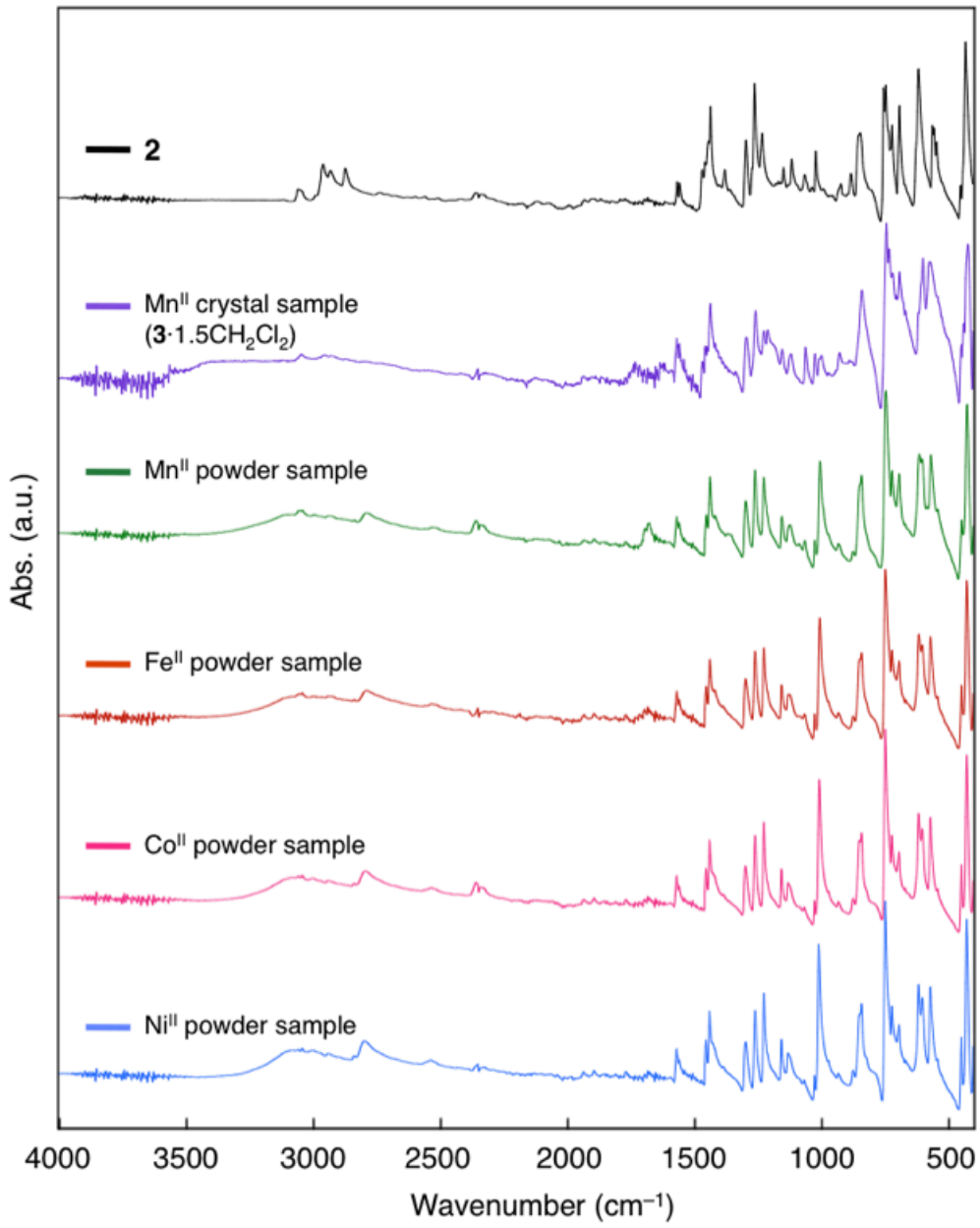


Figure 5. IR spectra of **2** (black line), Mn^{II} crystal sample (**3**·1.5CH_2Cl_2) (purple line), Mn^{II} powder sample (green line), Fe^{II} powder sample (orange line), Co^{II} powder sample (pink line), and Ni^{II} powder sample (right blue line) in the solid states.

2-3-4. Crystal Structure of 5

The unit structure of **5** is shown in Figure 6a. In contrast to the cases of **1**, **3**·1.5CH_2Cl_2, and **4**·1.5CH_2Cl_2, the Cu atoms in **5** are selectively bound to the S-atoms of [$Mo(C_6H_4OS)_3$] as indicated at synthetic step. Each Cu atom is coordinated by two [$Mo(C_6H_4OS)_3$] with Cu–S bond distances of 2.4373(14)-2.3905(12) Å, which fall in the range of previously reported Cu^I–S distances within a tetrahedral S_4 sphere.[28] Surprisingly, the *fac*-form of the starting material **1** is converted to a *mer*-form during a complexation reaction with the Cu^+. This is the first example of the *fac-mer* isomerization of Mp complexes. Such a structural change of the [$Mo(C_6H_4OS)_3$] indicates structural flexibility of the RML. As shown in Table 3, the Mo–O and Mo–S bond distances of **5** are very different from those of **1**-**4**·1.5CH_2Cl_2. Although the different geometries of [$Mo(C_6H_4OS)_3$] should also be carefully taken into account, the Mo–S distances in **5** are remarkably longer than those in **1**-**4**·1.5CH_2Cl_2 due to the attachment of Cu^+ on the S-atoms. Furthermore, the Mo–O distance in L3 (1.972(3) Å) of **5**, which is the lowest value in Table 3, accounts for the weakened Mo–S coordination bonds. On the other hand, as in the cases of **1**-**4**·1.5CH_2Cl_2, the C–O distances (1.352(6)-1.338(5) Å) and C–S (1.765(5)-1.748(4) Å) in **5** suggest to be single bonds. The C–C bond distances in the C_6H_4OS ring also substantiate these assignments (see Table 4). Therefore, C_6H_4OS in **5** are automatically described as Mp^{2-}, as well as in the cases of **1**-**4**·1.5CH_2Cl_2. Hereafter, *mer*-[$Mo(C_6H_4OS)_3$] in **5** should be described as *mer*-[$Mo^V(Mp)_3]^-$, and formulation [$Cu^I(CH_3CN)${*mer*-$Mo^V(Mp)_3$}]$_n$ for **5** is naturally leaded. In contrast to the discrete structures of **1**-**4**·1.5CH_2Cl_2, complex **5** has a 1-D polymeric structure along the *b*-axis, as shown in Figure 6b. These differences in the assembled structures indicate that the *mer*-[$Mo^V(Mp)_3]^-$ functions as a connector to form an infinite structure, while *fac*-form acts as an end-cap ligand, which leads to the formation of a discrete structure. The *ΔΛ*-chirality around the pseudo-octahedral Mo^V centers is unified in chain, and isomeric chains are stacked alternately in layers (see Figure 6c).

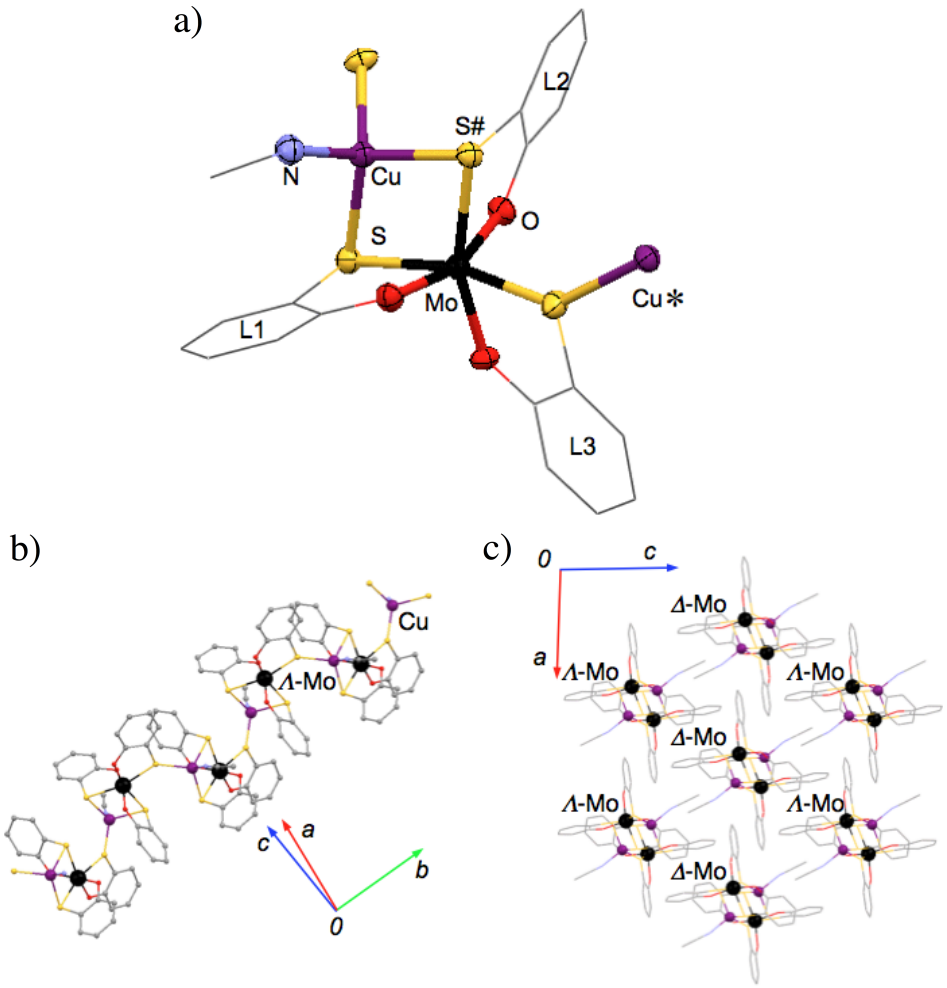


Figure 6. a) Asymmetric units of **5** with thermal ellipsoid plots for Mo (black), N (light blue), O (red), S (yellow), and Cu (purple) (50% probability). Cu/Cu∗ and S/S# denote pairs of crystallographically equivalent atoms related by center of symmetry (∗ symmetry code: 1/2–x, 1/2+y, 1.5–z, #: 1/2–x, –1/2+y, 1.5–z). b) 1D-chain structure with all the atoms drawn as ball and stick models. c) Crystal packing was projected along with the b-axis. Hydrogen atoms are omitted for clarity for both.

Based on the structures of **1**-**5**, characteristic coordination site-dependence of $[Mo^{V}(Mp)_3]^-$ on guest cation binding were confirmed. Such dependence can be understood in terms of the "hard-hard" and "soft-soft" (HSAB) interaction principle between coordinating chalcogen elements and guest metal ions.[29] Therefore, it can be said that the $[Mo^{V}(Mp)_3]^-$, having a simple structure, recognizes the chemical hardness of additional metal ions based on the HSAB theory, and captures the guest metal ions by its suitable coordination site by changing its *fac-mer* geometry flexibly in adapting to the types of guest metal ions.

2-3-5. Solvent-dependent Metal Ion Binding Behavior of *fac*-$[Mo^{V}(Mp)_3]^-$

In contrast to the static assembled structure of **5**, coordinative interactions between the *fac*-$[Mo^{V}(Mp)_3]^-$ and Na^+ or Mn^{2+} are sufficiently moderate to respond dynamically to external stimuli (*vide infra*). The UV-Vis-NIR spectra of **1**-**3**·1.5CH_2Cl_2, and **5** in solid state are shown in Figure 7. The odd-shaped spectrum of **2** with a non-coordinative *n*-Bu_4N^+ in the solid state has five absorption peaks in the visible region (300-800 nm) and a peak at 1150 nm (see Table 7). These absorptions could be assigned to CT transitions including ligand-to-metal charge transfer nature based on those of similar complex previously reported.[30] On another front, broad spectra comprising three (in **1**) or four (in **3**) peaks around 350-750 nm and a peak around 1150 nm are obtained in the solid state. The similarities between the spectra of **1** and **3**·1.5CH_2Cl_2 probably reflect the similar electronic and geometrical environments around the chromophore, *fac*-$[Mo^{V}(Mp)_3]^-$, with binding guest metal ions on its O-site. Furthermore, dissimilarities especially at visible region in the spectra of **1** and **3** from the spectrum of **2** are presumably related to the binding interaction of *fac*-$[Mo^{V}(Mp)_3]^-$ with guest metal ions in **1** and **3**. On another front, the presence of the peak at around 1150-1190 nm for **1**-**3**·1.5CH_2Cl_2 indicates these characteristic absorption should be correlated closely with *fac*-form of $[Mo^{V}(Mp)_3]^-$ RML. On the other hand, complex **5** shows a characteristic peak at 840 nm,

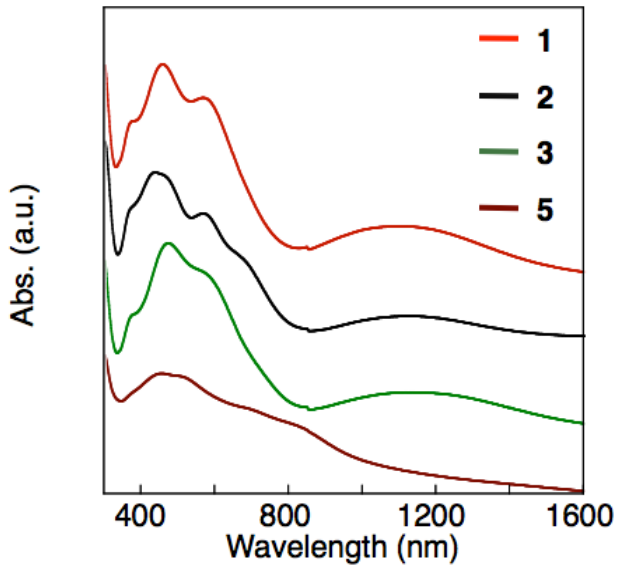


Figure 7. UV-Vis-NIR spectra of **1** (red line), **2** (black line), **3** (green line), and **5** (blown line) in the solid states using KBr pellets.

Table 7. UV-Vis-NIR spectroscopic data of **1**-**3**, and **5** in solution and solid states

Complex	Condition	λ / nm (ε / $M^{-1}cm^{-1}$)					
1[a]	Solid	370[sh]	455	565	1186		
2[a]	Solid	370[sh]	421	494[sh]	590	680[sh]	1150
3[a]	Solid	370[sh]	470	590[sh]	730[sh]	1152	
5[a]	Solid	390[sh]	440	520	690[sh]	840[sh]	
1	CH_3CN	360(10800)	419(12500)	465(11000)	562(6960)[sh]	667(3590)[sh]	1052(790)
	o-$Cl_2C_6H_4$	370(11800)	444(15900)	568(9840)[sh]	986(1860)		
2	CH_3CN	362(10900)	418(12600)	472(10800)	560(7090)[sh]	667(3640)[sh]	1052(790)
	o-$Cl_2C_6H_4$	367(12200)	420(14000)	470(11600)	562(7740)	667(3640)[sh]	1020(930)
3	CH_3CN	362(21500)	418(24800)	470(21500)	562(13900)	667(7120)[sh]	1052(1590)
	o-$Cl_2C_6H_4$	365(20600)	454(28900)	564(16400)	690(5510)[sh]	995(3800)	

[a] Measured for KBr pellets. [sh] Appeared as shoulder peak.

while the peak at 1150-1190 nm found in **1**-**3**·1.5CH_2Cl_2, was absent. These differences suggest that the observed spectroscopic differences could originate from either S-coordination or the *mer*-form of the RML, or both.

In contrast to the spectral differences of **1** and **3**·1.5CH_2Cl_2 from **2** in the solid state, due to the assembling, the spectra of **1**-**3** in CH_3CN solution show absorption maxima at almost the same wavelengths (Figure 8a). While complex **2** has an odd-shaped spectrum, with five absorption peaks in the visible region (300-700 nm) and a peak at 1052 nm, it completely overlaps with that of **1**. The spectrum of **3** is also very similar to that of **2** except for almost twice molar extinction coefficients compared with those of **1** and **2**, indicating the dissociation of ion pairs in highly polar CH_3CN (P' = 6.2).[31] Such a spectral similarity can be confirmed more clearly by differential spectra (see Figure 8b). Hence, under such conditions, the type of countercations (Na^+ for **1**, *n*-Bu_4N^+ for **2**, and Mn^{2+} for **3**) should have no further influence on the spectra. On the other hand, the spectra of **1** and **3** in less polar *o*-$Cl_2C_6H_4$ (P' = 2.7) are notably different from the spectrum of **2** (Figure 8c). The spectra of **2** in both CH_3CN and *o*-$Cl_2C_6H_4$ solutions are very similar, indicating less solvent influence on the ground and excited states of *fac*-$[Mo^V(Mp)_3]^-$. On the other hand, broad spectra comprising three and four peaks around 350-750 nm for **1** and **3**, and a peak around 1000 nm, are obtained in *o*-$Cl_2C_6H_4$. These spectral differences can be seen more clearly in the differential spectra, shown in Figure 8d. It

is worth noting that the spectral similarities of **1** and **3** compared to **2**, dependent upon the type of solvent molecules, can be understood in relation with association/dissociation behavior of the *fac*-$[Mo(Mp)_3]^-$ with guest metal ions (Na^+ for **1** and Mn^{2+} for **3**). Briefly, the coordination of the *fac*-$[Mo^V(Mp)_3]^-$ with guest metal ions is maintained with a higher degree of association in solvents that have relatively low polarity, affording absorption spectra different from that of cation-free-*fac*-$[Mo(Mp)_3]^-$. Based on the spectral features of these complexes, it can be said that the guest metal ion capture/release properties of the *fac*-$[Mo^V(Mp)_3]^-$ can be controlled by solvent polarity, and the degree of association is spectroscopically detectable.

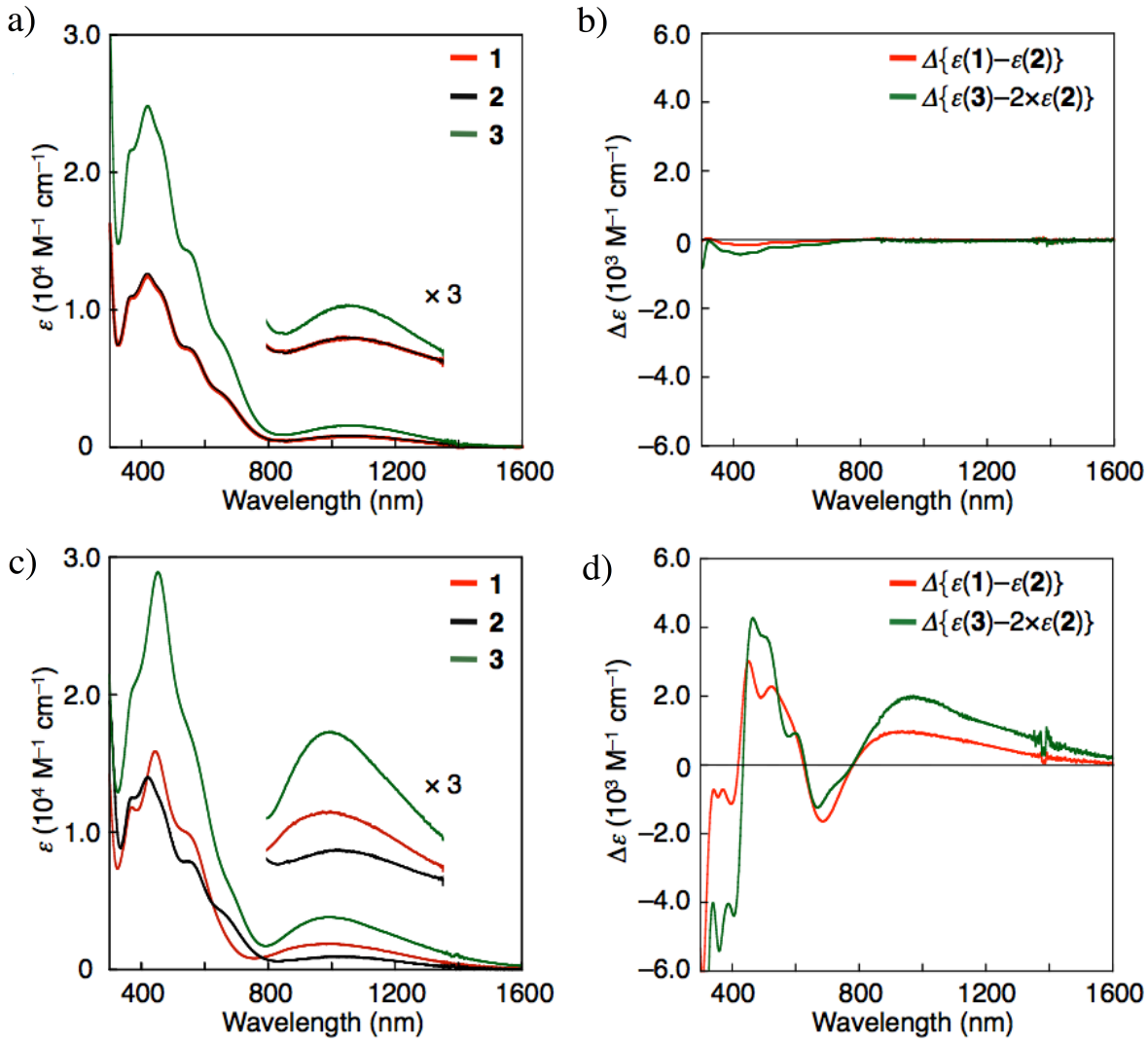


Figure 8. UV-Vis-NIR spectra of **1** (red line), **2** (black line), **3** (green line), and **5** (blown line) a) CH_3CN solution at 3×10^{-4} M and b) differential spectra of $\Delta\{\varepsilon(\mathbf{1}) - \varepsilon(\mathbf{2})\}$ (red line) and $\Delta\{\varepsilon(\mathbf{3}) - 2 \times \varepsilon(\mathbf{2})\}$ (green line), and c) *o*-$Cl_2C_6H_4$ solution at 3×10^{-4} M and d) differential spectra of $\Delta\{\varepsilon(\mathbf{1}) - \varepsilon(\mathbf{2})\}$ (red line) and $\Delta\{\varepsilon(\mathbf{3}) - 2 \times \varepsilon(\mathbf{2})\}$ (green line).

2-3-6. Guest Metal Ion- and Electrolyte-dependent Electrochemical Properties

The abovementioned solvent dependency prompted us to evaluate the redox behavior of the complexes in terms of not only the nature of the solvent but also the coexisting electrolytes, which might interact with the complexes. The UV-Vis-NIR spectra, cyclic voltammograms (CVs), and differential pulse voltammograms (DPVs) of **2** in CH_3CN with *n*-Bu_4NClO_4 (TBAP) (black line) and in *o*-$Cl_2C_6H_4$ with TBAP (blue line) or *n*-$Bu_4NB(C_6F_5)_4$ (TBAFB) (red line) are shown in Figures 9a, 9b, and 10, and the data are summarized in Table 8. All spectra of **2** shows similar spectroscopic features with that recorded in the absence of electrolytes, suggesting a less influence from the electrolytes at the ground and excited states (Figures 9a and 10a). In the CVs, one oxidation and two or one reduction waves are commonly observed at

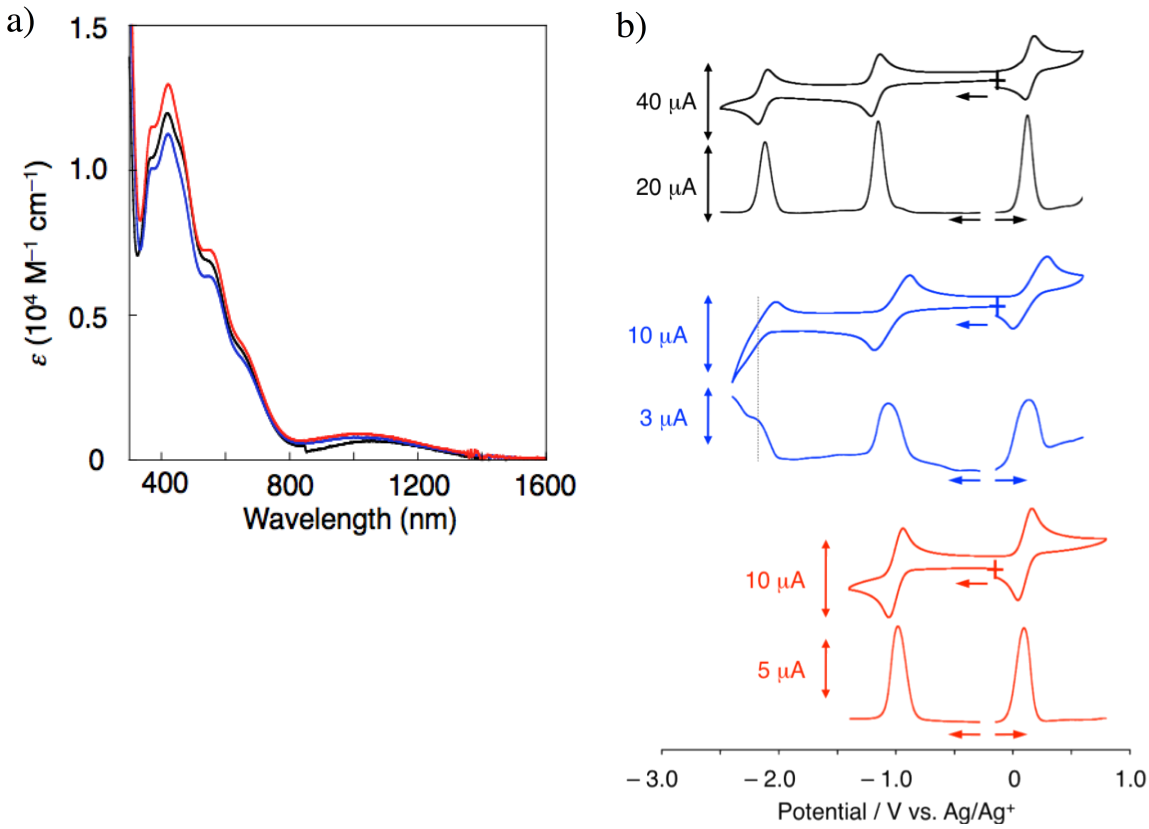


Figure 9. a) UV-Vis-NIR spectra of **2** (3×10^{-4} M) in CH_3CN with 1.5×10^{-2} M TBAP (black line), *o*-$Cl_2C_6H_4$ with 1.5×10^{-2} M TBAP (blue line), and *o*-$Cl_2C_6H_4$ with 1.5×10^{-2} M TBAFB (red line). b) CVs and DPVs of **2** (1×10^{-3} M) in CH_3CN with 0.05 M TBAP (black line), *o*-$Cl_2C_6H_4$ with 0.05 M TBAP (blue line), and *o*-$Cl_2C_6H_4$ with 0.05 M TBAFB (red line). For *o*-$Cl_2C_6H_4$ with TBAFB, negative region than –1.4 V could not be investigated due to its potential window.

almost the same potential, as shown in Figure 9b. The observed redox couples correspond to three one-electron redox processes of guest-cation-free $[Mo(C_6H_4OS)_3]^{n-}$ (n = 0, 1, 2, and 3) (eq. 1).

$$[Mo^{III}]^{3-} \underset{+e^-}{\overset{-e^-}{\rightleftharpoons}} [Mo^{IV}]^{2-} \underset{+e^-}{\overset{-e^-}{\rightleftharpoons}} [Mo^{V}]^{-} \underset{+e^-}{\overset{-e^-}{\rightleftharpoons}} [Mo]^{0} \qquad \text{eq. 1}$$

$$[Mo^{III}]^{3-} = [Mo^{III}(Mp)_3]^{3-} \quad [Mo^{V}]^{-} = [Mo^{V}(Mp)_3]^{-}$$

$$[Mo^{IV}]^{2-} = [Mo^{IV}(Mp)_3]^{2-} \quad [Mo]^{0} = [Mo(C_6H_4OS)_3]^{0}$$

Complex **1** in CH_3CN (black line) and *o*-$Cl_2C_6H_4$ with TBAP (blue line) demonstrates spectra that are identical to those of **2**, indicating dominant dissociation of the Na^+ from *fac*-$[Mo^{V}(Mp)_3]^-$ at the rest potential (Figure 11a). The CV of **1** in CH_3CN with TBAP shows one oxidation and two reduction waves (Figure 11b (black line)), where the $E^{1}_{1/2}{}^{Ox}$ is almost the

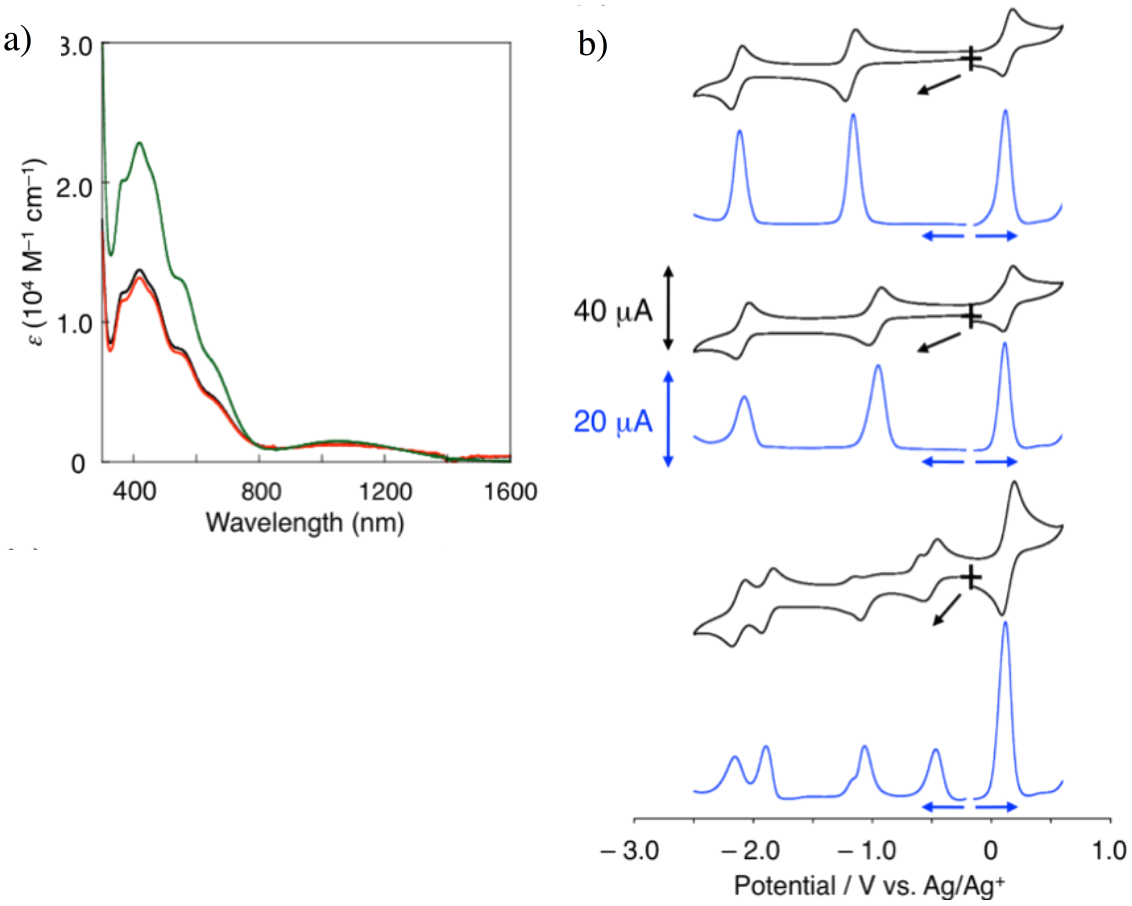


Figure 10. a) UV-Vis-NIR spectra of **1** (red line), **2** (black line), and **3** (green line) (3×10^{-4} M) in CH_3CN solution containing 1.5×10^{-2} M TBAFB. b) CVs (black line) and DPVs (blue line) of **2** (top), **1** (middle), and **3** (bottom) (1×10^{-3} M) in CH_3CN solution containing 0.05 M TBAFB.

same as that of **2**, while $E^{1}_{1/2}{}^{Red}$ and $E^{2}_{1/2}{}^{Red}$ are positively shifted by 190 and 50 mV, respectively, compared with **2**. These results indicate that the oxidized species of **1** should be dissociated from the Na^+, but the reduced species with dianionic nature have dominant association with the Na^+ (eq. 2).[32]

$$[Na\{Mo^{III}\}]^{2-} \underset{+e^-}{\overset{-e^-}{\rightleftharpoons}} [Na\{Mo^{IV}\}]^{-} \underset{+e^-}{\overset{-e^-}{\rightleftharpoons}} Na^+ + [Mo^{V}]^{-} \underset{+e^-}{\overset{-e^-}{\rightleftharpoons}} Na^+ + [Mo]^0 \quad \text{eq. 2}$$

On the other hand, dominant dissociation of **1** (Figure 11a (blue line)) at the rest potential, despite the lower polarity of *o*-$Cl_2C_6H_4$, can be explained based on the nucleophilicity of the ClO_4^-.[33] Briefly, coordination from a ClO_4^- to a Na^+ should be competitive with that from a

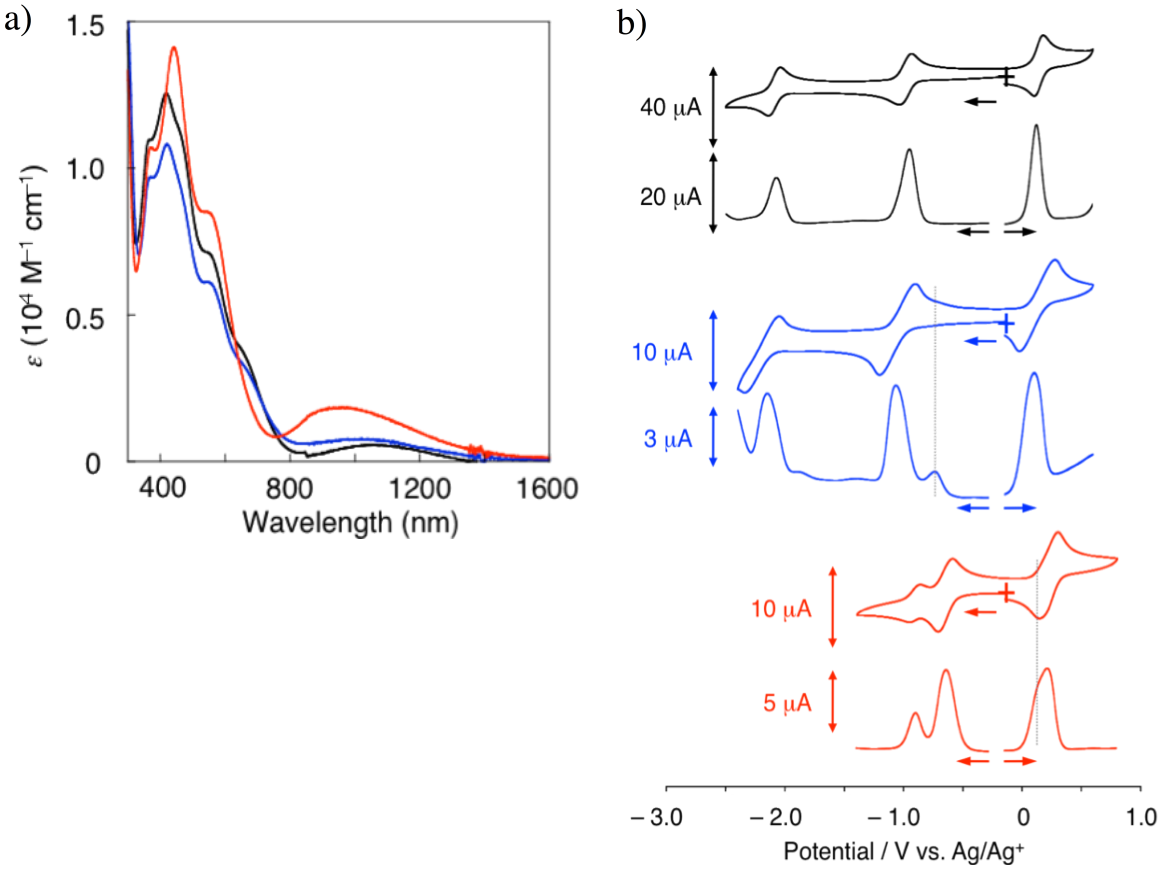


Figure 11. a) UV-Vis-NIR spectra of **1** (3×10^{-4} M) in CH_3CN with 1.5×10^{-2} M TBAP (black line), *o*-$Cl_2C_6H_4$ with 1.5×10^{-2} M TBAP (blue line), and *o*-$Cl_2C_6H_4$ with 1.5×10^{-2} M TBAFB (red line). b) CVs of **1** (1×10^{-3} M) in CH_3CN with 0.05 M TBAP (black line), *o*-$Cl_2C_6H_4$ with 0.05 M TBAP (blue line), and *o*-$Cl_2C_6H_4$ with 0.05 M TBAFB (red line), with DPVs. For *o*-$Cl_2C_6H_4$ with TBAFB, negative region than –1.4 V could not be investigated due to its potential window.

Table 8. Redox potentials of **1**, **2**, and **3**

Complex	Solvent	Supporting Electrolyte	vs. Ag/Ag^+					
			$E^3_{1/2}{}^{Red}$	$E^2_{1/2}{}^{Red}$	$E^1_{1/2}{}^{Red}$	$E^1_{1/2}{}^{Ox}$	$E^2_{1/2}{}^{Ox}$	$E^3_{1/2}{}^{Ox}$
2	CH_3CN	*n*-Bu_4NClO_4		–2.14[a]	–1.17	0.14		
	CH_3CN	*n*-$Bu_4NB(C_6F_5)_4$		–2.14	–1.18	0.14		
	o-Cl_2C_6H	*n*-Bu_4NClO_4		–2.15[a]	–1.04	0.14		
	o-Cl_2C_6H	*n*-$Bu_4NB(C_6F_5)_4$			–0.99	0.11		
1	CH_3CN	*n*-Bu_4NClO_4		–2.09	–0.98	0.14		
	CH_3CN	*n*-$Bu_4NB(C_6F_5)_4$		–2.09	–0.98	0.14		
	o-Cl_2C_6H	*n*-Bu_4NClO_4	–2.19	–1.05	–0.74[a]	0.11		
	o-Cl_2C_6H	*n*-$Bu_4NB(C_6F_5)_4$		–0.88	–0.64	0.10[a]	0.25	
3	CH_3CN	*n*-Bu_4NClO_4		–1.10[irr]	–0.53	0.14		
	CH_3CN	*n*-$Bu_4NB(C_6F_5)_4$		–1.14[irr]	–0.52	0.14		
	o-Cl_2C_6H	*n*-Bu_4NClO_4	–1.94	–1.08	–0.40	0.12		
	o-Cl_2C_6H	*n*-$Bu_4NB(C_6F_5)_4$	–0.99	–0.40[a]	–0.28[a]	0.11	0.32[a]	0.43[a]

[a] The recorded potentials are estimated by DPV. [irr] Irreversible; the recorded potentials are cathodic potentials at a scan rate of 50 mV s^{-1}.

RMLs, $[Mo(C_6H_4OS)_3]^{n-}$ (n = 0-3), and a RMLs associating with a Na^+ is possibly exchanged by ClO_4^- because of contact interaction between Na^+ and ClO_4^- in a less polar solution. This presumption is also supported by similarities in CVs of **1** (Figure 11b (blue line)) and **2** in *o*-$Cl_2C_6H_4$ with TBAP, commonly comprising one oxidation and two reduction processes. However, the differential pulse voltammetry (DPV) of **1** (Figure 11b (blue line)) also detects the associated species as minor component at the potential positively shifted by 300 mV from $E^1_{1/2}{}^{Red}$ of **2**. All of these data are consistent with the redox scheme expressed in eq. 3. From these results, the coexisting anion appears to also have a strong influence on associative interactions between RML and guest metal ions. This provisional consideration was finally confirmed by utilizing a more inert anion, as described below.

$$\begin{array}{ccccccc} Na^+ + [Mo^{III}]^{3-} & \underset{+e^-}{\overset{-e^-}{\rightleftarrows}} & Na^+ + [Mo^{IV}]^{2-} & \underset{+e^-}{\overset{-e^-}{\rightleftarrows}} & Na^+ + [Mo^{V}]^{-} & \underset{+e^-}{\overset{-e^-}{\rightleftarrows}} & Na^+ + [Mo]^0 \\ & & \updownarrow & & \updownarrow & & \\ & & [Na\{Mo^{IV}\}]^- & \underset{+e^-}{\overset{-e^-}{\rightleftarrows}} & [Na\{Mo^{V}\}]^0 & & \end{array} \qquad \text{eq. 3}$$

It is widely known that fluorinated tetraphenylborate type bulky soft anions serve as inert anions to the cationic moiety rather than ClO_4^-.[34] The deformed spectrum of **1** in *o*-$Cl_2C_6H_4$

with TBAFB (red line; Figure 11a) indicates enhanced association of *fac*-$[Mo^{V}(Mp)_3]^-$ with the Na^+, derived from lower nucleophilicity of $B(C_6F_5)_4^-$ compared with ClO_4^-. These effects are also seen in the CV; complex **1** shows one oxidation and two reduction processes, with different current ratios (red line; Figure 11b). Here, the oxidation potential is positively shifted by 140 mV, compared with **2**, indicating that associative interaction exists at the rest potential. However, the DPV (red line; Figure 11b) detects a shoulder peak around 0.1 V, indicating a small amount of Na^+-free-*fac*-$[Mo^{V}(Mp)_3]^-$. The observed $E^{1}_{1/2}{}^{Red}$ and $E^{2}_{1/2}{}^{Red}$ demonstrate significant positive shifts, by 350 and 110 mV, respectively, from the $E^{1}_{1/2}{}^{Red}$ of **2**, indicating the reduced species in associating states (eq. 4).

$$\begin{array}{ccccc} [Na\{Mo^{IV}\}]^- & \underset{+e^-}{\overset{-e^-}{\rightleftharpoons}} & [Na\{Mo^{V}\}]^0 & \underset{+e^-}{\overset{-e^-}{\rightleftharpoons}} & [Na\{Mo\}^0]^+ \\ \Big\uparrow\!\Big\downarrow & & \Big\uparrow\!\Big\downarrow & & \Big\uparrow\!\Big\downarrow \\ & \overset{-e^-}{\underset{+e^-}{\longrightarrow}} & Na^+ + [Mo^{V}]^- & \underset{+e^-}{\overset{-e^-}{\rightleftharpoons}} & Na^+ + [Mo]^0 \end{array} \qquad \text{eq. 4}$$

Finally, UV-Vis-NIR spectra and CVs of **3** are shown in Figures 12a and 12b, respectively. The spectral features of **3** in CH_3CN with TBAP (black line) are similar to those of **2**, except for the molar extinction coefficient that is twice as great, indicating dominant dissociation of the Mn^{2+} from *fac*-$[Mo^{V}(Mp)_3]^-$, as in the case of **1**. Complex **3** demonstrates one oxidation wave with a larger current value and quasi-reversible and irreversible wave, followed by two quasi-reversible reduction processes (black line; Figure 12b). The observed current values suggest two- and one-electron processes for oxidation and reduction, respectively. The unshifted $E^{1}_{1/2}{}^{Ox}$ of **3** with respect to that of **2** is compatible with the oxidation process of the Mn^{2+}-free-*fac*-$[Mo^{V}(Mp)_3]^-$. On the other hand, the reduction potential, $E^{1}_{1/2}{}^{Red}$, shows a significant positive shift, by 640 mV, compared with that of **2**, suggesting redox-induced associative interaction of the reduced RML $[Mo^{IV}(Mp)_3]^{2-}$ with the Mn^{2+}, with enhanced electron acceptability, as shown in eq. 5.

$$\underset{+e^-}{\overset{\text{irr.}}{\longleftarrow}} [Mn^{II}\{Mo^{IV}\}]^0 + [Mo^{V}]^- \underset{+e^-}{\overset{-e^-}{\rightleftharpoons}} Mn^{2+} + 2[Mo^{V}]^- \underset{+2e^-}{\overset{-2e^-}{\rightleftharpoons}} Mn^{2+} + 2[Mo]^0 \qquad \text{eq. 5}$$

or

$$[Mn^{II}\{Mo^{IV}\}\{Mo^{V}\}]^-$$

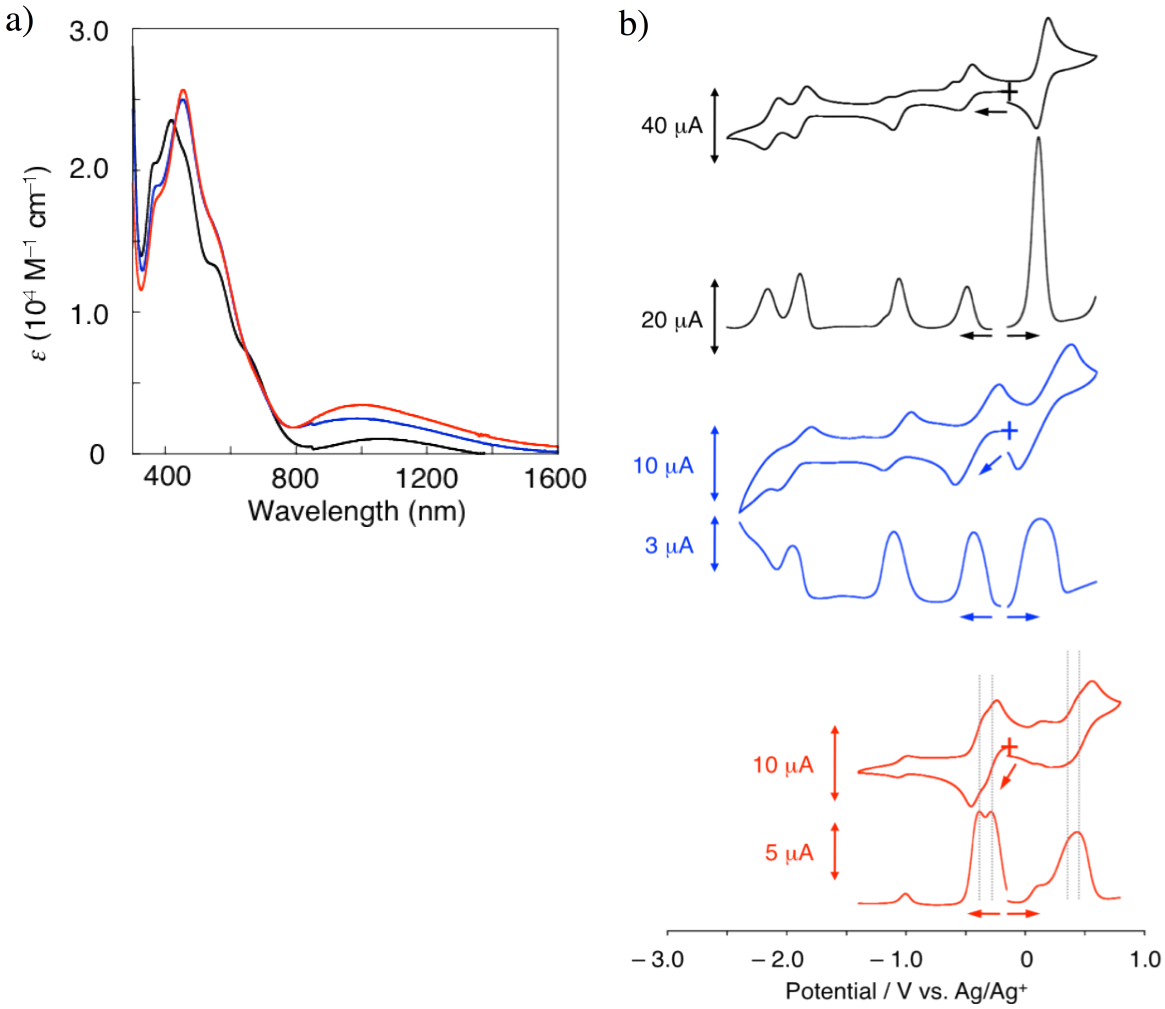


Figure 12. a) UV-Vis-NIR spectra of **3** (3×10^{-4} M) in CH_3CN with 1.5×10^{-2} M TBAP (black line), *o*-$Cl_2C_6H_4$ with 1.5×10^{-2} M TBAP (blue line), and *o*-$Cl_2C_6H_4$ with 1.5×10^{-2} M TBAFB (red line). b) CVs of **3** (1×10^{-3} M) in CH_3CN with 0.05 M TBAP (black line), *o*-$Cl_2C_6H_4$ with 0.05 M TBAP (blue line), and *o*-$Cl_2C_6H_4$ with 0.05 M TBAFB (red line), with DPV. For *o*-$Cl_2C_6H_4$ with TBAFB, negative region than –1.4 V could not be investigated due to its potential window.

Regarding the one-electron reduced species, both di- and trinuclear species are plausible; however, the former seems to be a more likely candidate because of the reduced electron deficiency on the Mn^{2+} bound with $[Mo^{IV}(Mp)_3]^{2-}$. It is noted that Mn^{2+} is redox inert in this potential region (Figure 13). Therefore, the following irreversible process might be due to the electrochemically-driven activation of the CH_3CN molecule mediated by a Mn^{2+} and/or a Mo^{4+} metal centers (Scheme 2).[35]

In contrast, the spectrum of **3** in *o*-$Cl_2C_6H_4$ with TBAP (blue line; Figure 12a) shows less influence of the coexisting ClO_4^-, suggesting dominant association of the *fac*-$[Mo^V(Mp)_3]^-$ with the Mn^{2+}. Under this condition, complex **3** shows a redox wave with larger currents in both the positive and the negative regions, and two additional waves with smaller currents in the region from –1 to –2 V (blue line; Figure 12b). Based on the observed current values, it is proposed that the processes at $E^1_{1/2}{}^{Ox}$ and $E^1_{1/2}{}^{Red}$ correspond to two-electron redox processes, while redox processes at $E^2_{1/2}{}^{Red}$ and $E^3_{1/2}{}^{Red}$ correspond to one-electron redox processes. The oxidation potential of **3** is obtained at the almost same potential as that of **2**, indicating the dominant dissociation of the RML from the Mn^{2+} in the oxidized state. In contrast, $E^1_{1/2}{}^{Red}$ and $E^3_{1/2}{}^{Red}$ tend to be positively shifted by 640 and 210 mV, respectively, implying that the RML maintains associative interaction with the Mn^{2+} throughout these reduction reactions. The second reduction process is obtained at the same potential with $E^1_{1/2}{}^{Red}$ of **2**, which is indicative of the process corresponding to the reduction of the partially existing Mn^{2+}-free *fac*-$[Mo^V(Mp)_3]^-$ as formulated in eq. 6.

$$\begin{array}{ccccc} [Mn^{II}\{Mo^{III}\}\{Mo^{IV}\}]^- & \underset{+e^-}{\overset{-e^-}{\rightleftharpoons}} & [Mn^{II}\{Mo^{IV}\}_2]^{2-} & \underset{+2e^-}{\overset{-2e^-}{\rightleftharpoons}} & [Mn^{II}\{Mo^{V}\}_2]^0 \underset{+2e^-}{\overset{-2e^-}{\rightleftharpoons}} Mn^{2+} + 2[Mo]^0 \\ & & \updownarrow & & \updownarrow \\ & & Mn^{2+} + 2[Mo^{IV}]^{2-} & \underset{+2e^-}{\overset{-2e^-}{\rightleftharpoons}} & Mn^{2+} + 2[Mo^{V}]^- \end{array} \qquad \text{eq. 6}$$

The coexisting anion dependency was also examined for **3**. The spectrum of **3** in *o*-$Cl_2C_6H_4$ in the presence of TBAFB shown in Figure 12a (red line) indicates a dominative association of *fac*-$[Mo^V(Mp)_3]^-$ with the Mn^{2+}. Complex **3** under this condition shows one minor oxidation and subsequent major oxidation processes, where the latter processes can be divided into two consequent oxidations, $E^2_{1/2}{}^{Ox}$ and $E^3_{1/2}{}^{Ox}$, with positive shifts by 320 and 210 mV, respectively, from $E^1_{1/2}{}^{Ox}$ of **2** (red line in Figure 12b and DPV (red line in Figure 12b)). Likewise, two reductions at $E^1_{1/2}{}^{Red}$ and $E^2_{1/2}{}^{Red}$ are found at the potentials positively shifted by 710 and 590 mV, respectively, from the $E^1_{1/2}{}^{Red}$ of **2**. These positively shifted redox potentials should correspond to the redox processes of the RML in association with the Mn^{2+}. The $E^1_{1/2}{}^{Ox}$ and $E^3_{1/2}{}^{Red}$

processes recorded at almost the same potentials as in **2**, can be assigned as redox process of the Mn^{2+}-free-*fac*-$[Mo^{V}(Mp)_3]^{-}$, and the total redox scheme of **3** under these conditions can be represented by eq. 7. The fact that major oxidation and reduction comprised two closely related processes means that the mixed-valence species, $[Mn^{II}\{Mo^{IV}\}\{Mo^{V}\}]^{-}$ (**A**) and $[Mn^{II}\{Mo^{V}\}\{Mo\}^{0}]^{+}$ (**B**) exist during these redox reactions.

$$[Mn^{II}\{Mo^{IV}\}_2]^{2-} \underset{+e^-}{\overset{-e^-}{\rightleftharpoons}} \mathbf{A} \underset{+e^-}{\overset{-e^-}{\rightleftharpoons}} [Mn^{II}\{Mo^{V}\}_2]^{0} \underset{+e^-}{\overset{-e^-}{\rightleftharpoons}} \mathbf{B} \underset{+e^-}{\overset{-e^-}{\rightleftharpoons}} [Mn^{II}\{Mo\}^{0}_2]^{2+}$$

$$Mn^{2+} + 2[Mo^{IV}]^{2-} \underset{+2e^-}{\overset{-2e^-}{\rightleftharpoons}} Mn^{2+} + 2[Mo^{V}]^{-} \underset{+2e^-}{\overset{-2e^-}{\rightleftharpoons}} Mn^{2+} + 2[Mo]^{0} \qquad \text{eq. 7}$$

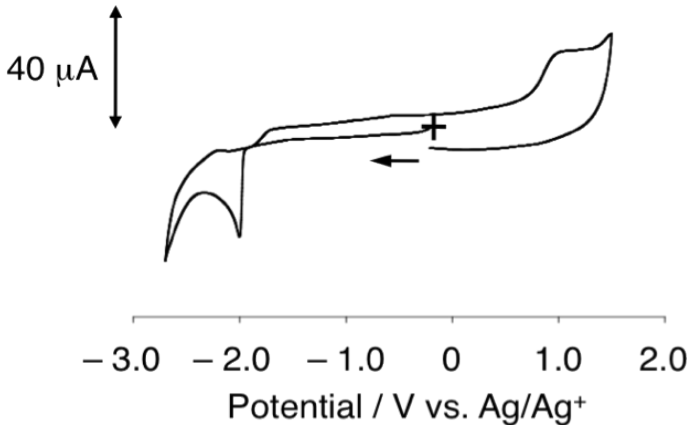
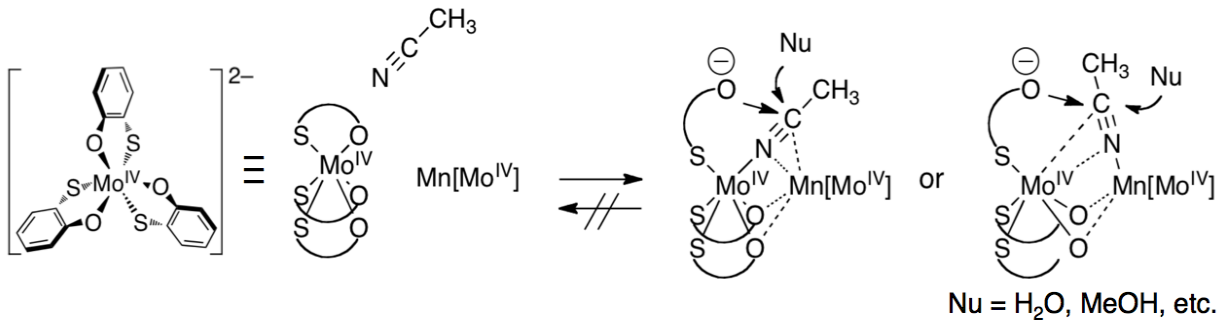


Figure 13. CV of $Mn^{II}(H_2O)_6(ClO_4)_2$ (1×10^{-3} M) in CH_3CN with 0.1 M $TBAPF_6$.

Scheme 2. Plausible mechanisms of electrochemically irreversible reactions of **3** in CH_3CN solution.[35]



2-4. Conclusions

The guest metal ion binding behavior of the redox-active RML, *fac*-$[Mo^{V}(Mp)_3]^-$, bearing asymmetric coordination-sites (O-sites and S-sites) were investigated. Based on the structures of **1**-**5**, the characteristic coordination site-dependence of this Janus-head-type RML upon the type of guest metal ions was confirmed. It can be considered that such coordination site-dependence of *fac*-$[Mo^{V}(Mp)_3]^-$ is in agreement with the HSAB[29] interaction principle between guest metal ions and coordination-sites. In addition to the coordination site-dependence, geometrical flexibility of $[Mo^{V}(Mp)_3]^-$ is another contributory factor; it enables this RML to behave as an adaptable host molecule for a wider range of guest metal ions. Moreover, results of absorption spectroscopy strongly indicate that binding interactions of the RMLs and the guest metal ions are not very static; they are sufficiently moderate to respond to external environments, such as solvent polarity, electrochemical redox reactions of RMLs, and coexisting anions. On the other hand, comparative electrochemical investigations of **1**-**3** demonstrated an increased electron-accepting capacity, especially for **3**, induced by the association with guest metal ions. These results indicate that assembling of the RML by guest metal ion-mediated cross-linking is the efficient approach for creation of heterometallic multinuclear assemblies possessing remarkable electron acceptability. In this chapter, the electrochemical properties of O-site-linked assemblies by hard metal ions were demonstrated, while it would be possible to investigate assemblies where the S-site is involved in cross-linking by utilizing a wider range of soft metal ions. Therefore, the presented results illustrate the potential usefulness of $[M(dichalcogenolato)_m]^{n-}$ as a RML for the creation of assembled structures possessing remarkable electronic flexibility.

2-5. References

1. a) P. L. Boulas, M. Gomez-Kaifer, L. Echegoyen, *Angew. Chem., Int. Ed.*, **1998**, *37*, 216; b) T. G. Drummond, M. G. Hill, J. K. Barton, *Nat. Biotechnol.*, **2003**, *21*, 1192; c) N. G. Connelly, W. E. Geiger, *Chem. Rev.*, **1996**, *96*, 877.
2. a) M. D. Ward, *Chem. Soc. Rev.*, **1997**, *26*, 365; (b) J. S. Lindsey, S. Prathapan, T. E. Johnson, R. W. Wagner, *Tetrahedron*, **1994**, *50*, 8941.
3. a) G. N. Schrauzer, *Acc. Chem. Res.*, **1969**, *2*, 72; b) E. I. Stiefel, *Dithiolene Chemistry: Synthesis, Properties, and Applications*., John Wiley & Sons, New Jersey, 2004; c) G. N. Schrauzer, V. Mayweg, *J. Am. Chem. Soc.*, **1962**, *84*, 3221; d) A. Davison, N. Edelstein, R. H. Holm, A. H. Maki, *J. Am. Chem. Soc.*, **1963**, *85*, 3049; e) A. Davison, N. Edelstein, R. H. Holm, A. H. Maki, *Inorg. Chem.*, **1963**, *2,* 1227; f) A. Davison, N. Edelstein, R. H. Holm, A. H. Maki, *J. Am. Chem. Soc.*, **1963**, *85*, 2029; g) R. Eisenberg, *Progr. Inorg. Chem.*, **1970**, *12,* 295; h) H. B. Gray, E. Billig, *J. Am. Chem. Soc.*, **1963**, *85*, 2019; i) J. A. McCleverty, *Prog. Inorg. Chem.*, **1968**, *10*, 49; j) C. Mahadevan, *J. Crystallogr. Spectrosc. Res.*, **1986**, *16*, 347; k) J. M. Williams, H. H. Wang, T. J. Emge, U. Geiser, M. A. Beno, P. C. W. Leung, K. D. Carlson, R. J. Thorn, A. J. Schultz, M. H. Whangbo, *Prog. Inorg. Chem.*, **1987**, *35*, 51; l) M. Fourmigue, *Coord. Chem. Rev.*, **1998**, *178-180*, 823; m) M. Nomura, T. Cauchy, M. Fourmigue, *Coord. Chem. Rev.*, **2010**, *254*, 1406.
4. a) C. G. Pierpont, R. M. Buchanan, *Coord. Chem. Rev.*, **1981**, *38*, 45; b) C. G. Pierpont, *Coord. Chem. Rev.*, **2001**, *216-217*, 99; c) C. G. Pierpont, *Coord. Chem. Rev.*, **2001**, *219-221*, 415; d) R. Yamahara, S. Ogo, H. Masuda, Y. Watanabe, *J. Inorg. Biochem.*, **2002**, *88*, 284; e) A. Dei, L. Sorace, *Appl. Magn. Reson.*, **2010**, *38*, 139; f) H.-C. Chang, K. Mochizuki, S. Kitagawa, *Inorg. Chem.*, **2005**, *44*, 3799; g) H.-C. Chang, K. Mochizuki, S. Kitagawa, *Inorg. Chem.*, **2005**, *44*, 3810.
5. T. Matsumoto, H.-C. Chang, A. Kobayashi, K. Uosaki, M. Kato, *Inorg. Chem.*, **2011**, *50*, 2859.

6. a) V. P. Boricha, S. Patra, Y. S. Chouhan, P. Sanavada, E. Suresh, P. Paul, *Eur. J. Inorg. Chem.*, **2009**, 1256; b) A. Chesney, M. R. Bryce, A. S. Batsanov, J. A. K. Howard, L. M. Goldenberg, *Chem. Commun.*, **1998**, 677.
7. a) B.-S. Kang, X.-J. Wang, C.-Y. Su, H.-Q. Liu, T.-B. Wen, Q.-T. Liu, *Transition Met. Chem.*, **1999**, *24*, 712; b) Y. Hu, L. Weng, B. Kang, *Jiegou Huaxue,* **1991**, *10,* 84; c) B. Zhuang, L. Huang, A. Lan, L. He, X. Zhao, J. Lu, *Polyhedron*, **1992**, *11*, 2557.
8. a) T. Stey, J. Henn, D. Stalke, *Chem. Commun.*, **2007,** 413; b) C. Kling, D. Leusser, T. Stey and D. Stalke, *Organometallics*, **2011**, *30*, 2461; c) T. Stey, M. Pfeiffer, J. Henn, S. K. Pandey, D. Stalke, *Chem. Eur. J.*, **2007**, *13*, 3636; d) F. Baier, Z. Fei, H. Gornitzka, A. Murso, S. Neufeld, M. Pfeiffer, I. Rudenauer, A. Steiner, T. Stey, D. Stalke, *J. Organomet. Chem.*, **2002**, *661*, 111.
9. a) P. Hemmerich and C. Sigwart, *Experientia*, **1963**, *19*, 488; b) I. Csoregh, P. Kierkegaard and R. Norrestam, *Acta Crystallogr.*, **1975**, *B31*, 314; c) S. Kitagawa, M. Munakata, *Inorg. Chem.*, **1981**, *20*, 2261; d) T. C. Deivaraj, J. J. Vittal, *J. Chem. Soc., Dalton Trans.*, **2001**, 322.
10. a) D. Alberti and K.-R. Pörschke, *Organometallics*, **2004**, *23*, 1459; b) A. Nafady, P. J. Costa, M. J. Calhorda, W. E. Geiger, *J. Am. Chem. Soc.*, **2006**, *128*, 16587; c) R. J. LeSuer, C. Buttolph, W. E. Geiger, *Anal. Chem.*, **2004**, *76*, 6395; d) A. G. Massey, A. J. Park, *J. Organomet. Chem.*, **1964**, *2*, 245.
11. O. Kahn, *Molecular Magnetism*, Willey-VCH, New York, 1993.
12. M. C. Burla, R. Caliandro, M. Camalli, B. Carrozzini, G. L. Cascarano, L. De Caro, C. Giacovazzo, G. Polidori, R. Spagna, *J. Appl. Crystallogr.*, **2005**, *38*, 381.
13. CrystalStructure 3.8.2, Crystal Structure Analysis Package; Rigaku and Rigaku/MSC: The Woodlands, TX, 2000−2006.
14. G. Sheldrick, SHELX-97 Program for Crystal Structure Solution and the Refinement of Crystal Structures, Institüt für Anorganische Chemie der Universität Göttingen, Tammanstrasse 4, D-3400 Göttingen, Germany, 1997.

15. The only bidentate ligand, that charge is clearly assigned as dianionic, is written as Mp(2–).

16. A. Cervilla, E. Llopis, A. Domenech, A. Ribera, P. Palanca, P. Gomez-Romero, *J. Chem. Soc., Dalton Trans*., **1992**, 1005.

17. K. Sugimoto, T. Kuroda-Sowa, M. Maekawa and M. Munakata, *Bull. Chem. Soc. Jpn*., **2000**, *73*, 391.

18. M. Cowie, M. J. Bennett, *Inorg. Chem*., ***1976***, *15*, 1584.

19. a) S. Liu, S. N. Shaikh and J. Zubieta, *J. Chem. Soc., Chem. Commun*., **1988**, 1017; b) C. G. Pierpont, H. H. Downs, *Inorg. Chem*., **1977**, *16*, 2970; c) C. G. Pierpont, H. H. Downs, *J. Am. Chem. Soc*., **1975**, *97*, 2123; d) C. G. Pierpont, R. M. Buchanan, *J. Am. Chem. Soc*., **1975**, *97*, 4912; e) S. Liu, S. N. Shaikh and J. Zubieta, *Inorg. Chem*., **1989**, *28*, 723.

20. C. G. Pierpont, R. M. Buchanan, *J. Am. Chem. Soc*., ***1975***, *97*, 6450.

21. a) H.-C. Chang, H. Miyasaka, S. Kitagawa, *Inorg. Chem*., **2001**, *40*, 146; b) H.-C. Chang, K. Mochizuki, S. Kitagawa, *Inorg. Chem*., **2002**, *41*, 4444.

22. a) R. J. Butcher, E. Sinn, *J. Chem. Soc., Dalton Trans*., **1976**, 1186; b) D. Martinez, M. Motevalli, M. Watkinson, *Acta Crystallogr. Sect. C: Cryst. Struct. Commun*., **2002**, *C58*, m258; c) J. M. Li, *Acta Crystallogr. Sect. E: Struct. Rep. Online*, **2007**, *E63*, m2266; d) D. A. Beauchamp, S. J. Loeb, *Chem. Eur. J*., **2002**, *8*, 5084; e) T. S. Lobana, I. Kinoshita, K. Kimura, T. Nishioka, D. Shiomi, K. Isobe, *Eur. J. Inorg. Chem*., **2004**, 356; f) D. Huang, W. Wang, X. Zhang, C. Chen, F. Chen, Q. Liu, D. Liao, L. Li, L. Sun, *Eur. J. Inorg. Chem*., **2004**, 1454; g) D. Dobrzynska, L. B. Jerzykiewicz, *J. Am. Chem. Soc*., **2004**, *126*, 11118; h) T. P. J. Garrett, J. M. Guss, H. C. Freeman, *Acta Crystallogr. Sect. C: Cryst. Struct. Commun*., **1983**, *C39*, 1031.

23. a) J.-Z. Wu, E. Bouwman, A. M. Mills, A. L. Spek, J. Reedijk, *Inorg. Chim. Acta*, **2004**, *357*, 2694; b) J.-P. Costes, F. Dahan, B. Donnadieu, M.-J. Rodriguez Douton, M.-I. Fernandez Garcia, A. Bousseksou, J.-P. Tuchagues, *Inorg. Chem*., **2004**, *43*, 2736; c) H. Miyasaka, T. Nezu, K. Sugimoto, K.-i. Sugiura, M. Yamashita, R. Clerac, *Chem. Eur. J*., **2005**, *11*, 1592; d) C. Pelizzi, G. Pelizzi, G. Predieri, F. Vitali, *J. Chem. Soc., Dalton Trans*., **1985**, 2387; e)

J.-B. Lin, J.-P. Zhang, W.-X. Zhang, W. Xue, D.-X. Xue, X.-M. Chen, *Inorg. Chem.*, **2009**, *48*, 6652.

24. a) J. R. Galán-Mascarós, C. Giménez-Saiz, S. Triki, C. J. Gómez-García, E. Coronado, L. Ouahab, *Angew. Chem. Int. Ed.*, **1995**, *34*, 1460; b) F. M. MacDonnell, N. L. P. Fackler, C. Stern, T. V. O'Halloran, *J. Am. Chem. Soc.*, **1994**, *116*, 7431; c) R. Gupta, C. E. MacBeth, V. G. Young, A. S. Borovik, *J. Am. Chem. Soc.*, **2002**, *124*, 1136.
25. a) A. A. Eroy-Reveles, Y. Leung, C. M. Beavers, M. M. Olmstead, P. K. Mascharak, *J. Am. Chem. Soc.*, **2008**, *130*, 4447; b) Z. Shirin, B. S. Hammes, V. G. Young, Jr., A. S. Borovik, *J. Am. Chem. Soc.*, **2000**, *122*, 1836; c) Z. Shirin, V. G. Young, Jr., A. S. Borovik, *Chem. Commun.*, **1997**, 1967; d) T. J. Hubin, J. M. McCormick, N. W. Alcock, D. H. Busch, *Inorg. Chem.*, **2001**, *40*, 435; e) G. Yin, J. M. McCormick, M. Buchalova, A. M. Danby, K. Rodgers, V. W. Day, K. Smith, C. M. Perkins, D. Kitko, J. D. Carter, W. M. Scheper, D. H. Busch, *Inorg. Chem.*, **2006**, *45*, 8052.
26. a) M. J. Camenzind, F. J. Hollander, C. L. Hill, *Inorg. Chem.*, **1982**, *21*, 4301; b) K. Ghosh, A. A. Eroy-Reveles, M. M. Olmstead, P. K. Mascharak, *Inorg. Chem.*, **2005**, *44*, 8469; c) R. J. Cross, L. J. Farrugia, P. D. Newman, R. D. Peacock, D. Stirling, *Inorg. Chem.,* **1999**, *38*, 1186.
27. L. C. Allen, *J. Am. Chem. Soc.*, **1989**, *111*, 9003.
28. a) G. A. Bowmaker, C. Pakawatchai, B. W. Skelton, P. Thavornyutikarn, Y. Wattanakanjana, A. H. White, *Aust. J. Chem.,* **1994**, *47*, 15; b) S. C. Kokkou, V. Schramm, P. Karagiannidis, *Acta Crystallogr. Sect. C: Cryst. Struct. Commun.*, **1985**, *C41*, 1040.
29. a) R. G. Pearson, *J. Am. Chem. Soc.*, **1963**, *85*, 3533; b) T.-L. Ho, *Chem. Rev.*, **1975**, *75*, 1.
30. a) E. I. Stiefel, R. Eisenberg, R. C. Rosenberg, H. B. Gray, *J. Am. Chem. Soc.*, **1966**, *88*, 2956; b) J. L. Martin, J. Takats, *Inorg. Chem.*, **1975**, *14*, 73; c) S. Sproules, P. Banerjee, T. Weyhermüller, Y. Yan, J. P. Donahue, K. Wieghardt, *Inorg. Chem.,* **2011**, *50*, 7106.
31. a) L. R. Snyder, *J. Chromatogr. Sci.*, **1978**, *16*, 223; b) L. R. Snyder, *J. Chromatogr.*, **1974**, *92*, 223.

32. a) J. Park, Y. Morimoto, Y.-M. Lee, W. Nam, S. Fukuzumi, *J. Am. Chem. Soc*., **2011**, *133*, 5236; b) Y. Morimoto, H. Kotani, J.-Y. Park, Y.-M. Lee, W.-W. Nam, S. Fukuzumi, *J. Am. Chem. Soc*., **2011**, *133*, 403; c) T. Kawashima, K. Ohkubo, S. Fukuzumi, *Phys. Chem. Chem. Phys*., **2011**, *13*, 3344; d) S. Fukuzumi, K. Ohkubo, *Coord. Chem. Rev*., **2010***, 254*, 372; e) S. Fukuzumi, *Chem. Lett*., **2008**, *37*, 808.

33. a) H. Plenio, R. Diodone, *J. Am. Chem. Soc*., **1996**, *118*, 356; b) A. Merz, T. Futterer, J. Lex, H. Inerowicz, *Angew. Chem. Int. Ed*., **1997**, *36*, 278; c) T. Futterer, A. Merz, J. Lex, *Angew. Chem. Int. Ed*., **1997***, 36*, 611.

34. W. E. Geiger, F. Barriére, *Acc. Chem. Res*., ***2010***, *43*, 1030.

35. a) R. A. Michelin, M. Mozzon, R. Bertani, *Coord. Chem. Rev*., **1996***, 147*, 299; b) V. Y. Kukushkin, A. J. L. Pombeiro, *Chem. Rev*., **2002**, *102*, 1771.

Chapter 3

Interactions Between the Trianionic Ligand-centered Redox-active Metalloligand $[Cr^{III}(perfluorocatecholato)_3]^{3-}$ and Guest Metal Ions

Abstract

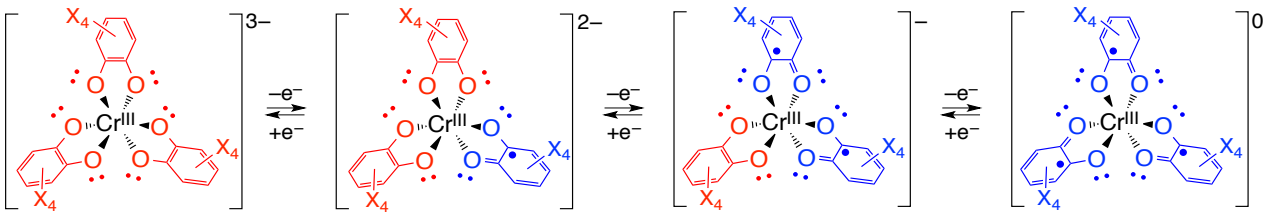
The redox-active metalloligand (RML) $(Et_3NH)_3[Cr^{III}(F_4Cat)_3]$ (F_4Cat = perfluorocatecholato) (**1**) was synthesized and its interactions with the guest metal ions Li^+, Mn^{2+}, Fe^{2+}, Co^{2+}, Cu^{2+}, and Zn^{2+} were examined. Cyclic voltammetry measurements and spectroelectrochemical studies revealed that complex **1** shows three-step ligand-centered one-electron oxidations to consecutively generate $[Cr^{III}(F_4Cat)_2(F_4SQ)]^{2-}$ (F_4SQ = perfluorosemiquinonato), $[Cr^{III}(F_4Cat)(F_4SQ)_2]^{-}$, and $[Cr^{III}(F_4SQ)_3]$ at –0.12, 0.23, and 0.53 V vs. Ag/Ag^+ in dichloromethane, or at –0.21, 0.08, and 0.50 V in acetonitrile (MeCN), respectively. Titration experiments in MeCN revealed that treatment of **1** with Cu^{2+} leads to the formation of $[Cr^{III}(F_4Cat)_2(F_4SQ)]^{2-}$ and Cu^+ *via* a redox reaction. However, when **1** was treated with Li^+, Mn^{2+}, Fe^{2+}, Co^{2+}, and Zn^{2+}, further titration experiments revealed that these metal ions coordinated *via* the lone pairs on the coordinating oxygen atoms of the F_4Cat^{2-} moieties in a one-to-one ratio, and the binding constants of 3.7 (±0.3) × 10^4 (Li^+), 1.5 (±0.2) × 10^5 (Mn^{2+}), 2.2 (±0.4) × 10^5 (Fe^{2+}), 1.9 (±0.2) × 10^5 (Co^{2+}), and 3.8 (±0.4) × 10^5 M^{-1} (Zn^{2+}) were established. Moreover, the oxidation potentials of **1** were positively shifted by 0.08-0.33 V upon addition of guest metal ions. Spectroelectrochemical studies of **1** in the presence of guest metal ions suggested that ligand-centered one- and two-electron oxidation of the RML occurred for Li^+, Mn^{2+}, Co^{2+}, and Zn^{2+}, respectively, while guest metal-centered one-electron oxidation was observed for Fe^{2+}. Considering all the aforementioned results, this study demonstrated for the first time the ability of $[Cr^{III}(F_4Cat)_3]^{3-}$ to act as a RML in solution.

3-1. Introduction

The development of molecules and/or supramolecular assemblies that exhibit multi-electron transfer is an attractive research target not only in basic chemistry but also in advanced chemistry, including catalytic substrate conversions *via* redox reactions.[1] So far, several types of multi-electron transfer molecules have been reported, *e.g.*, π-conjugated organic compounds,[2] polyoxometalates,[3] and metal complexes[4] containing redox-active metals. For example, ferrocene is one of the most useful transition metal complexes, demonstrating "metal-centered" one-electron transfer reactions.[5] Supramolecular assemblies such as hexaferrocenylbenzene or ferrocenyl dendrimers have also been reported to show multi-electron transfer reactions on the Fe(II) centers of each ferrocenyl moiety.[5] Ito and Yamaguchi *et al*. reported a dodeca-nuclear Ru complex consisting of four $[Ru_3O(CH_3CO_2)_6]$ units linked *via* bridging pyrazine ligands, which exhibits a 14-step-15-electron transfer reaction on the Ru centers.[6] These examples have demonstrated that the aggregation of multiple redox-active metal centers can be regarded as a powerful method for the creation of multi-electron transfer systems.

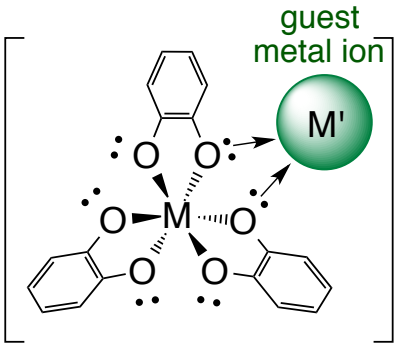
In addition to the aforementioned metal-*cent*ered electron transfer processes, the corresponding ligand-centered processes have also been studied, so far.[7] For instance, catechol ($CatH_2$),[8] 2-benzeneditiol ($BdtH_2$),[9] and 2-mercaptophenol (MpH_2)[10] have been reported to coordinate to transition metal ions, and to exhibit both metal- and ligand-centered redox reactions. Especially, the redox properties of tris- Cat/SQ (SQ = semiquinonato) complexes, have been well established.[11] For example, $[Re^{VI}(Cl_4Cat)_3]$ shows two-step metal-centered $Re^{VI}/Re^{V}/Re^{IV}$ redox couples,[12] while $[Cr^{III}(X_4SQ)_3]$ (X = Cl and Br) exhibits three-step ligand-centered Cat/SQ redox couples as shown in Scheme 1.[13]

Scheme 1. Scheme for the redox processes in $[Cr^{III}(X_4SQ)_3]$ (X = Cl and Br).[9b, 9c]



Here we noted that Cat complexes may be used as metalloligands (MLs)[14] that bind to guest metal ions *via* the lone pairs on the coordinating oxygen atoms of the ligands as shown in Chart 1. Previously reported $[K_3(H_2O)_{1.5}\{M^{III}(Cat)_3\}]_n$ (M = Cr and Fe),[15a] $[K_3\{V^{III}(Cat)_3\}]_n$,[15b] $[Li_2(C_4H_8O)_4\{Mn^{III}(Br_4Cat)_3\}]^-$,[15c] and $[K_2(MeCN)_6\{Mn^{IV}(3,5\text{-DTBCat})_3\}]$ (3,5-DTBCat = 3,5-di-*tert*-butylcatecholato)[15d] exhibited binding interactions between the oxygen atoms of the Cat^{2-} moieties and alkaline metal ions. Although the molecular structures of these complexes in the crystalline state have been published, details on their physicochemical properties in solution remain to be reported. One of our previous studies demonstrated that $[Mo^V(Bdt)_3]^-$, with metal-centered redox properties, is able to capture soft Cu^+ and Ag^+ ions by interaction with the lone pairs on the sulfur atoms, resulting in the formation of 1-D chains and 3-D network structures in the solid state.[16] Moreover, we reported that *fac*-$[Mo^V(Mp)_3]^-$, a redox-active metalloligand (RML) with possible coordination sites at the oxygen and sulfur atoms, exhibits a site-dependent binding of guest metal ions such as Na^+, Mn^{2+}, Fe^{2+}, Co^{2+}, and Ni^{2+} on the oxygen sites, while Cu^+ is coordinated at the sulfur sites.[17] It is noteworthy that the binding of the metal ions at the oxygen sites of the RML, leads to an enhancement of the electron-accepting properties of the RML, *i.e.* the reduction potential of the thus obtained complex is positively shifted by approximately 0.6 V relative to that of the guest metal-free RML in solution. These studies thus indicate that the redox properties of RML(s) may be modulated in solution by interactions with guest metal ions even in solution.

Chart 1. Representative structure for an assembly consisting of an RML and a guest metal ion.



Redox-active Metalloligand
(RML)

Even though binding properties of metal-centered RMLs with guest metal ions have been reported,[16,17] those of ligand-centered RMLs have not been reported so far; neither in solution, nor in the solid state. The combination of the ligand-centered redox function of the RML and the chemical properties of guest metal ions may allow the design of novel functional assemblies, in which ligands act as electron/hole reservoirs.

In this chapter, it was aimed to unveil the interactions between ligand-centered RMLs and guest metal ions. For that purpose, the RML $(Et_3NH)_3[Cr^{III}(F_4Cat)_3]$ (F_4Cat = perfluorocatecholato) (**1**) was designed as an alternative multi-electron transfer system. In order to increase its electron-accepting properties, perfluoro-groups were introduced in the Cat ligands, as they combine stronger electron-withdrawing properties with smaller atom size relative to perchloro and perbromo groups.[18] Herein, this chapter discussed the synthesis and redox properties of **1** as well as its interactions with the guest metal ions Li^+, Mn^{2+}, Fe^{2+}, Co^{2+}, Cu^{2+}, and Zn^{2+}, that differ in charge and redox properties.

3-2. Experimental Section

General Procedures. All synthetic operations were performed under an atmosphere of N_2 using Schlenk-line techniques. The compounds $CrCl_3 \cdot 6H_2O$, $LiClO_4$, $M(ClO_4)_2 \cdot 6H_2O$, (M = Mn, Fe, Co, Cu, and Zn), and benzene were purchased from Wako Pure Chemical Industries. Anhydrous solvents, methanol (MeOH), acetonitrile (MeCN), dichloromethane (CH_2Cl_2), and *n*-hexane, were purchased from Kanto Chemical Co. Inc. Triethylamine (Et_3N) was purchased from Tokyo Kasei Kogyo Co. Ltd. Perfluorocatechol (F_4CatH_2),[19] $[Cr^{III}(X_4SQ)_3]$ (X = Cl and Br),[13b] and $[Cu(MeCN)_4]PF_6$[20] were synthesized according to literature procedures. All solvents were degassed by at least five freeze-pump-thaw cycles immediately prior to use. **Caution!** Although we did not experience any difficulties with the perchlorate salts, these should be regarded as potentially explosive, and therefore be handled with the utmost care.

Synthesis of $(Et_3NH)_3[Cr^{III}(F_4Cat)_3]$ (1). A colorless 5 mL MeOH solution of Et_3N (333 mg, 3.30 mmol) was added to a green 15 mL MeOH solution of $CrCl_3 \cdot 6H_2O$ (147 mg, 0.55 mmol) and F_4CatH_2 (300 mg, 1.65 mmol). Upon mixing the two solutions, a green suspension was formed immediately. After continuous stirring for 12 h, the green precipitate dissolved to afford a green solution. After removing MeOH under reduced pressure, the product was extracted with 8 mL benzene, and a white by-product was filtered off, affording a green benzene solution. Addition of 16 mL *n*-hexane to this solution afforded a green powder. After filtration, the powder was washed three times with each 3mL *n*-hexane and dried *in vacuo*; complex **1** was isolated as green powder in 60% yield. Anal. Found: C, 48.14; H, 5.59; N, 4.56. Calcd. for $C_{36}H_{48}CrF_{12}N_3O_6$ (**1**): C, 48.11; H, 5.38; N, 4.68. ESI-MS (*m*/*z*): Calcd for $[\mathbf{1}+H]^+$: 899.28; found: 899.31.

Physical Measurements. Elemental analyses were carried out at the analysis center of Hokkaido University. Cyclic voltammetry measurements were recorded with a BAS model

650A electrochemical analyzer, using a glassy carbon (GC) working electrode and a platinum (Pt) auxiliary electrode under an atmosphere of argon (Ar). The reference electrode consisted of a silver wire, inserted into a small glass tube fitted with a porous Vycor frit at the tip, filled with a MeCN solution containing 0.1 M *n*-Bu_4NClO_4 and 0.01 M $AgNO_3$. All three electrodes were immersed in 2 mL of a CH_2Cl_2 or MeCN solution containing 0.1 M *n*-Bu_4NPF_6 as the supporting electrolyte and the analytes. In all cases, redox potentials were measured relative to the Ag/Ag^+ redox couple. UV-Vis-NIR spectra were recorded on a Hitachi U-4100 spectrophotometer over the range 200-3300 nm at 296 K under an atmosphere of N_2. Spectroelectrochemical measurements were carried out in 0.1 M *n*-Bu_4NPF_6 solution using Pt, Pt mesh, and the reference electrodes under an atmosphere of N_2. Electrospray ionization mass (ESI-MS) spectra were recorded on a JEOL JMS-T100LC AccuTOF spectrometer under an atmosphere of N_2.

3-3. Results and Discussion

3-3-1. Synthesis and Characterization of 1

Two tris-Cat Cr(III) complexes, $K_3[Cr^{III}(Cat)_3]$[15a,21a] and $K_3[Cr^{III}(3,5\text{-DTBCat})_3]$,[21b] have previously been reported by Raymond *et al*. These complexes were synthesized in aqueous solution by the treatment of Cr(III) chloride or acetate with three equivalents of $CatH_2$ or 3,5-$DTBCatH_2$ in the presence of an excess of KOH under an inert atmosphere, and the products were isolated as green solids. Complex **1** was obtained in a similar fashion from the treatment of $CrCl_3 \cdot 6H_2O$ with three equivalents of F_4CatH_2 in MeOH in the presence of six equivalents of Et_3N under an atmosphere of N_2. Similarly to the previously reported tris-Cat Cr(III) complexes,[15a,21] complex **1** was isolated as a green solid. A positive-mode ESI-MS spectrum of the product showed the main peak at *m/z* = 899.31 (Figures 1a and 2a), which is consistent with the exact mass of $\{(Et_3NH)_3[Cr(C_6F_4O_2)_3] + H^+\}^+$ (899.28). Moreover, the analysis of the elemental composition for **1** supports the assigned formula, $(Et_3NH)_3[Cr(C_6F_4O_2)_3]$.

For the trianion in **1**, $[Cr(C_6F_4O_2)_3]^{3-}$, several valence tautomers such as $[Cr^{III}(F_4Cat)_3]^{3-}$, $[Cr^{II}(F_4Cat)_2(F_4SQ)]^{3-}$, $[Cr^{I}(F_4Cat)(F_4SQ)_2]^{3-}$, or $[Cr^{0}(F_4SQ)_3]^{3-}$ (F_4SQ = perfluorosemiquinonato)

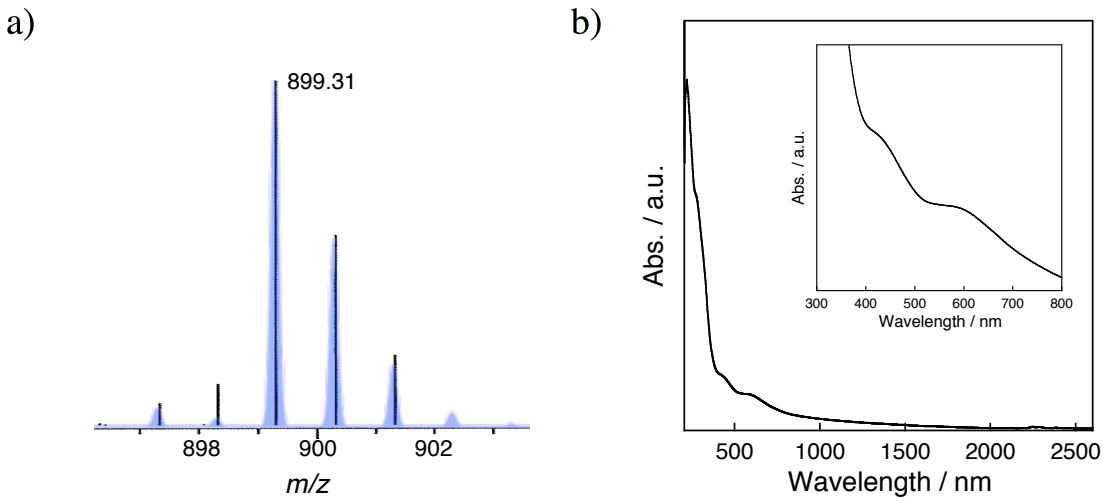


Figure 1. a) Positive-mode ESI-MS spectrum of **1** in MeCN (black lines) and the corresponding simulated spectrum (pale blue cones). b) Solid state (KBr pellet) UV-vis-NIR spectrum of **1**. The insert shows a magnification of the 300-800 nm region.

are conceivable, all of which differ with respect to their intramolecular charge distribution. The UV-vis-NIR spectrum of **1** in the solid state is shown in Figure 1b. Complex **1** shows a strong absorption peak at 220 nm with a shoulder at 280 nm, together with two weak absorption peaks at 420 and 590 nm. The two bands in the UV region can be assigned to π-π* transitions of the F_4Cat^{2-} moieties,[22] while the two bands in the visible region are comparable to those of

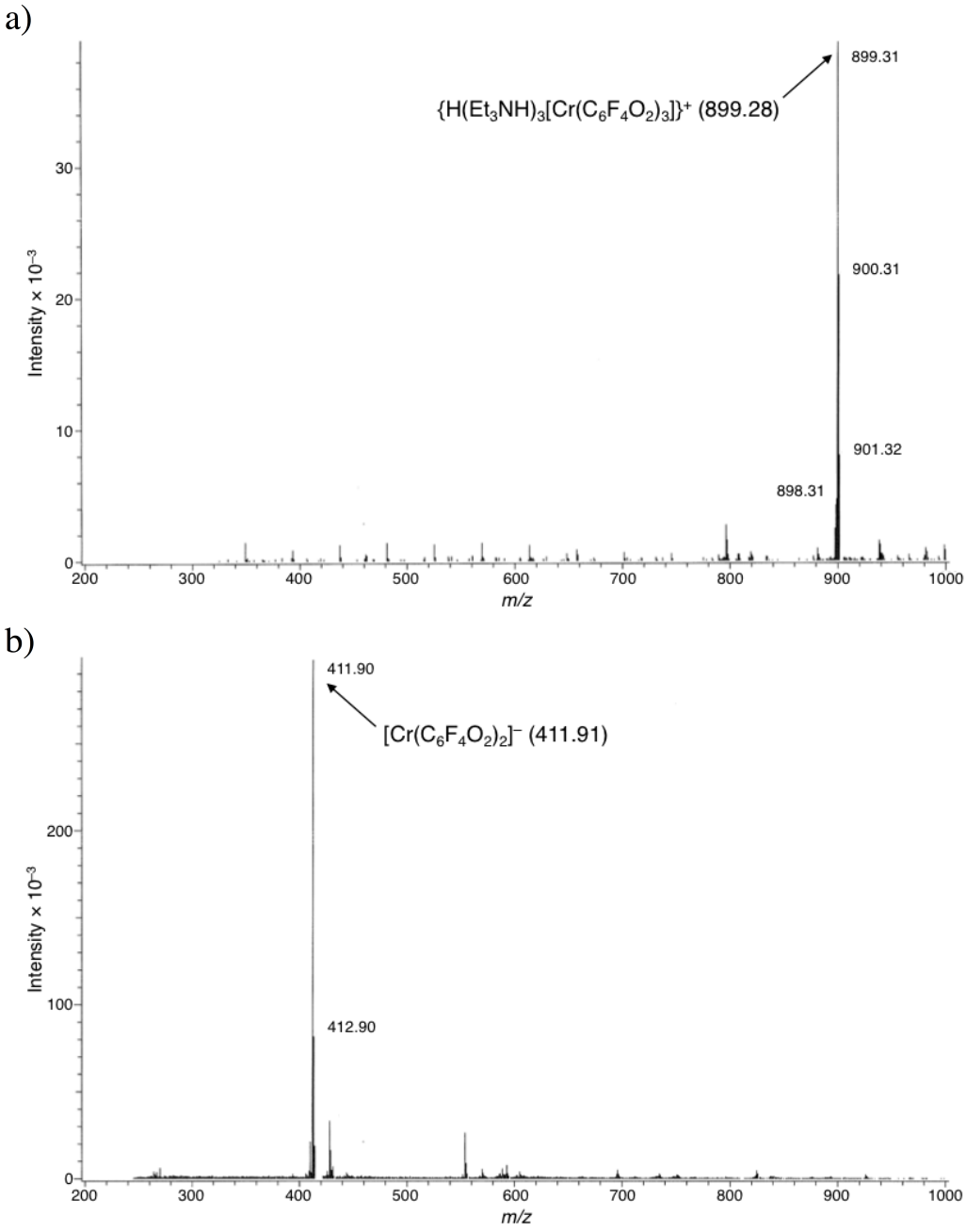


Figure 2. a) Positive- and b) negative-mode ESI-MS spectra of **1** in MeCN in the *m/z* = 200-1000 region.

$K_3[Cr^{III}(Cat)_3]$ in water (425 and 592 nm) and were accordingly assigned to d-d transitions on the Cr(III) centre.[21a] Furthermore, the absence of charge transfer (CT; Cr^{III}/SQ^{-}) bands in the visible region and intervalence CT (IVCT; $SQ^{-}\leftarrow Cat^{2-}$) bands in the NIR region supported the absence of F_4SQ^{-} or F_4Cat^{2-}/F_4SQ^{-} mixed valence ligands. Based on these experimental results, the charge distribution of the three $C_6F_4O_2$ ligands should be assigned as F_4Cat^{2-}, leading to the formulation of **1** as $(Et_3NH)_3[Cr^{III}(F_4Cat)_3]$.

3-3-2. Solution UV-vis-NIR Spectra of 1

The UV-vis-NIR spectra of **1** in CH_2Cl_2 and MeCN are shown in Figures 3a and 3b. In CH_2Cl_2, complex **1** exhibited three absorption peaks at 281 (13500 $M^{-1}cm^{-1}$), 441 (81), and 613 (73) nm. In MeCN, two absorption peaks at 285 (12500 $M^{-1}cm^{-1}$) and 600 (66) nm with one shoulder at 425 (88) nm were observed. The strong absorption bands at 281 and 285 nm in CH_2Cl_2 and MeCN, respectively, should be assigned to π-π* transitions on the aromatic ring of the F_4Cat^{2-},[22] while the weak absorption bands in the visible region should be ascribed to d-d transitions on the Cr(III) centre.[21a] In addition, the absence of absorption bands assignable to CT and IVCT bands suggests that complex **1** contains exhaustively reduced Cat ligands, in CH_2Cl_2 and MeCN solution, as well as in the solid state.

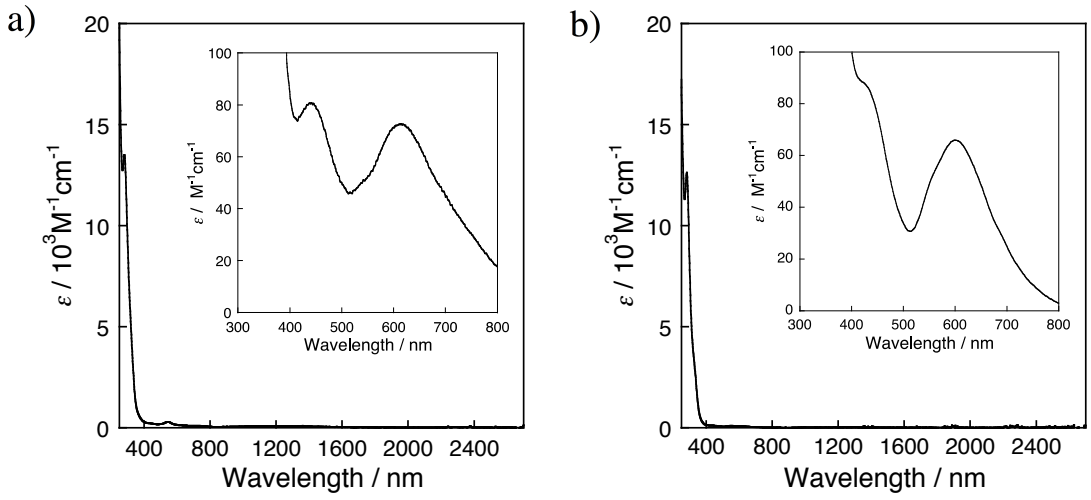


Figure 3. UV-vis-NIR spectra of **1** (5×10^{-4} M) in a) CH_2Cl_2 and b) MeCN under an atmosphere of N_2. The insets show a magnification of the 300-800 nm region.

3-3-3. Redox properties of 1

The cyclic voltammogram (CV) of **1** in CH_2Cl_2 is shown in Figure 4a, and the corresponding data is summarized in Table 1. During an anodic scan, complex **1** showed three one-electron transfer waves at $E_{1/2}$ = –0.12, 0.23, and 0.53 V vs. Ag/Ag^+. The first and second waves appear at more positive potentials than those of $[Cr^{III}(X_4SQ)_3]$ (for X = Cl: $E_{1/2}$ = –0.28, 0.15, and 0.53 V;[13c] for X = Br: $E_{1/2}$ = –0.15, 0.11, and 0.51 V[13b]) measured under similar conditions. The redox potentials of these three-step processes might be closely related to not only the electron-withdrawing properties of the perhalogeno-groups but also to the electronic interactions between the three ligands. Potential gaps, *i.e.*, $\Delta E^a = E_{1/2}{}^2 - E_{1/2}{}^1$ and $\Delta E^b = E_{1/2}{}^3 - E_{1/2}{}^2$, of 0.43 and 0.38 V for $[Cr^{III}(Cl_4SQ)_3]$, as well as 0.26 and 0.40 V for $[Cr^{III}(Br_4SQ)_3]$, respectively, were

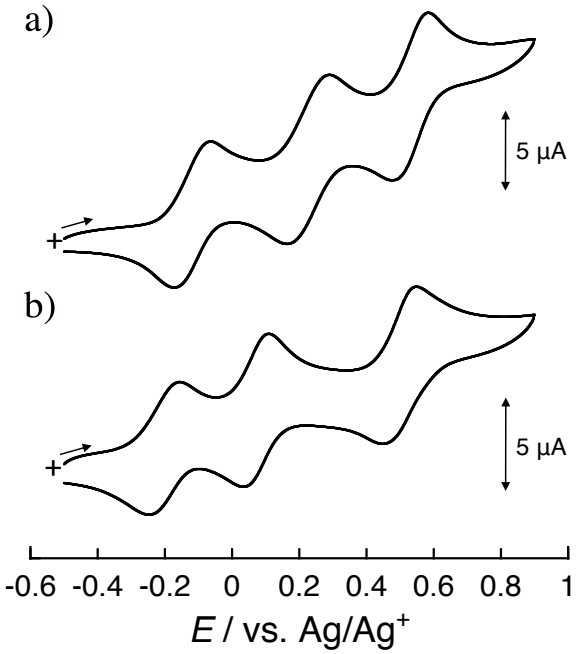


Figure 4. CVs of **1** (1 mM) in a) CH_2Cl_2 and b) MeCN: recorded at 20 mV s^{-1} under an atmosphere of Ar using *n*-Bu_4NPF_6 (0.1 M).

Table 1. Electrochemical data of **1** in CH_2Cl_2 and MeCN at 20 mV s^{-1}

	(V vs. Ag/Ag^+)								
Solvent	$E_{pa}{}^1$	$E_{pc}{}^1$	$E_{1/2}{}^1$ (ΔE^1)	$E_{pa}{}^2$	$E_{pc}{}^2$	$E_{1/2}{}^2$ (ΔE^2)	$E_{pa}{}^3$	$E_{pc}{}^3$	$E_{1/2}{}^3$ (ΔE^3)
CH_2Cl_2	–0.06	–0.17	–0.12 (0.11)	0.29	0.16	0.23 (0.13)	0.58	0.48	0.53 (0.10)
MeCN	–0.16	–0.25	–0.21 (0.09)	0.11	0.04	0.08 (0.07)	0.55	0.45	0.50 (0.10)

estimated. The corresponding ΔE^{a} and ΔE^{b} values for $[Cr^{III}(Cl_4SQ)_3]$, as well as the ΔE^{b} value for $[Cr^{III}(Br_4SQ)_3]$ are larger than those of **1** (ΔE^{a} = 0.35 and ΔE^{b} = 0.30 V). The observed strong electron-accepting ability should be attributed to the strong electron-withdrawing effect of the perfluoro-groups. CV experiments at different scan rates (10, 20, 50, 100, 200 and 400 mV s^{-1}) demonstrated that ΔE^{1}, ΔE^{2}, and ΔE^{3} ($\Delta E = \Delta E_{pa} - \Delta E_{pc}$) values decrease with decreasing scan rates as shown in Figures 5a and 6. Therefore, these three redox waves can be assigned to quasi-reversible processes.

In non-polar solvents such as CH_2Cl_2, complexes of the type $[Cr^{III}(X_4Cat)_x(X_4SQ)_{3-x}]^{x-}$ (X = Cl and Br; x = 0, 1, 2) are known to be stable, whereas $[Cr^{III}(Cl_4SQ)_3]$ exhibits the ligand substitution reaction in highly polar solvents such as MeCN, resulting in the formation of $[Cr^{III}(Cl_4Cat)(Cl_4SQ)(MeCN)_2]$.[23]

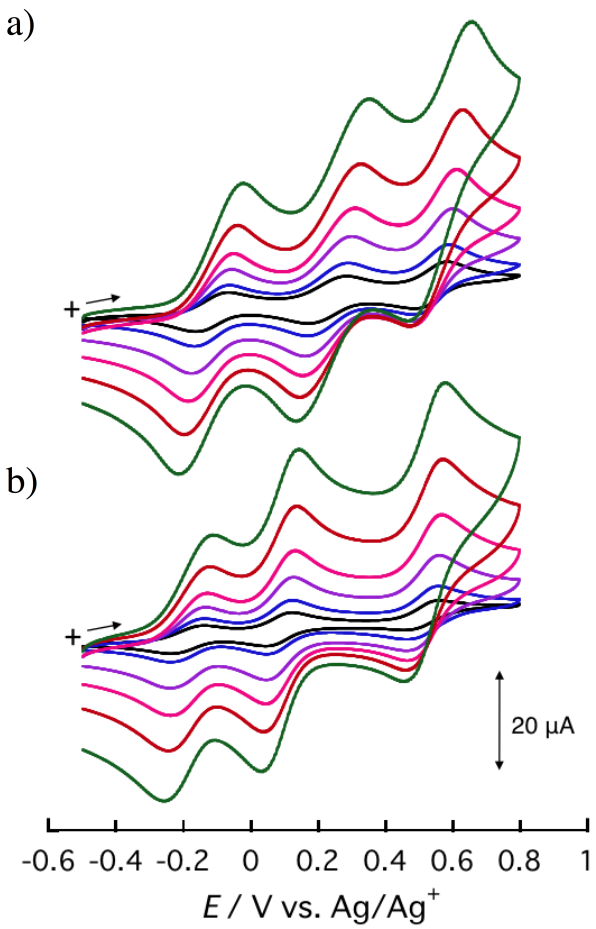


Figure 5. CVs of **1** (1 mM) in a) CH_2Cl_2 and b) MeCN at 10 (black line), 20 (blue line), 50 (purple line), 100 (pink line), 200 (brown line), and 400 mV s^{-1} (green line) under an atmosphere of Ar using *n*-Bu_4NPF_6 (0.1 M).

Despite the previously reported instability of $[Cr^{III}(Cl_4SQ)_3]$ in MeCN,[23] a MeCN solution of **1** exhibited three redox waves at $E_{1/2}$ = –0.21, 0.08, and 0.50 V, all of which are very similar to those in CH_2Cl_2 (Figure 4b). These waves appear at more negative potentials ($E_{1/2}$(MeCN) – $E_{1/2}(CH_2Cl_2)$ = –0.09, –0.20, and –0.03 V) relative to those in CH_2Cl_2. The observed potential shifts should accordingly relate to differences in solvent polarity between CH_2Cl_2 and MeCN.[24] If the ligands act as redox-centers in theses reactions (for the assignment of redox-sites, see the next section), the one- and two-electron oxidized species of **1**, *i.e.* $[Cr^{III}(F_4Cat)_2(F_4SQ)]^{2-}$ and $[Cr^{III}(F_4Cat)(F_4SQ)_2]^{-}$, should possess a dipole moment. This dipole moment should arise from

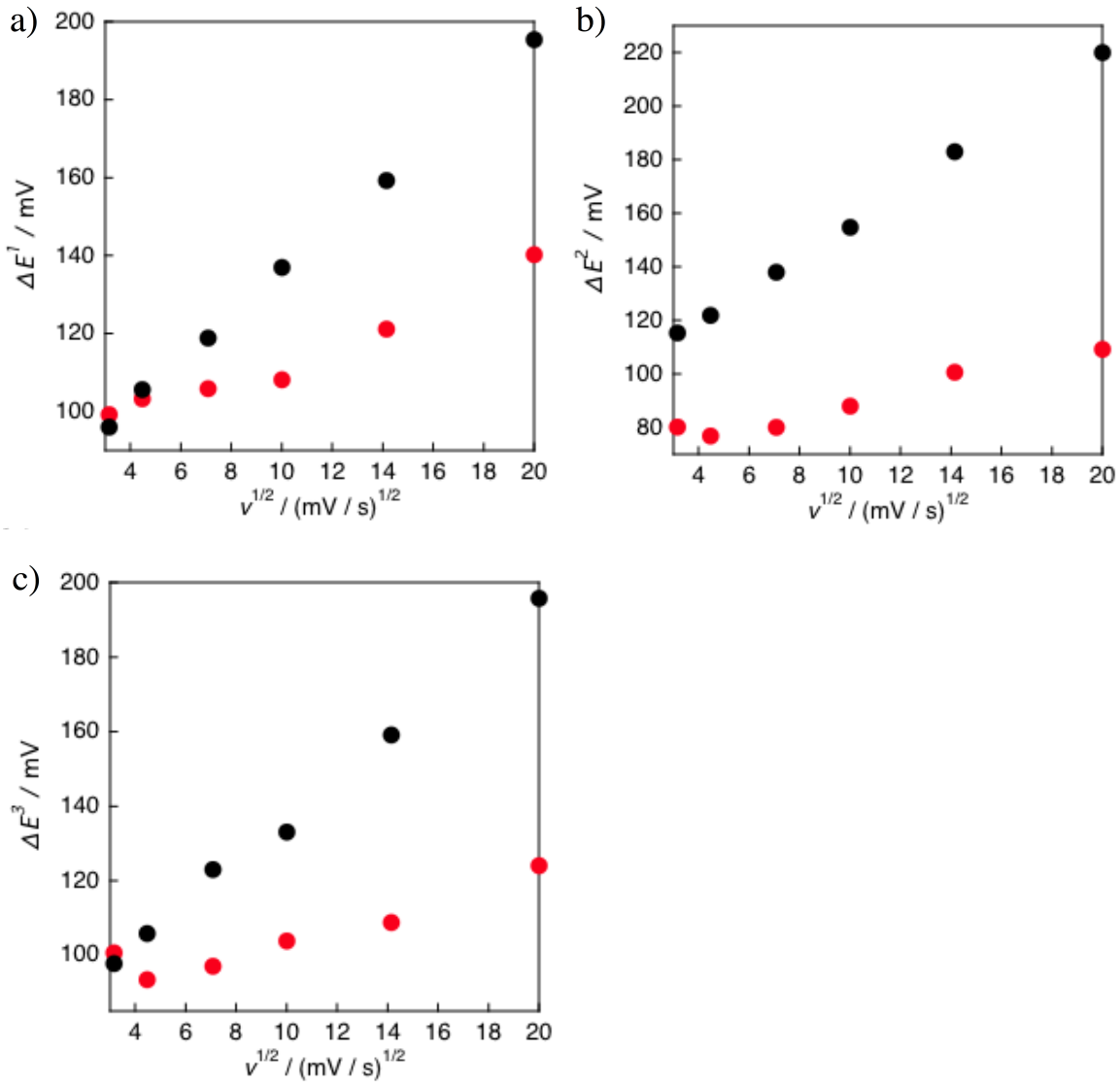


Figure 6. Plots of ΔE as a function of $v^{1/2}$; a) ΔE^1, b) ΔE^2, c) and ΔE^3 values of **1** (1 mM) in CH_2Cl_2 (black circles) and MeCN (red circles) at 10, 20, 50, 100, 200, and 400 mV s^{-1} under an atmosphere of Ar using *n*-Bu_4NPF_6 (0.1 M).

the asymmetric, mixed valence charge distribution in the ligands, which is dissimilar to **1** with homoleptic ligands. Following this notion, the high solvent polarity of MeCN may be able to influence to the solvation energy of the redox-isomers of **1**.[25] On the basis of variable scan rate experiments in MeCN, the three waves were assigned to quasi-reversible processes in the 20-400 mV s^{-1} range (Figures 5b and 6). Moreover, the voltammogram for **1** showed remarkable reproducibility upon repeating the cyclic scans at 20 mV s^{-1} (Figure 7). Therefore, complex **1** and its one-, two-, and three-electron oxidized species can be expected to kinetically maintain their structures in MeCN solution.

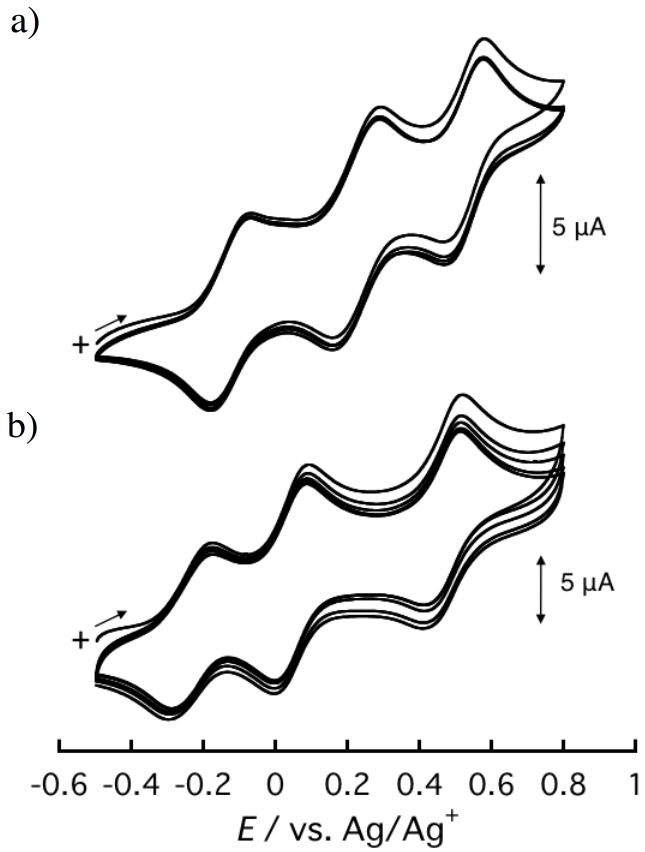


Figure 7. Repeat scan (5 cycles) CVs of **1** (1 mM) in a) CH_2Cl_2 and b) MeCN at 20 mV s^{-1} under an atmosphere of Ar using *n*-Bu_4NPF_6 (0.1 M).

3-3-4. Assignment of Redox Sites in 1

The assignments of redox sites in metal complexes, bearing both redox-active metals and ligands, should be undertaken carefully. For example, $[Cr^{III}(X_4SQ)_3]$ (X = Cl and Br), accepts electrons on the ligand sites to form $[Cr^{III}(X_4Cat)(X_4SQ)_2]^-$, $[Cr^{III}(X_4Cat)_2(X_4SQ)]^{2-}$, and $[Cr^{III}(X_4Cat)_3]^{3-}$.[13] In CH_2Cl_2, the one-electron reduced $[Cr^{III}(X_4Cat)(X_4SQ)_2]^-$ shows CT and IVCT bands at 546 (CT) and 2180 (IVCT) nm for X = Cl, and at 546 (CT) and 2200 nm (IVCT) for X = Br. The corresponding bands of the two-electron reduced $[Cr^{III}(X_4Cat)_2(X_4SQ)]^{2-}$ appear at 540 (CT) and 1680 nm (IVCT) with a shoulder at 1200 nm for X = Cl, and at 540 (CT) and 1660 nm (IVCT) with a shoulder at 1200 nm for X = Br.[13a]

The UV-vis-NIR spectra of **1** during bulk electrolysis in CH_2Cl_2 are shown in Figure 8. Strong absorption bands appeared in the visible and NIR regions (446, 536, 630sh., 750, 1140sh., and 1380 nm) during the first oxidation at –0.05 V vs. Ag/Ag^+ (blue line). The characteristic bands at 536, 1140sh., and 1380 nm thereby resemble those of $[Cr^{III}(X_4Cat)_2(X_4SQ)]^{2-}$ (X = Cl and Br).[13a] Accordingly, the electrochemically generated one-electron oxidized species of **1** should be assigned the empirical formula $[Cr^{III}(F_4Cat)_2(F_4SQ)]^{2-}$. The bands observed at 536

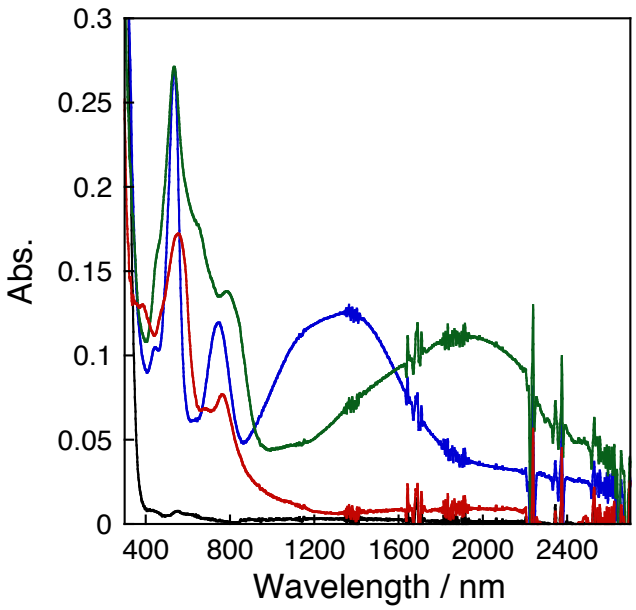
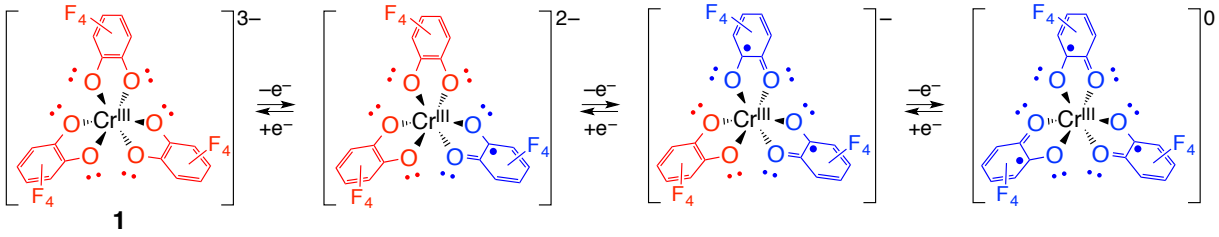


Figure 8. UV-vis-NIR spectra of **1** (5×10^{-4} M) in CH_2Cl_2 at rest potential (black line), –0.05 V (blue line), 0.35 V (green line), and 0.9 V vs. Ag/Ag^+ (red line) under an atmosphere of Ar using *n*-Bu_4NPF_6.

Scheme 2. Scheme for the redox processes of **1**.



1

and 1380 with 1140sh. nm were assigned to CT (Cr^{III}/F_4SQ^-) and IVCT ($F_4SQ^-\leftarrow F_4Cat^{2-}$) bands, respectively. The second oxidation at 0.35 V (green line) exhibited an unchanged CT band at 536 nm and a red-shifted IVCT band around 1950 nm. These characteristics are very similar to those of $[Cr^{III}(X_4Cat)(X_4SQ)_2]^-$ (X = Cl and Br),[13a] and accordingly, the electrochemically generated two-electron oxidized species of **1** should be assigned the empirical formula $[Cr^{III}(F_4Cat)(F_4SQ)_2]^-$. Upon further oxidation at 0.9 V (red line), the CT band remained at 554 nm, whereas a strong absorption band assignable to IVCT could not be observed, similar to the case of $[Cr^{III}(X_4SQ)_3]$.[13a] It should therefore be reasonable to assume that the valence states of the ligands in the three-electron oxidized species of **1** became equivalent to the F_4SQ^- state, leading to the formulation of $[Cr^{III}(F_4SQ)_3]$. Considering all these spectral results, the three oxidation steps of **1** can be assigned to three ligand-centered one-electron transfer steps, consecutively generating $[Cr^{III}(F_4Cat)_2(F_4SQ)]^{2-}$, $[Cr^{III}(F_4Cat)(F_4SQ)_2]^-$, and $[Cr^{III}(F_4SQ)_3]$ as shown in Scheme 2.

3-3-5. Redox Reaction between 1 and Cu^{2+} Ion

As previously discussed, complex **1** shows well-defined three-step redox behavior in MeCN. As MeCN is a good solvent not only for **1**, but also for several metal perchlorate salts, titration experiments were carried out in this solvent. The addition of one equivalent of $Cu(ClO_4)_2\cdot 6H_2O$ to a MeCN solution of **1**, resulted in the emergence of new bands at 443, 536, 629, 763, 1230sh., and 1540 nm as shown in Figure 9a. The resulting spectrum is thus identical to that of the electrochemically generated one-electron oxidized form of **1**, $[Cr^{III}(F_4Cat)_2(F_4SQ)]^{2-}$ (black line; Figure 9b). $[Cr^{III}(F_4Cat)_2(F_4SQ)]^{2-}$ was prepared from

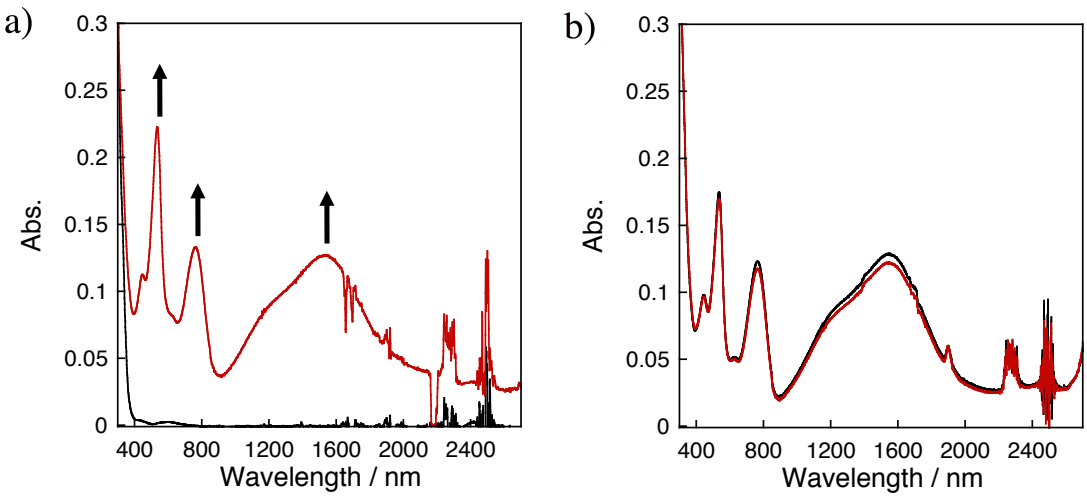
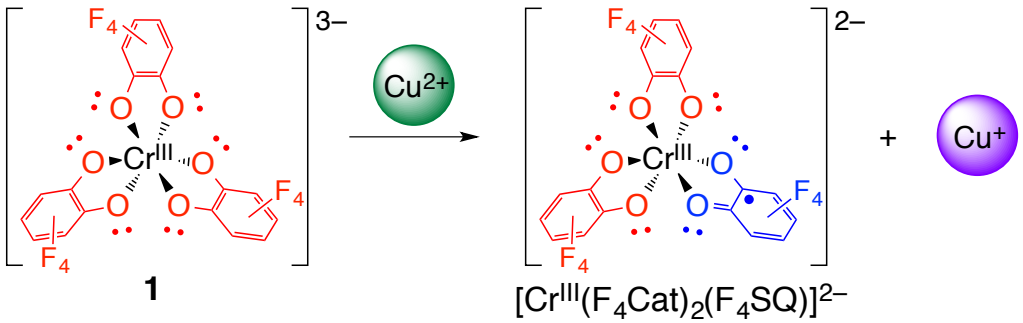


Figure 9. a) Changes of the UV-vis-NIR spectrum of **1** (5×10^{-5} M, black line) upon addition of one equivalent of $Cu(ClO_4)_2 \cdot 6H_2O$ (red line) in MeCN. b) UV-vis-NIR spectra of **1** (5×10^{-5} M) electrolyzed at –0.1 V vs. Ag/Ag^+ (black line) and upon addition of one equivalent of $[Cu(MeCN)_4]PF_6$ (red line) under an atmosphere of N_2 using *n*-Bu_4NPF_6 (1×10^{-2} M).

Scheme 3. Redox reaction scheme between **1** and Cu^{2+}.



MeCN solution of **1** electrolyzed at –0.10 V vs. Ag/Ag^+ for 21 min (Figure 10a). One-electron oxidation of **1** was chemically reversible (Figure 10b). Two-electron oxidized species of **1** was generated by electrolysis at 0.35 V for 21 min (Figure 10c), but it was irreversible (Figure 10d, *vide infra*). A spectrum which shows very similar absorption bands with one-electron oxidized species of **1** is also obtained from the addition of $[Cu^{I}(MeCN)_4]PF_6$ to an electrochemically generated solution of $[Cr^{III}(F_4Cat)_2(F_4SQ)]^{2-}$ in MeCN (red line; Figure 9b). It was thus confirmed that $Cu^{II}(ClO_4)_2 \cdot 6H_2O$ shows a Cu^+/Cu^{2+} redox couple at $E_{1/2} = 0.75$ V vs. Ag/Ag^+ in MeCN (Figure 11). The potential of the Cu^+/Cu^{2+} couple is higher than that of $[Cr^{III}(F_4Cat)_3]^{3-}$ /$[Cr^{III}(F_4Cat)_2(F_4SQ)]^{2-}$ ($E_{1/2}^1 = -0.21$ V). Accordingly, complex **1** should be oxidized by Cu^{2+}

to give $[Cr^{III}(F_4Cat)_2(F_4SQ)]^{2-}$ and Cu^+ (Scheme 3). The close resemblance of the spectra of this mixture with electrochemically generated $[Cr^{III}(F_4Cat)_2(F_4SQ)]^{2-}$, independent of the absence or presence of Cu^+, is thereby indicative of a negligible interaction between $[Cr^{III}(F_4Cat)_2(F_4SQ)]^{2-}$ and Cu^+. In general, Cu^+ is considered a soft metal ion,[26] and the interactions between Cu^+ and the hard lone pairs on the oxygen atoms of the F_4Cat^{2-} moieties in $[Cr^{III}(F_4Cat)_2(F_4SQ)]^{2-}$ should be minimal (*vide infra*).

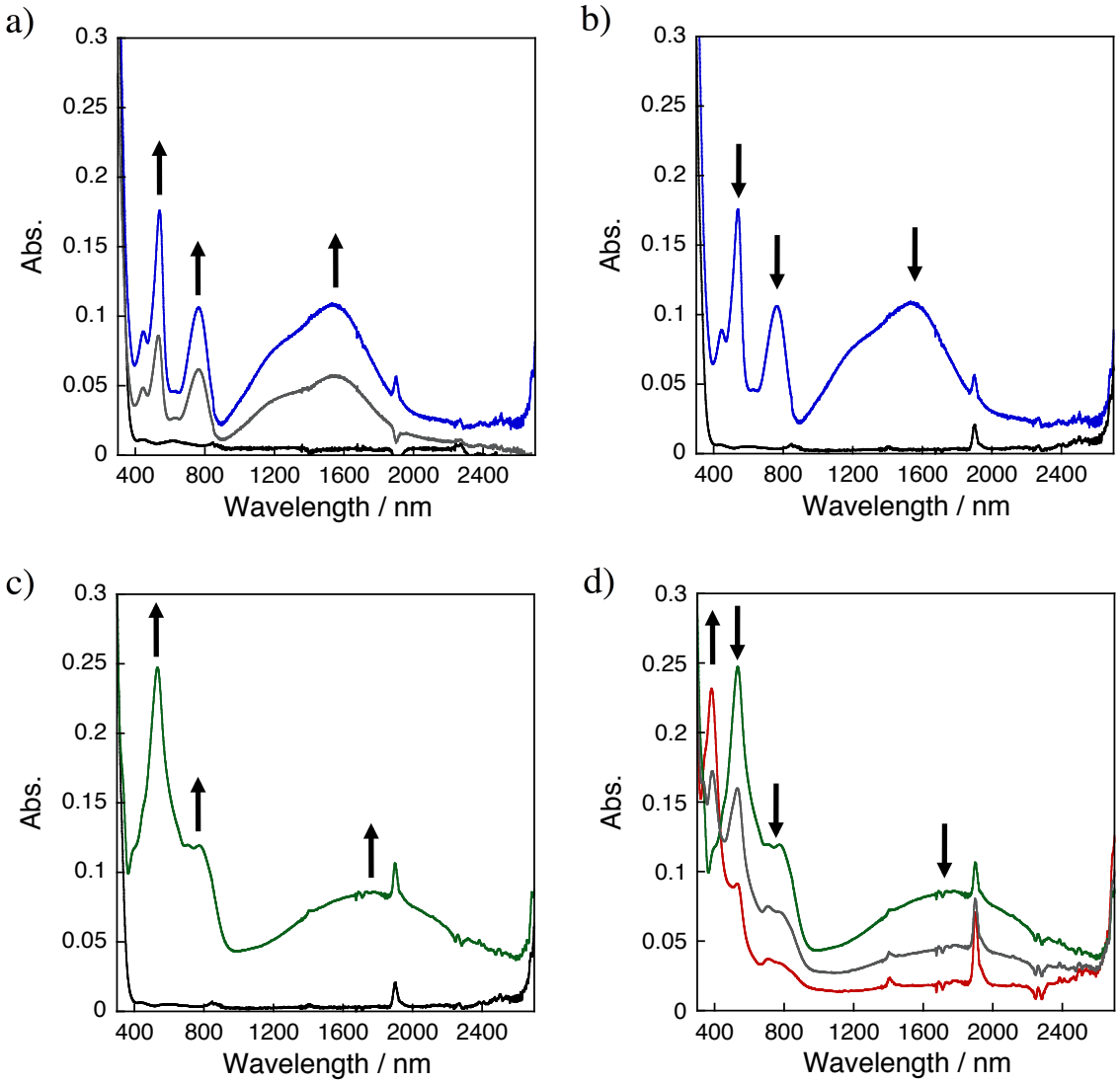


Figure 10. Changes of the UV-vis-NIR spectra of **1** (5×10^{-4} M) in MeCN at a) –0.10 V vs. Ag/Ag^+ for 0 (black line), 6 (grey line), and 21 min (blue line); b) –0.4 V for 0 (blue line) and 6 min (black line) after electrolysis at –0.1 V for 21 min; c) 0.35 V for 0 (black line) and 21 min (green line); and d) 0.35 V for 21 (green line), 66 (grey line), and 141 min (red line). All spectra recorded under an atmosphere of N_2 using *n*-Bu_4NPF_6 (0.1 M).

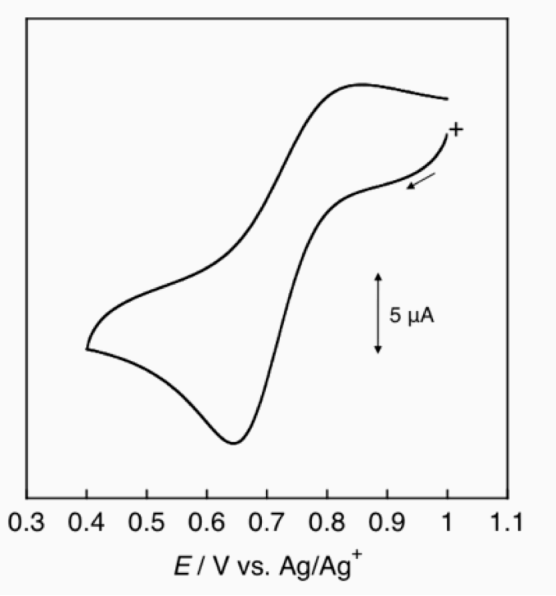


Figure 11. CV of $Cu(ClO_4)_2 \cdot 6H_2O$ (1 mM) in MeCN at 20 mV s^{-1} under an atmosphere of Ar using *n*-Bu_4NPF_6 (0.1 M).

3-3-6. Interaction of 1 with Guest Metal Ions

Figure 12 shows the UV-vis-NIR spectral changes of **1** upon addition of 0.5 and 1 equivalent of metal perchlorates, *i.e.*, $LiClO_4$ or $M(ClO_4)_2 \cdot 6H_2O$ (M = Mn, Fe, Co, and Zn) in MeCN. The addition of Li^+ to the MeCN solution of **1** led to a decrease of the absorbance at 285 nm, whereas no change was observed in the visible and NIR regions (Figure 12a). The spectral changes at 285 nm (π-π* transition) suggest an interaction between **1** and Li^+, indicating a modulation of the π-π* transition on the F_4Cat^{2-} moieties. Similar spectral changes were observed for $[Na(thf)_3\{fac\text{-}Mo^V(Mp)_3\}]$ and $[Mn^{II}(H_2O)(MeOH)\{fac\text{-}Mo^V(Mp)_3\}_2]$ in *o*-dichlorobenzene (Figure 13).[17] The absorbance of the π-π* band in the Mp^{2-} moieties decreases as a result of the binding interactions with Na^+ and Mn^{2+} *via* the lone pairs on the coordinating oxygen atoms. Therefore, it is reasonable to conclude that complex **1** should interact with Li^+ in a similar manner *via* the lone pairs on the coordinating oxygen atom(s) of the F_4Cat^{2-} moieties. As shown in Figure 14a, a Job's plot obtained from a continuous variation method, monitoring the absorbance at 285 nm, shows a peak top at a mole fraction $([Li^+]/[Li^+]+[\mathbf{1}]) = 0.5$,[27] indicating a one-to-one interaction between **1** and Li^+.

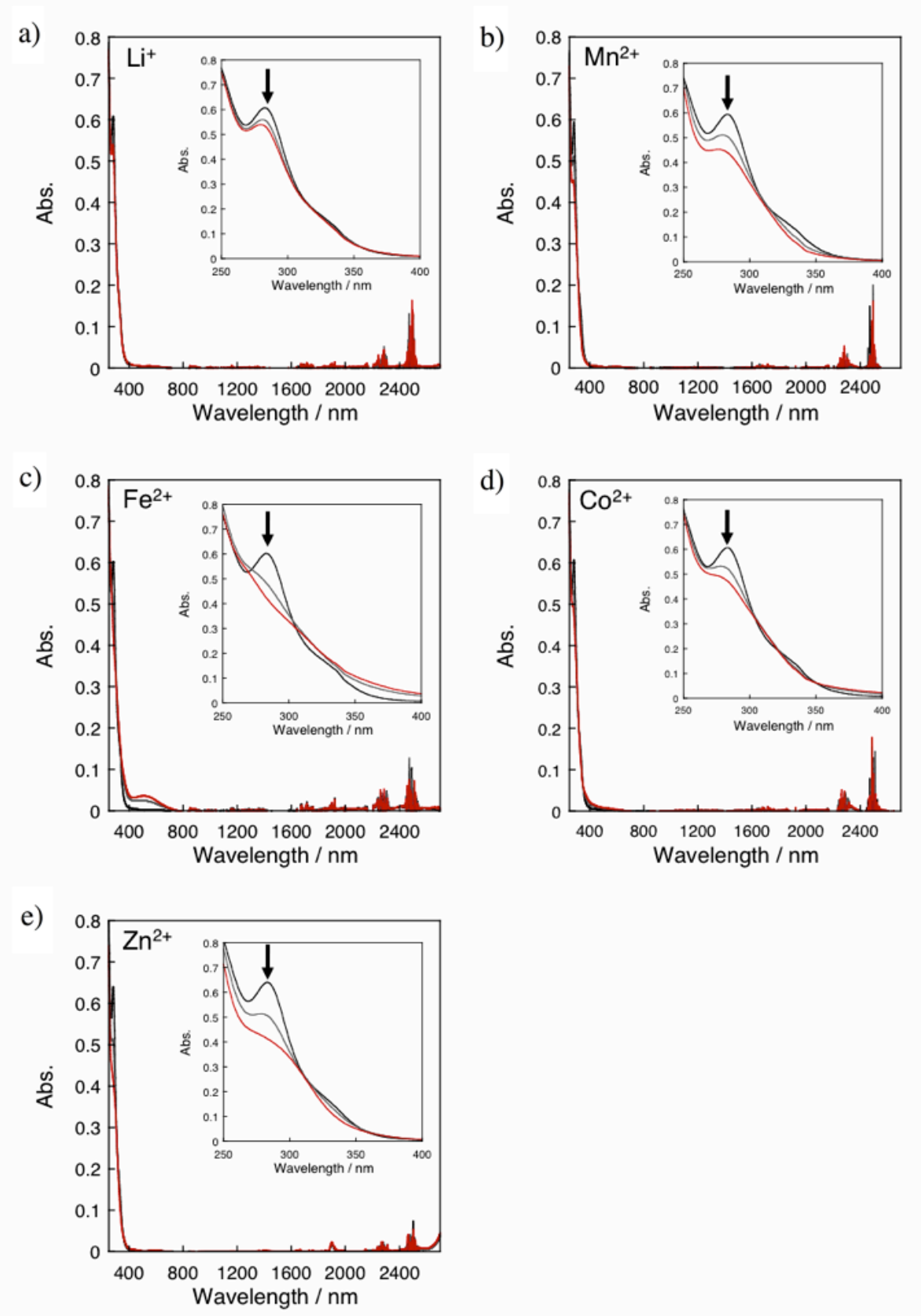


Figure 12. Changes of the UV-vis-NIR spectrum of **1** (5×10^{-5} M, black line) in MeCN upon addition of 0.5 (grey line) and one equivalent (red line) of a) $LiClO_4$, b) $Mn(ClO_4)_2 \cdot 6H_2O$, c) $Fe(ClO_4)_2 \cdot 6H_2O$, d) $Co(ClO_4)_2 \cdot 6H_2O$, or e) $Zn(ClO_4)_2 \cdot 6H_2O$. The insets show a magnification of the 250-400 nm region.

Similarly with this case, addition of Mn^{2+}, Fe^{2+}, Co^{2+}, or Zn^{2+} induced similar spectral changes as shown in Figures 12b-12e. In contrast to the case of Cu^{2+}, these spectral features indicate that complex **1** interacts with these guest metal ions without changing its original oxidation state and charge distribution. Each Job's plot exhibits a peak at a mole fraction of 0.5 (Figures 14b-14e). Accordingly, complex **1** should interact with Mn^{2+}, Fe^{2+}, Co^{2+}, and Zn^{2+} in a one-to-one ratio, similarly to the case of Li^{+}. The plots also indicate that further interaction with one or two more guest metal ions did not occur in MeCN. The Coulomb interactions between the one-to-one complexes and further guest metal ions might be weaker than that between **1** and guest metal ion, because the effective anionic charge of the RML is decreased by the interaction with the first guest metal ion.

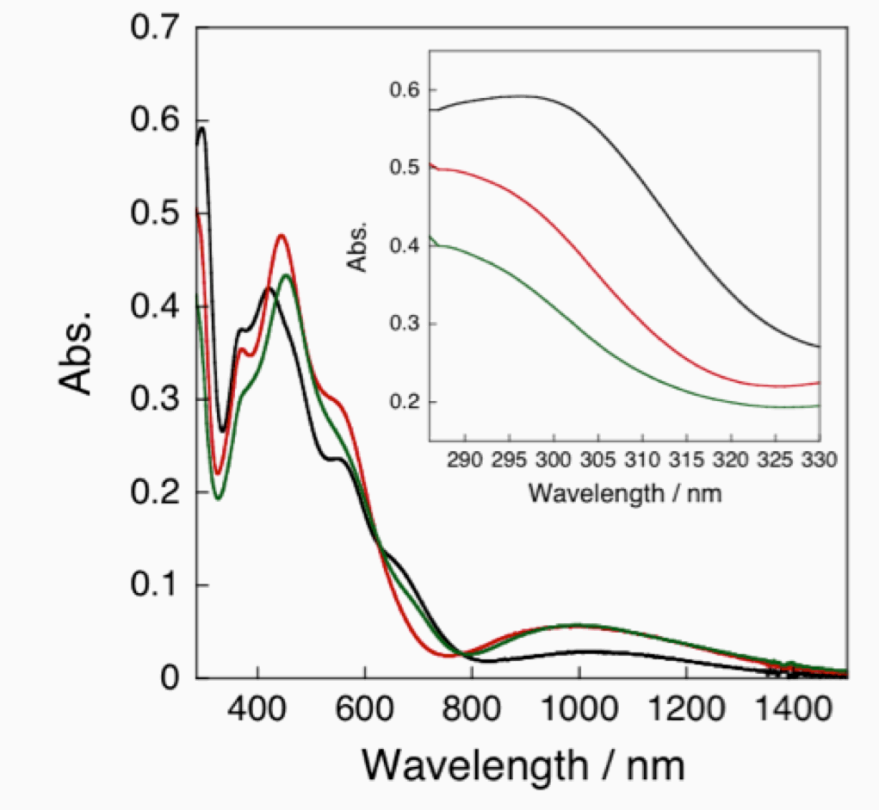


Figure 13. UV-vis-NIR spectra of (n-Bu_4N)[*fac*-$Mo^{V}(Mp)_3$] (3×10^{-5} M, black line), [$Na(thf)_3${*fac*-$Mo^{V}(Mp)_3$}] (3×10^{-5} M, red line), and [$Mn^{II}(H_2O)(MeOH)${*fac*-$Mo^{V}(Mp)_3$}$_2$] (1.5×10^{-5} M, green line) in *o*-dichlorobenzene under an atmosphere of Ar. The inset shows a magnification of the UV region (285-330 nm).[17]

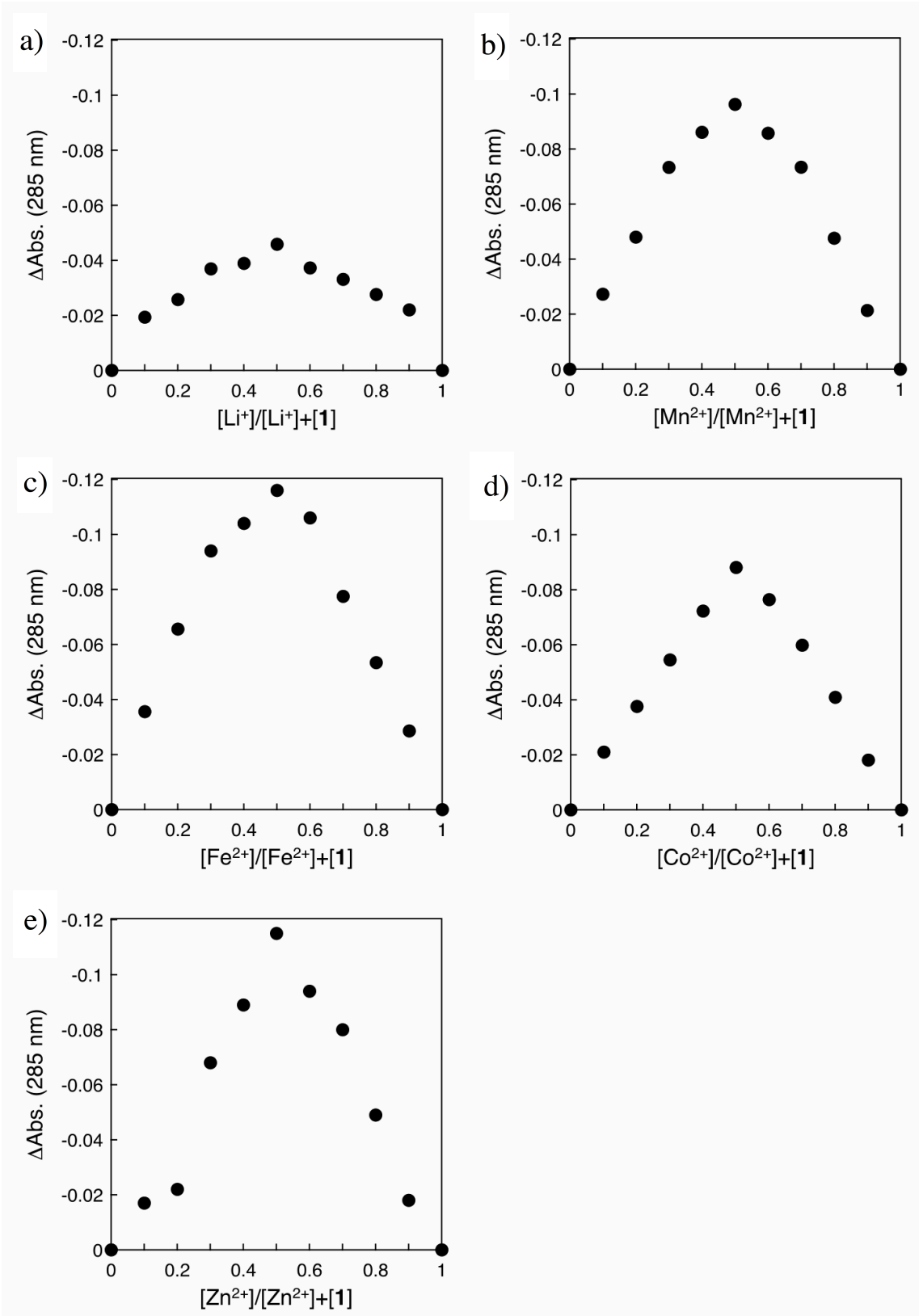


Figure 14. Job's plots for **1** upon addition of a) $Li(ClO_4)$, b) $Mn(ClO_4)_2 \cdot 6H_2O$, c) $Fe(ClO_4)_2 \cdot 6H_2O$, d) $Co(ClO_4)_2 \cdot 6H_2O$, or e) $Zn(ClO_4)_2 \cdot 6H_2O$, monitored by differential absorbances at 285 nm.

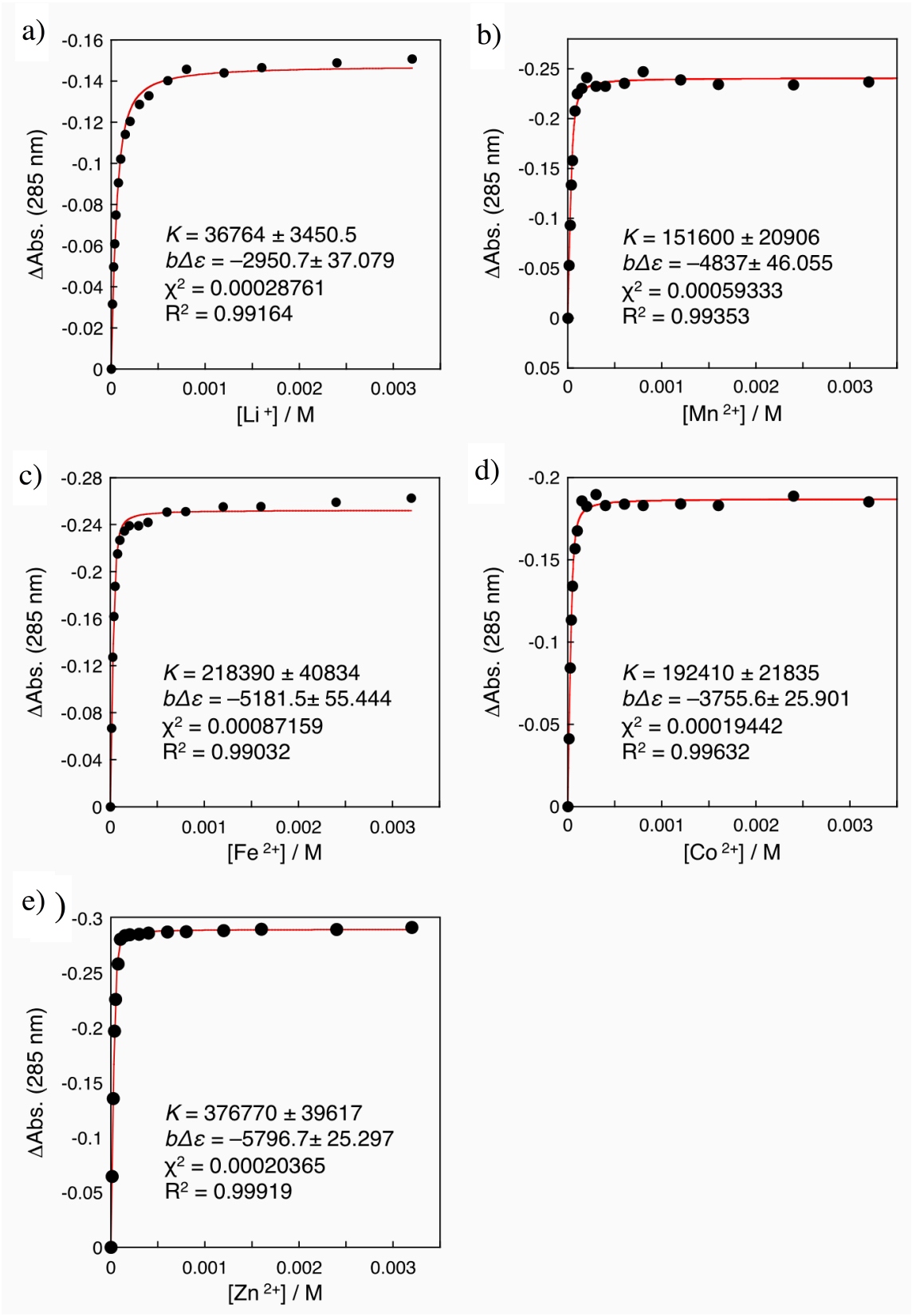


Figure 15. Differential absorbance profiles (285 nm) and fitting curves (red line) for mixtures of **1** (5×10^{-5} M) and 0, 1.25, 2.5, 3.75, 5, 7.5, 10, 15, 20, 30, 40, 60, 80, 120, 160, 240, and 320×10^{-5} M of a) $LiClO_4$, b) $Mn(ClO_4)_2 \cdot 6H_2O$, c) $Fe(ClO_4)_2 \cdot 6H_2O$, d) $Co(ClO_4)_2 \cdot 6H_2O$, and e) $Zn(ClO_4)_2 \cdot 6H_2O$; monitored in MeCN solution using a 1.0 cm cell at room temperature.

In order to quantitatively determine the affinity between **1** and the guest metal ions, further UV-vis titration experiments were carried out as shown in Figure 15. The binding constant (K) values can be estimated by applying eq. 1 in a region that contains no absorption bands of the guest molecule:[28]

$$\Delta A_{obs} = \frac{b\Delta\varepsilon}{2K}\left(X - \{X^2 - 4K^2[H]_0[G]_0\}^{1/2}\right) \qquad \text{eq. 1}$$

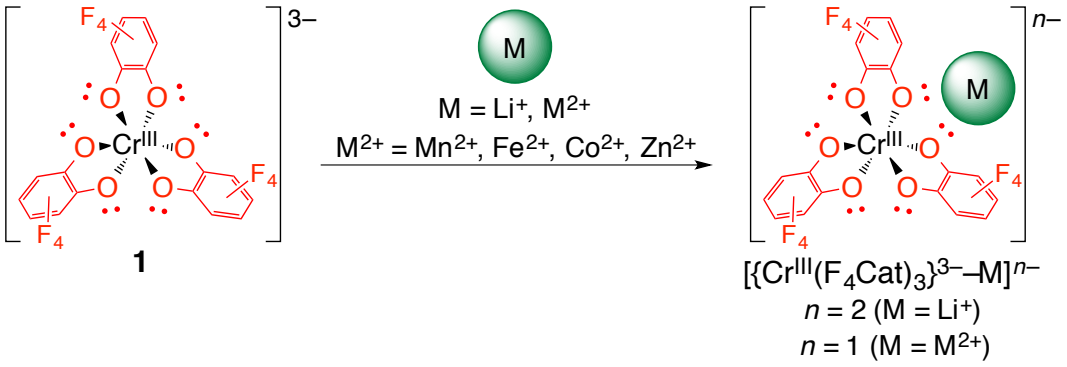
$$X = 1 + K[H]_0 + K[G]_0$$

where $[H]_0$, $[G]_0$, ΔA_{obs}, b, and $\Delta\varepsilon$ refer to the initial concentration of the host, the initial concentration of the guest, the observed differential absorbance of the mixture and $[H]_0$, the optical path length, and the differential molar extinction coefficient of the host-guest complex and the host, respectively.

The K value for Li^+ was estimated to be 3.7 (±0.3) × 10^4 M^{-1}, while those for Mn^{2+}, Fe^{2+}, Co^{2+}, and Zn^{2+} were estimated to be 1.5 (±0.2) × 10^5, 2.2 (±0.4) × 10^5, 1.9 (±0.2) × 10^5, and 3.8 (±0.4) × 10^5 M^{-1}, respectively. These results suggest that the interaction between divalent guest metal ions and **1** is by one order of magnitude higher than that of monovalent cations such as Li^+. Nabeshima *et al*. have reported that the neutral ML [Al^{III}(dipyrrin)$(H_2O)_2$] (dipyrrin = $C_{27}H_{17}N_2O_2$) binds to $ZnCl_2$ in toluene/MeOH (99/1) in a one-to-one ratio *via* the lone pairs of two oxygen atoms of the dipyrrin, and a K value was of 6.1 (±1.3) × 10^6 M^{-1} was reptrted.[29] This value suggests that not only electrostatic (Coulombic), but also covalent interactions between the ML and guest metal ion play an important role.

In order to obtain further information about the interactions between **1** and guest metal ions, ESI-MS measurements of MeCN solutions containing **1** and one equivalent of metal perchlorates were carried out. As shown in Figures 16-21, these solutions exhibited peaks at

Scheme 4. Binding interaction between **1** and guest metal ions.



m/z = 599.92 (Li^+), 646.83 (Mn^{2+}), 647.83 (Fe^{2+}), 650.83 (Co^{2+}), and 655.83 (Zn^{2+}). These values are consistent with the exact mass of $\{H^+Li^I[Cr^{III}(F_4Cat)_3]\}^-$ (599.91), $\{Mn^{II}[Cr^{III}(F_4Cat)_3]\}^-$ (646.83), $\{Fe^{II}[Cr^{III}(F_4Cat)_3]\}^-$ (647.83), $\{Co^{II}[Cr^{III}(F_4Cat)_3]\}^-$ (650.82), and $\{Zn^{II}[Cr^{III}(F_4Cat)_3]\}^-$ (655.82), whereby each isotopic composition was found to be in agreement with simulated patterns. Therefore, these results support the formation of one-to-one complexes between **1** and guest metal ions in MeCN (Scheme 4).

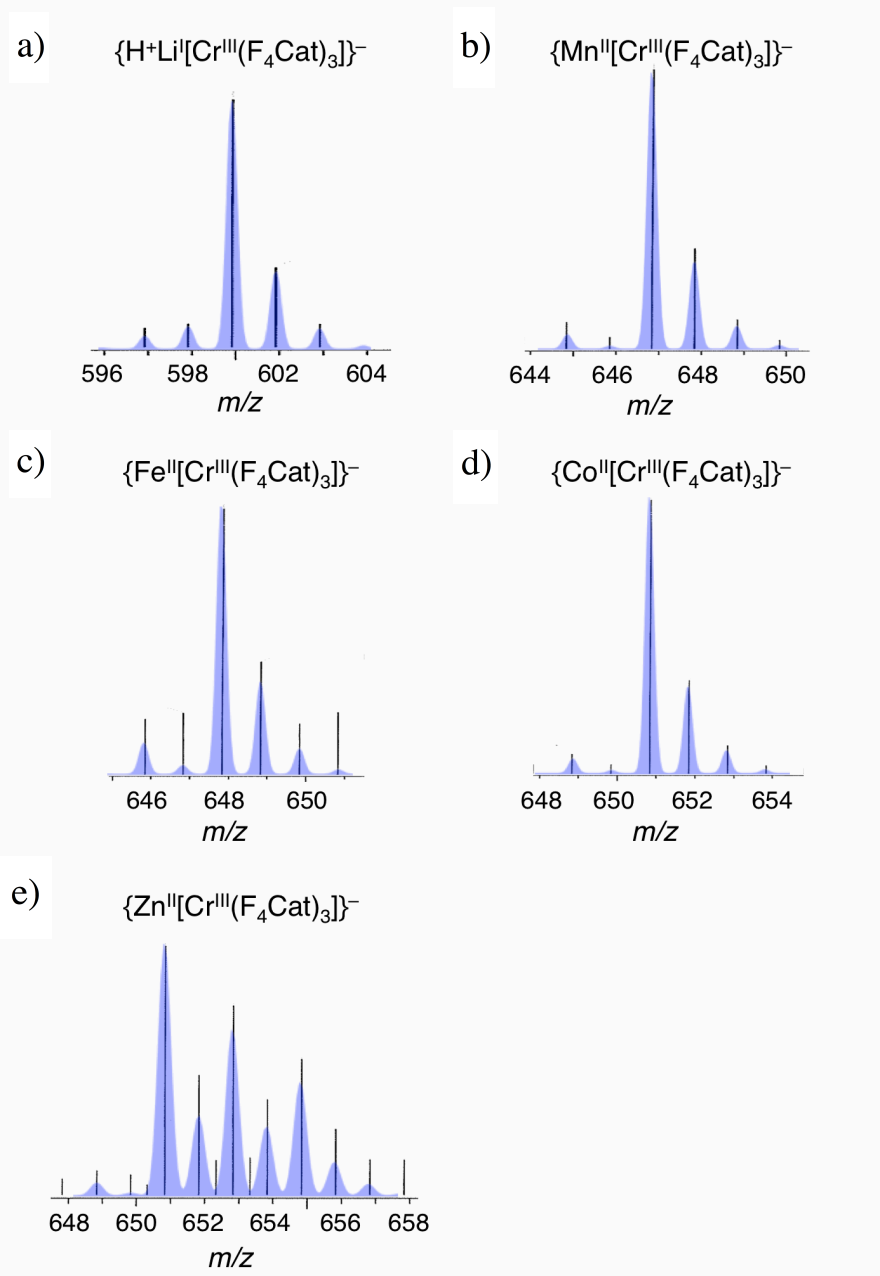


Figure 16. Negative-mode ESI-MS spectra in the *m/z* = 590-660 region of MeCN solutions containing **1** and one equivalent of a) $LiClO_4$, b) $Mn(ClO_4)_2{\cdot}6H_2O$, c) $Fe(ClO_4)_2{\cdot}6H_2O$, d) $Co(ClO_4)_2{\cdot}6H_2O$, and e) $Zn(ClO_4)_2{\cdot}6H_2O$. Pale-blue cones represent the corresponding simulated spectra.

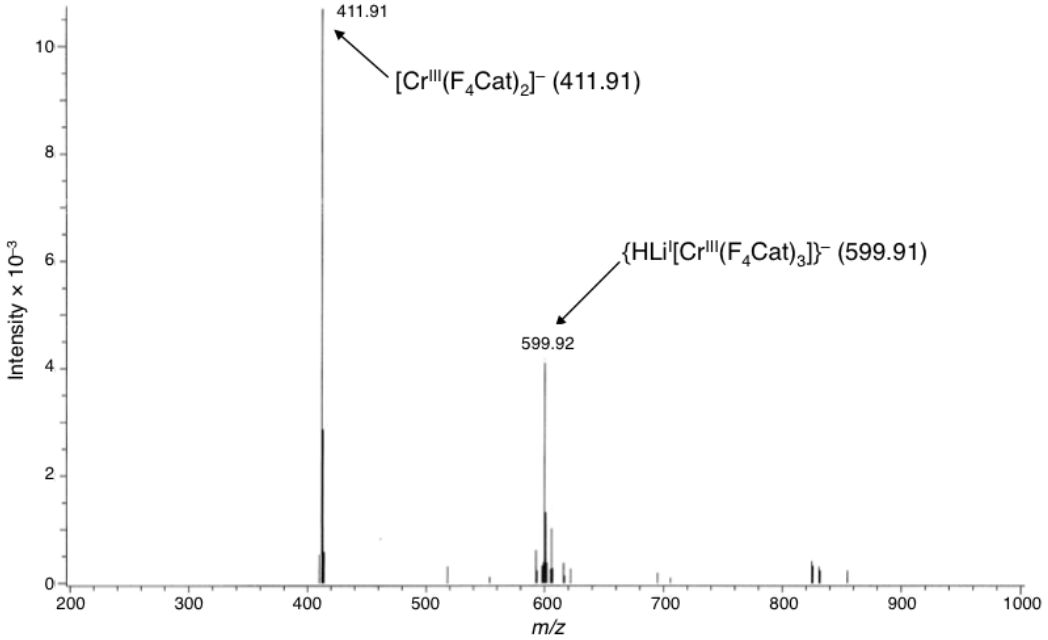


Figure 17. Negative-mode ESI-MS spectrum of **1** and 1 eq. of $LiClO_4$ in MeCN in the *m/z* = 200-1000 region.

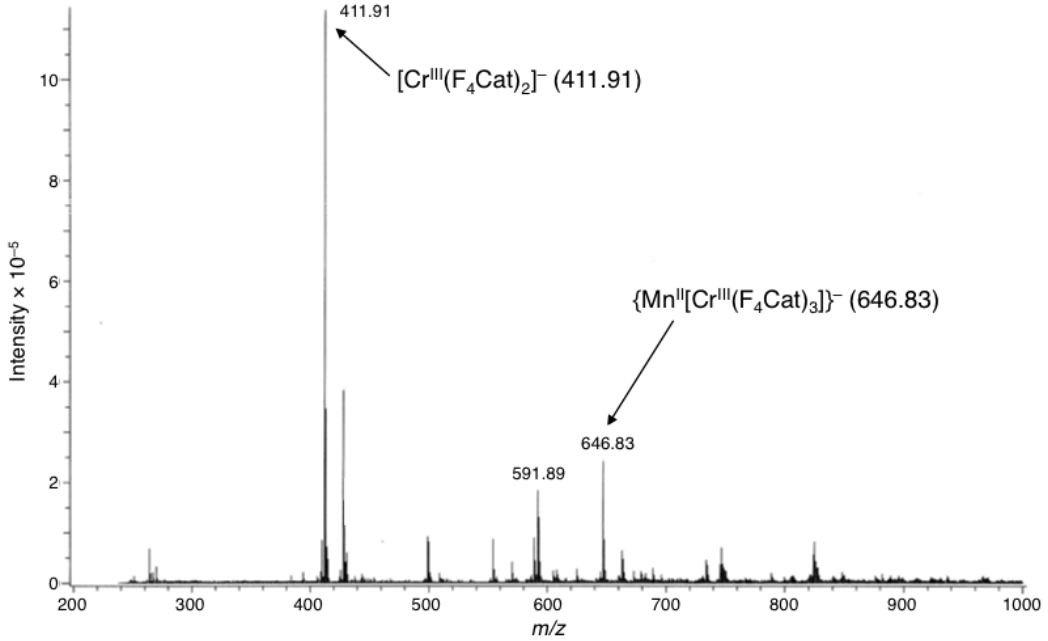


Figure 18. Negative-mode ESI-MS spectrum of **1** and 1 eq. of $Mn(ClO_4)_2 \cdot 6H_2O$ in MeCN in the *m/z* = 200-1000 region.

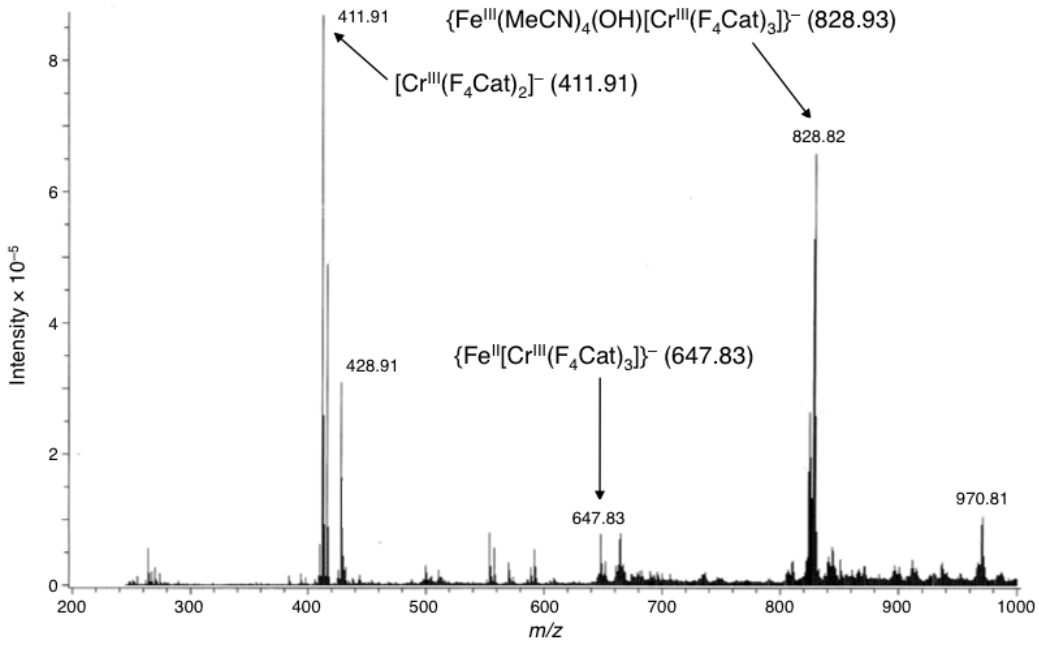


Figure 19. Negative-mode ESI-MS spectrum of **1** and 1 eq. of $Fe(ClO_4)_2 \cdot 6H_2O$ in MeCN in the m/z = 200-1000 region.

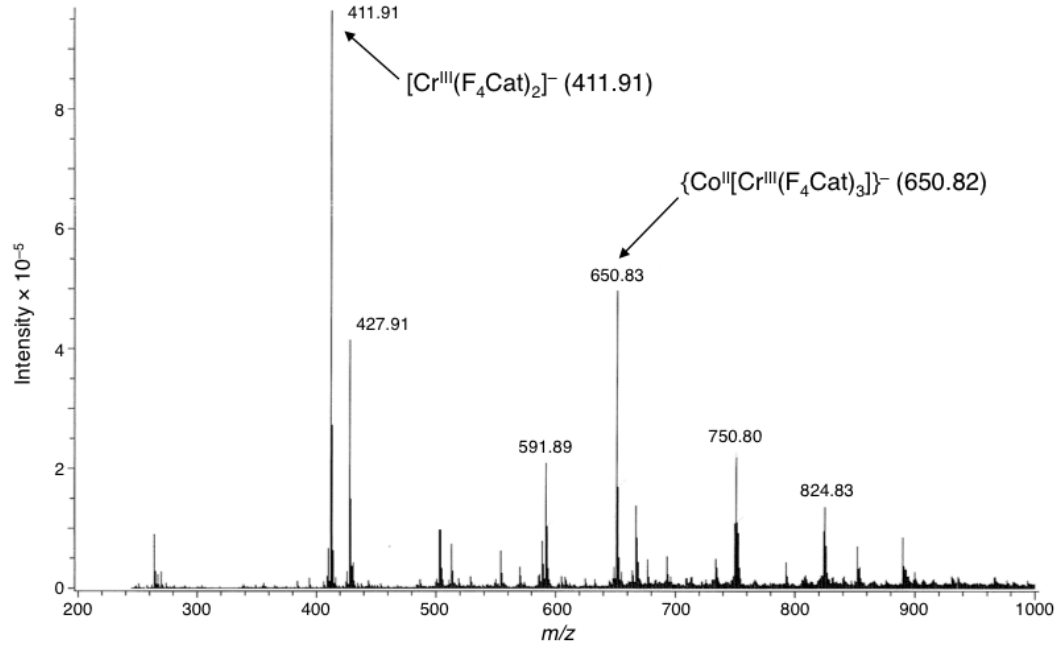


Figure 20. Negative-mode ESI-MS spectrum of **1** and 1 eq. of $Co(ClO_4)_2 \cdot 6H_2O$ in MeCN in the m/z = 200-1000 region.

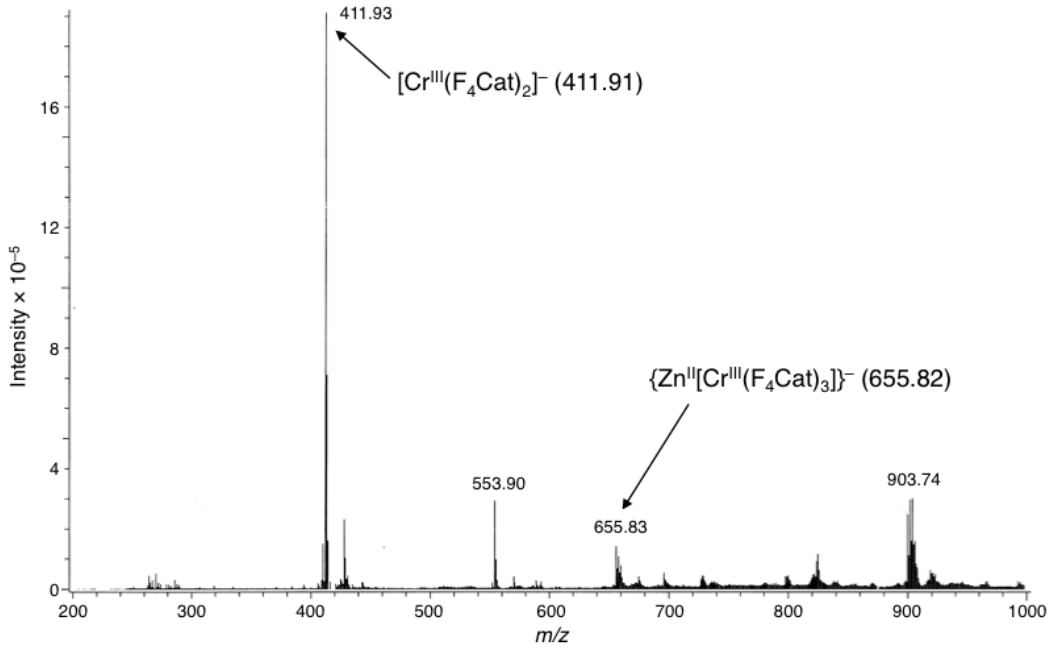


Figure 21. Negative-mode ESI-MS spectrum of **1** and 1 eq. of $Zn(ClO_4)_2 \cdot 6H_2O$ in MeCN in the m/z = 200-1000 region.

3-3-7. Redox Properties of 1 with Guest Metal Ions

Figure 22 shows the CVs of **1** upon addition of one equivalent of guest metal ions in MeCN, and the electrochemical data is summarized in Table 2. As shown in the figure, addition of the guest metal ions led to variations in all of the voltammograms. Addition of Li^+ resulted in a

Table 2. Electrochemical data of **1** and of **1** in the presence of $M(ClO_4)_n$ (n = 1 and 2) in MeCN at 20 mV s^{-1}

	(V vs. Ag/Ag^+)									
	E_{pa}^1	E_{pc}^1	$E_{1/2}^1$ (ΔE^1)	E_{pa}^2	E_{pc}^2	$E_{1/2}^2$ (ΔE^2)	E_{pa}^3	E_{pc}^3	$E_{1/2}^3$ (ΔE^3)	E_{pa}^4
1	–0.16	–0.25	–0.21	0.11	0.04	0.08	0.55	0.45	0.50	
1+Li^+	–0.08	–0.18	–0.13 (0.10)	0.12	0.05	0.09 (0.07)	0.56	0.46	0.51 (0.10)	
1+Mn^{2+}	0.10[a]	0.04	0.07 (0.06)	0.21	0.15[a]	0.18 (0.06)	0.55	0.45	0.50 (0.10)	
1+Fe^{2+}	0.10[a]	0.14		0.30[a]	0.51[a]		0.40[a]			0.59
1+Co^{2+}	0.17[b]	0.09[b]	0.13 (0.08)	0.57	0.46	0.52 (0.11)				
1+Zn^{2+}	0.17[a]	0.14		0.37[a]	0.37[a]		0.46[a]	0.48[a]		0.55

[a]Shoulder peak. [b]Two-electron transfer process.

slight positive shift of the first oxidation peak by 0.08 V relative to that of parent **1**, while maintaining three well-defined redox couples (Figure 22b). The observed positive shift indicates an interaction between Li^+ and **1**,[17] which should decrease the electron density on the $[Cr^{III}(F_4Cat)_3]^{3-}$ moiety. On the other hand, the second and third oxidation peaks appeared at potentials similar to those of **1**. Based on these results, it is suggested that Li^+ binds to **1**, while it exerted negligible impact on the electronic environment of the oxidized species. Among the four divalent metal ions used, Mn^{2+} and Co^{2+} led to a disappearance of the first oxidation peak observed at –0.16 V for **1** (Figures 22c and 22e). Instead, the oxidation peaks appeared at significantly positive-shifted potentials at *ca*. 0.1 V. Finally, addition of Fe^{2+} or Zn^{2+} afforded

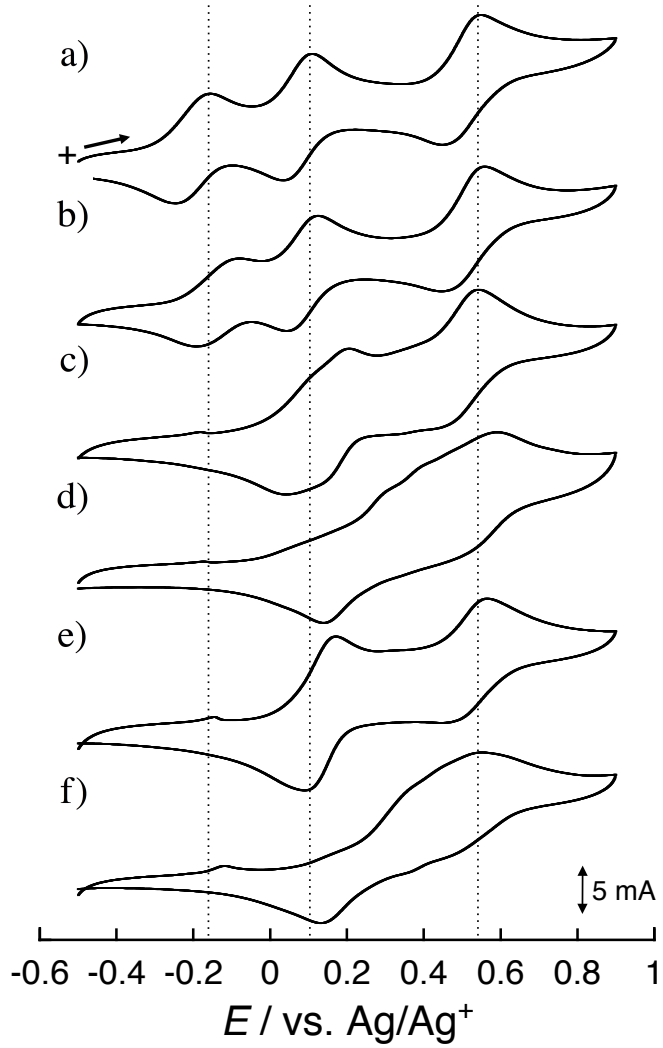


Figure 22. a) CVs of **1** (1 mM) in MeCN upon addition of one equivalent of b) $LiClO_4$, c) $Mn(ClO_4)_2{\cdot}6H_2O$, d) $Fe(ClO_4)_2{\cdot}6H_2O$, e) $Co(ClO_4)_2{\cdot}6H_2O$, or f) $Zn(ClO_4)_2{\cdot}6H_2O$ at 20 mV s^{-1} under an atmosphere of Ar using *n*-Bu_4NPF_6 (0.1 M).

the voltammograms with weak anodic currents at *ca*. 0.1 V, and subsequent oxidation peaks (Figures 22d and 22f). The electrochemical data thus support interactions between **1** and the divalent metal ions not only at rest potentials, which is revealed by the titration experiments, but also at more positive potentials. In order to reveal the electrochemically generated species in the presence of guest metal ions, spectroelectrochemical measurements were carried out.

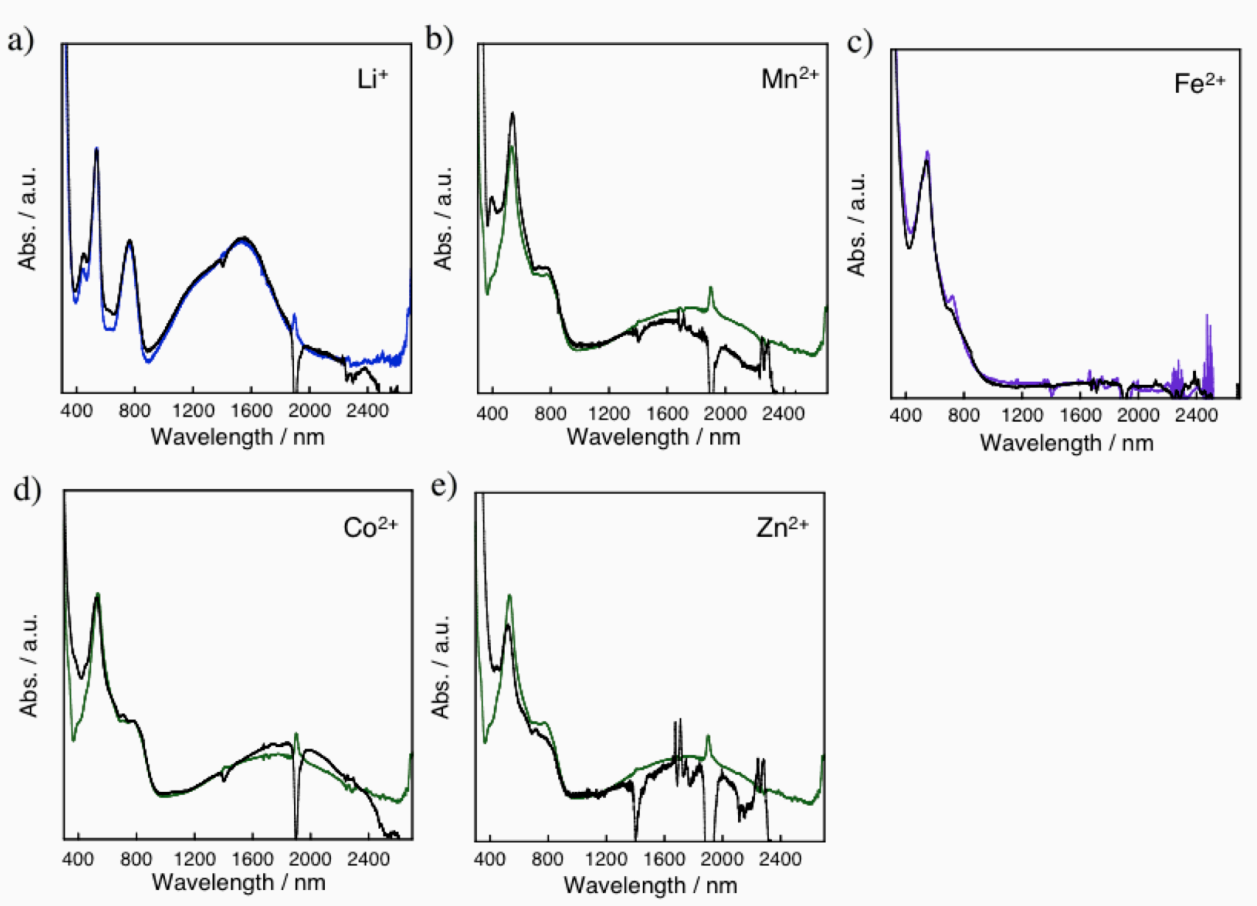


Figure 23. The UV-vis-NIR spectra of **1** (5×10^{-4} M) with 1 eq. of a) $LiClO_4$ electrolyzed at –0.08 V vs. Ag/Ag^+ for 36 min (black line) and electrochemically generated $[Cr^{III}(F_4Cat)_2(F_4SQ)]^{2-}$ prepared from **1** (5×10^{-4} M) electrolyzed at –0.1 V for 21 min (blue line), b) $Mn(ClO_4)_2 \cdot 6H_2O$ electrolyzed at 0.12 V for 6 min (black line) and electrochemically generated $[Cr^{III}(F_4Cat)(F_4SQ)_2]^-$ prepared from **1** (5×10^{-4} M) electrolyzed at 0.35 V for 21 min (green line), c) $Fe(ClO_4)_2 \cdot 6H_2O$ electrolyzed at 0.15 V for 21 min (black line), and **1** upon addition of 1 eq. of $Fe(ClO_4)_3 \cdot 6H_2O$ (purple line), d) $Co(ClO_4)_2 \cdot 6H_2O$ electrolyzed at 0.26 V for 26 min (black line), and electrochemically generated $[Cr^{III}(F_4Cat)(F_4SQ)_2]^-$ (green line), and e) $Zn(ClO_4)_2 \cdot 6H_2O$ electrolyzed at 0.20 V for 21 min (black line) and electrochemically generated $[Cr^{III}(F_4Cat)(F_4SQ)_2]^-$ (green line), in MeCN using *n*-Bu_4NPF_6 (0.1 M) under an atmosphere of N_2.

First, Figure 23a shows a spectrum of a MeCN solution containing **1** and one equivalent of Li^+ electrolyzed at –0.08 V vs. Ag/Ag^+ for 36 min (black line) together with that of **1** electrolyzed at –0.10 V (blue line). The electrolysis of **1** with Li^+ gave absorption peaks at 445, 535, 626, 764, 1230sh., and 1540 nm, which are identical with those of the electrochemically generated $[Cr^{III}(F_4Cat)_2(F_4SQ)]^{2-}$. A similar spectrum can be also obtained by adding one equivalent of Li^+ to a solution of the electrochemically generated $[Cr^{III}(F_4Cat)_2(F_4SQ)]^{2-}$ (Figure 24a).

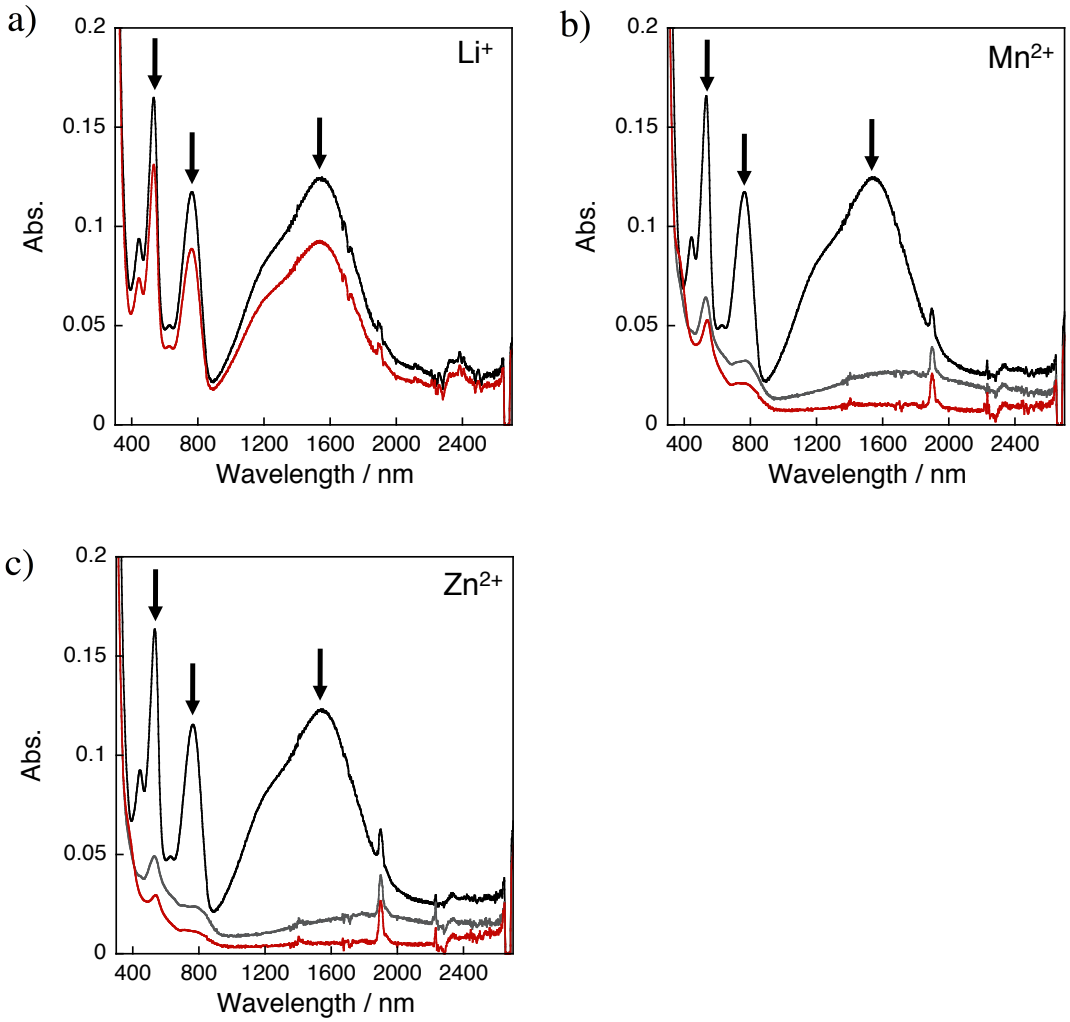


Figure 24. Changes of the UV-vis-NIR spectra of $[Cr^{III}(F_4Cat)_2(F_4SQ)]^{2-}$ generated by the electrolysis of **1** (5×10^{-4} M) at –0.1 V vs. Ag/Ag^+ in MeCN using *n*-Bu_4NPF_6 (0.1 M) upon addition of one equivalent of a) $LiClO_4$ standing for 0 (black line) and 6 min (red line); b) $Mn(ClO_4)_2 \cdot 6H_2O$ standing for 0 (black line), 6 (grey line), and 26 min (red line); and c) $Zn(ClO_4)_2 \cdot 6H_2O$ standing for 0 (black line), 6 (grey line), and 26 min (red line). All spectra recorded under an atmosphere of N_2.

Accordingly, the one-electron oxidation should proceed on the ligand moiety of $[\{Cr^{III}(F_4Cat)_3\}^{3-}–Li^+]^{2-}$ similar to the case of **1**. Although information on the interaction between $[Cr^{III}(F_4Cat)_2(F_4SQ)]^{2-}$ and Li^+ is not available at this stage, the one-electron oxidation process is confirmed to be sufficiently reversible (eq. 2, Figures 25a and 25b).

$$[\{Cr^{III}(F_4Cat)_3\}^{3-}–Li^+]^{2-} \underset{+e^-}{\overset{-e^-}{\rightleftharpoons}} [Cr^{III}(F_4Cat)_2(F_4SQ)]^{2-}\cdots Li^+ \qquad \text{eq. 2}$$

Further oxidation at 0.35 V for 6 min gave a transient spectrum showing characteristic features of the two-electron oxidized species $[Cr^{III}(F_4Cat)(F_4SQ)_2]^-$ (Figure 25c). After these

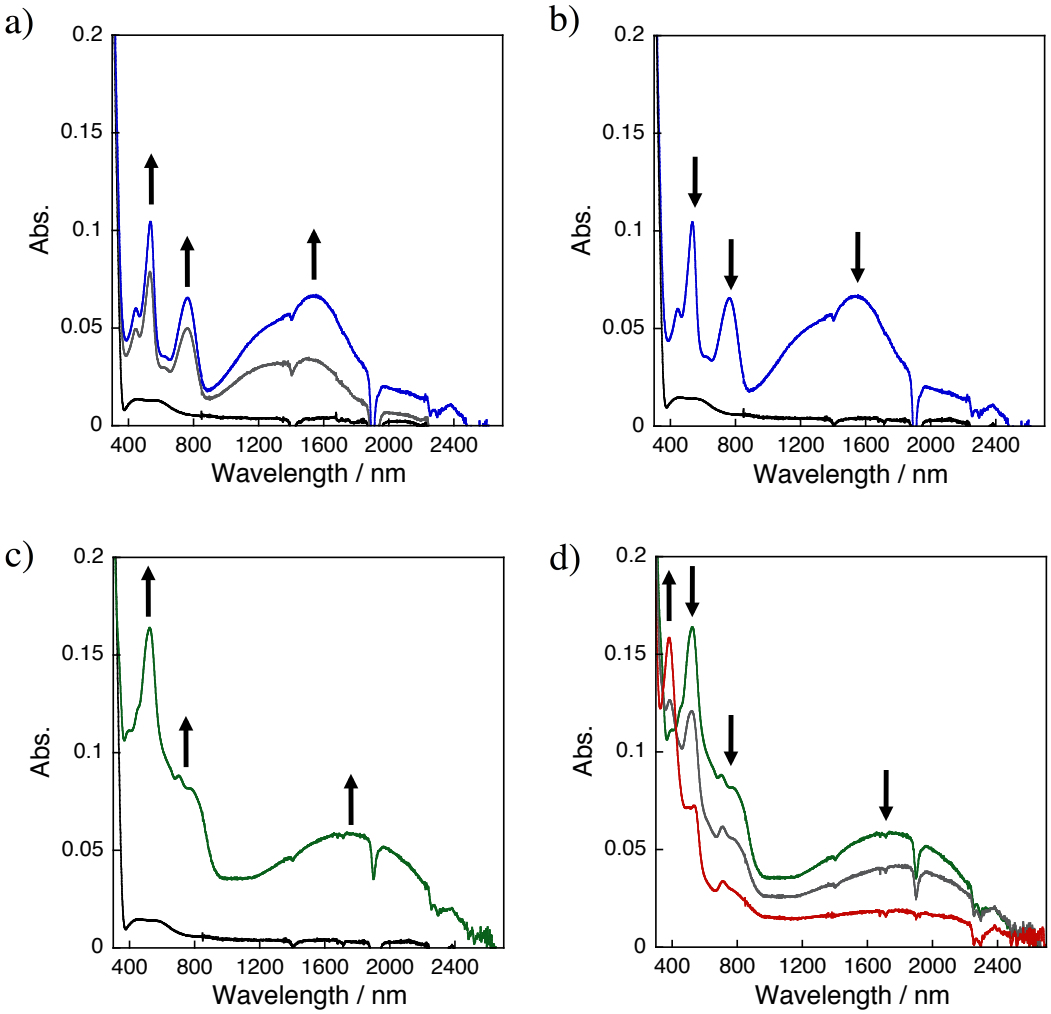
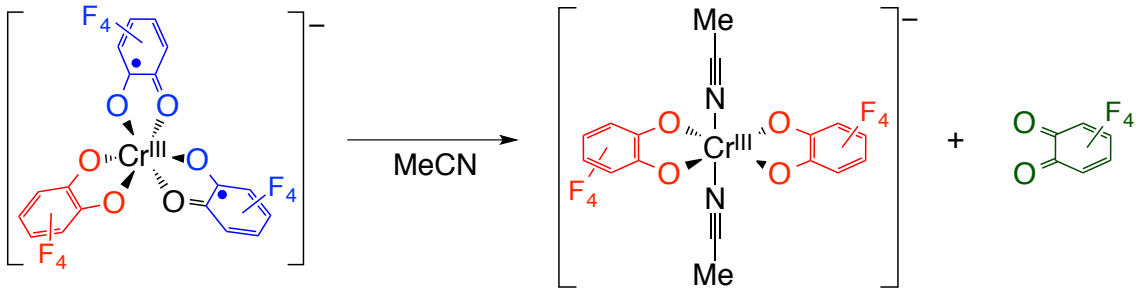


Figure 25. Changes of the UV-vis-NIR spectra of **1** (5×10^{-4} M) with one equivalent of $LiClO_4$ in MeCN at a) –0.08 V vs. Ag/Ag^+ for 0 (black line), 6 (grey line), and 36 min (blue line); b) –0.4 V for 0 (blue line) and 21 min (black line) after electrolysis at –0.08 V for 36 min; c) at 0.35 V for 0 (black line) and 6 min (green line); and d) 0.35 V for 6 (green line), 21 (grey line), 51 min (red line). All spectra recorded under an atmosphere of N_2 using *n*-Bu_4NPF_6 (0.1 M).

Scheme 5. Plausible scheme for the ligand exchange reaction of $[Cr^{III}(F_4Cat)(F_4SQ)_2]^-$ in MeCN.



initial changes relative to the original spectrum, the spectrum exhibited further variations and afforded a different spectrum. This is due to instability of the two-electron oxidized species in MeCN (Figures 10d and 25d), and a ligand exchange reaction can be suspected (Scheme 5).[23]

In contrast, electrolysis of a solution of **1** in the presence of one equivalent of Co^{2+} at 0.26 V for 26 min furnished the transient spectrum shown in Figures 23d (black line) and Figure 26. The observed absorption peaks at 381sh., 448sh., 526, 650sh., 710sh., 779sh., and 1830 nm are identical to those of the electrochemically generated $[Cr^{III}(F_4Cat)(F_4SQ)_2]^-$ (green line). The formation of the two-electron oxidized species suggests that the first oxidation process at 0.13 V (Figure 22e) should be most likely ascribed to a ligand-centered two-electron oxidation of $[\{Cr^{III}(F_4Cat)_3\}^{3-}–Co^{2+}]^-$ (eq. 3).

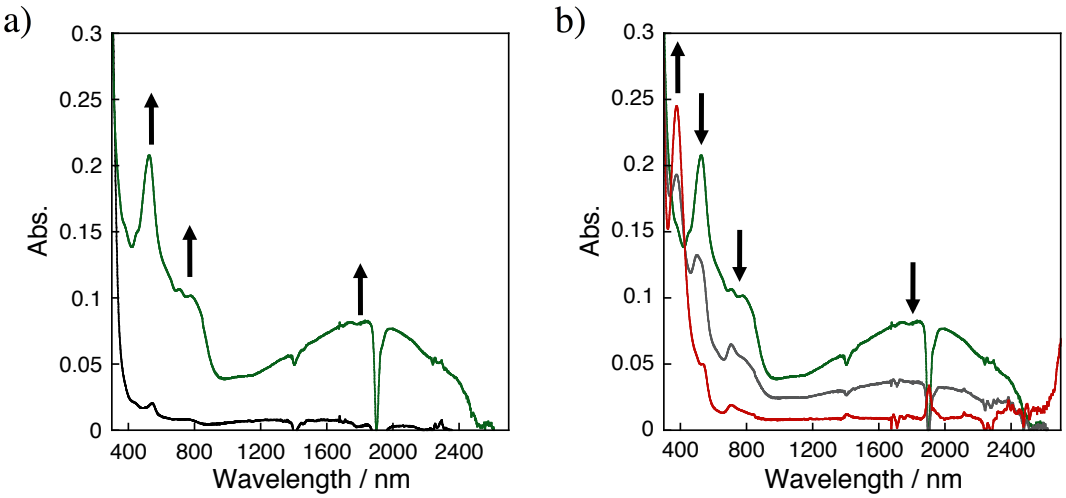


Figure 26. Changes of the UV-vis-NIR spectra of **1** (5×10^{-4} M) with one equivalent of $Co(ClO_4)_2 \cdot 6H_2O$ in MeCN at a) 0.26 V vs. Ag/Ag^+ for 0 (black line) and 26 min (green line) and b) 0.26 V for 26 (green line), 106 (grey line), and 246 min (red line). All spectra recorded under an atmosphere of N_2 using *n*-Bu_4NPF_6 (0.1 M).

$$[\{Cr^{III}(F_4Cat)_3\}^{3-}\text{–}Co^{2+}]^- \xrightarrow{-2e^-} [Cr^{III}(F_4Cat)(F_4SQ)_2]^-\cdots Co^{2+} \qquad \text{eq. 3}$$

Electrolysis of **1** in the presence of Mn^{2+} or Zn^{2+} at 0.12 V for 6 min or 0.20 V for 21 min, respectively, resulted in the emergence of new bands at 390, 538, 714, 775, and 1620 nm (Mn^{2+}), or at 443, 523, 635sh., 715, 795sh., and 1750 nm (Zn^{2+}) as shown in Figures 23b (black line), 23e (black line), 27, and 28. The spectral features are very similar to that of $[Cr^{III}(F_4Cat)(F_4SQ)_2]^-$ (green lines in Figures 23b and 23e), suggesting the generation of the two-electron oxidized species of **1**. In addition, similar spectra were obtained by adding one equivalent of Mn^{2+} or Zn^{2+} to electrochemically generated $[Cr^{III}(F_4Cat)_2(F_4SQ)]^{2-}$ (Figures 24b and 24c). One reasonable mechanism for the generation of $[Cr^{III}(F_4Cat)(F_4SQ)_2]^-$ would be disproportionation of $[Cr^{III}(F_4Cat)_2(F_4SQ)]^{2-}$ in the presence of Mn^{2+} or Zn^{2+} (eq. 4).

$$\begin{aligned} [\{Cr^{III}(F_4Cat)_3\}^{3-}\text{–}M^{2+}]^- &\xrightarrow{-e^-} [Cr^{III}(F_4Cat)_2(F_4SQ)]^{2-}\cdots M^{2+} \\ M = Mn, Zn \qquad & \\ &\longrightarrow \begin{array}{c} 1/2\ [\{Cr^{III}(F_4Cat)_3\}^{3-}\text{–}M^{2+}]^- \\ + \\ 1/2\ [Cr^{III}(F_4Cat)(F_4SQ)_2]^-\cdots 1/2\ M^{2+} \end{array} \end{aligned} \qquad \text{eq. 4}$$

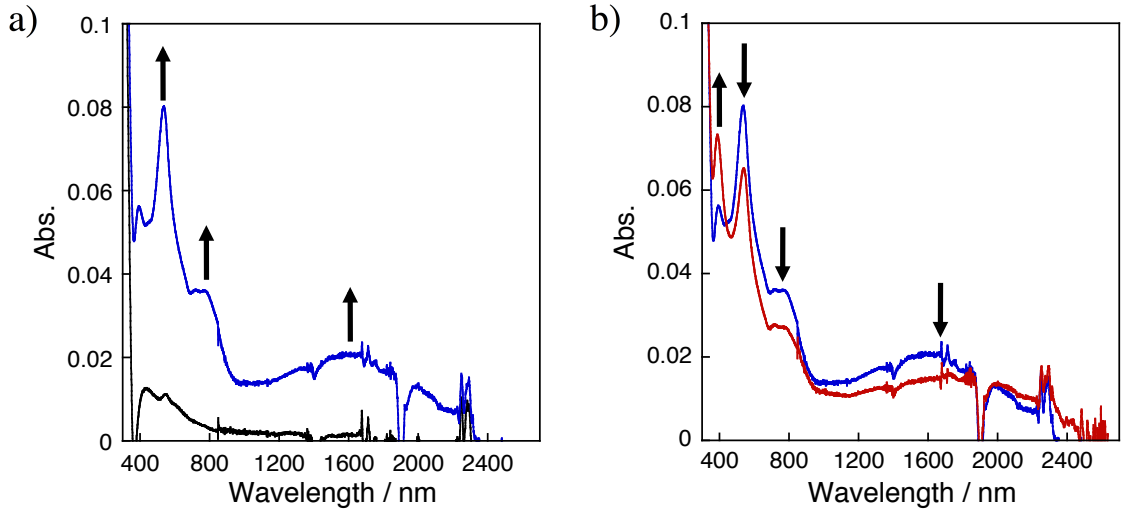


Figure 27. Changes of the UV-vis-NIR spectra of **1** (5×10^{-4} M) with one equivalent of $Mn(ClO_4)_2 \cdot 6H_2O$ in MeCN at a) 0.12 V vs. Ag/Ag^+ for 0 (black line) and 6 min (blue line) and b) 0.12 V for 6 (blue line) and 21 min (red line). All spectra recorded under an atmosphere of N_2 using *n*-Bu_4NPF_6 (0.1 M).

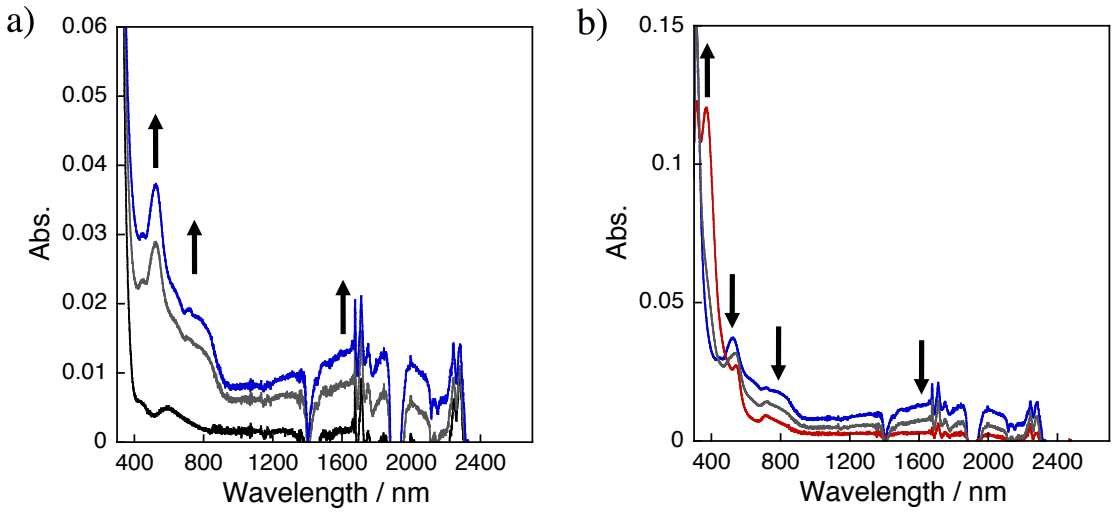


Figure 28. Changes of the UV-vis-NIR spectra of **1** (5×10^{-4} M) in MeCN upon addition of one equivalent of $Zn(ClO_4)_2 \cdot 6H_2O$ at 0.20 V vs. Ag/Ag^+ for a) 0 (black line), 6 (grey line), and 21 min (blue line), and b) 21 (blue line), 81 (grey line), and 291 min (red line). All spectra recorded under an atmosphere of N_2 using *n*-Bu_4NPF_6 (0.1 M).

Electrolysis of **1** at 0.15 V for 21 min in the presence of one equivalent of Fe^{2+} generated absorption bands at 507sh., 541, and 715sh. nm (black line in Figure 23c and Figure 29), while no bands were observed in the NIR region.[30] The absence of any IVCT bands indicates that the RML moiety maintains the original oxidation state of $[Cr^{III}(F_4Cat)_3]^{3-}$ after the electrolysis. Therefore, oxidation of Fe^{2+} bound to the RML is suggested. The iron-centered oxidation process could be confirmed by adding one equivalent of Fe^{3+} to a MeCN solution of **1**. After the addition, absorption bands appeared at 507sh., 550, and 722 nm (purple line in Figure 23c and Figure 30), which can be assigned to ligand-to-metal charge transfer bands ($Fe^{3+} \leftarrow F_4Cat^{2-}$).[31] Therefore, Fe^{2+} acts as an active center for the oxidation of $[\{Cr^{III}(F_4Cat)_3\}^{3-}–Fe^{2+}]^-$ (eq. 5).

$$[\{Cr^{III}(F_4Cat)_3\}^{3-}–Fe^{2+}]^- \underset{+e^-}{\overset{-e^-}{\rightleftharpoons}} [Cr^{III}(F_4Cat)_3]^{3-}\cdots Fe^{3+} \qquad \text{eq. 5}$$

These results indicate that complex **1** is a ligand-centered RML and that its electron transfer processes can be modulated by the choice of guest metal ion.

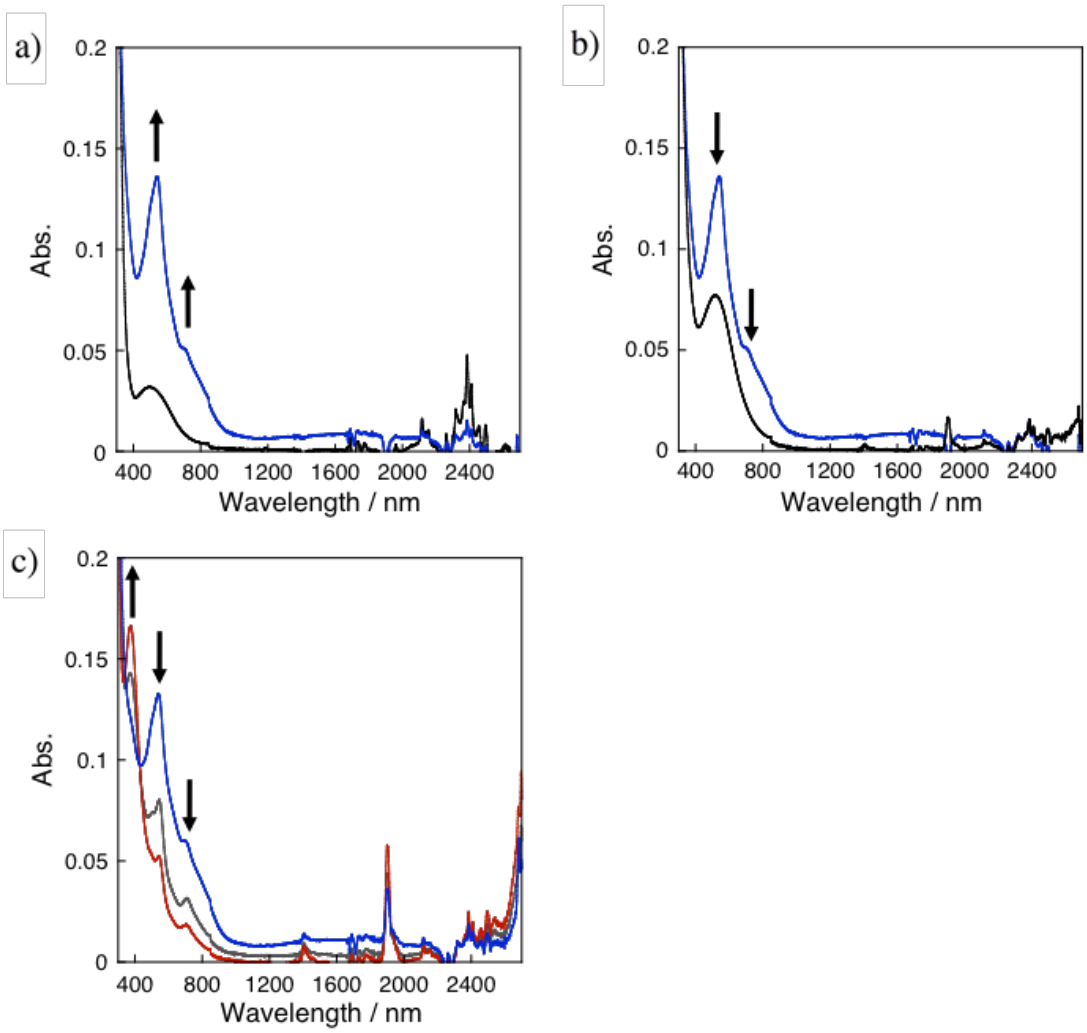


Figure 29. Changes of the UV-vis-NIR spectra of **1** (5×10^{-4} M) with one equivalent of $Fe(ClO_4)_2 \cdot 6H_2O$ in MeCN at a) 0.15 V vs. Ag/Ag^+ for 0 (black line) and 21 min (blue line); b) – 0.4 V for 0 (blue line) and 21 min (black line) after electrolysis at 0.15 V for 21 min; c) 0.30 V for 6 (blue line), 66 (grey line), and 146 min (red line). All spectra recorded under an atmosphere of N_2 using *n*-Bu_4NPF_6 (0.1 M).

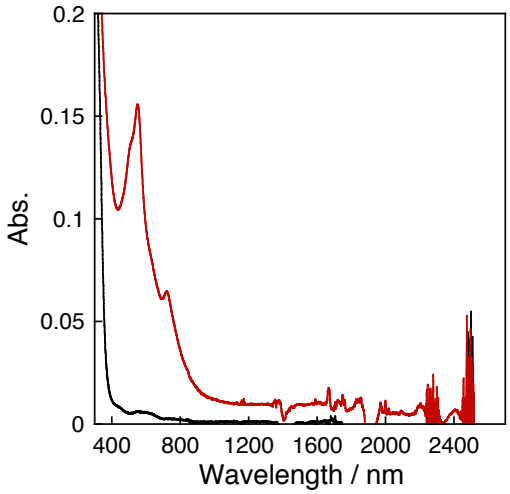


Figure 30. Changes of the UV-vis-NIR spectrum of **1** (5×10^{-4} M, black line) in MeCN upon addition of one equivalent of $Fe(ClO_4)_3 \cdot 6H_2O$ (red line) under an atmosphere of N_2.

3-4. Conclusions

In summary, this chapter described the binding interactions between the RML $[Cr^{III}(F_4Cat)_3]^{3-}$ and the guest metal ions Li^+, Mn^{2+}, Fe^{2+}, Co^{2+}, Cu^{2+}, and Zn^{2+}. As Cu^{2+} is a relatively strong oxidizing agent, the reaction between $[Cr^{III}(F_4Cat)_3]^{3-}$ and Cu^{2+} resulted in the formation of the ligand-centered one-electron oxidized species $[Cr^{III}(F_4Cat)_2(F_4SQ)]^{2-}$ and Cu^+. However, in the presence of relatively hard and weakly oxidizing metal ions such as Li^+, Mn^{2+}, Fe^{2+}, Co^{2+}, and Zn^{2+}, $[Cr^{III}(F_4Cat)_3]^{3-}$ binds to the guest metal ions *via* the lone pairs on the coordinating oxygen atom(s) of the F_4Cat^{2-} moieties. Furthermore, the present chapter demonstrated that the redox properties of this RML, *i.e.* oxidation potentials, number of transferred electrons, and redox reaction centers, can be modulated *via* the interactions with the guest metal ions. Current efforts are focused on revealing the redox properties of guest metal-bound RMLs, as well as on the construction of multi-electron transfer reactions using RMLs as an electron/hole reservoir.

3-5. Notes and References

1 a) P. Du, R. Eisenberg, *Energy Environ. Sci.,* **2012**, *5*, 6012; b) A. J. Esswein, D. G. Nocera, *Chem. Rev.,* **2007**, *107*, 4022; c) J. J. Concepcion, J. W. Jurss, M. K. Brennaman, P. G. Hoertz, A. O. T. Patrocinio, N. Y. M. Iha, J. L. Templeton, T. J. Meyer, *Acc. Chem. Res.,* **2009**, *42*, 1954.

2 a) S. Günes, H. Neugebauer, N. S. Sariciftci, *Chem. Rev.,* **2007**, *107*, 1324; b) R. H. Friend, R. W. Gymer, A. B. Holmes, J. H. Burroughes, R. N. Marks, C. Taliani, D. D. C. Bradley, D.A. D. Santos, J. L. Brédas, M. Löngdlund, W. R. Salaneck, *Nature,* **1999**, *397*, 121; c) J. Roncali, *Chem. Rev.,* **1992**, *92*, 711.

3 a) D.-L. Long, E. Burkholder, L. Cronin, *Chem. Soc. Rev.,* **2007**, *36*, 105; b) C. L. Hill, C. M. Prosser-McCartha, *Coord. Chem. Rev.,* **1995**, *143*, 407; c) M. T. Pope, A. Müller, *Angew. Chem. Int. Ed.,* **1991**, *30*, 34.

4 a) F. E. Hahn, M. C. Jahnke, *Angew. Chem. Int. Ed.,* **2008**, *47*, 3122; b) S. Kitagawa, R. Kitaura, S. Noro, *Angew. Chem. Int. Ed.,* **2004**, *43*, 2334; c) B. J. Holloday, C. A. Mirkin, *Angew. Chem. Int. Ed.,* **2001**, *40*, 2022.

5 a) D. Astruc, *New. J. Chem.,* **2011**, *35*, 764; b) C. M. Casado, I. Cuadrado, M. Morán, B. Alonso, B. García, B. González, J. Losada, *Coord. Chem. Rev.,* **1999**, *185-186*, 53.

6 T. Hamaguchi, H. Nagino, K. Hoki, H. Kido, T. Yamaguchi, B. Breedlove, T. Ito, *Bull. Chem. Soc. Jpn.,* **2005**, *78*, 591.

7 a) R. F. Munhá, R. A. Zarkesh, A. F. Feyduk, *Dalton Trans.,* **2013**, *42*, 3751; b) W. Kaim, B. Schwederski, *Coord. Chem. Rev.,* **2010**, *254*, 1580; c) M. D. Ward, J. A. McCleverty, *J. Chem. Soc. Dalton Trans.,* **2002**, 275.

8 a) M. Costas, M. P. Mehn, M. P. Jensen, L. Que, Jr., *Chem. Rev.* **2004**, *104*, 939; b) C. G. Pierpont, R. M. Buchanan, *Coord. Chem. Rev.,* **1981**, *38*, 45; c) F. Röhrscheid, A. L. Balch, R. H. Holm, *Inorg. Chem.,* **1966**, *5*, 1542.

9 a) P. R. Klich, A. T. Daniher, P. R. Challen, D. B. McConville, W. J. Youngs, *Inorg. Chem.,* **1996**, *35*, 347; b) B.-S. Kang, M.-C. Hong, T.-B. Wen, H.-Q. Liu, J.-X. Lu, *J.*

Clust. Sci., **1995**, *6*, 379; c) B. Kang, L. Weng, H. Liu, D. Wu, L. Huang, C. Lu, J. Cai, X. Chen, J. Lu, *Inorg. Chem.,* **1990**, *29*, 4873.

10 a) K. Ray, S. D. George, E. I. Solomom, K. Wieghardt, F. Neese, *Chem. Eur. J.,* **2007**, *13*, 2783; b) F. E. Hahn, C. S. Isfort, T. Pape, *Angew. Chem. Int. Ed.,* **2004**, *43*, 4807; c) N. Robertson, L. Cronin, *Coord. Chem. Rev.,* **2002**, *227*, 93.

11 a) C. G. Pierpont, *Inorg. Chem.,* **2011**, *50*, 9766; b) P. Zanello, M. Corsini, *Coord. Chem. Rev.,* **2006**, *250*, 2000.

12 a) L. A. deLearie, R. C. Haltiwanger, C. G. Pierpont, *Inorg. Chem.,* **1987**, *26*, 817; b) W. P. Griffith, C. A. Pumphrey, T.-A. Rainey, *J. Chem. Soc. Dalton Trans.,* **1986**, 1125.

13 a) H.-C. Chang, H. Miyasaka, S. Kitagawa, *Inorg. Chem.,* **2001**, *40*, 146; b) H.-C. Chang, T. Ishii, M. Kondo, S. Kitagawa, *J. Chem. Soc. Dalton Trans.,* **1999**, 2467; c) H. H. Downs, R. M. Buchanan, C. G. Pierpont, *Inorg. Chem.,* **1979**, *18*, 1736.

14 a) B. Chen, S. Xiang, G. Qian, *Acc. Chem. Res.,* **2010**, *43*, 1115; b) S. R. Halper, L. Do, J. R. Stork, S. M. Cohen, *J. Am. Chem. Soc.,* **2006**, *128*, 15255; c) S. Noro, H. Miyasaka, S. Kitagawa, T. Wada, T. Okubo, M. Yamashita, T. Mitani, *Inorg. Chem.,* **2005**, *44*, 133.

15 a) K. N. Raymond, S. S. Isied, L. D. Brown, F. R. Fronczek, J. H. Nibert, *J. Am. Chem. Soc.,* **1976**, *98*, 1767; b) S. R. Cooper, Y. B. Koh, K. N. Raymond, *J. Am. Chem. Soc.,* **1982**, *104*, 5092; c) C. J. Rolle III, K. I. Hardcastle, J. D. Soper, *Inorg. Chem.,* **2008**, *47*, 1892; d) J. R. Hartman, B. M. Foxman, S. R. Cooper, *Inorg. Chem.,* **1984**, *23*, 1381.

16 T. Matsumoto, H.-C. Chang, A. Kobayashi, K. Uosaki, M. Kato, *Inorg. Chem.,* **2011**, *50*, 2859.

17 T. Matsumoto, M. Wakizaka, H. Yano, A. Kobayashi, H.-C. Chang, M. Kato, *Dalton Trans.,* **2012**, *41*, 8303.

18 a) R. Berger, G. Resnati, P. Metrangolo, E. Weber, J. Hulliger, *Chem. Soc. Rev.,* **2011**, *40*, 3496; b) M. Hird, *Chem. Soc. Rev.,* **2007**, *36*, 2070; c) N. M. Doherty, N. W.

Hoffman, *Chem. Rev.,* **1991**, *91*, 553.

19 W. Weng, Z. Zhang, J. A. Schlueter, P. C. Redfern, L. A. Curtiss, K. Amine, *J. Power Sources,* **2011**, *196*, 2171.

20 B. T. Worrell, J. A. Malik, V. V. Fokin, *Science,* **2013***, 340*, 457.

21 a) S. S. Isied, G. Kuo, K. N. Raymond, *J. Am. Chem. Soc.,* **1976***, 98*, 1763; b) S. R. Sofen, D. C. Ware, S. R. Cooper, K. N. Raymond, *Inorg. Chem.,* **1979***, 18*, 234.

22 a) F. Morishima, R. Kusaka, Y. Inokuchi, T. Haino, T. Ebata, *J. Phys. Chem. B,* **2015**, *119*, 2557.

23 H.-C. Chang, K. Mochizuki, S. Kitagawa, *Inorg. Chem.,* **2002***, 41*, 4444.

24 C. Reichardt, *Chem. Rev.,* **1994***, 94*, 2319.

25 D. Ajloo, B. Yoonesi, A. Soleymanpour, *Int. J. Electrochem. Sci.,* **2010**, *5*, 459.

26 R. G. Pearson, *J. Am. Chem. Soc.,* **1963**, *85*, 3533.

27 a) J. S. Renny, L. L. Tomasevich, E. H. Tallmadge, D. B. Collum, *Angew. Chem. Int. Ed.,* **2013**, *52*, 11998; b) G. M. Dykes, D. K. Smith, *Tetrahedron,* **2003***, 59*, 3999; c) S. C. Zimmerman, W. Wu, Z. Zeng, *J. Am. Chem. Soc.,* **1991**, *113*, 196.

28 a) K. Hirose, *J. Incl. Phenom. Macrocycl. Chem.,* **2001**, *39*, 193. b) H.-J. Böhm, *J. Comput. Aid. Mol. Des.,* **1994**, *8*, 243; c) H.-J. Schneider, *Angew. Chem. Int. Ed.,* **1991**, *30*, 1417; d) K. A. Connors, *Binding Constants: The Measurements of Molecular Complex Stability*, John Wiley + Sons, 1987.

29 C. Ikeda, S. Ueda, T. Nabeshima, *Chem. Commum.,* **2009***,* 2544.

30 Electrolysis at –0.4 V furnished the original spectrum, supporting the reversibility of the oxidation process (Figure 29b).

31 a) Y. Hitomi, M. Yoshida, M. Higuchi, H. Minami, T. Tanaka, T. Funabiki, *J. Inorg. Biochem., 2005*, **99**, 755; b) A. Dei, D. Gatteschi, L. Pardi, *Inorg. Chem.,* **1993**, *32*, 1389; c) H. G. Jang, D. D. Cox, L, Que, Jr., *J. Am. Chem. Soc.,* **1991**, *113*, 9200.

Chapter 4

Guest Metal Ion Binding of Ligand-centered Redox-active $[Cr^{III}(2\text{-mercaptophenolato})_3]^{3-}$ Metalloligand with Heteroleptic Coordination Site

Abstract

The redox-active metalloligand (ML) *fac*-$(Me_4N)_3[Cr^{III}(Mp)_3]$ (**1**) (Mp = 2-mercaptophenolato), was synthesized, and characterized structurally as well as spectroscopically. The cyclic voltammogram of **1** in MeCN revealed a reversible one-electron oxidation process at –1.04 V vs. Ag/Ag^+. A spectroelectrochemical examination of the one electron-oxidized species of **1** demonstrated characteristic intervalence charge transfer bands at λ = 1180 and 1700 nm. These arise from a mixed-valence state of the ligands and thus demonstrated for the first time the presence of a mercaptosemiquinonato (MSQ) ligand in $[Cr^{III}(Mp)_2(MSQ)]^{2-}$. Furthermore, *fac*-$[Cr^{III}(Mp)_3]^{3-}$ was able to coordinate K^+ cations *via* its O and S sites, which resulted in the formation of the honeycomb-like 2-D coordination polymer $[K_3\{fac\text{-}Cr^{III}(Mp)_3\}]\cdot 6H_2O$ (**2**·$6H_2O$). Coordination polymer **2** exhibited reversible ligand-centered oxidations at –0.86 V, indicating that *fac*-$[Cr^{III}(Mp)_3]^{3-}$ acts as a ligand-centered redox-active metalloligand (RML). Upon addition of 0.5 equivalents of Co^{2+} to **1**, the resulting complex showed a reversible guest metal-centered one-electron oxidation at –0.89 V, indicative for the formation of a 2:1 complex between *fac*-$[Cr^{III}(Mp)_3]^{3-}$ and Co^{2+}. It was confirmed that Co^{2+} was automatically oxidized to Co^{3+}, and that coordination occurred selectively *via* the S sites on *fac*-$[Cr^{III}(Mp)_3]^{3-}$, resulting in the formation of $[Co^{II}(H_2O)_6]_2[K_2\{Co^{III}\{fac\text{-}Cr^{III}(Mp)_3\}_2\}]$ $[Co^{III}\{fac\text{-}Cr^{III}(Mp)_3\}_2]$ (**3**), which included discrete structure $[Co^{III}\{fac\text{-}Cr^{III}(Mp)_3\}_2]^{3-}$. This study thus demonstrated for the first time that **1** can act as a RML that exhibits ligand-centered redox properties with K^+, but guest metal-centered redox properties with Co^{2+}.

4-1. Introduction

Electron transfer is one of the most important reactions for the design and development of molecular electronic devices[1] and small molecule-activation catalysts, which require multi-electron transfer reaction.[2] Polyoxometalates such as α-$[P_2W^{VI}_{18}O_{62}]^{6-}$,[3] multi-nuclear transition metal complexes such as $[Ru_3O(CH_3CO_2)_6(pyridine)_3(bpe)]^+$ (bpe = trans-1,2-bis(4-pyridyl)ethylene),[4] and ferrocenyl dendrimers such as hexa(ferrocenylethynyl) benzene[5] exhibit metal-centered multi electron-transfer reactions.

In contrast to the aforementioned examples, transition metal complexes with redox-active ligands, *e.g.* catecholato (Cat), exhibit not only metal-centered but also ligand-centered electron transfer reactions.[6] For example, $[Cr^{III}(X_4SQ)_3]$ (X = Cl or Br, SQ = semiquinonato) affords $[Cr^{III}(X_4Cat)\ (X_4SQ)_2]^-$, $[Cr^{III}(X_4Cat)_2(X_4SQ)]^{2-}$, and $[Cr^{III}(X_4Cat)_3]^{3-}$ by a reversible ligand-centered three-step reduction.[7] Moreover, catalytic activity was reported for transition metal complexes with redox-active ligands in the context of *e.g.* oxidation of water,[8] alcohols,[9] and hydrogen,[10] as well as in the context of cross coupling reactions.[11] In these catalytic reactions, redox-active ligands act as electron/hole poolers.

Recently, it was reported that the redox-active metalloligand (RML) $[Mo^V(Bdt)_3]^-$ (Bdt = 2-benzenedithiolato), which exhibits metal-centered redox properties, is able to bind Cu^+ and Ag^+ *via* the lone pairs of its sulfur atoms, resulting in the formation of 1-D coordination polymers.[12] Furthermore, the previous chapter demonstrated that the RML $[Cr^{III}(F_4Cat)_3]^{3-}$, which shows ligand-centered three-step one-electron transfer properties, interacts with several guest metal ions such as Li^+, Mn^{2+}, Fe^{2+}, Co^{2+}, and Zn^{2+} *via* the lone pairs on its oxygen atoms.[13] The interactions between RMLs and guest metal ions led to a significant increase of the electron-accepting properties of the RML, in addition to the number of transferred electrons.

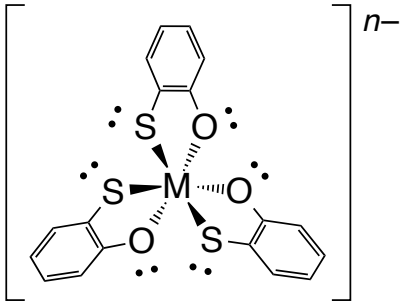
The Cat or Bdt ligands contain homoleptic coordination sites that consist of oxygen or sulfur atoms, whereas Mp contains heteroleptic coordination sites of oxygen and sulfur (Chart 1).[14] Complexes of Mp, such as *fac*-$[V^{IV}(4\text{-Me-Mp})_3]^{2-}$ and *fac*-$[Nb^V(4\text{-Me-Mp})_3]^-$ reported by Challen *et al.*,[15,16] or *fac*-$[V^{IV}(Mp)_3]^{2-}$, *fac*-$[Ti^{IV}(Mp)_3]^{2-}$, and *fac*-$[Mo^V(Mp)_3]^-$ reported by Kang

et al.,[17-19] as well as *fac*-$[Sn^{IV}(Mp)_3]^{2-}$ reported by Holmes *et al*.,[20] usually adopt *facial* geometry based on the *trans*-effect between the O and S atoms. Tris-(Mp) metal complexes contain therefore heteroleptic coordination sites and can bind guest metal ions *via* O[13] or S[12] sites. In the case of V complexes of Mp, the selective binding of metals *via* the O sites generates multi-nuclear complexes such as $[Co^{II}(MeCN)(pyridine)_2\{fac\text{-}V^{IV}(Mp)_3\}]$ and $[V^{III}\{fac\text{-}V^{IV}(Mp)_3\}_2]^-$, which have been reported by Kang *et al*.,[17,21] or $[Mo(CO)\{Mo(Mp)_3\}]^{2-}$, reported by Zhang *et al*.[22] For such Mp complexes, reversible metal-centered redox properties, for *e.g*. the V^{IV}/V^{V} redox couple in *fac*-$[V^{IV}(4\text{-Me-Mp})_3]^{2-}$,[15] or the Nb^{IV}/Nb^{V} redox couple in *fac*-$[Nb^{V}(4\text{-Me-Mp})_3]^-$,[16] have been reported.

The chapter 2 demonstrated that *fac*-$[Mo^{V}(Mp)_3]^-$ is able to selectively bind Mn^{2+} *via* its O sites to form the discrete assembly $[Mn^{II}(H_2O)(MeOH)\{fac\text{-}Mo^{V}(Mp)_3\}]$.[23] Conversely, Cu^+ is selectively bound *via* the S sites to form the 1-D coordination polymer $[Cu^{I}(MeCN)\{mer\text{-}Mo^{V}(Mp)_3\}]_n$. Even though *fac*-$[Mo^{V}(Mp)_3]^-$ and $[Mn^{II}(H_2O)(MeOH)\{fac\text{-}Mo^{V}(Mp)_3\}]$ both revealed reversible metal-centered redox properties, reversible ligand-centered redox properties have not yet been observed for Mp complexes. Therefore, the investigation of the Mp redox properties should deliver valuable design guidelines for the development of RML assemblies that exhibit multi-electron transfer.

In this chapter, *fac*-$(Me_4N)_3[Cr^{III}(Mp)_3]$ (**1**) was synthesized, as it is expected to exhibit ligand-centered redox properties together with metal-binding activity. Furthermore, the RML behavior of **1** was demonstrated by the site-selective coordination of the guest metal ions such as K^+ and $Co^{2+/3+}$. Herein, the synthesis, structures, as well as the redox properties of **1** and the corresponding supramolecular assemblies with K^+ or $Co^{2+/3+}$ are described.

Chart 1. Schematic structure of a tris(Mp) metal complex.



4-2. Experimental Section

General Procedures. Unless otherwise noted, all synthetic and analytic operations were carried out under an atmosphere of N_2 using Schlenk-line techniques. $CrCl_3 \cdot 6H_2O$, $Cr(OAc)_3$ (OAc = acetate), $CoCl_2 \cdot 6H_2O$, KOH, and tetra-*n*-butylammonium hexafluorophosphate (*n*-Bu_4NPF_6) were purchased from Wako Pure Chemical Industries. Dehydrated methanol (MeOH) and dehydrated acetonitrile (MeCN) were purchased from Kanto Chemical Co. Inc. Tetramethylammonium hydroxide pentahydrate ($Me_4NOH \cdot 5H_2O$) and MpH_2 were purchased from Tokyo Kasei Kogyo Co. Ltd. All solvents used under anaerobic conditions were degassed by at least five freeze-pump-thaw cycles immediately prior to use. **Caution!** Although we did not experience any difficulties with perchlorate salts, these should be regarded as potentially explosive, and therefore handled with the utmost care.

***fac*-$(Me_4N)_3[Cr^{III}(Mp)_3] \cdot EtOH \cdot H_2O$ (1·EtOH·H_2O).** A pale yellow EtOH solution (10 mL) of MpH_2 (630 mg, 4.99 mmol) and $Me_4NOH \cdot 5H_2O$ (1.80 g, 9.93 mmol) was slowly layered onto a green EtOH (10 mL) solution of $CrCl_3 \cdot 6H_2O$ (353 mg, 1.32 mmol) under an atmosphere of N_2. After allowing the solution to stand for 1 week at room temperature, green crystals suitable for X-ray diffraction analysis were obtained, which were isolated by filtration, washed with EtOH (4 × 5 mL), and dried *in vacuo* to afford **1**·EtOH·H_2O as green crystals in 67% yield. As these crystals were found to be highly hygroscopic, they usually contained small amounts (~0.2 molecules of H_2O per molecule of **1**) of water in addition to the water molecules in the crystal lattice. Anal. Found: C, 53.68; H, 8.10; N, 6.06%. Calc. for $C_{32}H_{56.4}CrN_3O_{5.2}S_3$ (**1**·EtOH·H_2O + 0.2H_2O): C, 53.78; H, 7.96; N, 5.88%.

$[K_3\{fac\text{-}Cr^{III}(Mp)_3\}]$ (2·6H_2O). A pale yellow MeOH solution (20 mL) of MpH_2 (1.27 g, 10.1 mmol) and KOH (1.12 g, 20.0 mmol) was added to a green MeOH solution (20 mL) of $Cr(OAc)_3$ (748 mg, 3.26 mmol), which afforded a green solution after heating to reflux for 1 h.

After slow cooling to room temperature and standing for 1 week, green crystals suitable for X-ray diffraction analysis were obtained. The crystals were isolated by filtration, washed with cooled EtOH (5 mL), and dried *in vacuo* to furnish **2**·6H_2O as green crystals in 76% yield. The crystals of **2**·6H_2O easily loss the water molecules. Anal. Found: C, 35.88; H, 3.20%. Calc. for $C_{18}H_{19}CrO_{6.5}S_3$ (**2**·6H_2O – 2.5H_2O): C, 35.75; H, 3.17%.

$[Co^{II}(H_2O)_6]_2[K_2\{Co^{III}\{fac\text{-}Cr^{III}(Mp)_3\}_2\}][Co^{III}\{fac\text{-}Cr^{III}(Mp)_3\}_2]\cdot 30H_2O\cdot(3\cdot 30H_2O)$. Adding a pink aqueous solution (10 mL) of $CoCl_2\cdot 6H_2O$ (95.0 mg, 0.399 mmol) to a green aqueous solution (10 mL) of **2**·6H_2O (200 mg, 0.299 mmol) afforded an olive-green suspension after heating to reflux for 1 h. After filtration, an olive-green solution was obtained, whose color turned to purple upon exposure to air. From this solution, purple crystals were obtained after standing for 1 d. After filtration and washing with water (3 × 5 mL), followed by drying *in vacuo*, complex **3**·30H_2O was isolated in the form of purple crystals in 15% yield. The crystals of **3**·30H_2O easily loss the water molecules. Anal. Found: C, 38.20; H, 3.38%. Calc. for $C_{72}H_{76}Co_4Cr_4K_2O_{26}S_{12}$ (**3**·30H_2O – 29H_2O): C, 38.20; H, 3.38%. Purple single crystals suitable for X-ray diffraction analysis were obtained by layering an aqueous solution of $CoCl_2\cdot 6H_2O$ onto an aqueous solution of **2**·6H_2O.

Physical Measurements. Elemental analyses were carried out on a Perkin-Elmer 2400 II CHN analyzer. Solution and in the solid state (KBr pellets) absorption spectra (200-3300 nm) were recorded on a Hitachi U-4100 spectrophotometer at 296 K. Cyclic voltammetry measurements were recorded on a BAS model 650A electrochemical analyzer, using a glassy carbon (GC) working electrode and a platinum (Pt) auxiliary electrode under an atmosphere of argon (Ar). The reference electrode consisted of a silver wire, inserted into a small glass tube fitted with a porous Vycor frit at the tip, filled with a MeCN solution containing 0.1 M *n*-Bu_4NClO_4 and 0.01 M $AgNO_3$. All three electrodes were immersed in 2 mL of a MeCN solution containing 0.1 M *n*-Bu_4NPF_6 as the supporting electrolyte and 1 mM analyte. In all

cases, redox potentials were measured relative to the Ag/Ag^+ redox couple. Spectroelectrochemical measurements were carried out in 0.1 M *n*-Bu_4NPF_6 solution using Pt, Pt mesh, and the reference electrodes under an atmosphere of N_2.

Collection of Crystallographic Data and Structure Refinements. Crystallographic measurements were carried out on a Rigaku VariMax with Saturn equipment, using graphite-monochromated Mo-Kα radiation (λ = 0.71075 Å). Specimen of suitable size and quality were selected under paraffin oil or silicon grease and mounted onto MicroMounts (MiTeGen). Crystals were cooled using a N_2 flow-type temperature controller. Structures were solved by direct methods (SIR2004),[24] which successfully located all non-hydrogen atoms within the unit cell. All calculations were carried out using the CrystalStructure crystallographic software package,[25] except for refinement calculations, which were performed using SHELXL-97.[26] A summary of the crystallographic data for **1**·EtOH·H_2O, **2**·6H_2O, and **3**·30H_2O is shown in Table 1.

Table 1. Crystallographic data of **1**·EtOH·H_2O, **2**·$6H_2O$, and **3**·$30H_2O$

	1·EtOH·H_2O	**2**·$6H_2O$	**3**·$30H_2O$
Formula	$C_{32}H_{56}CrN_3O_5S_3$	$C_{18}H_{24}CrK_3O_9S_3$	$C_{36}H_{42}Co_2Cr_2KO_{27}S_6$
fw	710.99	649.85	1384.22
Crystal size (mm^3)	0.30×0.30×0.03	0.07×0.05×0.02	0.20×0.20×0.02
Crystal system	monoclinic	trigonal	triclinic
Space group	$P2_1/n$(No. 14)	P-3(No. 147)	P-1(No. 2)
a (Å)	14.984(4)	13.127(3)	12.586(4)
b (Å)	14.526(3)	13.127(3)	14.735(5)
c (Å)	17.641(4)	8.825(2)	16.648(4)
α (°)	90	90	70.421(10)
β (°)	107.837(4)	90	73.654(11)
γ (°)	90	120	88.852(13)
V ($Å^3$)	3655.0(16)	1316.9(5)	2781.7(13)
T (K)	133	93	93
Z	4	2	2
D_{calc} (g cm^{-3})	1.292	1.639	1.653
F (000)	1524.00	666.00	1430.00
μ(Mo Kα) (cm^{-1})	5.253	11.915	13.488
Measured	10534	5323	22670
Unique reflections	5713	2022	12294
Refined parameters	397	103	679
GOF on F^2	1.076	1.042	1.093
R_{int}	0.0279	0.0433	0.0359
R_1 [a]	0.0683	0.0557	0.0768
wR_2 [b] (all data)	0.2072	0.1585	0.2127

[a] $R_1 = \Sigma||F_o| - |F_c||/\Sigma|F_o|$. [b] $wR_2 = \{[\Sigma w(F_o^2 - F_c^2)^2]/[\Sigma w(F_o^2)^2]\}^{1/2}$.

4-3. Results and Discussion

4-3-1. Crystal Structures of 1·EtOH·H_2O and 2·6H_2O

Green crystals of **1**·EtOH·H_2O and **2**·6H_2O were grown by mixing $CrCl_3$·6H_2O or $Cr(OAc)_3$ with slightly more than three equivalents of MpH_2 and a corresponding amount of Me_4NOH or KOH in EtOH or MeOH under an atmosphere of N_2. The molecular structure of **1**·EtOH·H_2O is shown in Figure 1, and selected bond lengths are summarized in Tables 2 and 3. The molecular structure of **1** revealed a trianionic [$Cr(C_6H_4OS)_3$] moiety, which was accompanied by three Me_4N^+ cations. The Cr center exhibited *pseudo*-octahedral coordination geometry, whereby the *facial* isomer was formed selectively, due to the *trans* effect between the O and S atoms.[15-20] Accordingly, **1**·EtOH·H_2O contains heteroleptic coordination sites *via* the lone pairs on the O and S atoms. For the chelating ligands, three electronically different forms are conceivable, *i.e.* Mp^{2-}, $MSQ^{\cdot-}$ ($MSQ^{\cdot-}$ = mercaptosemiquinonato), or MBQ (MBQ = monothio-*o*-benzoquinone). The observed C–O and C–S bond distances of 1.311-1.336(6) Å and 1.764-1.768(5) Å, respectively, indicate a single bond character for these bonds.[15-20] In addition, the C–C bond distance values in the six-membered rings of 1.377-1.426(7) Å, which lie between typical C–C single and double bonds, suggest, together with the lack of significant bond alternation, aromatic character. Consequently, the structure of the three chelating ligands is consistent with an Mp^{2-} structure. Moreover, the obtained Cr–O and Cr–S bond distances of

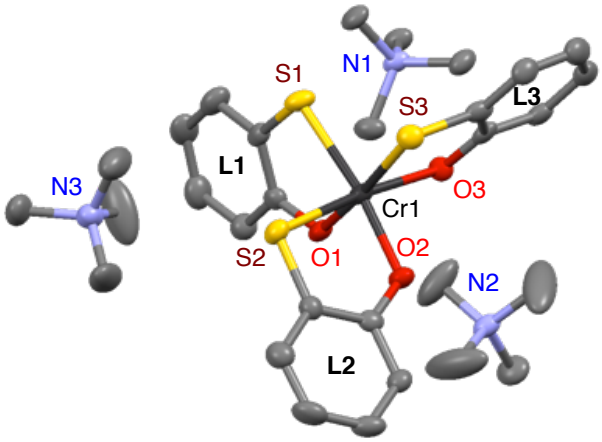


Figure 1. Molecular structure of **1**·EtOH·H_2O with atomic displacement parameters set at 50% probability; color code: Cr = black, O = red, S = yellow, N = light blue, and C = gray; all hydrogen atoms are omitted for clarity and only selected atoms are labeled.

1.989-2.015(4) Å and 2.388-2.393(2) Å, respectively is in good agreement with previously reported values for Cr^{III}–O (1.981-1.992(2) Å) and Cr^{III}–S (2.351-2.373(1) Å) bonds in complexes with *fac*-O_3S_3 geometry.[27] On the basis of this structural analysis, **1** was assigned the formula *fac*-$(Me_4N)_3[Cr^{III}(Mp)_3]$.

The structure of **2** consists of a Cr complex with three chelating ligands and three K^+ counter cations (Figure 2). The Cr center, which is located on a three-fold symmetry axis, adopts, as in the case of **1**, *pseudo*-octahedral and *facial* geometry. The observed bond distances in **2** are consistent with chelating Mp^{2-} ligands and hence the anion in **2** was assigned the structure *fac*-$[Cr^{III}(Mp)_3]^{3-}$. Interestingly, the K^+ cation was bound *via* the O and S sites on the Mp^{2-} ligands, indicating that *fac*-$[Cr^{III}(Mp)_3]^{3-}$ acts as an ML. The coordination of *fac*-$[Cr^{III}(Mp)_3]^{3-}$ to K^+ was not site-selective, which suggests that K^+ does not show a significant preference for coordination on O or S sites.[28] Moreover, the MLs assembled in a supramolecular fashion *via* bridging K^+ cations coordinated to the S sites (Figure 2b), resulting in the formation of a 2-D

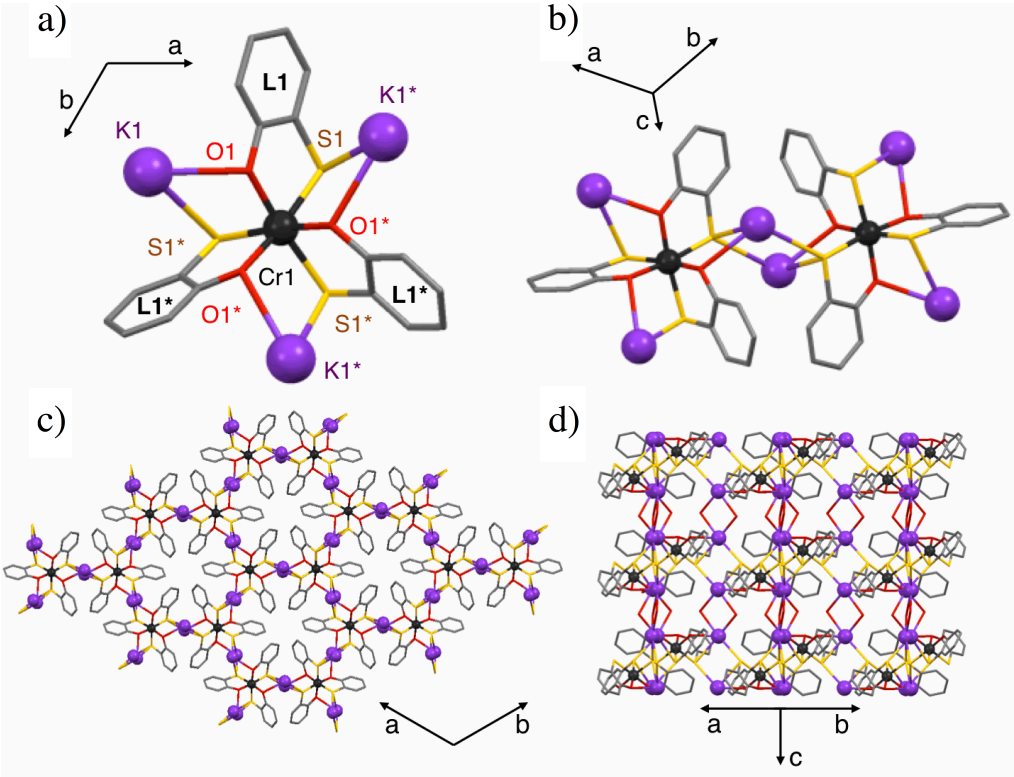


Figure 2. Molecular structure of **2**·$6H_2O$: a) atomic displacement parameters set at 50% probability and b-d) ball-and-stick plots; color code: Cr = black, K = purple O = red, S = yellow, and C = gray; all hydrogen atoms are omitted for clarity, and only selected atoms are labeled.

honeycomb-like sheet structure (Figure 2c). These sheets are furthermore connected by water molecules to construct a 3-D network structure (Figure 2d).

Table 2. Selected bond distances around Cr-center of **1**·EtOH·H_2O, **2**·6H_2O, and **3**·30H_2O

Complex	Ligand	Cr–O (Å)	Cr–S (Å)
1·EtOH·H_2O	L1	2.015(4)	2.393(1)
	L2	1.989(3)	2.388(1)
	L3	2.006(2)	2.391(2)
2·6H_2O	L1	1.985(4)	2.385(1)
3·30H_2O	L1	1.986(4)	2.374(2)
	L2	1.967(4)	2.368(2)
	L3	1.979(5)	2.356(1)
	L4	1.973(4)	2.356(2)
	L5	1.985(5)	2.376(2)
	L6	1.960(4)	2.363(2)

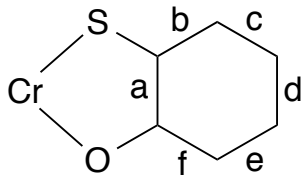


Table 3. Selected bond distances in ligands of **1**·EtOH·H_2O, **2**·6H_2O, and **3**·30H_2O

Complex	L	C–O (Å)	C–S	C–C(a)	C–C(b)	C–C(c)	C–C(d)	C–C(e)	C–C(f)
1·EtOH	L1	1.336(5)	1.767(5)	1.418(6)	1.391(6)	1.382(8)	1.374(7)	1.409(7)	1.398(7)
·H_2O	L2	1.323(5)	1.764(4)	1.401(5)	1.410(6)	1.381(7)	1.396(6)	1.394(6)	1.407(6)
	L3	1.311(6)	1.768(4)	1.426(7)	1.377(7)	1.382(6)	1.385(8)	1.387(7)	1.404(5)
2·6H_2O	L1	1.353(7)	1.776(5)(	1.415(6)	1.400(5)	1.391(7)	1.401(7)	1.386(8)	1.416(8)
3·30H_2O	L1	1.351(7)	1.783(6)	1.406(9)	1.396(7)	1.385(9)	1.402(10)	1.376(9)	1.400(9)
	L2	1.345(8)	1.774(5)	1.422(7)	1.401(9)	1.391(8)	1.381(8)	1.383(10)	1.404(7)
	L3	1.361(6)	1.761(6)	1.412(7)	1.405(7)	1.373(10)	1.393(9)	1.381(8)	1.409(10)
	L4	1.353(7)	1.769(6)	1.411(6)	1.404(9)	1.382(9)	1.387(8)	1.392(9)	1.401(9)
	L5	1.357(6)	1.783(6)	1.405(7)	1.392(8)	1.388(9)	1.395(8)	1.387(9	1.405(9)
	L6	1.356(7)	1.785(6)	1.404(8)	1.396(8)	1.377(8)	1.399(9)	1.395(8)	1.399(8)

4-3-2. Absorption Spectra of 1·EtOH·H_2O and 2·$6H_2O$

The absorption spectra of **1**·EtOH·H_2O and **2**·$6H_2O$ in the solid state are shown in Figure 3. For **1**·EtOH·H_2O, five absorption bands were observed at λ = 320, 520sh., 636, 680sh., and 780sh. nm. The strong absorption band at 330 nm was assigned to the π-π* transition[29] of the Mp^{2-} moieties, whereas the four relatively weak bands were assigned to d-d transitions on the Cr(III) center.[13,30] It should be noted that no bands appeared in the NIR region, which is indicative of the absence of intervalence charge transfer (IVCT) bands that may arise from mixed-valence states of the ligands. For **2**·$6H_2O$, a strong absorption band at λ = 318 nm was assigned to the ligand π-π* transition, while absorptions at λ = 450sh., 636, and 682 nm were assigned to d-d transitions on the Cr(III) center. The observed peak shifts of **2**·$6H_2O$ relative to those of **1**·EtOH·H_2O most likely reflect coordination and assembling between *fac*-$[Cr^{III}(Mp)_3]^{3-}$ and K^+.

As **1**·EtOH·H_2O is a discrete ion pair, it is soluble in polar solvents such as MeCN, especially in the presence of electrolytes *n*-Bu_4NPF_6 (0.1 M). The color of the MeCN solution of **1** gradually changed from pale green to pale purple, and the spectral features of the pale purple

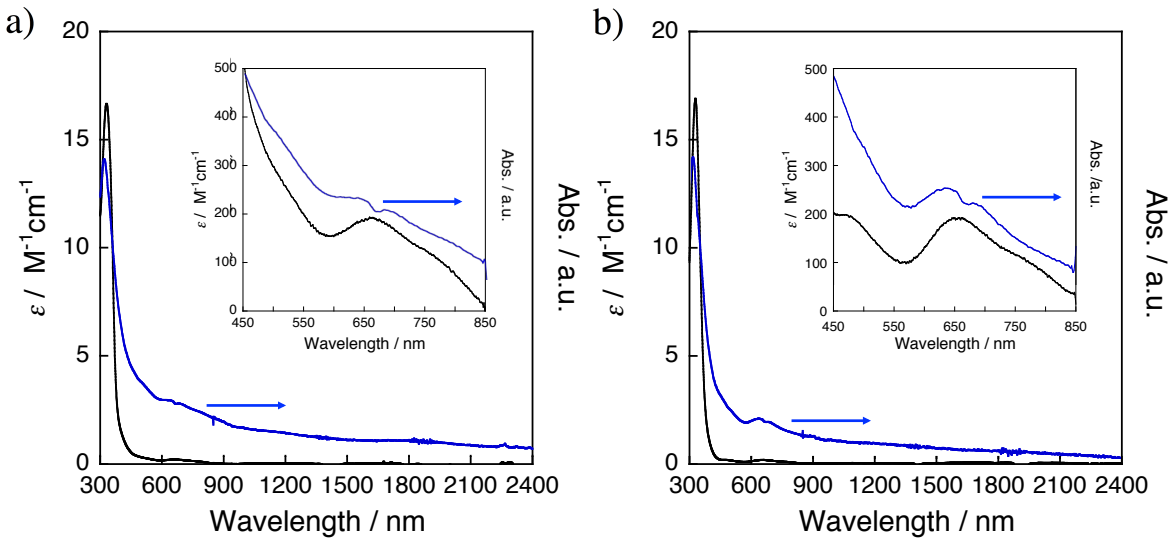


Figure 3. Absorption spectra of a) **1**·EtOH·H_2O in the solid state (KBr, blue line) and **1**·EtOH·H_2O (1.02 mM) in MeCN with 0.1 M *n*-Bu_4NPF_6 electrolyzed at –1.3 V vs. Ag/Ag^+ (black line), b) **2**·$6H_2O$ in the solid state (KBr, blue line) and **2**·$6H_2O$ (0.998 mM) in MeCN with 0.1 M *n*-Bu_4NPF_6 electrolyzed at –1.3 V vs. Ag/Ag^+ (black line), under an atmosphere of N_2. The insets show the magnification of the 450-900 nm region.

solution are identical to the one-electron oxidized species of **1** (*vide infra*). As the rest potential of **1** was relatively low (–1.3 V vs. Ag/Ag^+; *vide infra*), complex **1** might be automatically oxidized by oxygen contaminations. However, when the absorption spectrum of **1** was recorded in MeCN in the presence of 0.1 M *n*-Bu_4NPF_6 while being electrolyzed at the rest potential under an atmosphere of N_2, a steady spectrum was observed (Figure 3a). Complex **2**·$6H_2O$ also dissolves in MeCN with 0.1 M *n*-Bu_4NPF_6, and an equally steady absorption spectrum of **2** was recorded while being electrolyzed at the rest potential (–1.2 V; *vide infra*) (Figure 3b). Complex **1** showed four absorption bands at λ = 331 ($\varepsilon = 1.67 \times 10^4$ M^{-1} cm^{-1}), 520sh. (258 M^{-1} cm^{-1}), 661 (191 M^{-1} cm^{-1}), and 760sh. (118 M^{-1} cm^{-1}) nm. The band at 331 nm was assigned to the π-π* transition, whereas those at 520, 661, and 760 nm were assigned to d-d transitions on the metal center, and accordingly, a spectrum similar to that in the solid state was observed. Consequently, it can be concluded that **1** maintained its solid state structure in MeCN solution. Conversely, complex **2** exhibited an absorption band at λ = 329 (1.42×10^4 M^{-1} cm^{-1}) nm, which was assigned to the π-π* transition, as well as bands at λ = 475 (196 M^{-1} cm^{-1}), 651 (188 M^{-1} cm^{-1}), and 765 (114 M^{-1} cm^{-1}) nm, which were assigned to d-d transitions.

4-3-3. Redox Properties of 1·EtOH·H_2O and 2·$6H_2O$

Figure 4 shows the cyclic voltammograms (CVs) of **1**·EtOH·H_2O and **2**·$6H_2O$ (1 mM) in the presence of 0.1 M *n*-Bu_4NPF_6 in MeCN, and the electrochemical data are summarized in Table 4. Complex **1** showed one reversible oxidation peak at $E_{1/2}^{1}$ = –1.04 V vs. Ag/Ag^+, as well as two irreversible oxidation peaks at E_{pa}^{2} = –0.55 V and E_{pa}^{3} = –0.55 V. The previously reported $[Cr^{III}(F_4Cat)_3]^{3-}$ showed, under similar conditions, reversible ligand-centered three-step one-electron oxidations. On the other hand, for MpH_2, catalytic one-electron oxidations by oxygen or hydrogen peroxide under simultaneous deprotonation of the thiol moiety have been reported.[31] These oxidations/deprotonations led to the formation of bis(hydroxyphenyl) disulfide dimers that contain an S–S bond. If oxidation processes on **1** proceed ligand-centered,

similar dimerization reactions could be expected for Mp^{2-}. The potential gap between the first and last oxidation event can be used in this context as a diagnostic tool for the determination of ligand- or metal-centered redox processes. For example, MLs with ligand-centered redox properties such as $[Cr^{III}(X_4SQ)_3]$ (ΔE_{gap} = 0.9 for X = Br and Cl)[7a] or $[Cr^{III}(F_4Cat)_3]^{3-}$ (ΔE_{gap} = 0.7 V)[13] exhibit relatively narrow potential gaps, while MLs with metal-centered redox properties, such as $[Mo^{V}(Mp)_3]^{-}$ (ΔE_{gap} = 2.3 V)[23,32] show larger gaps. The observed potential gap between the three oxidation peaks in **1** ($\Delta E_{gap} = E_{pa}^{3} - E_{pa}^{1}$ = 0.8 V) was relatively narrow, and accordingly, the redox processes in **1** should be considered as ligand-centered.

In addition, complex **2** exhibited a reversible oxidation peak at $E_{1/2}^{1}$ = –0.86 V, accompanied by a shoulder (E_{pa}^{2} = –0.55) and two irreversible oxidation peaks at E_{pa}^{3} = –0.47 and E_{pa}^{4} = –0.15 V. It is noteworthy that the $E_{1/2}^{1}$ of **2** is by 0.18 V positively shifted relative to that of **1**, which directly reflects the coordination between *fac*-$[Cr^{III}(Mp)_3]^{3-}$ and K^+ in solution.[12,13,23] The second oxidation peak (E_{pa}^{3}) of **2** was also positively shifted (0.08 V) relative to the corresponding peak (E_{pa}^{2}) of **1**, whereas the potential for the shoulder (E_{pa}^{2}) of **2** was the same as the E_{pa}^{2} of **1**. These results suggest that the one-electron oxidized species *fac*-$[Cr^{III}(Mp)_3]^{2-}$ may be able to interact with K^+, but that these ions are most likely partly dissociated.

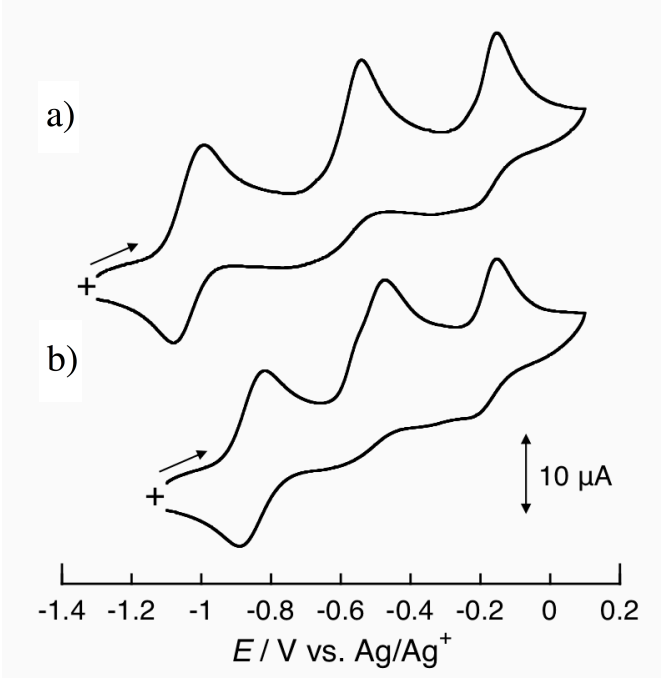


Figure 4. CV of a) **1**·EtOH·H_2O and b) **2**·$6H_2O$ (1 mM) in MeCN: recorded at 50 mV s^{-1} under an atmosphere of N_2 in the presence of 0.1 M *n*-Bu_4NPF_6 as the supporting electrolyte.

Table 4. Electrochemical data for **1** and **2** in MeCN at 50 mV s^{-1}

	E / V vs. Ag/Ag^+					
Complex	E_{pa}^{1}	E_{pc}^{1}	$E_{1/2}^{1}$ (ΔE)	E_{pa}^{2}	E_{pa}^{3}	E_{pa}^{4}
1·EtOH·H_2O	–0.99	–1.08	–1.04 (0.09)	–0.55[a]	–0.16[a]	
2·6H_2O	–0.82	–0.89	–0.86 (0.07)	–0.55sh.[a]	–0.47[a]	–0.15[a]

[a] Irreversible process.

The absorption spectra of **1**·EtOH·H_2O during bulk electrolysis in MeCN are shown in Figure 5. New absorption bands emerged at λ = 460, 525, 784, 1180, and 1700 nm during the first oxidation at –0.9 V vs. Ag/Ag^+ (t = 21 min) (Figure 5a). The bands in the NIR region (1180 and 1700 nm) are very similar to those of $[Cr^{III}(X_4Cat)_2(X_4SQ)]^{2-}$ (X = Br: 1200sh. and 1660 nm; X = Cl: 1200sh. and 1680 nm) in dichloromethane[7a] and the electrochemically generated $[Cr^{III}(F_4Cat)_2(F_4SQ)]^{2-}$ (1230sh. and 1540 nm) in MeCN.[13] These results suggest that the one-electron oxidized species of **1** should be assigned the formula $[Cr^{III}(Mp)_2(MSQ)]^{2-}$. This notion is corroborated by the fact that the one-electron oxidized species of **1** showed a strong band at 525 nm, which was assigned to a CT between Cr^{III} and $MSQ^{\cdot-}$ similar to the case of $[Cr^{III}(X_4Cat)_2(X_4SQ)]^{2-}$.[7a,13] These results are consistent with the results of previous studies,[7a,13] which demonstrated that $[Cr^{III}(X_4Cat)_2(X_4SQ)]^{2-}$ shows strong $Cr^{III}/X_4SQ^{\cdot-}$ charge transfer bands

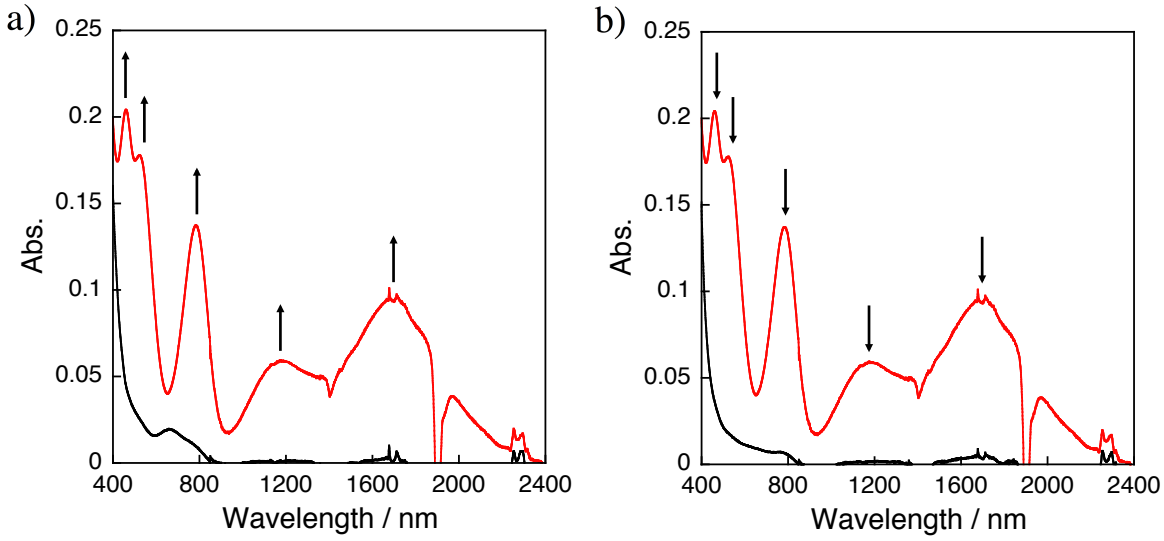


Figure 5. Changes in the absorption spectra of **1**·EtOH·H_2O (1 mM) in MeCN at a) –0.9 V vs. Ag/Ag^+ for t = 0 (black line) and t = 21 min (red line), b) –1.3 V for t = 0 (red line) and t = 21 min (black line) after electrolysis at –0.9 V for t = 21 min. All spectra were recorded under an atmosphere of N_2 using 0.1 M n-Bu_4NPF_6 as the supporting electrolyte.

at 540 (X = Br and Cl),[7a] or 536 nm (X = F).[13] It should be noted that the absorption spectrum of **1** during bulk electrolysis at –1.3 V (t = 21 min) after electrolysis at –0.9 V (t = 21 min) afforded a similar spectrum to that of **1** (Figure 5b), which suggests that the redox process between $[Cr^{III}(Mp)_3]^{3-}$ and $[Cr^{III}(Mp)_2(MSQ)]^{2-}$ is reversible (Scheme 1). These results in their entirety clearly demonstrate for the first time the reversible ligand-centered redox properties of Mp^{2-}.

During the bulk electrolysis of **2**·6H_2O at –0.74 V, new absorption bands emerged at λ = 458, 529, 782, 1093, and 1745 nm (Figure 6a). Theses bands resemble those of the electrochemically generated one-electron oxidized species of **1**, except for minor shifts of the absorption peak wavelengths, which should be attributed to binding interactions with one or more K^+ ions. These results unambiguously demonstrate a ligand-centered oxidation process of **2** (eq. 1).

$$[K_n\{\textit{fac}\text{-}Cr^{III}(Mp)_3\}]^{3-n} \underset{+(n-m)K^+ \; +e^-}{\overset{-e^- \; -(n-m)K^+}{\rightleftharpoons}} [K_m\{Cr^{III}(Mp)_2(MSQ)\}]^{2-m} \qquad \text{eq. 1}$$

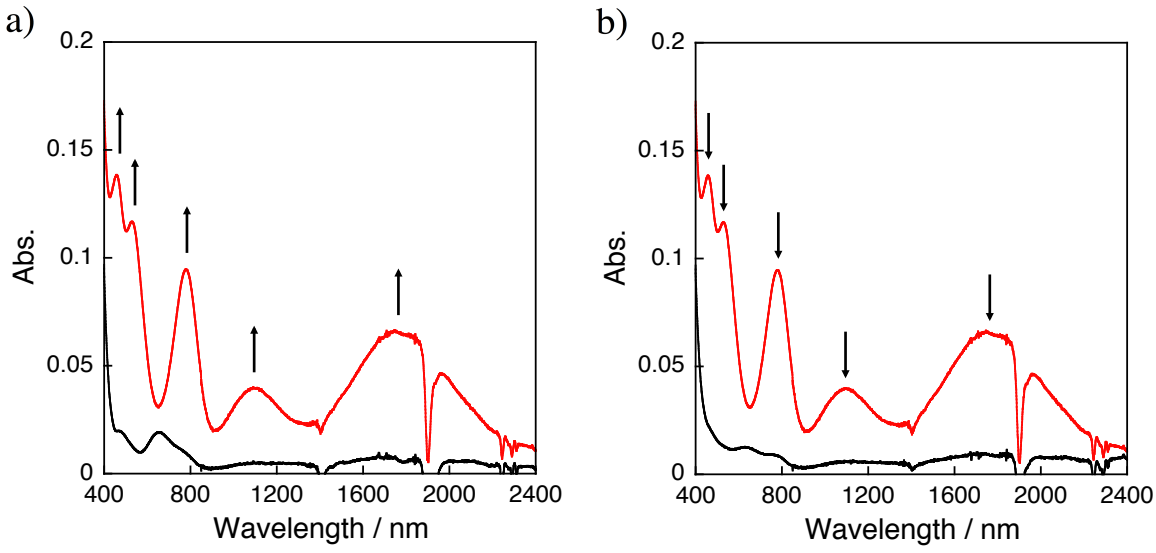
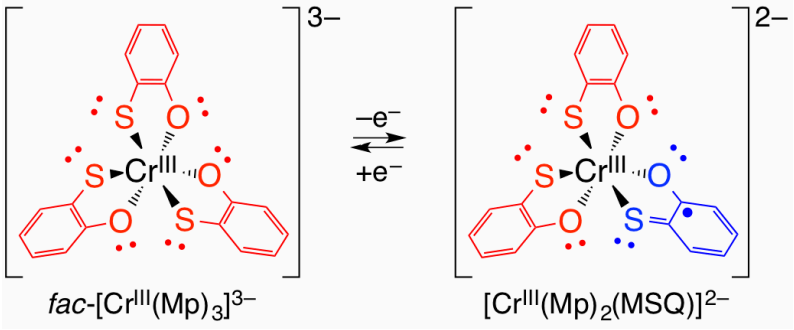


Figure 6. a) Changes in the absorption spectra of **2**·6H_2O (1 mM) at a) –0.72 V vs. Ag/Ag^+ for t = 0 (black line) and t = 21 min (red line), b) –1.2 V for t = 0 (red line) and t = 36 min (black line) after electrolysis at –0.72 V for t = 21 min. All spectra were recorded under an atmosphere of N_2 using 0.1 M n-Bu_4NPF_6 as the supporting electrolyte.

Scheme 1. Ligand-centered redox reactions in *fac*-$[Cr^{III}(Mp)_3]^{3-}$.



4-3-4. Interaction between 1 and Co^{2+} in Solution

Figure 7 shows the CVs of **1**·EtOH·H_2O (1 mM) upon addition of 0.25 and 0.5 equivalents of $Co(ClO_4)_2·6H_2O$ in MeCN; the electrochemical data upon addition of 0.5 equivalents $Co(ClO_4)_2·6H_2O$ are summarized in Table 5. Addition of 0.25 equivalents of Co^{2+} changed the CV of **1**, and a new redox couple emerged at –0.89 V vs. Ag/Ag^+ accompanied by a decrease of the original redox couple at –1.04 V (Figure 6b). The other irreversible oxidation waves of **1** were also changed upon the addition of Co^{2+}. Therefore, it may be concluded that *fac*-$[Cr^{III}(Mp)_3]^{3-}$interacts with Co^{2+} in solution. Upon addition of 0.5 equivalents of Co^{2+}, the

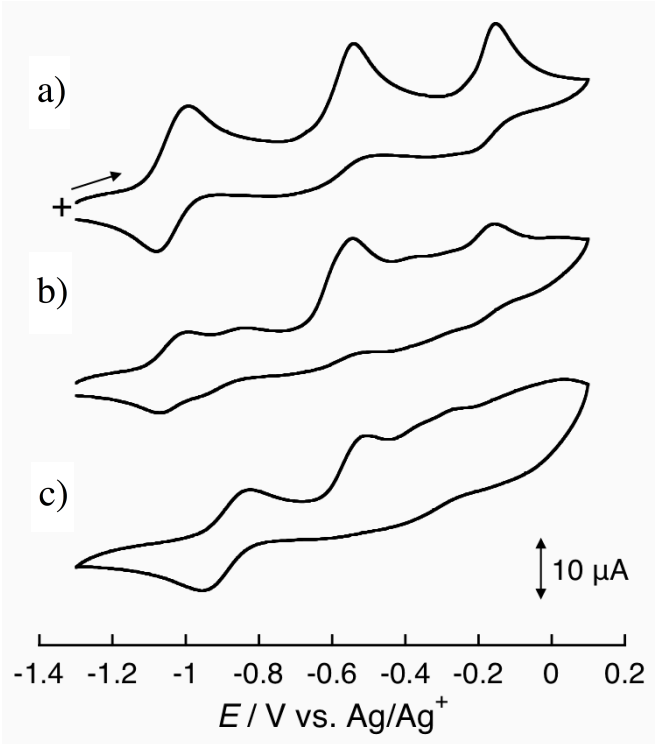


Figure 7. CVs of a) **1** (1 mM) in the presence of b) 0.25 and c) 0.5 equivalents of $Co(ClO_4)_2·6H_2O$ in MeCN; CVs were recorded at 50 mV s^{-1} under an atmosphere of N_2 using 0.1 M *n*-Bu_4NPF_6 as the supporting electrolyte.

new redox couple at –0.89 V increased, while the original redox couple completely disappeared (Figure 7c). This result is consistent with the formation of a 2:1 complex between *fac*-$[Cr^{III}(Mp)_3]^{3-}$ and Co^{2+}. Interestingly, the redox couples for **1** in the presence of 0.5 equivalents of Co^{2+} were decreased by almost 50% relative to those of neat **1**. Coulometry measurements on **1** (1.0 mM × 8.0 mL, 8.0 μmol) in the presence of 0.5 equivalents of Co^{2+}, revealed a charge count of –0.37 C by electrolysis at –0.78 V for t = 10 h (Figure 8), which suggests a transfer of 0.5 electrons. In other words, the complex, which consists of two molecules of *fac*-$[Cr^{III}(Mp)_3]^{3-}$ and one molecule of Co^{2+} exhibited a one-electron oxidation process that should occur on the ligand or on the Co center.

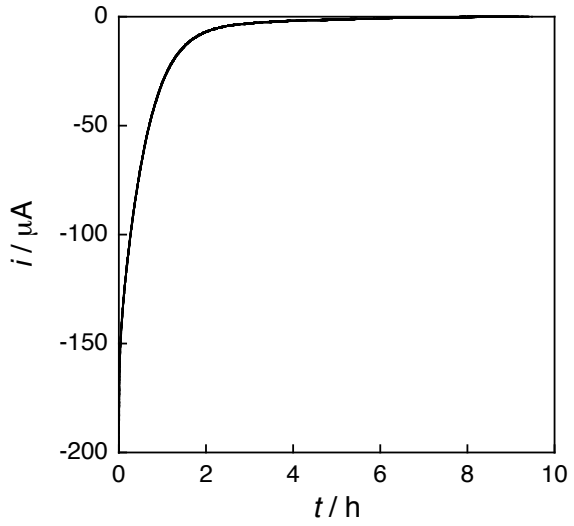


Figure 8. The *i-t* curve of **1** (1.0 mM, 8 mL) in the presence of 0.5 equivalents of $Co(ClO_4)_2 \cdot 6H_2O$ in MeCN electrolyzed at –0.78 V; recorded at under an atmosphere of N_2 using 0.1 M *n*-Bu_4NPF_6 as the supporting electrolyte.

Table 5. Electrochemical data for **1**·EtOH·H_2O and **1**·EtOH·H_2O in the presence of 0.5 eq. Co^{2+} in MeCN at 50 mV s^{-1}

	E / V vs. Ag/Ag^+							
Complex	E_{pa}^1	E_{pc}^1	$E_{1/2}^1(\Delta E)$	E_{pa}^2	E_{pa}^3	E_{pa}^4	E_{pa}^5	E_{pa}^6
1·EtOH·H_2O	–0.99	–1.08	–1.04 (0.09)	–0.55[a]	–0.16[a]			
1·EtOH·H_2O +0.5Co^{2+}	–0.82	–0.96	–0.89 (0.14)	–0.50[a]	–0.35[a, b]	–0.27[a]	–0.09[a, b]	0.04[a]

[a] Irreversible process. [b] Shoulder peak

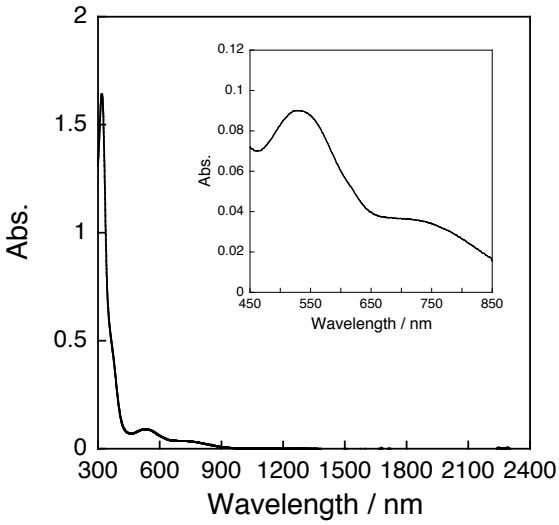


Figure 9. Absorption spectra of **1**·EtOH·H_2O (1 mM) in the presence of 0.5 equivalents of $Co(ClO_4)_2 \cdot 6H_2O$ in MeCN electrolyzed at –1.2 V vs. Ag/Ag^+; recorded under an atmosphere of N_2 using 0.1 M *n*-Bu_4NPF_6 as the supporting electrolyte.

In order to obtain further information on the redox center in the complex, spectroelectrochemical measurements were carried out on **1**·EtOH·H_2O in the presence of 0.5 equivalents of $Co(ClO_4)_2 \cdot 6H_2O$. Initially, the absorption spectrum of **1** with 0.5 equivalents of Co^{2+} electrolyzed at the rest potential (–1.2 V) exhibited four absorption bands at λ = 319, 375sh. 529, and 740sh. nm (Figure 9). The relatively strong band at 319 nm should be assigned to the

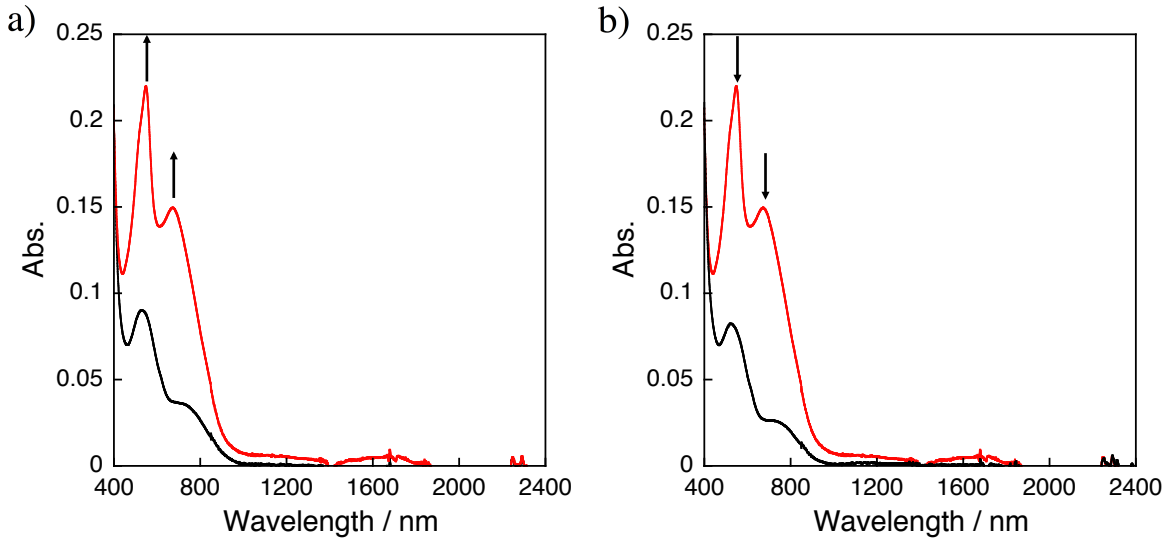


Figure 10. a) Changes in the absorption spectra of **1**·EtOH·H_2O (1 mM) upon addition of 0.5 equivalents of $Co(ClO_4)_2 \cdot 6H_2O$ in MeCN at a) –0.78 V vs. Ag/Ag^+ for t = 0 (black line) and t = 6 min (red line), b) –1.2 V for t = 0 min (red line) and t = 6 min (black line) after electrolysis at –0.78 V for t = 6 min; all spectra were recorded under an atmosphere of N_2 using 0.1 M *n*-Bu_4NPF_6 as the supporting electrolyte.

π-π* transition, but the relatively weak bands at 375sh., 529, and 740sh. nm should be assigned to d-d transitions on the Cr(III) and/or Co(II) centers. Additionally, the absence of IVCT bands contradicts a potential redox reaction between *fac*-$[Cr^{III}(Mp)_3]^{3-}$ and Co^{2+}. During bulk electrolysis at –0.78 V for t = 6 min, new absorption bands emerged in the visible region at λ = 512sh., 547, and 673 nm, whereas no absorption bands emerged in the NIR region (Figure 10a). The absence of absorption bands in the NIR region renders the formation of a $[Cr^{III}(Mp)_2(MSQ)]^{2-}$ species unlikely, although the generation of Co(III) as a result of a 0.5-electron oxidation is possible. It should be pointed out that the absorption spectrum of **1** in the presence of 0.5 equivalents of Co^{2+} electrolyzed at –1.2 V after electrolysis at –0.78 V for t = 6 min resembled that of the initial state (Figure 10b), indicating that the redox-process between **1** and 0.5 Co^{2+} and the corresponding oxidized species is reversible (eq. 2).

$$2\ \textit{fac}\text{-}[Cr^{III}(Mp)_3]^{3-} + Co^{2+} \longrightarrow [\{Cr^{III}(Mp)_3\}_2\text{–}Co^{2+}]^{4-} \quad \underset{+e^-}{\overset{-e^-}{\rightleftharpoons}} \quad [\{Cr(C_6H_4OS)_3\}_2\text{–}Co]^{3-} \qquad \text{eq. 2}$$

4-3-5. Crystal Structure and Identification of 3·30H_2O

In order to determine the structure of the complex that contains *fac*-$[Cr^{III}(Mp)_3]^{3-}$ and Co^{2+}, a crystallization experiment was carried out. Slow diffusion of aqueous solutions of **2** and $CoCl_2 \cdot 6H_2O$ afforded purple single crystals of **3**·30H_2O after standing for one week. The single-crystal X-ray diffraction analysis of these crystals revealed that the unit cell of **3**·30H_2O contained two trinuclear units (**A** and **B**), each consisting of two molecules of *fac*-$[Cr^{III}(Mp)_3]^{3-}$ and one Co^{2+} ion (Figure 11). The **A** and **B** units exhibited a common structure, *i.e.* two molecules of *fac*-$[Cr(C_6H_4OS)_3]^n$ are selectively bound the Co^{2+} ion *via* the S sites of *fac*-$[Cr(C_6H_4OS)_3]^n$. The Co center thus adopts octahedral coordination geometry and is located on an inversion center. The unit **A** is a discrete trinuclear complex, but **B** coordinates K^+ *via* the O sites to form a 1-D coordination polymer (Figure 12), in which the K^+ cations are coordinated to $[Co^{II}(H_2O)_6]^{2+}$ counter cations *via* H_2O ligands. Moreover, hydrogen bonds were observed between the O sites of **B** and the aquo ligands on the $[Co^{II}(H_2O)_6]^{2+}$ counter ions,

resulting in the formation of 2-D sheets. At this stage, the formula of **3** may then be summarized as $[Co^{II}(H_2O)_6]_2[K_2\{Co\{fac\text{-}Cr(C_6H_4OS)_3\}_2\}][Co\{fac\text{-}Cr(C_6H_4OS)_3\}_2]$.

In order to gain further information on the electronic distribution of **3**·30H_2O, absorption spectrum of **3**·30H_2O in the solid state was recorded and is shown in Figure 13. The spectrum revealed absorption bands at λ = 290sh., 345sh., 470sh., 500sh., 560, and 750sh. nm, whereas no absorption bands were observed in the NIR region. These results contradict a mixed-valence state of ligands in **3**·30H_2O. In other words, the six molecules of C_6H_4OS should have the same oxidation state, *i.e.* Mp^{2-}, MSQ^{-}, or MBQ. The observed Cr–O (**A**: 1.960-1.985(5) Å, **B**: 1.967-1.986(4) Å) and Cr–S bond distances (**A**: 2.356-2.376(2) Å, **B**: 2.356-2.374(2) Å) are similar to those of **1**·EtOH·H_2O and **2**·6H_2O, thus indicating a Cr(III)

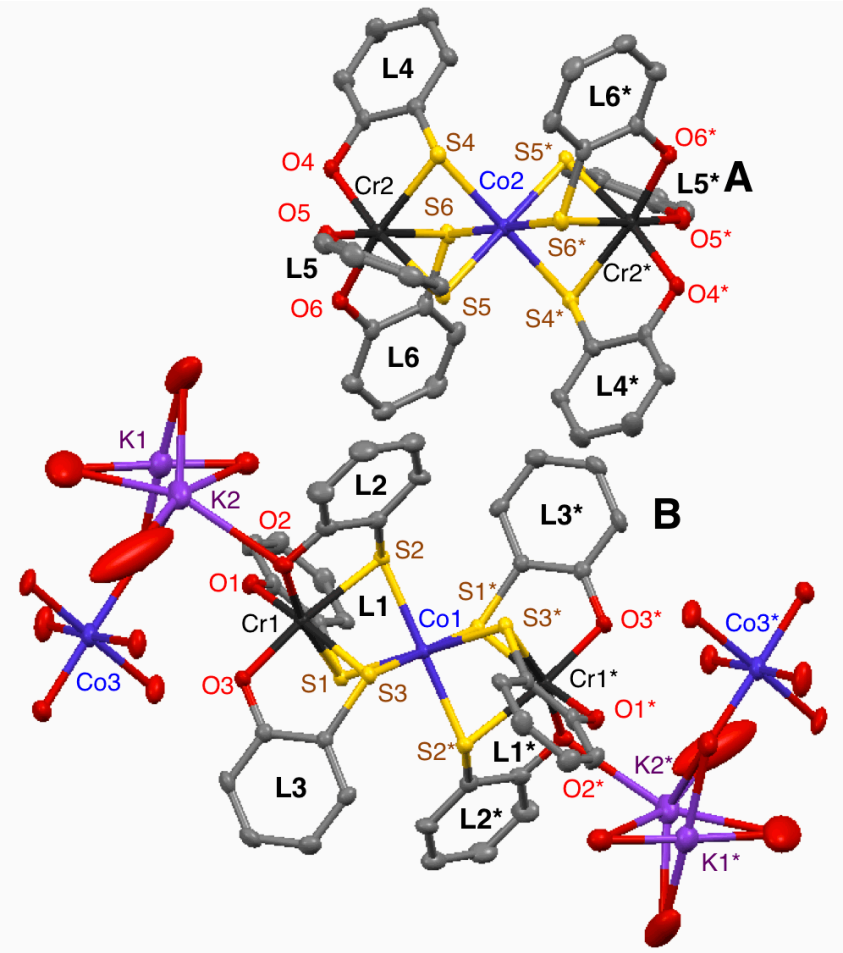


Figure 11. Structure of **3**·30H_2O with atomic displacement parameters set at 50% probability; color code: Cr = black, Co = blue, K = purple O = red, S = yellow, and C = gray; all hydrogen atoms are omitted for clarity and only selected atoms are labeled. The K1/K2 atom is disordered over two positions with a relative occupancy of 0.5:0.5.

center. Both the C–O (**A**: 1.353-1.357(7) Å, **B**: 1.345-1.361(8) Å) and the C–S bond distances (**A**: 1.769-1.785(6), **B**: 1.761-1.783(6) Å) clearly indicate single bond character, while the C–C bond distances in all six-membered rings suggest aromaticity. Therefore, all C_6H_4OS ligands in **3**·30H_2O should be assigned an Mp^{2-} structure. In addition, the observed Co–S bond distances (**A**: 2.301-2.319(1) Å, **B**: 2.300-2.321(1) Å) are very similar to those of previously reported Co(III)–S bond distances (2.2853-2.3069(9) Å) in *fac*-O_3S_3 coordination geometry.[33] Thus, **3** is probably best described as $[Co^{II}(H_2O)_6]_2[K_2\{Co^{III}\{fac\text{-}Cr^{III}(Mp)_3\}_2\}][Co^{III}\{fac\text{-}Cr^{III}(Mp)_3\}_2]$. The $[Co^{III}\{fac\text{-}Cr^{III}(Mp)_3\}_2]^{2-}$ moiety should be considered as the 0.5-electron oxidation product of **1** in the presence of 0.5 equivalents of Co^{2+}. Thus, eq. 2 should be modified to eq. 3, taking a guest metal-centered redox process into account.

$$2\ fac\text{-}[Cr^{III}(Mp)_3]^{3-} + Co^{2+} \longrightarrow [\{Cr^{III}(Mp)_3\}_2\text{–}Co^{2+}]^{4-}$$
$$[\{Cr^{III}(Mp)_3\}_2\text{–}Co^{2+}]^{4-} \underset{+e^-}{\overset{-e^-}{\rightleftharpoons}} [Co^{III}\{fac\text{-}Cr^{III}(Mp)_3\}_2]^{3-} \qquad \text{eq. 3}$$

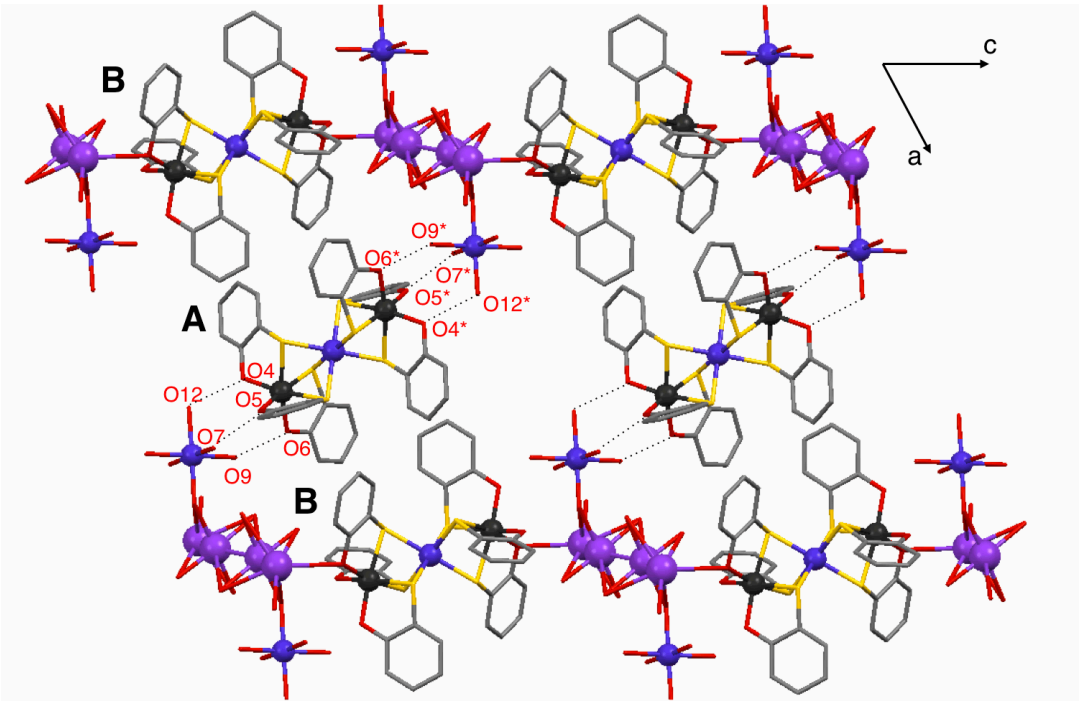


Figure 12. Solid state structure of the 1-D coordination polymer and 2-D sheet structure of **3**·30H_2O (ball-and-stick plots); color code: Cr = black, Co = blue, K = purple O = red, S = yellow, and C = gray; all hydrogen atoms are omitted for clarity and only selected atoms are labeled. K^+ cations are disordered over two positions with a relative occupancy of 0.5:0.5.

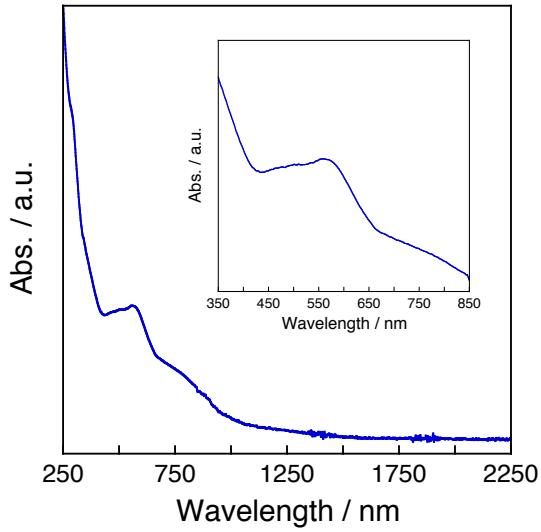


Figure 13. Absorption spectrum of **3**·30H_2O in the solid state (KBr). The inset shows a magnification of the 300-900 nm region.

4-4. Conclusions

In summary, this chapter described the coordination of K^+ and $Co^{2+/3+}$ guest metal ions by the RML *fac*-$[Cr^{III}(Mp)_3]^{3-}$, which exhibits reversible ligand-centered one-electron oxidation properties. The RML binds three molecules of K^+ *via* its O and S sites to form 2-D honeycomb structure **2**. Conversely, Co^{3+} is selectively bounded *via* the S sites of two RMLs, resulting in the formation of **3**, which exhibits a trinuclear structure $[Co^{III}\{fac\text{-}Cr^{III}(Mp)_3\}_2]^{2-}$. Binding mode of the RML can be controlled by the nature of guest metal ions. While **2** displayed a ligand-centered reversible one-electron oxidation in MeCN, the one-electron oxidation of the 2:1 complex between RML and Co^{2+} generated a $[Co^{III}\{fac\text{-}Cr^{III}(Mp)_3\}_2]^{2-}$ species, indicating a guest metal-centered redox process. This chapter thus demonstrated for the first time that *fac*-$[Cr^{III}(Mp)_3]^{3-}$ is able to act as a RML with ligand-centered redox properties, in which the assembled structures and redox centers are tunable by the binding with guest metal ions.

4-5. References

1. a) M. A. Reed, C. Zhou, C. J. Muller, T. P. Burgin, J. M. Tour, *Science*, **1997**, *278*, 252; b) C. Joachim, J. K. Gimzewski, A. Aviram, *Nature*, **2000**, *408*, 541.
2. a) P. Du, R. Eisenberg, *Energy. Environ. Sci.,* **2012**, *5*, 6012; b) A. J. Esswein, D. G. Nocera, *Chem. Rev.,* **2007**, *107*, 4022.
3. B. Keita, L. Nadjo, *J. Electroanal. Chem.*, **1987**, *227*, 77.
4. J. A. Baumann, D. J. Salmon, S. T. Wilson, T. J. Meyer, *Inorg. Chem.*, **1978**, *17*, 3342.
5. A. K. Diallo, J.-C. Daran, F. Varret, J. Ruiz, D. Astruc, *Angew. Chem. Int. Ed.,* **2009**, *48*, 3141.
6. a) C. G. Pierpont, *Inorg. Chem.,* **2011**, *50*, 9766; b) P. Zanello, M. Corsini, *Coord. Chem. Rev.,* **2006**, *250*, 2000.
7. a) H.-C. Chang, H. Miyasaka, S. Kitagawa, *Inorg. Chem.,* **2001**, *40*, 146; b) H.-C. Chang, T. Ishii, M. Kondo, S. Kitagawa, *J. Chem. Soc. Dalton Trans.,* **1999**, 2467; c) H. H. Downs, R. M. Buchanan, C. G. Pierpont, *Inorg. Chem.,* **1979**, *18*, 1736.
8. T. Wada, K. Tsuge, K. Tanaka, *Inorg. Chem.,* **2001**, *40*, 329.
9. a) P. Chaudhuri, M. Hess, J. Müller, K. Hildenbrand, E. Bill, T. Weyhermüller, K. Wieghardt, *J. Am. Chem. Soc.,* **1999**, *121*, 9599; b) C. Mukherjee, U. Pieper, E. Bothe, V. Bachler, E. Bill, T. Weyhermüller, P. Chaudhuri, *Inorg. Chem.,* **2008**, *47*, 8943; c) C. Mukherjee, T. Weyhermüller, E. Bothe, P. Chaudhuri, *Inorg. Chem.,* **2008**, *47*, 11620; d) S. E. Balaghi, E. Safaei, L. Chiang, E. W. Y. Wong, D. Savard, R. M. Clarke, T. Storr, *Dalton Trans.,* **2013**, *42*, 6829.
10. a) M. R. Ringenberg, S. L. Kokatam, Z. M. Heiden, T. B. Rauchfuss, *J. Am. Chem. Soc.,* **2008**, *130*, 788; b) M. R. Ringenberg, M. J. Nilges, T. B. Rauchfuss, S. R. Wilson, *Organometallics,* **2010**, *29*, 1956.
11. A. L. Smith, K. I. Hardcastle, J. D. Soper, *J. Am. Chem. Soc.,* **2010**, *132*, 14358.
12. T. Matsumoto, H.-C. Chang, A. Kobayashi, K. Uosaki, M. Kato, *Inorg. Chem.,* **2011**, *50*,

2859.

13. M. Wakizaka, T. Matsumoto, A. Kobayashi, M. Kato, H.-C. Chang, *Dalton Trans.,* **2015**, *44*, 14304.
14. B.-S. Kang, M.-C. Hong, T.-B. Wen, H.-Q. Liu, J.-X. Lu, *J. Clust. Sci.,* **1995**, *6*, 379.
15. P. R. Klich, A. T. Daniher, P. R. Challen, *Inorg. Chem.,* **1996**, *35*, 347.
16. P. R. Challen, D. H. Peapus, K. A. Mabnus, *Polyhedron,* **1997**, *16*, 1447.
17. B.-S. Kang, X.-J. Wang, C.-Y. Su, H.-Q. Liu, *Transit. Met. Chem.,* **1999***, 24*, 712.
18. T.-B. Wen, B.-S. Kang, C.-Y. Su, D.-X. Wu, L.-G. Wang, S. Liao, H.-Q. Liu, *Bull. Chem. Soc. Jpn.,* **1998**, *71*, 2339.
19. Y.-H. Hu, L.-H. Weng, B.-S. Kang, *Jiego Huaxue*, **1991**, *10*, 84.
20. R. R. Holmes, S. Shafieezad, V. Chandrasekhar, A. C. Sau, J. M. Holmes, R. O. Day, *J. Am. Chem. Soc.,* **1988**, *110*, 1168.
21. B.-S. Kang, L.-H. Weng, H.-Q. Liu, D. Wu, L. Huang, C. Lu, J. Cai, X. Chen, J. Lu, *Inorg. Chem.,* **1990**, *29*, 4873.
22. B. Zhuang, L. Huang, L. He, P. Yu, A. Lan, J. Lu, *Inorg. Chim. Acta,* **1991**, *179*, 179.
23. T. Matsumoto, M. Wakizaka, H. Yano, A. Kobayashi, H.-C. Chang, M. Kato, *Dalton Trans.,* **2012**, *41*, 8303.
24. M. C. Burla, R. Caliandro, M. Camalli, B. Carrozzini, G. L. Cascarano, L. De Caro, C. Giacovazzo, G. Polidori, R. Spagna, *J. Appl. Crystallogr.,* **2005**, *38*, 381.
25. CrystalStructure 3.8.2, Crystal Structure Analysis Package; Rigaku and Rigaku/MSC: The Woodlands, TX, 2000-2006.
26. G. Sheldrick, SHELX-97 Program for Crystal Structure Solution and the Refinement of Crystal Structures, Institüt für Anorganische Chemie der Universität Göttingen, Tammanstrasse 4, D-3400 Göttingen, Germany, 1997.
27. T.-B. Wen, J.-C. Shi, Q.-T. Lin, B.-S. Kang, B.-M. Wu, T. C. W. Mak, *Acta Cryst.,* **1996**, *C52*, 1240.
28. R. G. Pearson, *J. Am. Chem. Soc.,* **1962**, *84*, 3533.

29. a) F. Morishima, R. Kusaka, Y. Inokuchi, T. Haino, T. Ebata, *J. Phys. Chem. B,* **2015**, *119*, 2557; b) M. C. Capello, M. Broquier, S. Ishiuchi, W. Y. Sohn, M. Fujii, C. Dedonder-Lardeux, C. Jouvet, G. A. Pino, *J. Phys. Chem. A,* **2014**, *118*, 2056.
30. S. R. Sofen, D. C. Ware, S. R. Cooper, K. N. Raymond, *Inorg. Chem.,* **1979**, *18*, 234.
31. a) A. F. Shojaei, M. Alirezvani, M. Heravi, *J. Serb. Chem. Soc.,* **2011**, *76*, 955; b) H. Golchoubian, F. Hosseinpoor, *Catal. Commun.,* **2007**, *8*, 697.
32. R. Colorado-Peralta, M. Sanchez-Vazquez, I. F. Hernández-Ahuactzi, S. A. Sánchez-Ruiz, R. Contreras, A. Flores-Parra, S. E. Castillo-Blum, *Polyhedron,* **2012**, *48*, 72.
33. N. Amir, M. Motonishi, M. Fujita, Y. Miyashita, K. Fujisawa, K. Okamoto, *Eur. J. Inorg. Chem.,* **2006**, 1041.

Chapter 5

Nonprecious-Metal-Assisted Photochemical Hydrogen Production from *ortho*-Phenylenediamine

Abstract

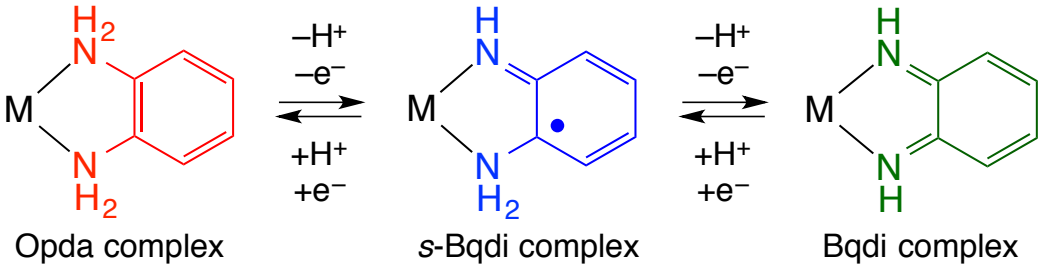
The combination of *o*-phenylenediamine (Opda), which possesses two proton- and electron-pooling capability, with Fe(II) leads to the photochemical hydrogen evolution reaction (PHER) in tetrahydrofuran (THF) at room temperature without addition of photosensitizers. From the THF solution, the tris-Opda iron(II) complex, $[Fe^{II}(Opda)_3](ClO_4)_2$ (**1**), was isolated as a photoactive species, while the deprotonated oxidized species was characterized by X-ray crystallographic analysis, electrospray ionization-mass spectrometry, and UV-vis-NIR spectra. Furthermore, the PHER is catalyzed by hydroquinone, which serves as a H^+/e^- donor. The present chapter demonstrates that the use of a metal-bound aromatic amine as a H^+/e^- pooler opens an alternative strategy for designing nonprecious-metal-based molecular photochemical H_2 production/storage materials.

5-1. Introduction

Energy is the most important issue in the 21st century.[1] The growing global energy demand, decreasing fossil fuel supply, and increased concerns over climate issues have spurred the development of alternative and sustainable energy carriers.[2] Among the several types of energy carriers,[3] molecular hydrogen is one of the most promising and cleanest energy carriers with the least effect on the environment.[4] Therefore, the creation of hydrogen production/storage systems is currently the subject of intensive investigations.[5] The development of materials for hydrogen production/storage has been investigated using a wide range of materials, such as metal hydride,[6] complex hydride,[7] chemical hydride,[8] clathrates,[9] inorganic nanotubes,[10] organic nanotubes,[11] and metal-organic frameworks.[5a,12] In particular, organic hydrides are fascinating hydrogen production/storage materials that have excellent values for gravimetric capacities (*e.g.*, 7.1 wt% H_2, 64.8 kg/m^3 for benzene/cyclohexane conversion).[5b] Recently, quinoline/1,2,3,4-tetrahydro quinoline[13] or secondary alcohol/ketone[14] systems have been reported as efficient hydrogen production/storage material that can be operated at relatively low temperatures (*ca.* 80-140 °C), especially in the hydrogen-evolution reaction (HER) processes, using Ir complexes as a catalyst. However, even in these excellent examples, the operating temperature for the HER is higher than those of hydrogenation-reaction processes. Therefore, the creation of a HER that can be driven at moderate temperature[15] with the use of nonprecious-metal catalysts[16] is an important issue to be investigated.

These considerations inspired us to utilize an organic skeleton possessing multi proton- and electron-pooling capability. The aromatic amines or hydroxides, such as phenylenediamine[17] or hydroquinone[18] derivatives, are widely known to possess $2H^+/2e^-$ pooling capability. Furthermore, *o*-phenylenediamine (Opda) has a coordinating ability toward transition metal ions and undergoes multi proton- and electron-transfer processes to produce the corresponding oxidized species, such as *semi*-benzoquinodiimine (*s*-Bqdi) or *o*-benzoquinodiimine (Bqdi)

Chart 1. H^+ and e^- Pooling Activity of Opda Complexes.



complexes.[19] Therefore, they should be fascinating candidates as building modules for multi proton- and electron-pooling materials (Chart 1).

The ultra-fast dynamics of N–H σ-bond activation pathways were previously investigated for aromatic amines, such as aniline, using several spectroscopic and theoretical techniques.[20] In these reactions, it was elucidated that the generation of transient anilino radical species ($C_6H_5NH\cdot$) *via* hydrogen atom elimination was initiated by photo-excitation of π-π* transition through 3s Rydberg states of the nitrogen atoms. Similar photoreactions were also investigated for aromatic diamines, such as Opda and *p*-phenylenediamine.[21] In these cases, transient Bqdi and *p*-benzoquinodiimine intermediates were detected by infrared spectra, as the results of photochemical N–H σ-bond activations and hydrogen atom eliminations. These studies prompted us to investigate the photoreaction of Opda interacting with nonprecious metal ions, where the photoreactivity of Opda is expected to be influenced by the metal ions. This chapter described the structure, multiple H^+/e^- transfer reactions, and photochemical hydrogen evolution reaction (PHER) utilizing $[Fe^{II}(Opda)_3](ClO_4)_2$ (**1**), which can be isolated by a one-pot reaction between three equivalents of Opda and Fe(II) ion.

5-2. Experimental Section

General Procedures. All synthetic operations and measurements were performed under a N_2 atmosphere using Schlenk-line techniques. $[Fe^{II}(H_2O)_6](ClO_4)_2$ was purchased from Aldrich. Opda and hydroquinone (HQ) were purchased from Wako Pure Chemical Industries and used as received. Deuterated Opda ($C_6H_4N_2D_4$) and HQ ($C_6H_4O_2D_2$) were prepared according to conventional methods. *n*-Hexane and tetrahydrofuran (THF) were purchased from Kanto Chemical Co. Inc. and distilled twice from Na metal under a N_2 atmosphere. Dichloromethane (CH_2Cl_2), *tert*-butyl alcohol (*t*-BuOH), methanol (MeOH), and toluene were purchased from Wako Pure Chemical Industries and used without purification. All of the solvents were finally degassed in at least four freeze-pump-thaw cycles just prior to use. Molecular sieves 4A (MS4A) were purchased from Wako Pure Chemical Industries and activated by heating in vacuo prior to use. **Caution!** Although we experienced no difficulties with the perchlorate salts, they should be regarded as potentially explosive, and therefore handled with care.

$[Fe^{II}(Opda)_3](ClO_4)_2$·THF (1·THF). *n*-Hexane/THF mixed solvent (*v* : *v* = 2 : 1) (20 mL) was layered onto a colorless THF solution (10 mL) of $[Fe^{II}(H_2O)_6](ClO_4)_2$ (1.09 g, 3 mmol). Then, colorless *n*-hexane/THF (*v* : *v* = 1 : 1) solution (30 mL) of Opda (975 mg, 9 mmol) was layered on this solution. Storage of the mixture for 4 d at room temperature afforded crystals suitable for X-ray crystallographic analysis. After filtration and washing with THF (2 mL × 2), drying *in vacuo*, afforded **1**·THF as colorless crystals in 36% yield. Anal. Found: C, 40.49; H, 4.91; N, 12.77. Calc. for $C_{22}H_{32}Cl_2FeN_6O_9$ (**1**·THF): C, 40.57; H, 4.94; N, 12.90. $\chi_M T_{300K}$ = 3.96 emu·K·mol^{-1}.

$[Fe^{II}(Bqdi)_3](ClO_4)_2$·THF (2·THF).[19b] The complex **1**·THF (912 mg, 1.4 mmol) was dissolved in CH_2Cl_2/*t*-BuOH mixed solvent (*v* : *v* = 1 : 1) (50 mL) to afford a white suspension, with the co-presence of MS4A (20 g). O_2 gas was slowly introduced to this suspension and the color of the suspension changed to navy after 5 min, and to dark navy after 1 h. After bubbling O_2 for 5

h, the color of the suspension was finally bright green. The MS4A was removed by filtration and the green product was extracted using MeOH (40 mL × 2). After evaporation of the solvent, a dark-green powder was obtained and washed with THF (15 mL) and toluene (10 mL × 2). Drying *in vacuo* afforded **2** as a greenish purple powder in 38% yield. ^{1}H NMR (270 MHz, CD_3CN, 298 K) *d* 6.95-6.99 (m, 6H), 7.06-7.10 (m, 6H), 11.75 (br s, 6H). Diamagnetic. Anal. Found: C, 39.76; H, 4.02; N, 12.49. Calc. for $C_{22}H_{28}Cl_2FeN_6O_{10}$ (**2**·THF + H_2O): C, 39.84; H, 4.26; N, 12.67. For synthesis of a crystalline sample suitable for X-ray crystallographic analysis, this powder sample (5 mg) was dissolved in THF (2.5 mL), then *n*-hexane (2.5 mL) was layered onto this solution. After storage of this solution for 5 d at room temperature, greenish-purple crystals of **2**·THF were obtained.

Opda-d_4. D_2O (2 mL, 0.1 mol) was added to the $CDCl_3$ (3 mL) solution of Opda (50 mg, 0.46 mmol), and stirred for 30 min. Then D_2O was removed by decantation from this biphasic reaction mixture. After repeating this procedure twice, disappearance of the ^{1}H NMR ($CDCl_3$) signal corresponding to the amino proton in Opda was confirmed. After evaporation of $CDCl_3$ and D_2O, Opda-d_4 was purified by sublimation as colorless crystals.

HQ-d_2. HQ (1 g, 9.08 mmol) was added to D_2O (5 mL, 275 mmol) and the white suspension was heated at 90 °C for 10 min. The pale pink solution was cooled at room temperature and a slightly pink-colored white powder was obtained. After removal of D_2O by decantation and drying *in vacuo*, D_2O (5 mL) was added to these crystals and the same procedures were repeated. After removal of D_2O, pink-colored white powder was washed with D_2O (2 mL) and dried *in vacuo*.

Equipment Used in PHERs. A 100 W xenon lamp (LAX-103, Asahi Spectra Co., Ltd) was used as the light source with quartz light guide (ϕ5 × 1000L UD0030). For PHER under irradiation or in the dark, 500 W xenon lamp (SX-UI500XQ, Ushio Inc.) with a quartz light

guide (GFQ5L1000) was used as the light source. The light intensity was measured using a power meter (NOVA, Ophir Optronics Ltd) and a thermopile sensor (3A, Ophir Optronics Ltd). The amount of photochemically evolved H_2 was determined using a gas chromatograph (GC) (Shimadzu GC-14B, Ar carrier) equipped with a ShinCarbon ST 2 m long packed column (Shinwa Chemical Industries Ltd) and a recorder (Shimadzu C-R8A Chromatopac Data Processor). For H_2/HD/D_2 detections, the gas samples were analyzed using a GC (Shimadzu GC-2014ATF+GC Solution, He carrier) equipped with 8% (*w* / *w*) KOH coated on an activated alumina column, that was immersed in liquid N_2 during the GC measurements, and thermal conductivity detector.

PHERs. For photochemical hydrogen evolution, each sample was prepared in a hand-made Schlenk flask-equipped quartz cell 182 mL in volume. For PHER from Opda without Fe^{2+}, Opda (25.9 mg, 2.39×10^{-4} mol) was dissolved in 4 mL of THF in the presence of ground MS4A (250 mg) under a N_2 atmosphere. On the other hand, for the reaction from Opda in the presence of Fe^{2+}, THF (4 mL) solution of $[Fe^{II}(H_2O)_6](ClO_4)_2$ (28.9 mg, 7.98×10^{-5} mol) was introduced to the Opda (25.9 mg, 2.39×10^{-4} mol) in the presence of ground MS4A (250 mg) under a N_2 atmosphere. Each sample flask was doubly sealed with rubber septa. Before irradiation, gas (0.3 mL) was collected from the headspace using a gas-tight syringe (Tokyo Garasu Kikai Co. Ltd) and analyzed by GC to confirm the successful N_2 purge. Then, the samples were irradiated using the 100 W xenon lamp in a water bath at room temperature. The gas samples (0.3 mL) were collected from the headspace at each analysis time for determination of the amount of H_2 evolved as a function of the irradiation time.

PHER with HQ. For photochemical H_2 evolution from 3Opda/$[Fe^{II}(H_2O)_6](ClO_4)_2$ /10HQ/THF suspension, the same reaction systems as the aforementioned cases were used, but the sample preparation procedures were different from those cases. The THF (2 mL) solution of $[Fe^{II}(H_2O)_6](ClO_4)_2$ (28.9 mg, 7.98×10^{-5} mol) was added to the Opda (25.9 mg, 2.39×10^{-4}

mol) in the presence of ground MS4A (250 mg) under a N_2 atmosphere, and stirred for 30 s at room temperature. A THF solution (2 mL) of HQ (87.9 mg, 7.98×10^{-4} mol) was added to this white suspension. In these cases, no special changes were noticed in the appearance of the suspension. After the sample preparation, PHERs were investigated by similar methods to those mentioned above.

PHER Using Opda in THF-d_8. For PHER, the sample was prepared in a quartz cell equipped with a three-way cock and aluminum gas sampling bag (GL Sciences Inc., AAK-1L) in which the quartz cell head is *ca*. 10 mL in volume. $[Fe^{II}(H_2O)_6](ClO_4)_2$ (21.7 mg, 5.99×10^{-5} mol) was dissolved in the degassed THF-d_8 (3 mL), and this solution was introduced to the Opda (19.4 mg, 1.79×10^{-4} mol) in the presence of MS4A (190 mg) under a N_2 atmosphere. Before irradiation, the three-way cock and stopcock of the gas sampling bag were opened to connect the sample and aluminum gas bag to introduce the evolved H_2 into the bag. Then, the samples were irradiated in a water bath at room temperature. After the irradiation for 50 h, three-way cock and stopcock of gas sampling bag were closed and gas sample in the bag was analyzed.

PHER Using Opda-d_4 in THF. The general operating procedures were the same as with those for PHER using THF-d_8, except for using $[Fe^{II}(H_2O)_6](ClO_4)_2$ (28.9 mg, 7.98×10^{-5} mol), Opda-d_4 (25.9 mg, 2.39×10^{-4} mol), and THF (4 mL) in the presence of MS4A (250 mg).

PHER Using HQ-d_2. $[Fe^{II}(H_2O)_6](ClO_4)_2$ (28.9 mg, 7.98×10^{-5} mol) was dissolved in degassed THF (2 mL), and this solution was added to the Opda (25.9 mg, 2.39×10^{-4} mol) in the presence of MS4A (250 mg) under a N_2 atmosphere. Then, a THF (2 mL) solution of HQ-d_2 (89.4 mg, 7.98×10^{-4} mol) was added to this suspension. The photochemical reaction and evolved gas analysis were carried out using similar procedures to those used for $[Fe^{II}(H_2O)_6](ClO_4)_2$ and Opda in THF-d_8, except for the irradiation time (200 h).

Apparent Quantum Yield (Φ) Calculation. The THF suspension of **1** was irradiated at λ = 298 nm using a Xe lamp equipped with UVA-type mirror module (250 nm ≤ λ ≤ 480 nm) and HQBP300-UV-type band-pass filter (central wavelength: 298.06 nm, half bandwidth: 10.40 nm). The amount of hydrogen evolved (66.67 μL, 2.726×10^{-6} mol) in the subsequent 15 h was used to calculate the apparent quantum yield (Φ) using the equation below (eq. 1).[22]

$$\Phi = N_e/N_p = 2N_{H2}/N_p \qquad \text{eq. 1}$$

Here, N_e stands for the number of reacted electrons, N_{H2} is the number of the evolved H_2 molecules, and N_p is the number of incident photons. The value of Φ was calculated as 3.39% after irradiation (optical intensity: 1.33 mW) for 15 h based on the amount of photochemically evolved H_2 (2.726×10^{-6} mol).

Computational Details. Geometry optimization for $[Fe^{II}(Opda)_3]^{2+}$, Opda, and $[Fe^{II}(Bqdi)_3]^{2+}$ in the electronic ground state (S_0) was carried out in THF employing density functional theory (DFT) with the B3LYP combination of exchange and correlation functionals. The initial structures of $[Fe^{II}(Opda)_3]^{2+}$ and $[Fe^{II}(Bqdi)_3]^{2+}$ were taken from the X-ray crystallographic data. No symmetry constraints were imposed for $[Fe^{II}(Opda)_3]^{2+}$ and Opda, while C_3 symmetry was used for $[Fe^{II}(Bqdi)_3]^{2+}$. The spin multiplicities were set to quintet for $[Fe^{II}(Opda)_3]^{2+}$ and singlet for $[Fe^{II}(Bqdi)_3]^{2+}$ and Opda. The solvent effects were taken into account by the polarizable continuum solvation model (PCM)[23] and the radii were taken from the UFF force field.[24] The SDD effective core potential (ECP) and associated basis set was used for the Fe atom, and a 6-31G(d) basis set is employed for all other atoms. After the geometry optimization, the time-dependent (TD) DFT calculations[25] were performed to evaluate the vertical excitation energies at the equilibrium structures in THF employing the BLYP functionals with the long-range correction (LC)[26] (LC-BLYP). The basis set for C and N atoms was replaced by 6-31+G(d) in TD-DFT calculations to account for the Rydberg states in

Opda. All calculations were performed using the Gaussian 09 package.[27] The Cartesian coordinates of $[Fe^{II}(Bqdi)_3]^{2+}$, $[Fe^{II}(Opda)_3]^{2+}$, and Opda are given in Tables 1-3.

Table 1. Cartesian Coordinates (in Å) of $[Fe^{II}(Bqdi)_3]^{2+}$ in THF Optimized by DFT (B3LYP)

	x	*y*	*z*
Fe	0.0000	0.0000	0.0011
N	−0.5434	1.5616	1.0658
N	−1.6518	−0.0613	−1.0640
N	−1.0807	−1.2514	1.0658
N	0.7729	1.4612	−1.0640
N	1.6241	−0.3102	1.0658
N	0.8790	−1.3999	−1.0640
C	−0.1882	2.7392	0.6325
C	−0.4685	4.0213	1.2284
C	0.0000	5.1401	0.6155
C	−2.6194	−0.8216	−0.6323
C	−3.9150	−1.0276	−1.2295
C	−4.7863	−1.8723	−0.6179
C	−4.4515	−2.5700	0.6155
C	−3.2483	−2.4164	1.2284
C	−2.2781	−1.5326	0.6325
C	0.5982	2.6793	−0.6323
C	1.0675	3.9043	−1.2295
C	0.7717	5.0812	−0.6179
C	2.4663	−1.2066	0.6325
C	3.7168	−1.6049	1.2284
C	4.4515	−2.5700	0.6155
C	4.0146	−3.2089	−0.6179
C	2.8475	−2.8767	−1.2295
C	2.0212	−1.8576	−0.6323
H	1.6433	3.8671	−2.1491
H	1.1143	6.0160	−1.0503
H	4.0476	−1.1324	2.1481
H	5.3961	−2.8859	1.0468
H	4.6528	−3.9730	−1.0503
H	2.5274	−3.3567	−2.1491
H	0.5364	−1.8274	−1.9244
H	1.8978	0.1632	1.9268
H	−0.8075	−1.7251	1.9268
H	−1.8507	0.4491	−1.9244
H	−1.0902	1.5619	1.9268
H	1.3143	1.3782	−1.9244
H	−1.0431	4.0715	2.1481
H	−0.1988	6.1161	1.0468
H	−4.1706	−0.5104	−2.1491
H	−5.7671	−2.0430	−1.0503
H	−5.1973	−3.2302	1.0468

Table 2. Cartesian Coordinates (in Å) of $[Fe^{II}(Opda)_3]^{2+}$ in THF Optimized by DFT (B3LYP)

	x	*y*	*z*
Fe	0.3275	−0.5561	0.0651
N	0.9425	1.5942	−0.2144
N	−0.9658	0.6567	1.4836
N	2.0585	−1.0084	1.4739
N	2.0083	−1.4146	−1.2171
N	−0.8441	−2.4747	0.3403
N	−1.3231	−0.5224	−1.4971
C	−0.2398	2.4133	−0.0310
C	−0.4433	3.6074	−0.7234
C	−1.6313	4.3179	−0.5445
C	−2.6112	3.8377	0.3271
C	−2.4078	2.6453	1.0238
C	−1.2231	1.9302	0.8439
C	3.2651	−0.6961	0.7388
C	4.3973	−0.1470	1.3415
C	5.5009	0.2001	0.5599
C	5.4755	−0.0069	−0.8207
C	4.3453	−0.5594	−1.4263
C	3.2386	−0.9008	−0.6488
C	−2.2313	−2.1568	0.0554
C	−3.2947	−2.7686	0.7197
C	−4.6047	−2.3730	0.4431
C	−4.8505	−1.3725	−0.4994
C	−3.7882	−0.7642	−1.1706
C	−2.4772	−1.1540	−0.8938
H	1.6516	1.8151	0.4876
H	1.3756	1.7935	−1.1149
H	−1.8403	0.2036	1.7434
H	−0.4489	0.7858	2.3545
H	2.0612	−0.5365	2.3767
H	2.0083	−2.0060	1.6876
H	1.9905	−2.4342	−1.1595
H	1.9607	−1.1954	−2.2104
H	−0.5004	−3.1726	−0.3219
H	−0.7629	−2.9043	1.2605
H	−1.5601	0.4088	−1.8353
H	−1.0070	−1.0454	−2.3152
H	0.3230	3.9757	−1.3995
H	−1.7891	5.2450	−1.0857
H	−3.5348	4.3897	0.4667
H	−3.1680	2.2673	1.7012
H	4.4123	0.0115	2.4161
H	6.3787	0.6293	1.0316
H	6.3336	0.2599	−1.4287
H	4.3220	−0.7233	−2.4999
H	−3.0980	−3.5468	1.4517
H	−5.4297	−2.8474	0.9641
H	–5.8682	–1.0637	–0.7143

Table 3. Cartesian Coordinates (in Å) of Opda in THF Optimized by DFT (B3LYP)

	x	*y*	*z*
N	0.0865	1.3119	0.4534
N	1.4872	−0.7884	1.7060
C	−0.0079	0.0116	−0.0536
C	−0.7599	−0.2497	−1.2076
C	−0.7847	−1.5203	−1.7850
C	−0.0511	−2.5582	−1.2118
C	0.6800	−2.3169	−0.0457
C	0.7101	−1.0521	0.5494
H	−1.3141	0.5672	−1.6638
H	−1.3717	−1.6899	−2.6829
H	−0.0556	−3.5505	−1.6524
H	1.2350	−3.1256	0.4249
H	0.9378	−0.3831	2.4606
H	0.4574	1.4019	1.3875
H	−0.7328	1.8877	0.3147
H	1.9181	−1.6344	2.0641

Physical Measurements. Elemental analyses were performed at the analysis center at Hokkaido University. UV-vis-NIR spectra in solution were recorded on a Hitachi U-4100 spectrophotometer over the range 200-3300 nm at 296 K using crystalline samples of **1**·THF and **2**·THF. Infrared spectra were recorded on a Nicolet 6700 FT-IR spectrometer equipped with a Smart-Orbit (Diamond) ATR accessory. Magnetic susceptibility of the crystalline samples was measured using a Quantum Design MPMS-XL SQUID magnetometer with a magnetic field of 1 T. Diamagnetic corrections were made based on Pascal's constants.[29] ^{1}H NMR (270 MHz) spectra were measured in CD_3CN, $CDCl_3$, THF-d_8, or DMSO-d_6 with a JEOL EX-270 spectrometer. The signals from the residual solvent protons of CD_3CN (1.94 ppm), $CDCl_3$ (7.26 ppm), THF-d_8 (3.58 ppm), and DMSO-d_6 (2.50 ppm) were used as internal standards.[30]

Crystallographic Data Collection and Refinement of Structures. Crystallographic measurements were performed on a Rigaku AFC-7R diffractometer equipped with a Mercury CCD area detector, and graphite-monochromated Mo-Kα radiation (λ = 0.71069 Å). Specimens of suitable size and quality were selected under paraffin oil and mounted on MicroMounts (MiTeGen). The crystal was cooled using a N_2-flow-type temperature controller. The structures were solved by direct methods (SIR2004),[31] which successfully located

non-hydrogen atoms. All calculations were performed using the CrystalStructure crystallographic software package,[32] except for refinement calculations, which were performed using SHELXL-97.[33] A summary of the crystallographic data for **1**·THF and **2**·THF is given in Table 4. Full crystallographic details have been deposited with the Cambridge Crystallographic Data Centre as supplementary publication No. CCDC-909643 for **1**·THF and -909646 for **2**·THF.

Table 4. Crystallographic Data of **1**·THF and **2**·THF

	1·THF	**2**·THF
Formula	$C_{22}H_{32}Cl_2FeN_6O_9$	$C_{22}H_{26}Cl_2FeN_6O_9$
fw	651.28	645.24
Crystal size (mm^3)	0.30×0.16×0.16	0.40×0.16×0.08
Crystal system	monoclinic	monoclinic
Space group	$P2_1/n$(No. 14)	$P2_1/c$(No. 14)
a (Å)	17.849(2)	14.7311(19)
b (Å)	8.3097(9)	9.9389(11)
c (Å)	18.998(2)	18.389(2)
α (°)	100.5257(15)	98.0500(18)
β (°)	2770.4(6)	2665.8(6)
γ (°)	150	150
V ($Å^3$)	4	4
T (K)	1.561	1.608
Z	1352	1328
D_{calc} (g cm^{-3})	7.974	8.281
F (000)	22454	21537
μ(Mo Kα) (cm^{-1})	6242	6039
Measured reflections	362	380
Unique reflections	1.125	1.126
Refined parameters	0.048	0.033
GOF on F^2	0.0566	0.0652
R_{int}	0.1533	0.1761

[a] $R_1 = \Sigma||F_o| - |F_c||/\Sigma|F_o|$. [b] $wR_2 = \{[\Sigma w(F_o^2 - F_c^2)^2]/[\Sigma w(F_o^2)^2]\}^{1/2}$.

5-3. Results and Discussion

5-3-1. PHER from the Mixture of 3Opda and Fe(II)

The treatment of Opda (2.39×10^{-4} mol) with $[Fe^{II}(H_2O)_6](ClO_4)_2$ (7.98×10^{-5} mol) in THF immediately afforded a white suspension. On irradiation of the suspension with white light, gas evolution started, and GC analysis proved the formation of H_2 (red circles in Figure 1a; Figure 2). After irradiation for 57 h, the white suspension had changed to a green suspension and the amount of H_2 reached almost a plateau value, 8.77×10^{-5} mol of H_2, which leads to mole ratios of [evolved H_2]/[Opda] = 0.37 and [evolved H_2]/[Fe^{II}] = 1.10. In contrast, the PHER was not observed under a dark condition at all, suggesting PHER was driven as a photochemical reaction (Figure 1b). Two further control experiments without either Fe(II) or Opda under the same conditions showed that the evolved H_2 was only a twelfth as much as that in the presence of Fe(II) or undetectable, respectively (blue and black circles; Figure 1a). These results clearly demonstrate that coexistence of Opda and Fe(II) is necessary for efficient PHER, and stimulated us to characterize the active species of the PHER.

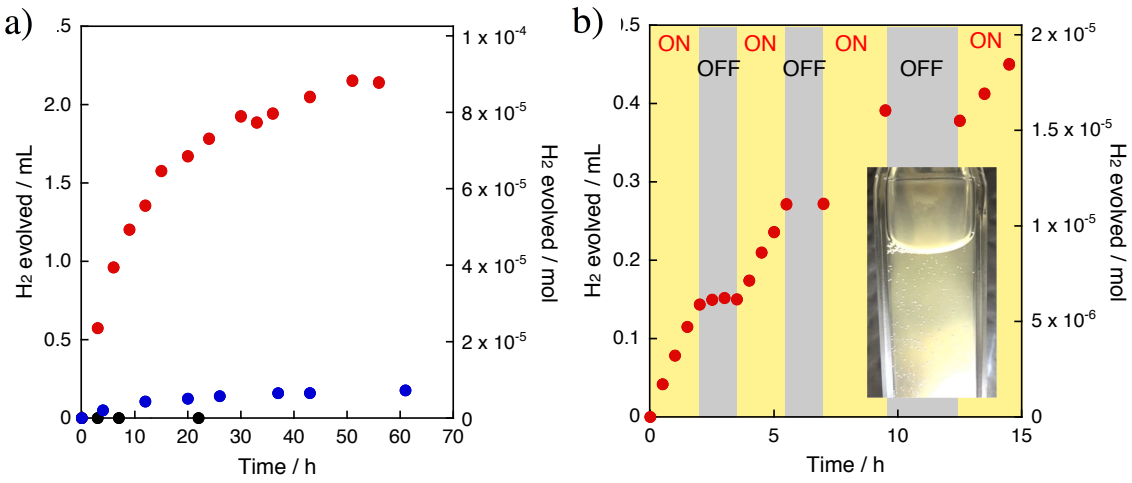


Figure 1. a) Amounts of photochemically evolved H_2 from 3Opda/$[Fe^{II}(H_2O)_6](ClO_4)_2$/THF suspension (red circles), 3Opda/THF solution (blue circles), and $[Fe^{II}(H_2O)_6](ClO_4)_2$/THF solution (black circles). b) PHER from a 3Opda/$[Fe^{II}(H_2O)_6](ClO_4)_2$/THF suspension under irradiation or in the dark. The sample suspension was kept under irradiation by white light for 0-2.0, 3.5-5.5, and 7.0-9.5 h (yellow background), and kept in the dark for 2.0-3.5, 5.5-7.0, and 9.5-12.5 h (gray background). After 12.5 h, the sample was put under irradiation. Insert: photograph of PHER. Bubbles were generated from the light path.

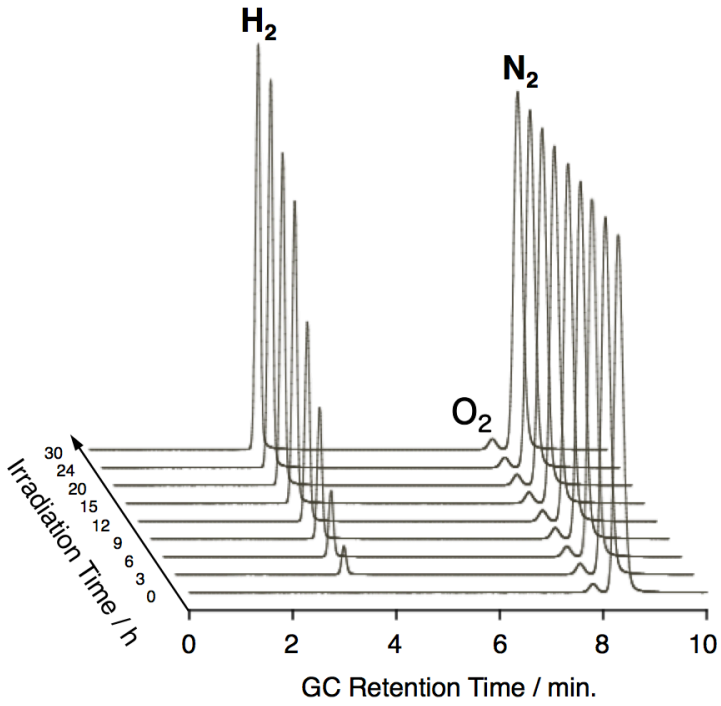


Figure 2. GC analyses results of PHER from a THF suspension containing $[Fe^{II}(H_2O)_6](ClO_4)_2$ (7.98×10^{-5} mol) and Opda (2.39×10^{-4} mol).

5-3-2. Characterization of the Active Species of the PHER

Slow diffusion of *n*-hexane/THF ($v : v = 1 : 1$) solution of three equivalents Opda into a THF solution of $[Fe^{II}(H_2O)_6](ClO_4)_2$ afforded air-sensitive colorless single crystals suitable for X-ray crystal structural analysis. The crystal is composed of a $[Fe(C_6H_4N_2H_4)_3]^{2+}$ cation and two ClO_4^- anions together with one THF molecule (Figure 3). The structure of the cation depicted in Figure 3a shows that three ligands (L1-L3) commonly coordinate to the Fe atom in bidentate chelating modes. The N–C (1.440(3)–1.450(3) Å) and the C–C bond distances of the six-membered ring are similar to those of non coordinating Opda (Table 5).[34] Here, we note that the dihedral angles (η) between the N–Fe–N and N–C–C–N planes indicate that the ligands are the neutral Opda form with two protons on each sp^3-type N atom. In addition, the Fe–N (2.204(2)–2.269(2) Å) bond distances and magnetic moment, $\chi_M T_{300K}$ = 3.96 emu·K·mol^{-1}, support the presence of a high-spin Fe(II) center. The cases of previously reported 3d-transition metal complexes bearing one or two Opda(s)[35] have remarkable dihedral angles (η)

between the N–Fe–N and N–C–C–N planes in Opda, and those of **1**·THF strongly support the structural assignment of **1**·THF as $[Fe^{II}(Opda)_3](ClO_4)_2$·THF (Table 6). All of these facts finally lead to the formulation of the crystal as $[Fe^{II}(Opda)_3](ClO_4)_2$·THF (**1**·THF), in which the ligands exist in the fully reduced form without forming oxidized *s*-Bqdi or Bqdi forms. In addition, there were two hydrogen bonds, (A) between N–H(L1) and O in the THF molecule (N1···O9 (2.885 Å)), (B) between NH(L3) and O in ClO_4^- (N6···O8 (2.897 Å)), in the crystal of **1**·THF as shown in Figure 3b.

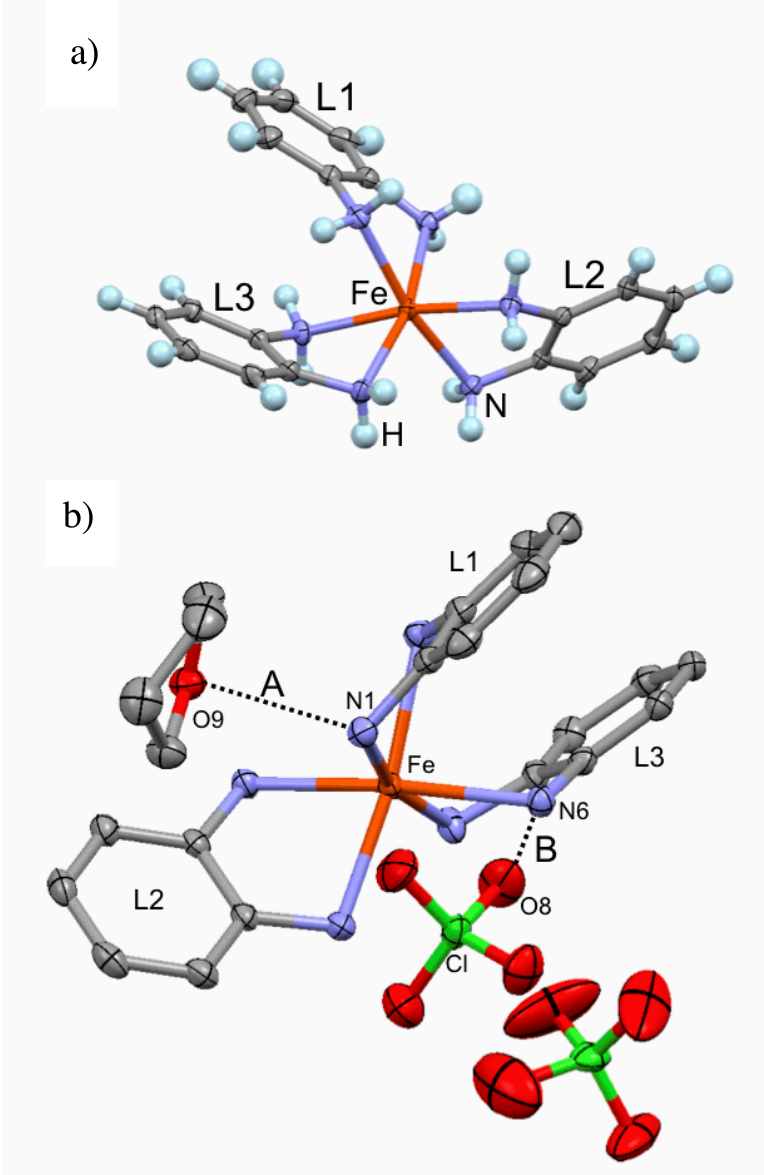


Figure 3. a) Molecular structure of the cation in **1**·THF and b) Crystallographically asymmetric unit of **1**·THF with thermal ellipsoid plots for Fe (brown), N (blue), and C (gray) (50% probability). Hydrogen atoms are depicted as ball-and-stick models colored light blue for a) and omitted for b) for clarity.

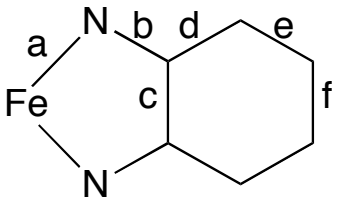


Table 5. Bond Distances (Å) of **1**·THF, **2**·THF, and Opda

		Å					
		a	b	c	d	e	f
1·THF	L1	2.207(2)	1.446(3)	1.396(4)	1.388(3)	1.384(4)	1.382(4)
		2.234(2)	1.450(3)		1.392(3)	1.384(4)	
	L2	2.204(2)	1.442(3)	1.405(3)	1.384(3)	1.387(4)	1.391(4)
		2.231(2)	1.443(3)		1.387(3)	1.386(4)	
	L3	2.269(2)	1.440(3)	1.403(3)	1.386(4)	1.385(3)	1.384(3)
		2.231(2)	1.445(3)		1.381(3)	1.394(4)	
	Av.	2.229(2)	1.444(3)	1.401(3)	1.386(3)	1.387(4)	1.386(4)
2·THF	L1	1.921(2)	1.311(3)	1.466(3)	1.445(3)	1.343(3)	1.436(4)
		1.919(2)	1.304(3)		1.432(3)	1.361(3)	
	L2	1.931(2)	1.319(3)	1.453(3)	1.424(4)	1.352(4)	1.435(4)
		1.931(2)	1.318(3)		1.429(4)	1.345(4)	
	L3	1.923(2)	1.301(3)	1.458(3)	1.432(4)	1.364(4)	1.427(4)
		1.925(2)	1.303(3)		1.447(3)	1.337(4)	
	Av.	1.925(2)	1.309(3)	1.459(3)	1.435(4)	1.350(4)	1.433(4)
Opda [a]			1.4004(16)	1.3996(16)	1.3795(16)	1.3833(18)	1.3711(18)
			1.4047(15)		1.3843(15)	1.3788(17)	
	Av.		1.4026(16)	1.3996(16)	1.3819(16)	1.3811(18)	1.3711(18)

[a] Ref. 36

Table 6. Dihedral Angles (η) of **1**·THF and **2**·THF

	η / °	
	1·THF	**2**·THF
L1	38.17	5.08
L2	35.90	1.88
L3	44.15	5.69
Av.	39.41	4.22

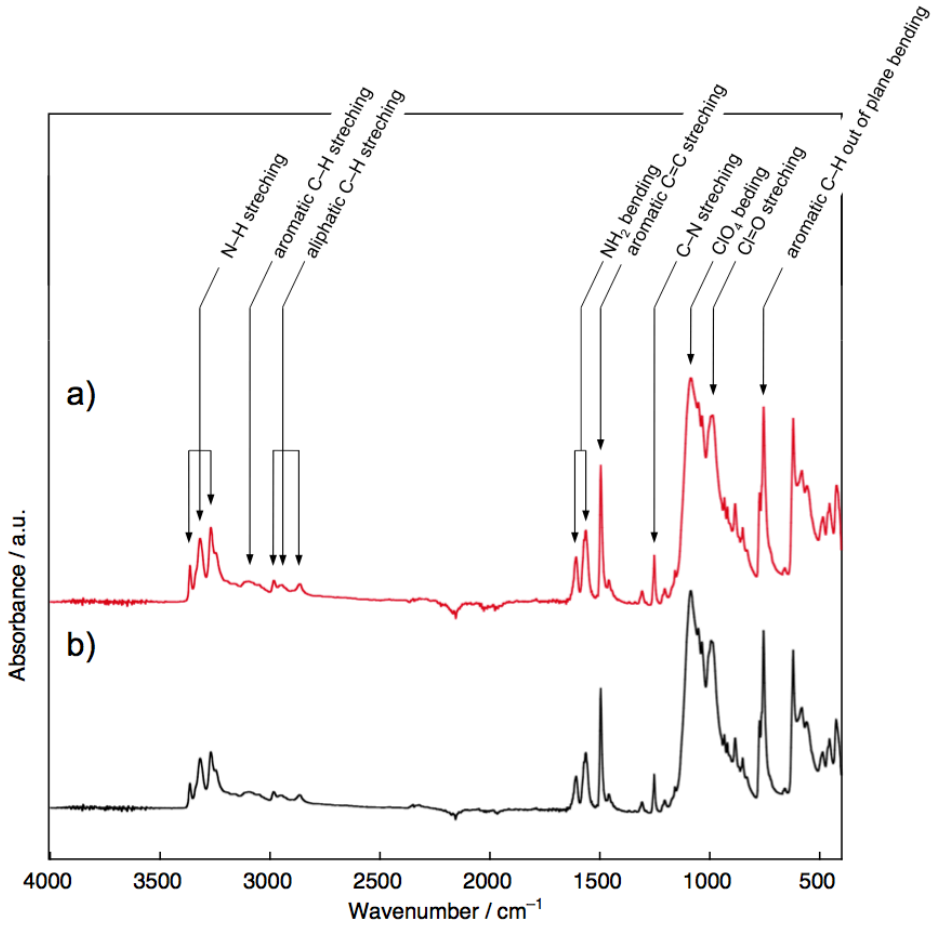


Figure 4. IR spectra of crystalline sample (red line) and white powder sample (black line) of **1**·THF, which was *in-situ* before PHER, in the solid state.

Table 7. IR spectral data of **1**·THF (crystalline sample)

Absorptions / cm^{-1}				
3365	2984	1564	1085	754
3317	2949	1496	1068	
3270	2865	1253	995	

Identical IR spectra were obtained for the crystal and the white powder prepared *in-situ* before PHER, indicating that both are **1**·THF as shown in Figure 4 and listed in Table 7.

5-3-3. Source and Irradiation Light Dependence of the PHER

To obtain clear information on the H^+ source in the PHER system, photo-irradiation of the mixture of Opda and $[Fe^{II}(H_2O)_6](ClO_4)_2$ in THF-d_8 was carried out. The GC analyses revealed

that only H_2 was obtained as the gaseous products, clearly excluding the contribution of the THF molecule as the H^+ source in this PHER (Figure 5c). In addition, the photo irradiation experiment using Opda-d_4 ($C_6H_4N_2D_4$), in which the deuteration ratio on the amino moieties was determined to be 92% (Figure 6), and $[Fe^{II}(H_2O)_6](ClO_4)_2$ in THF showed D_2 and HD evolution, showing that the H^+ in the photochemically evolved H_2 came from the amino protons of the Opda moieties (Figure 5d).

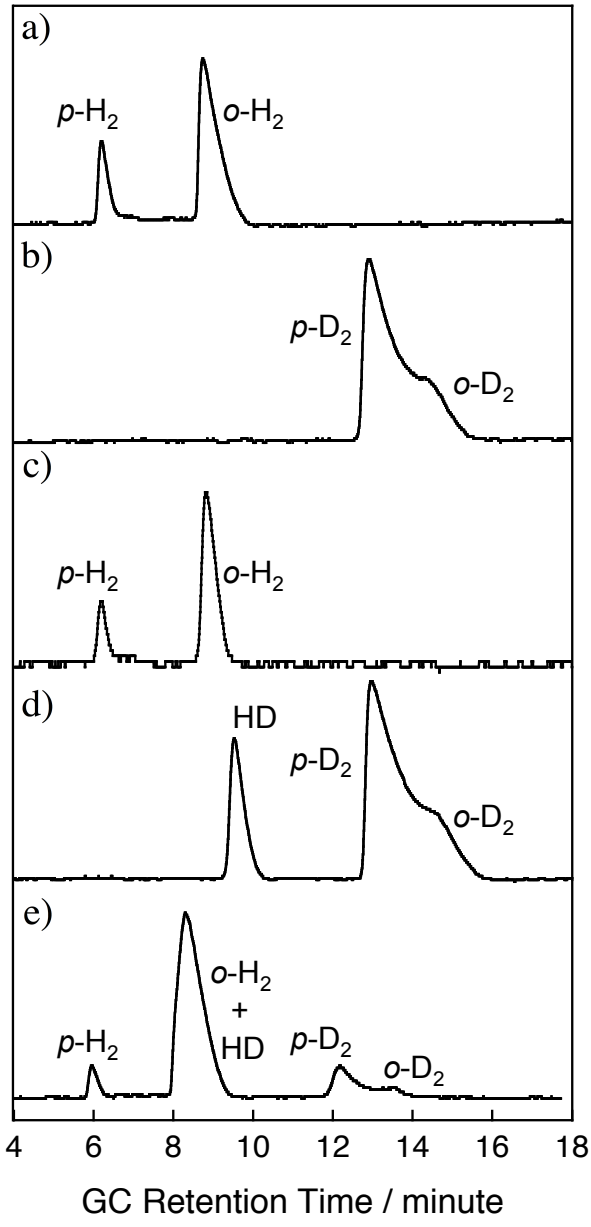


Figure 5. GCs of a) H_2 standard and b) D_2 standard gases, and photochemically evolved gas samples from c) 3Opda/$[Fe^{II}(H_2O)_6](ClO_4)_2$/THF-$d_8$, d) 3Opda-$d_4$/$[Fe^{II}(H_2O)_6](ClO_4)_2$/THF, and e) 3Opda/$[Fe^{II}(H_2O)_6](ClO_4)_2$/10HQ-$d_2$/THF mixtures.

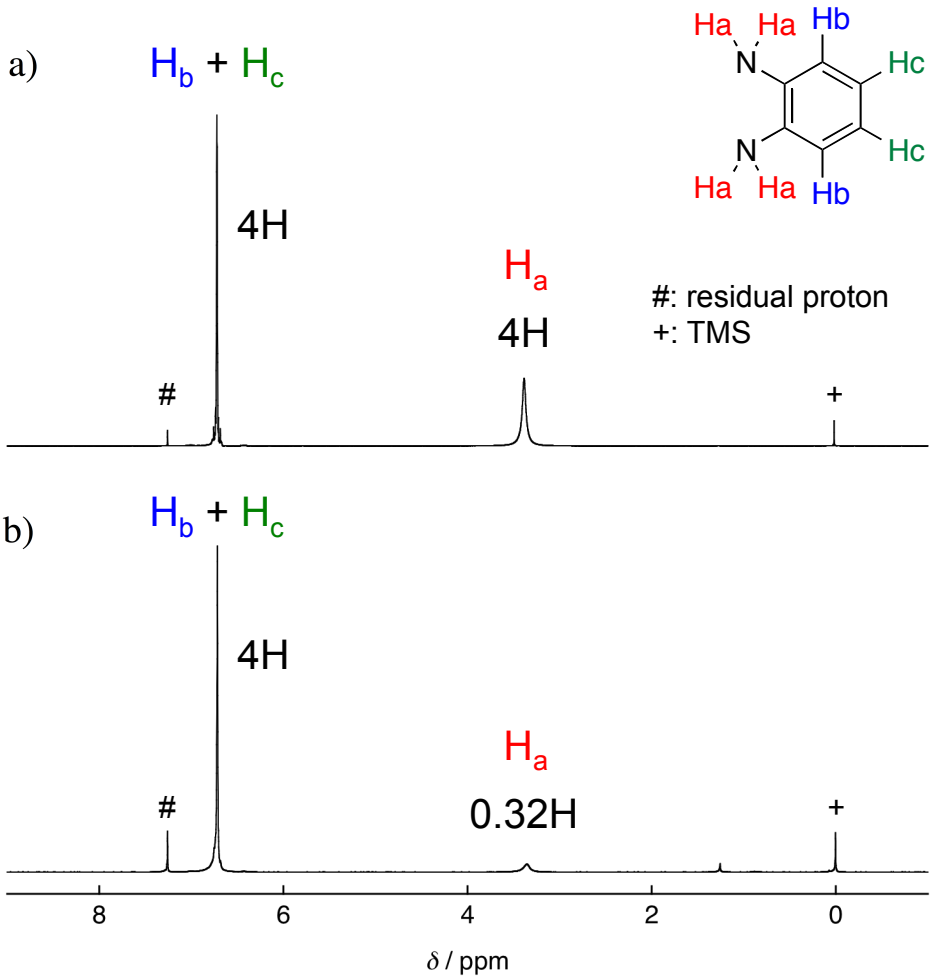


Figure 6. ^{1}H NMR spectra ($CDCl_3$) of a) Opda and b) Opda-d_4.

A UV-vis spectrum of **1** dissolved in THF is shown in Figure 7a (red line) together with that of Opda (black line) at the same conditions, and the data are summarized in Table 7. The UV-vis spectrum of **1** shows two strong absorption bands in the UV region at 240 (17,230 M^{-1} cm^{-1}) and 298 nm (9,230 M^{-1} cm^{-1}), which are similar in wavelength to those of Opda observed at 242 (6,080 M^{-1} cm^{-1}) and 298 nm (3,530 M^{-1} cm^{-1}). Complex **1** additionally shows a weak absorption band at 572 nm (110 M^{-1} cm^{-1}), which could be assignable to an Fe(II)-centered d-d transition. To characterize these absorptions, the density functional theory (DFT) calculations were performed for $[Fe^{II}(Opda)_3]^{2+}$ and Opda with the solvents effects taken into account by the polarizable continuum solvation model. First, it was confirmed that the optimized geometry for $[Fe^{II}(Opda)_3]^{2+}$ in the electronic ground state was in good agreement with that obtained in the X-ray crystallographic analysis (Figure 3 and 15a). The time-dependent DFT calculation

suggested that the absorptions in the UV region were attributed to two π-π* transitions (1^1π-π* and 2^1π-π*) localized on the Opda moieties (Figures 7b and 7c).

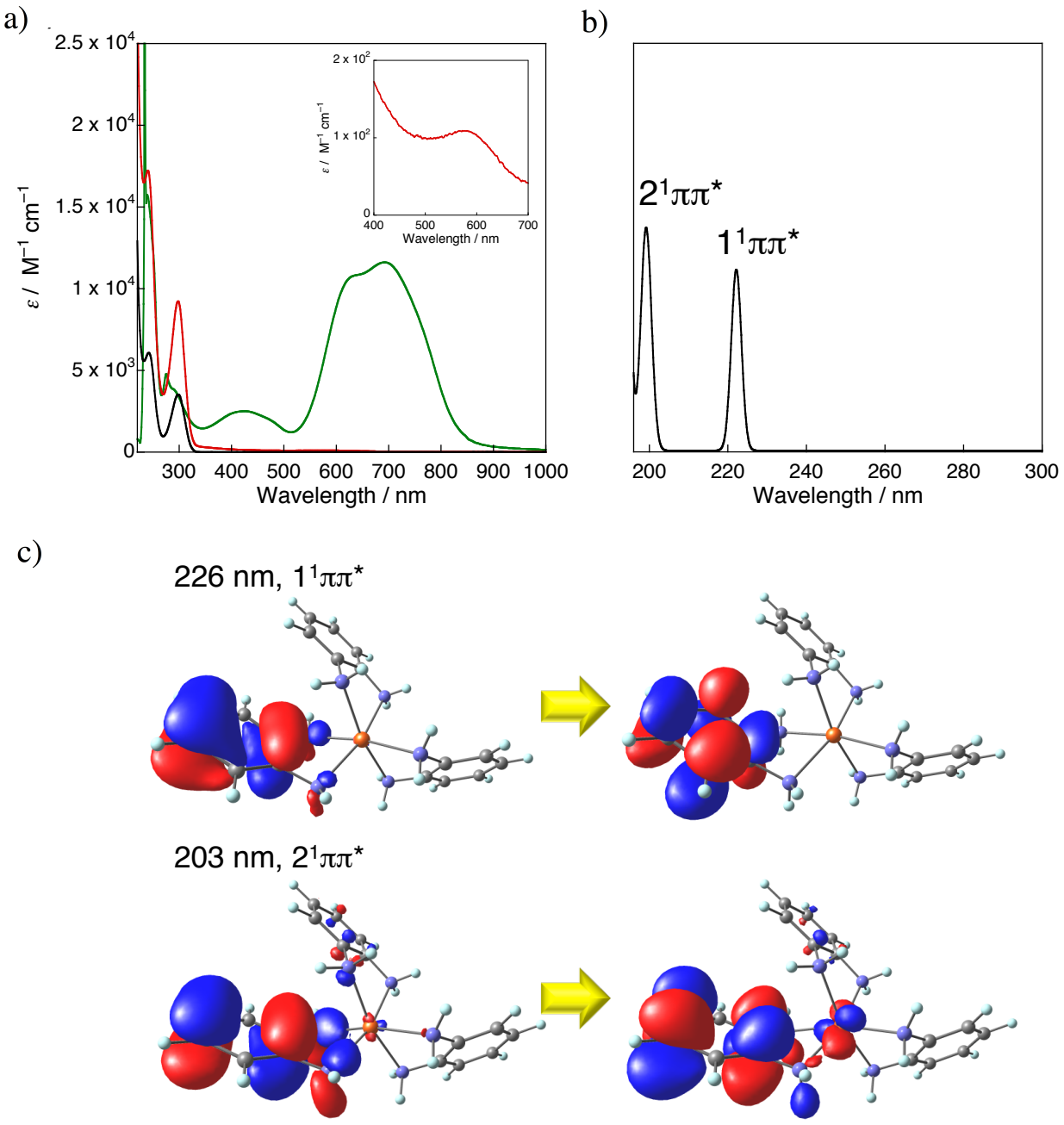


Figure 7. a) UV-vis-NIR spectra of **1** (red line) and Opda (black line) in THF at 1×10^{-4} M. b) Simulated absorption spectrum of $[Fe^{II}(Opda)_3]^{2+}$ in THF obtained by TD-DFT (LC-BLYP). c) Dominant natural transition orbital (NTO) pairs for selected ligand-^{1}π-π* transitions of $[Fe^{II}(Opda)_3]^{2+}$ in THF. For each state, the ''hole'' is on the left, the ''particle'' on the right.

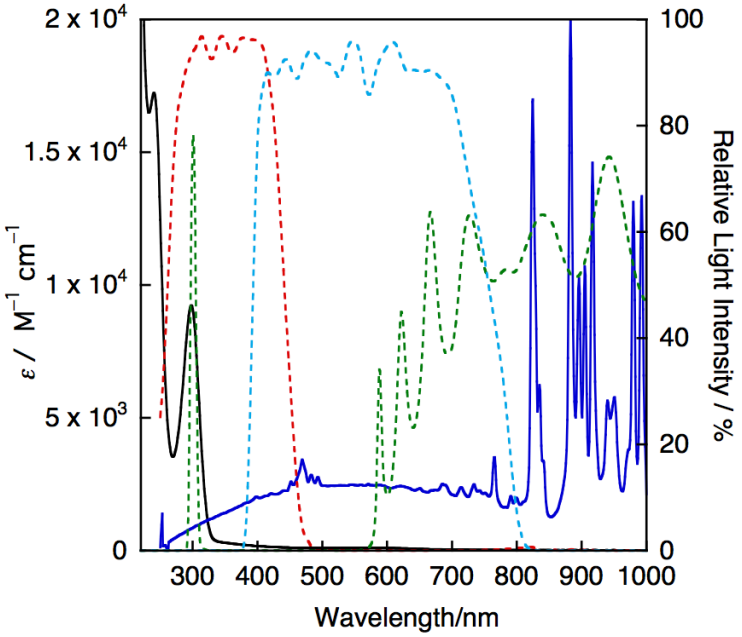


Figure 8. UV-vis-NIR absorption spectrum of **1** (1×10^{-4} M) in THF (black line), relative light intensity spectrum of the light source (Xe lamp) (blue line), transmission spectra of UVA-type mirror module (red dashed line), VIS-type mirror module (aqua dashed line), and band-pass filter (HQBP300-UV) (green dashed line).

To ascertain the excitation that initiates the PHER, excitation-light dependence was examined (Figures 8 and 9). By irradiation with visible light to the suspension for 19 h, no H_2 was obtained, suggesting that the excitation at 572 nm is negligible for the PHER. On the other hand, after irradiation with UV light at around 298 nm for 17 h, evolution of H_2 (2.72 μmol) was obtained. These results indicate that the PHER should be initiated by the π-π* transition of the coordinating Opda moiety. The apparent quantum yield (Φ) of this PHER in the aforementioned conditions was estimated to be 3.39%.[37]

5-3-4. H^+/e^- Pooling Ability of Opda

In the present PHER, the role of the Opda moiety as the H^+ source for PHER was successfully evaluated. These results inspired us to identify an electron source in the reaction. We found that complex **1** showed remarkable reactivity not only for photochemical reaction but also for air oxidation to produce a greenish-blue species both in CH_2Cl_2/*t*-BuOH ($v : v = 1 : 1$)[19a] and in THF solution under dark conditions. During this air oxidation, no PHER was observed.

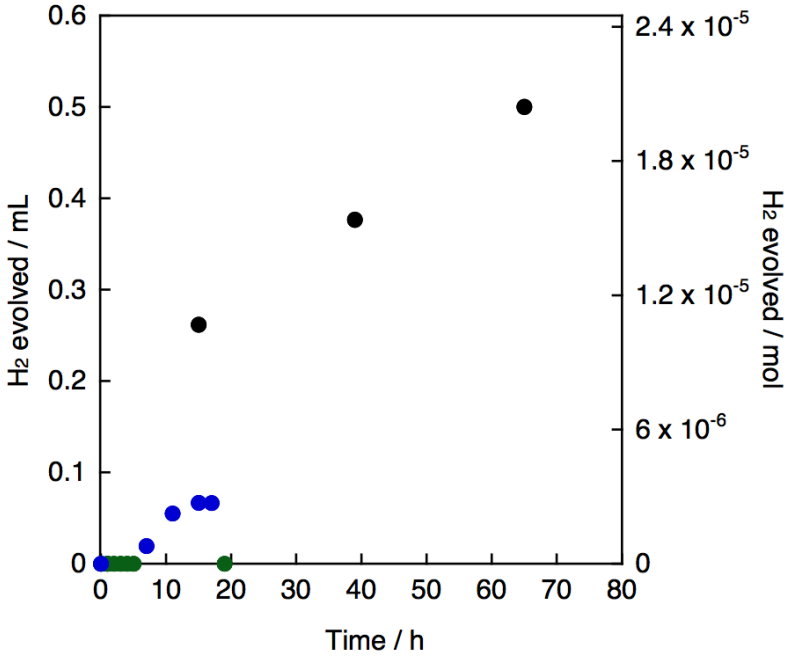


Figure 9. Amounts of photochemically evolved hydrogen from a THF suspension containing $[Fe^{II}(H_2O)_6](ClO_4)_2$ (7.98×10^{-5} mol) and Opda (2.39×10^{-4} mol) irradiated by a Xe lamp equipped with VIS-type mirror module (380 nm ≤ λ ≤ 800 nm) (green circles), with UVA-type mirror module (250 nm ≤ λ ≤ 480 nm) (black circles), or with both UVA-type mirror module and HQBP300-UV-type band-pass filter (central wavelength: 298 nm, half bandwidth: 10 nm) (blue circles).

The single crystal of the oxidized species grown from hexane/THF mixed solvent revealed that the crystal was composed of a $[Fe(C_6H_4N_2H_2)_3]^{2+}$ cation and two ClO_4^- anions together with one THF molecule (Figure 10). The cationic moiety demonstrates significant shortening in the N–C (1.301(3)–1.319(3) Å) and Fe–N (1.919(2)–1.931(2) Å) bond distances compared with those of **1**·THF (Table 5). In addition, the co-planarity of the N–Fe–N and N–C–C–N planes, together with the cyclohexa-3,5-diene character of the six-membered ring in each ligand indicate the sp^2-type hybridization state of the coordinating N atoms, accompanying the imino-proton on each N atoms.[19b-e,38] In contrast to the paramagnetic nature of **1**·THF, the oxidized species shows diamagnetic character (Figure 11), indicative of a low-spin Fe(II) center because of the relatively stronger ligand field of the Bqdi moiety compared with that of Opda. Based on all of the structural features, the oxidized species can be finally assigned as $[Fe^{II}(Bqdi)_3](ClO_4)_2$·THF (**2**·THF).[19b]

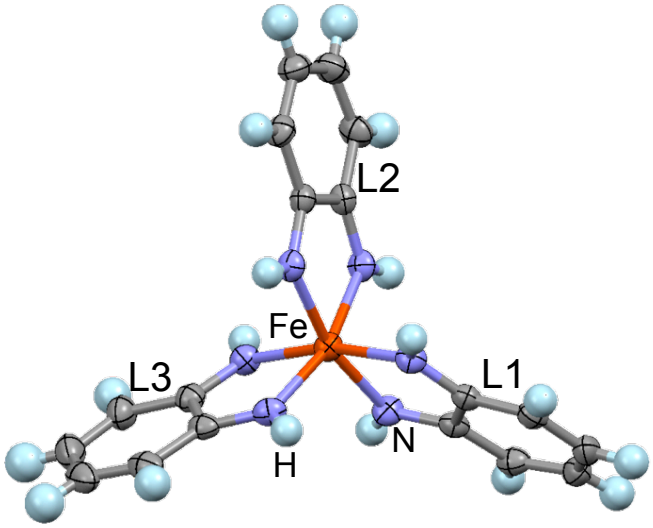


Figure 10. Molecular structure of the cation in **2**·THF with thermal ellipsoid plots for Fe (brown), N (blue), and C (gray) (50% probability). Hydrogen atoms are depicted as ball-and-stick models colored light blue. THF and ClO_4^- are omitted for clarity.

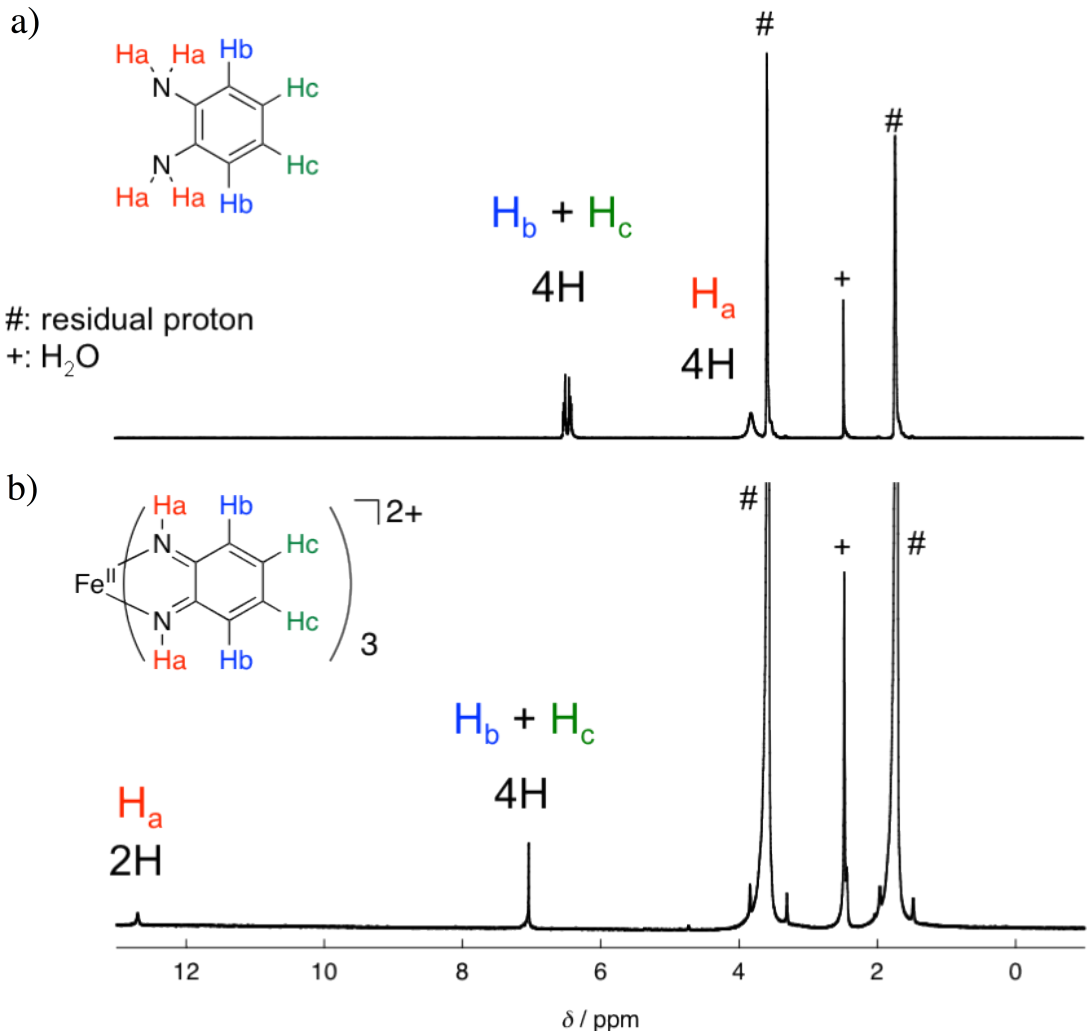


Figure 11. ^{1}H NMR spectra (THF-d_8) of a) Opda and b) **2**.

In contrast to the case of **1**, complex **2** shows characteristic absorption bands in the visible region at 420, 623, 692, and 770 nm, which were assigned as MLCTs and d-d transitions based on the DFT calculations on the $[Fe^{II}(Bqdi)_3]^{2+}$ moiety (green solid line; Figure 12). Such remarkable reactivity of the Opda moiety in **1**·THF toward air oxidation cannot be obtained for non-coordinating Opda, indicating the essential role of the Fe(II) ion. This Fe(II)-assisted ligand-centered air oxidation activity for **1** guarantees the $2H^+/2e^-$ pooling ability of Fe(II)-bound Opda.

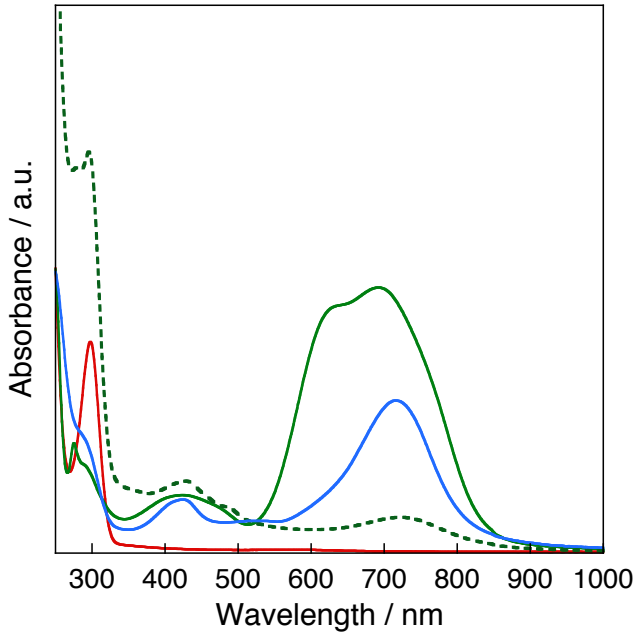


Figure 12. UV-vis-NIR spectra of **1** (red solid line) and **2** (green solid line) (1×10^{-4} M), PHER mixture from 3Opda/Fe^{II}/THF extracted by THF (green dashed line), air-oxidation mixture of **1** for 3 h (aqua solid line) in THF.

During the air oxidation of **1**, stepwise color changes were obtained (Figure 13). It is noteworthy that the reaction mixture after the PHER shows characteristic absorptions at 420, 620, and 690 nm (green dashed line; Figure 12), unlike those of **1**, with absorption maxima near to those observed during air oxidation of **1** (aqua dashed line; Figure 12). Moreover, in the electrospray ionization-mass spectrometry (ESI-MS) spectrum of the PHER mixture from 3Opda/Fe^{II}/THF in CH_3CN, several peaks, *i.e.*, $[Fe^{II}(Bqdi)_2(C_6H_4N_2H_3)]^+$ (m/z = 373.09), $[Fe^{II}(Bqdi)(Opda)_2(CH_3CN)_2]^{2+} - H^+$ (m/z = 459.36), assignable to fragments containing the Bqdi

moiety were obtained (Figure 14d). On the basis of these results, similar to the case of air oxidation of **1**, oxidation of the Opda moiety in **1** generating *s*-Bqdi or Bqdi can be considered also in the PHER. The residual Opda in the MS spectrum indicates the incompleteness of the PHER. The reason is not clear at this stage, but plausibly the side product could inhibit the PHER. In addition, fragment peaks implying oligomeric species of Opda were obtained in the MS spectrum of the PHER mixture from 3Opda/THF. They indicate the existence of Bqdi as

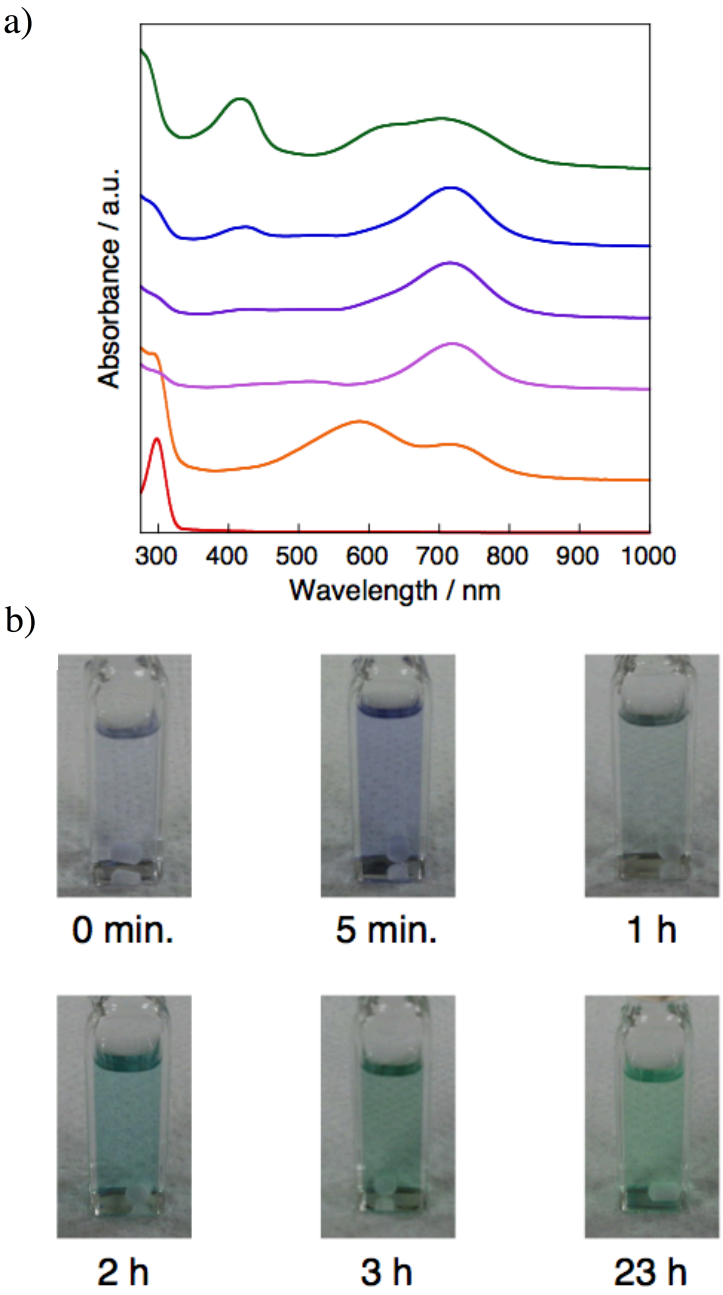


Figure 13. a) UV-vis-NIR spectra of air oxidation reaction mixture of **1** in THF for 0 min (red line), 5 min (orange line), 1 h (purple line), 2 h (navy line), 3 h (blue line), and 23 h (green line). b) Photographs of the mixture THF solutions used for UV-vis-NIR measurements.

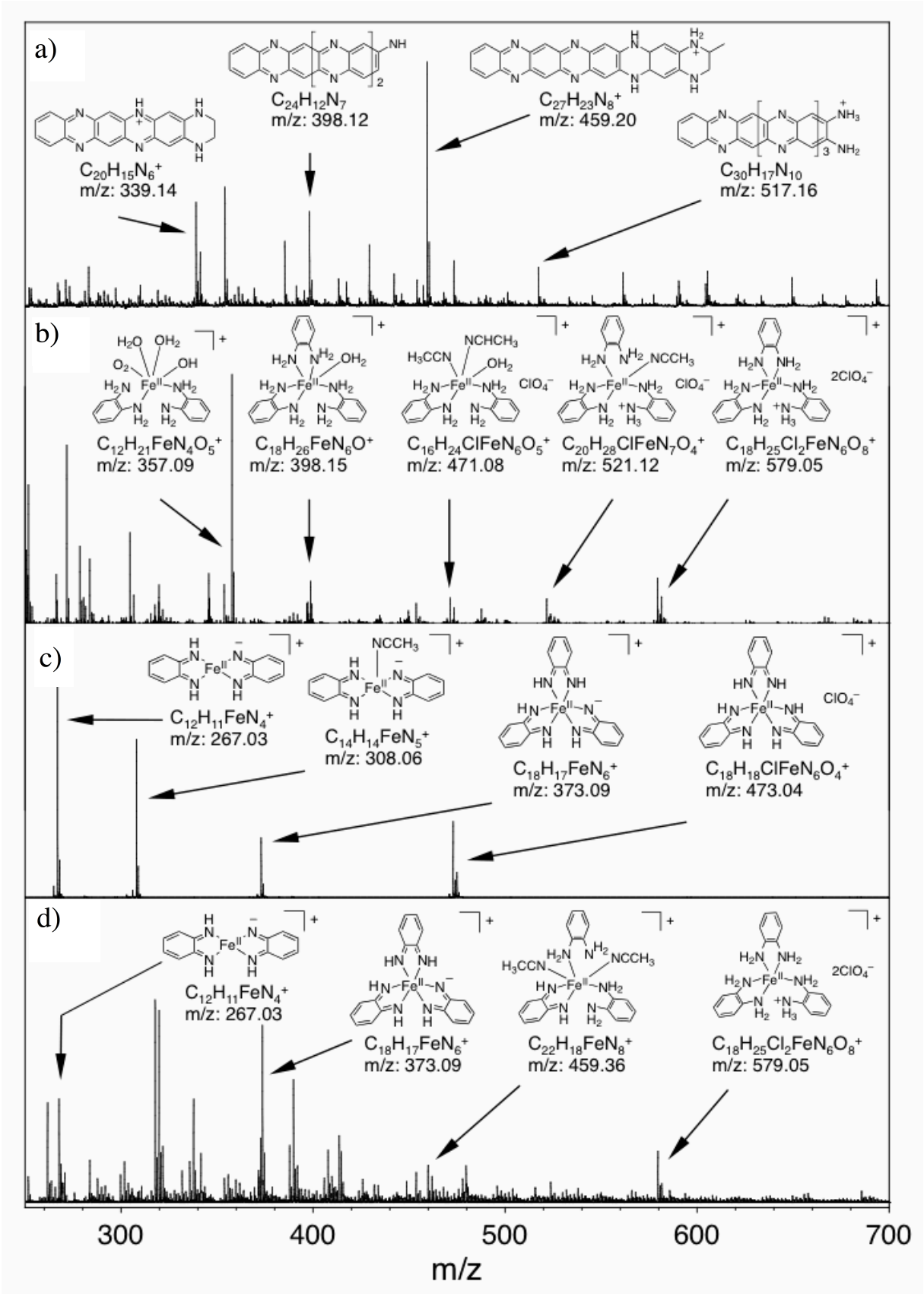


Figure 14. ESI-MS spectra of a) PHER reaction mixture from 3Opda/THF solution, b) **1**, c) **2**, and d) PHER reaction mixture from 3Opda/$[Fe^{II}(H_2O)_6](ClO_4)_2$/THF suspension ($CH_3CN$, *m/z* 250–700, positive ion mode).

transient species, which are known to produce 2,3-diaminophenazine derivatives through [2 + 4] cycloaddition processes with unreacted Opda.[39] These oligomeric species are not obtained in the PHER mixture from 3Opda/Fe^{II}/THF, suggesting that photochemically generated Bqdi should be stabilized by coordination to the coexisting Fe^{II} center by σ-donation and π-back donation,[40] thereby [2 + 4] cycloaddition with unreacted Opda should be inhibited.

5-3-5. Computational Studies

The optimized structures are given in Figure 15. It was found that the optimized structures for $[Fe^{II}(Opda)_3]^{2+}$ and $[Fe^{II}(Bqdi)_3]^{2+}$ are very close to those of the X-ray crystallographic data.

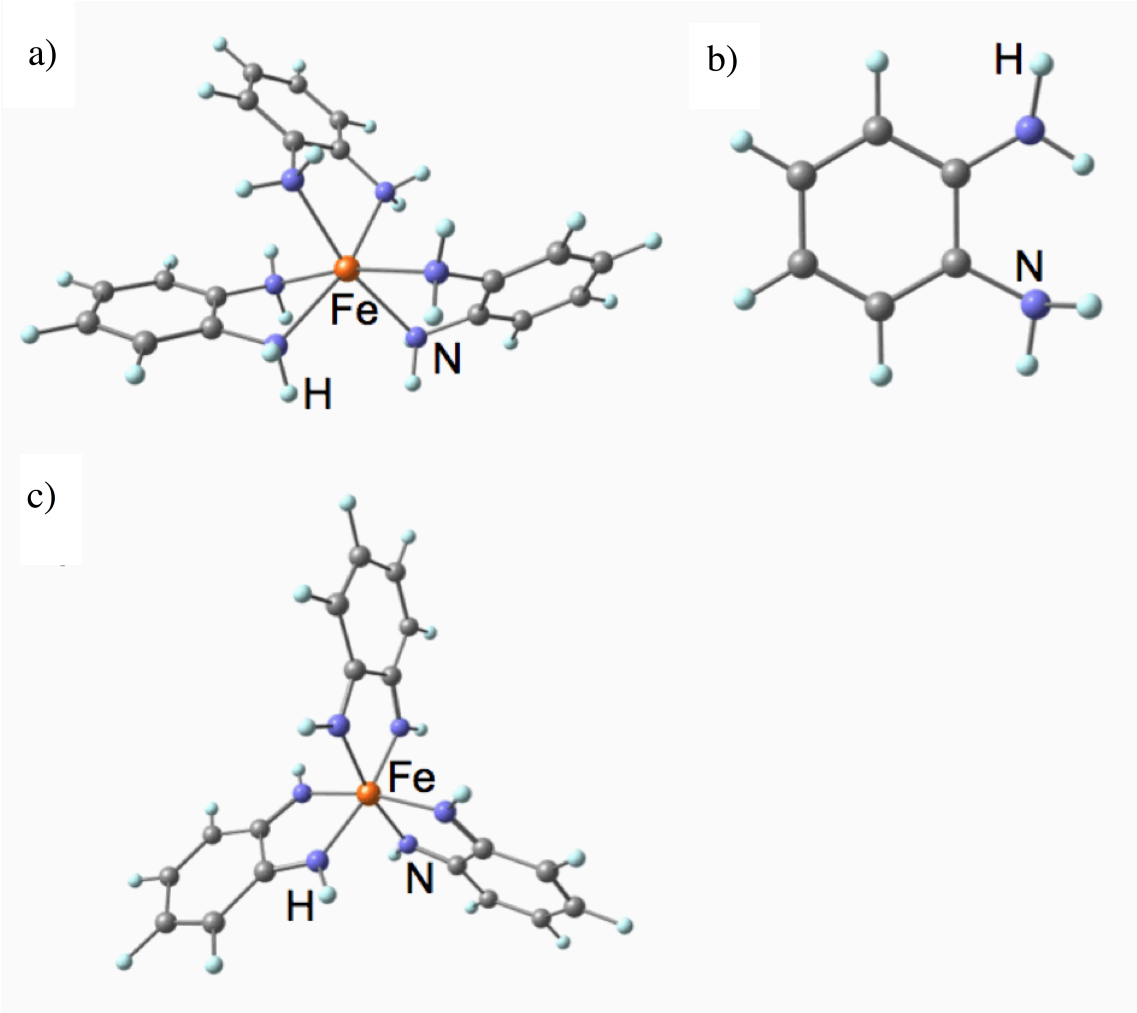


Figure 15. Equilibrium structures of a) $[Fe^{II}(Opda)_3]^{2+}$, b) Opda, and c) $[Fe^{II}(Bqdi)_3]^{2+}$ in THF obtained by DFT (B3LYP). Fe (brown), N (blue), C (gray), and H (light blue) atoms are depicted as ball-and-stick models.

Table 8. Vertical Excitation Energies, Wavelengths, and Oscillator Strengths (*f*) of Selected Transitions for Opda, $[Fe^{II}(Opda)_3]^{2+}$, and $[Fe^{II}(Bqdi)_3]^{2+}$ in THF Obtained by TD-DFT (LC-BLYP)

	E (eV)	λ (nm)	*f*
		Opda	
$1^1\pi$-π^*	4.97	252	0.104
$1^1\pi$-σ^*	5.37	231	0.012
2^1 π-π^*	5.59	222	0.083
		$[Fe^{II}(Opda)_3]^{2+}$	
1^1 π-π^* (Opda)	5.48	226	0.008
2^1 π-π^* (Opda)	6.10	203	0.003
LMCT	6.39	194	0.043
		$[Fe^{II}(Bqdi)_3]^{2+}$	
MLCT	2.81	442	0.023
MLCT	2.90	427	0.076
MLCT	3.16	392	0.256
d-d	3.56	348	0.016
MLCT	3.88	320	0.113

In the TD-DFT calculations of Opda, the first (S_1) and third (S_3) singlet excitations are characterized by $^1\pi$-π^* transitions, while the second (S_2) singlet excited state exhibits $^1\pi$-σ^* character. The transitions to $S_1(1^1\pi$-$\pi^*)$ and $S_3(2^1\pi$-$\pi^*)$ are mainly viewed as $2\pi \rightarrow 1\pi^*$ and $2\pi \rightarrow 2\pi^*$ excitations, respectively (Figure 16). The S_2 state involves an excitation of $2\pi \rightarrow 1\sigma^*$ and exhibits a 3s Rydberg character associated with the N atoms. This $^1\pi$-σ^* state is a dark state, and therefore it was not detected in the experimental spectra. The vertical excitation energies for $1^1\pi$-π^* and $2^1\pi$-π^* were calculated to be 4.97 eV (252 nm) and 5.59 eV (222 nm), respectively, and these values are overestimated in comparison with the experimental values (Table 8). In general, the LC-correction has a tendency to yield higher excitation

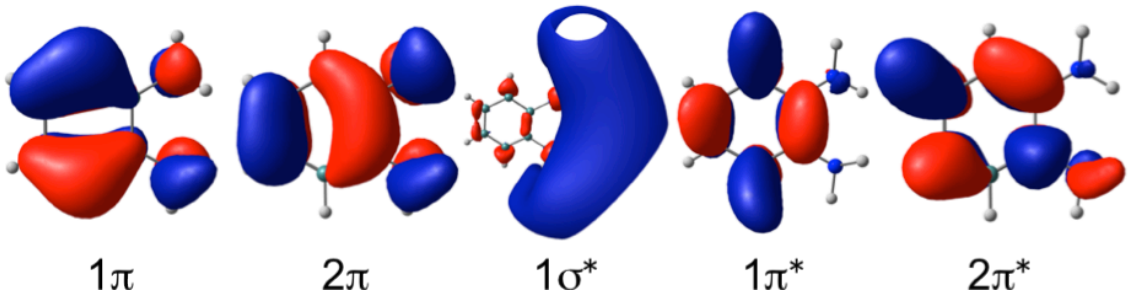


Figure 16. Relevant orbitals of Opda obtained by TD-DFT (LC-BLYP).

energy than that without the LC-correction even in the valence excitations. In fact, excitation energies calculated without the LC-correction (BLYP functional) are 4.22 eV (294 nm) and 4.90 eV (253 nm) for $1^1\pi$-π^* and $2^1\pi$-π^*, respectively, and these values are in good agreement with the experimental values. However, as is shown below in the calculations on $[Fe^{II}(Opda)_3]^{2+}$, the charge-transfer states that involve the ligand-metal charge transfer (LMCT) are observed in the UV region, and hence the LC-correction is essential to describe correctly the order of the excitations.

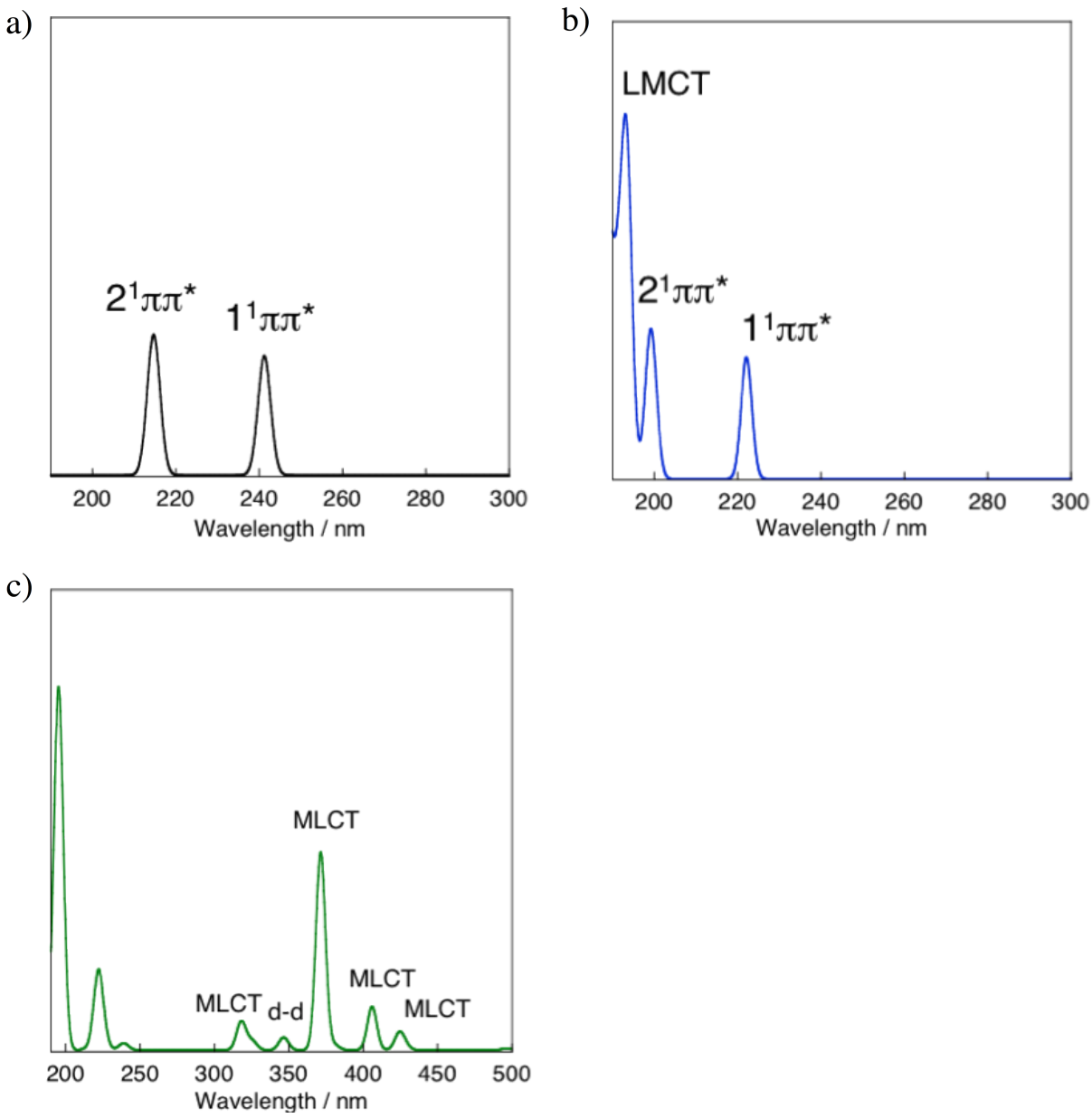


Figure 17. Simulated absorption spectra of a) Opda, b) $[Fe^{II}(Opda)_3]^{2+}$, and c) $[Fe^{II}(Bqdi)_3]^{2+}$ in THF obtained by TD-DFT (LC-BLYP).

The calculated UV absorption spectra of $[Fe^{II}(Opda)_3]^{2+}$ are shown in Figure 17, together with detailed information on selected excitations. The natural transition orbital (NTO) analysis[28] was carried out to understand better the results of the TD-DFT calculations. From this analysis, it is found that the first two low-lying peaks around 226 and 203 nm correspond to the $1^1\pi$-π^* and $2^1\pi$-π^* excitations of the Opda ligand moiety, respectively, and the next peaks above 190 nm correspond to the LMCT transitions. The dominant NTO pairs for the representative transitions are shown in Figure 18. Small blue-shifts of ~20 nm are observed for ligand $^1\pi$-π^* excitations when the $[Fe^{II}(Opda)_3]^{2+}$ complex is formed, but it is clear that the LMCT transition is well above the ligand $^1\pi$-π^* excitations. On the other hand, from the analysis for $[Fe^{II}(Bqdi)_3]^{2+}$, MLCT transitions are found in the longer wavelength regions that are not obtained for Opda and $[Fe^{II}(Opda)_3]^{2+}$ (Figures 17a and 17b). These results reflect the higher electron-accepting nature of the Bqdi moieties in $[Fe^{II}(Bqdi)_3]^{2+}$, compared with those of $[Fe^{II}(Opda)_3]^{2+}$.

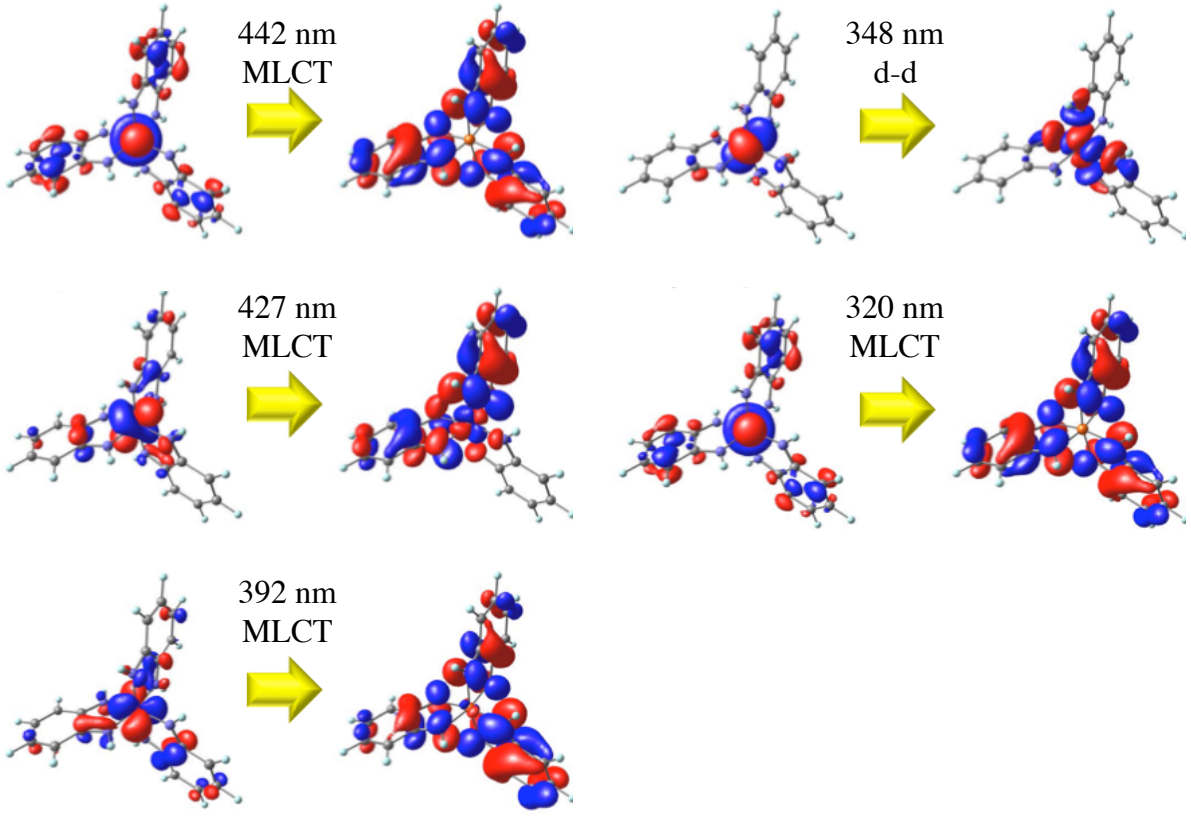


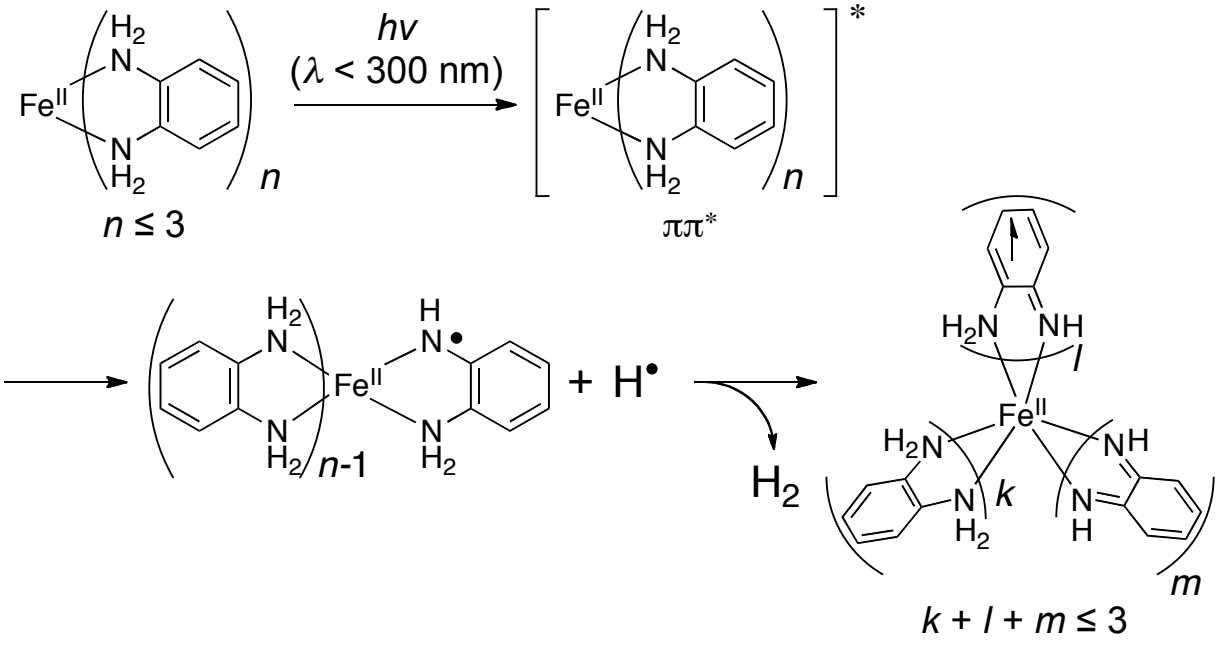
Figure 18. Dominant natural transition orbital (NTO) pairs for selected MLCT and d-d transitions of $[Fe^{II}(Bqdi)_3]^{2+}$ in THF. For each state, the ''hole'' is on the left, the ''particle'' on the right.

5-3-6. Reaction Mechanism of PHER

In previous reports on the photochemistry of aromatic amines or diamines, it was shown that photochemical N–H σ-bond activation generates a transient anilino radical ($C_6H_5NH\cdot$), *s*-Bqdi, or Bqdi *via* hydrogen atom elimination initiated by photo-excitation of a π-π^* transition through the 3s Rydberg state of the nitrogen atoms ($^1\pi$-σ^*), using several spectroscopic and theoretical techniques.[20-21] Based on these well-established studies, it is presumed that the PHER from the 3Opda/Fe(II)/THF mixture would proceed through a π-π^* transition followed by N–H dissociation in the Opda moiety to produce *s*-Bqdi or Bqdi that is plausibly coordinating to Fe ion. In the time-dependent DFT calculation for Opda, it was shown that the $^1\pi$-σ^* state lies slightly above the $^1\pi$-π^* state (see Table 4 for details), which supports this presumption. The higher PHER efficiency from the 3Opda/Fe(II)/THF sample than from the 3Opda/THF solution indicates the essential role of the Fe(II) ion in promoting PHER. As one of the possibilities, an assembling effect of Opda moieties could be considered by coordination to the cationic Fe(II) center throughout the reaction, which would let the photochemically generated hydrogen atom react with the other NH_2 groups coordinating the Fe(II) center.

From a consideration of these results, a plausible mechanism for the PHER of **1** could be

Scheme 1. Plausible Mechanism for PHER from the 3Opda/$[Fe^{II}(H_2O)_6](ClO_4)_2$/THF Mixture.



described as follows: (1) π-π* excited state formed by irradiation at around 298 nm; (2) N–H σ–bond elimination to produce hydrogen atom and Fe(II) complex of *o*-aminoanilino radical, equivalent to the *s*-Bqdi, species; (3) H atom abstraction from *s*-Bqdi or unreacted Opda to produce a H_2 molecule and partially oxidized species of the Fe(II) complex, probably such as $[Fe^{II}(Opda)_k(s\text{-}Bqdi)_l(Bqdi)_m]^{2+}$ ($k + l + m \leq 3$) (Scheme 1).

5-3-7. PHER Using HQ as a H^+/e^- Donor

For the creation of PHER systems, the PHER from a mixture of Opda and $[Fe^{II}(H_2O)_6](ClO_4)_2$ in the presence of HQ as an additional H^+/e^- mediator was conducted (green circles; Figure 19). HQ derivatives are known to possess reversible $2H^+/2e^-$ transfer capability, the same as for Opda.[41] By the addition of ten equivalents of HQ to the Opda and Fe(II) mixture, the amount of photochemically evolved hydrogen was continuously increased, even after 57 h, in contrast to the case without HQ (red circles; Figure 19). The amount of evolved hydrogen was 3.41×10^{-4} mol (TON = 4.28) after 196 h, which is about four times as much as that without HQ (8.77×10^{-5}

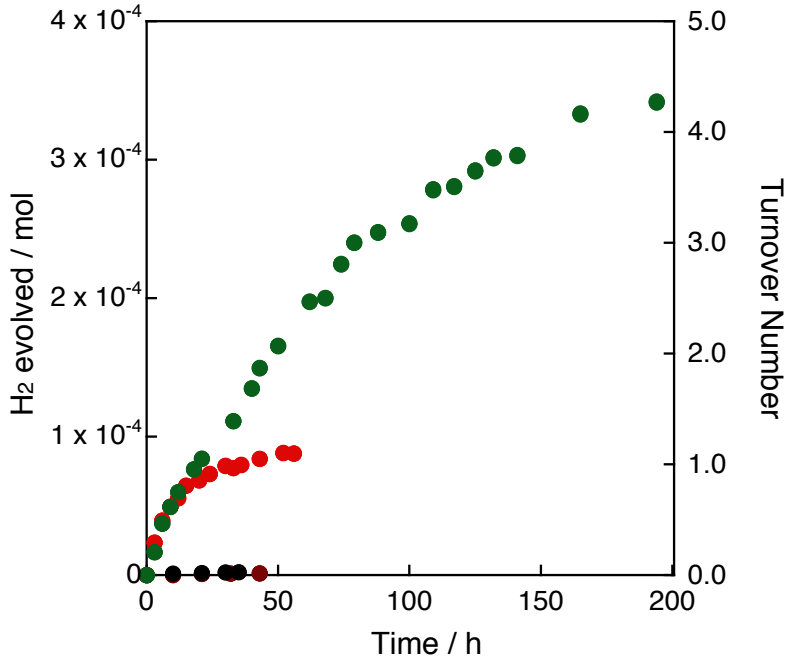


Figure 19. Amounts of photochemically produced hydrogen from 3Opda/$[Fe^{II}(H_2O)_6](ClO_4)_2$/10HQ/THF (green circles), 3Opda/$[Fe^{II}(H_2O)_6](ClO_4)_2$/THF (red circles) suspensions, 10HQ/THF (black circles), and $[Fe^{II}(H_2O)_6](ClO_4)_2$/10HQ/THF (brown circles) solutions.

mol after 57 h), suggesting that HQ serves as a H^+/e^- donor for these reactions. In the cases of two control experiments without both Opda and Fe(II) or Opda under the same conditions (Figure 19, black and brown circles), the PHER could not be obtained, suggesting the inertness of HQ itself for PHER together with the catalytic role of the complex species consisting of Opda(s) and Fe(II) or its partially oxidized species.

On the other hand, a similar PHER using Opda, $[Fe^{II}(H_2O)_6](ClO_4)_2$, and HQ-$d_2$ ($C_6H_4O_2D_2$), in which the deuteration ratio on the hydroxyl groups was determined to be 85% by ^{1}H NMR, instead of HQ, D_2 and HD were obtained (Figures 5e and 20). Although the possibilities not only that D^+ of HQ-d_2 transferred in the PHER mechanism but also that Opda was deuterated by H/D exchange between HQ-d_2 before photoirradiation should be taken into account, it is suggested that the H^+ of HQ can be the source of evolved H_2 in this PHER. In the ^{1}H NMR

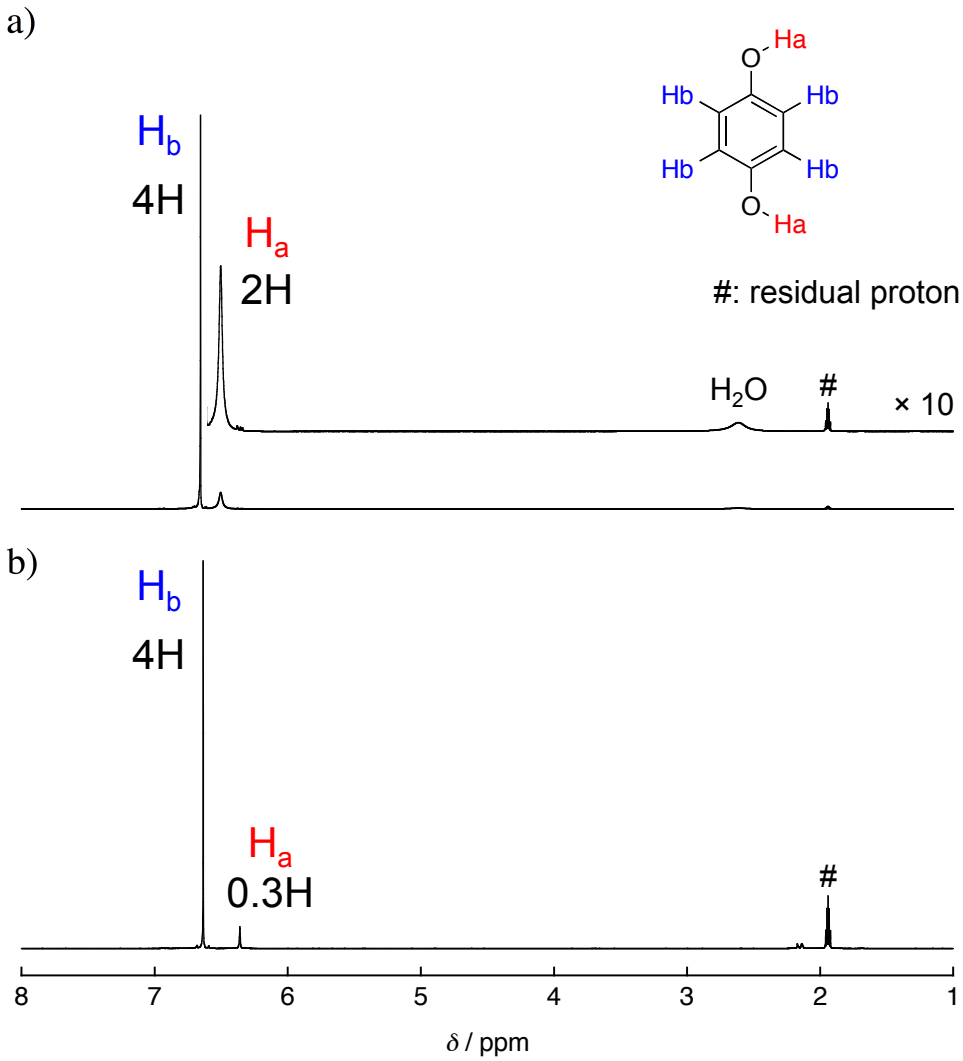


Figure 20. ^{1}H NMR spectra (CD_3CN) of a) HQ and b) HQ-d_2.

spectrum of product after the catalytic PHER in DMSO-d_6, the existence of *p*-benzoquinone (BQ) was indicated, supporting these considerations (Figure 21). From these comprehensive considerations, a plausible PHER reaction cycle can be described as shown in Scheme 2. The HQ apparently serves as the proton/electron sacrifice reagent during the PHER. Since the photo-irradiation experiments for **2**/10HQ/THF did not lead to detectable hydrogen, HQ might interact with partially oxidized species derived from **1** at either ground or excited states or both. Furthermore, HQ is an expected H^+ /e^- mediator in an extended system for hydrogen production based on this PHER cycle.

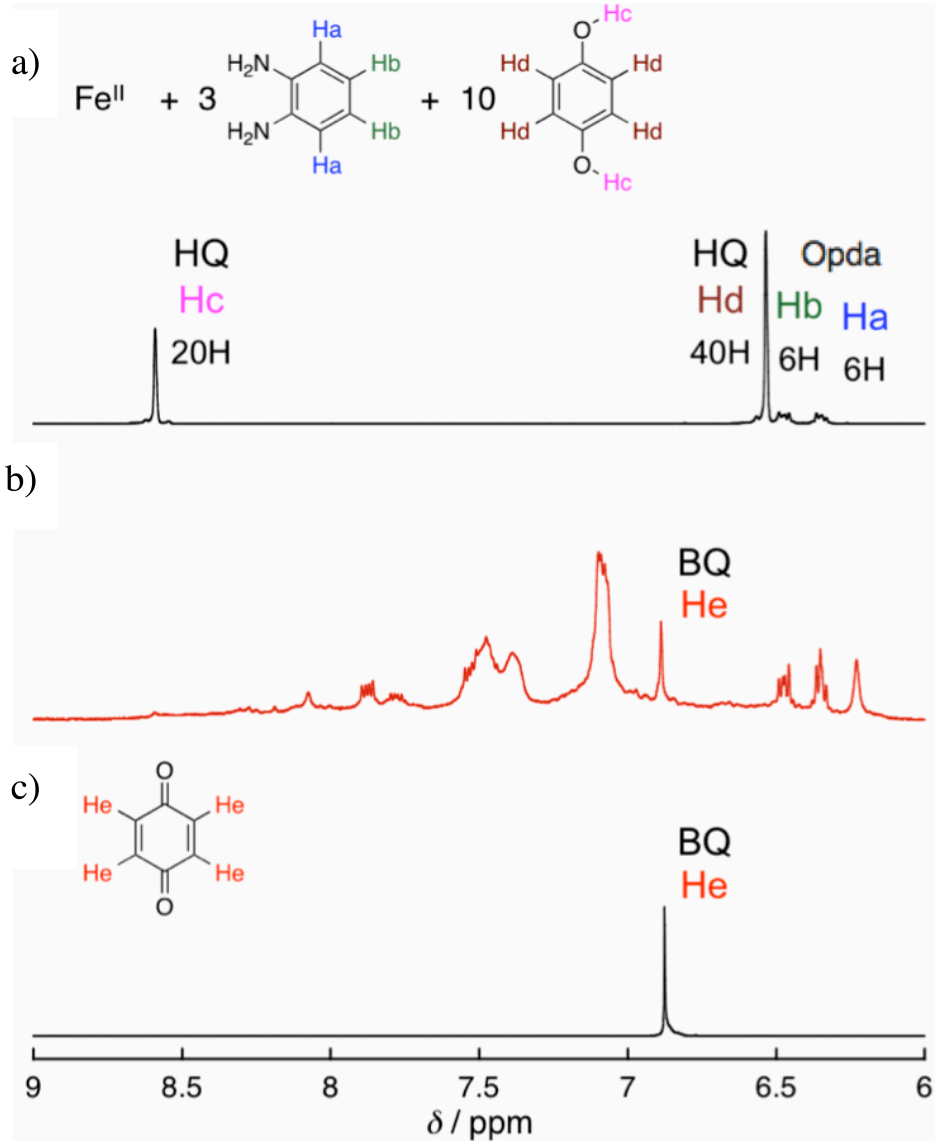
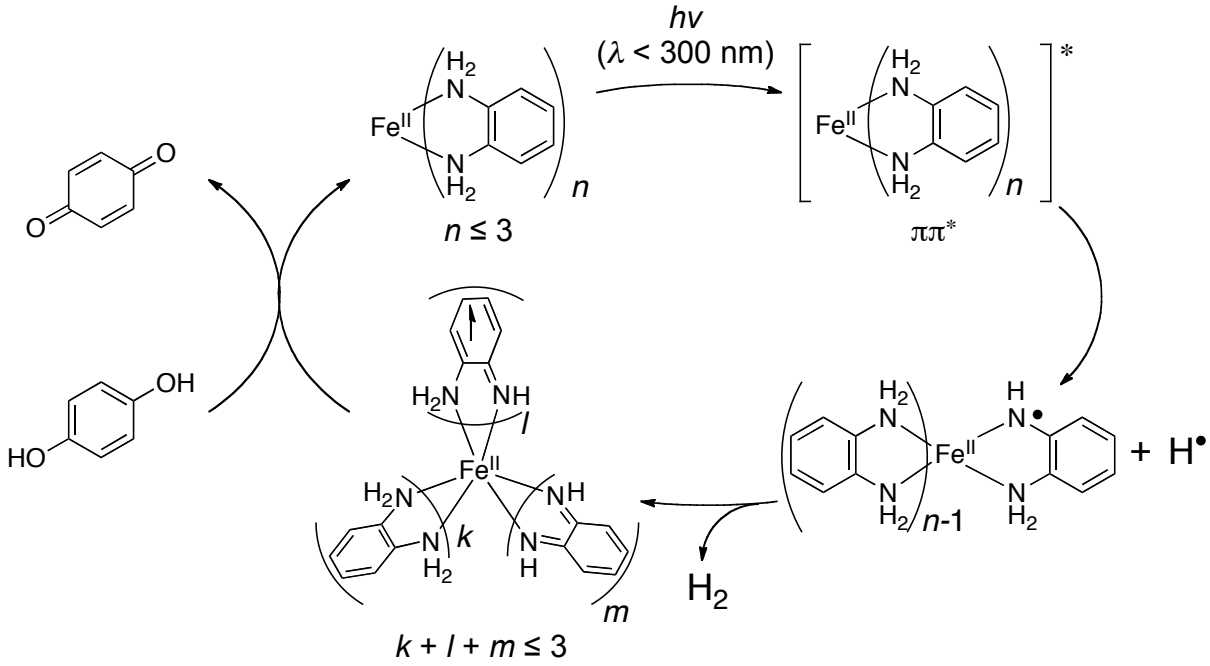


Figure 21. ^{1}H NMR spectra (DMSO-d_6) of a) 3opda/Fe^{II}/10HQ mixture (black line),[42] b) PHER mixture of 3opda/Fe^{II}/10HQ after 196 h irradiation (red line), and c) BQ (black line).

Scheme 2. Plausible Mechanism for PHER from the 3Opda/$[Fe^{II}(H_2O)_6](ClO_4)_2$/10HQ/THF Mixture.



5-4. Conclusions

In summary, this chapter exploited a novel system toward the PHER, where the Opda combined with a nonprecious metal ion, such as Fe^{II}, can effectively serve as H^+/e^- poolers. A key feature is to make effective coordination interaction between metal ions with the Opda moieties. Light irradiation onto the pooler initiates the PHER and successive H^+ and e^- transfers proceed from HQ. The results presented here provide one possible way to activate organic moieties supporting with nonprecious metals. Efforts are presently focused on deepening our understanding of the mechanism, as well as improvements in the catalytic activity, together with the tuning of HOMO-LUMO gaps to realize hydrogen production/storage operative with visible light.

5-5. Notes and References

1. N. Armaroli, V. Balzani, *Angew. Chem. Int. Ed.,* **2007**, *46*, 52.
2. P. V. Kamat, *J. Phys. Chem. C,* **2007**, *111*, 2834.
3. A. Züttel, A. Remhof, A. Borgschulte, O. Friedrichs, *Phil. Trans. R. Soc. A,* **2010***, 368*, 3329.
4. a) K. Mazloomi, C. Gomes, *Renew. Sust. Energ. Rev.,* **2012***, 16*, 3024; b) N. S. Lewis, D. G. Nocera, *Proc. Natl. Acad. Sci. U. S. A.,* **2006**, *103*, 15729.
5. a) M. P. Suh, H. J. Park, T. K. Prasad, D.-W. Lim, *Chem. Rev.,* **2011***, 112*, 782; b) U. Eberle, M. Felderhoff, F. Schüth, *Angew. Chem. Int. Ed.,* **2009**, *48*, 6608.
6. B. Sakintuna, F. Lamari-Darkrim, M. Hirscher, *Int. J. Hydrogen Energ.,* **2007***, 32***,** 1121.
7. a) F. Schuth, B. Bogdanovic, M. Felderhoff, *Chem. Commun.,* **2004***,* 2249; b) S.-I. Orimo, Y. Nakamori, J. R. Eliseo, A. Züttel, C. M. Jensen, *Chem. Rev.,* **2007***, 107*, 4111; c) W. Grochala, P. P. Edwards, *Chem. Rev.,* **2004***, 104*, 1283; d) C. H. Christensen, R. Z. Sorensen, T. Johannessen, U. J. Quaade, K. Honkala, T. D. Elmoe, R. Kohler, J. K. Norskov, *J. Mater. Chem.,* **2005***, 15*, 4106.
8. a) T. Hügle, M. Hartl, D. Lentz, *Chem. Eur. J.,* **2011**, *17*, 10184; b) G. Alcaraz, S. Sabo-Etienne, *Angew. Chem. Int. Ed.,* **2010**, *49*, 7170; c) C. W. Hamilton, R. T. Baker, A. Staubitz, I. Manners, *Chem. Soc. Rev.,* **2009**, *38*, 279.
9. V. V. Struzhkin, B. Militzer, W. L. Mao, H.-K. Mao, R. J. Hemley, *Chem. Rev.,* **2007**, *107*, 4133.
10. J. Chen, F. Wu, *Appl. Phys. A,* **2004**, *78*, 989.
11. a) H.-M. Cheng, Q.-H. Yang, C. Liu, *Carbon,* **2001**, *39*, 1447; b) R. H. Baughman, A. A. Zakhidov, W. A. de Heer, *Science,* **2002**, *297*, 787; c) R. Ströbel, J. Garche, P. T. Moseley, L. Jörissen, G. Wolf, *J. Power Sources,* **2006**, *159*, 781.
12. Y. Kubota, M. Takata, R. Matsuda, R. Kitaura, S. Kitagawa, K. Kato, M. Sakata, C. T. Kobayashi, *Angew. Chem. Int. Ed.,* **2005**, *44*, 920.
13. a) G. E. Dobereiner, A. Nova, N. D. Schley, N. Hazari, S. J. Miller, O. Eisenstein, R. H. Crabtree, *J. Am. Chem. Soc.,* **2011**, *133*, 7547; b) R. Yamaguchi, C. Ikeda, Y. Takahashi,

K.-I. Fujita, *J. Am. Chem. Soc.,* **2009**, *131*, 8410; c) P. Jessop, *Nat. Chem.,* **2009**, *1*, 350.

14. a) R. Kawahara, K.-I. Fujita, R. Yamaguchi, *Angew. Chem. Int. Ed.,* **2012**, *124*, 12962; b) R. Kawahara, K.-I. Fujita, R. Yamaguchi, *J. Am. Chem. Soc.,* **2012**, *134*, 3643.
15. a) L. L. Tinker, N. D. McDaniel, P. N. Curtin, C. K. Smith, M. J. Ireland, S. Bernhard, *Chem. Eur. J.,* **2007**, *13*, 8726; b) M. Elvington, J. Brown, S. M. Arachchige, K. J. Brewer, *J. Am. Chem. Soc.,* **2007**, *129*, 10644; c) J. I. Goldsmith, W. R. Hudson, M. S. Lowry, T. H. Anderson, S. Bernhard, *J. Am. Chem. Soc.,* **2005**, *127*, 7502; d) A. J. Esswein, D. G. Nocera, *Chem. Rev.,* **2007**, *107*, 4022; e) H. Ozawa, K. Sakai, *Chem. Commun.,* **2011**, *47*, 2227; f) K. Sakai, H. Ozawa, *Coord. Chem. Rev.,* **2007**, *251*, 2753; g) A. Inagaki, M. Akita, *Coord. Chem. Rev.,* **2010**, *254*, 1220; h) M. Wang, Y. Na, M. Gorlov, L. Sun, *Dalton Trans.,* **2009**, *6458*; i) S. Fukuzumi, T. Suenobu, *Dalton Trans.,* **2013**, *42*, 18; j) J. F. Hull, Y. Himeda, W.-H. Wang, B. Hashiguchi, R. Periana, D. J. Szalda, J. T. Muckerman, E. Fujita, *Nat. Chem.,* **2012**, *4*, 383; k) K. Maeda, M. Higashi, D. Lu, R. Abe, K. Domen, *J. Am. Chem. Soc.,* **2010**, *132*, 5858.
16. a) W. R. McNamara, Z. Han, P. J. Alperin, W. W. Brennessel, P. L. Holland, R. Eisenberg, *J. Am. Chem. Soc.,* **2011**, *133*, 15368; b) T. Lazarides, T. McCormick, P. Du, G. Luo, B. Lindley, R. Eisenberg, *J. Am. Chem. Soc.,* **2009**, *131*, 9192; c) S. Kaur-Ghumaan, L. Schwartz, R. Lomoth, M. Stein, S. Ott, *Angew. Chem. Int. Ed.,* **2010**, *49*, 8033; d) T. M. McCormick, Z. Han, D. J. Weinberg, W. W. Brennessel, P. L. Holland, R. Eisenberg, *Inorg. Chem.,* **2011**, *50*, 10660; e) C. H. Lee, D. K. Dogutan, D. G. Nocera, *J. Am. Chem. Soc.,* **2011**, *133*, 8775; f) Y. Sun, J. P. Bigi, N. A. Piro, M. L. Tang, J. R. Long, C. J. Chang, *J. Am. Chem. Soc.,* **2011**, *133*, 9212; g) W. Zhang, J. Hong, J. Zheng, Z. Huang, J. Zhou, R. Xu, *J. Am. Chem. Soc.,* **2011**, *133*, 20680; h) D. Streich, Y. Astuti, M. Orlandi, L. Schwartz, R. Lomoth, L. Hammarström, S. Ott, *Chem. Eur. J.,* **2010**, *16*, 60; i) H. I. Karunadasa, C. J. Chang, J. R. Long, *Nature,* **2010**, *464*, 1329; j) M. Rakowski Dubois, D. L. Dubois, *Acc. Chem. Res.,* **2009**, *42*, 1974; k) V. Artero, M. Chavarot-Kerlidou, M. Fontecave, *Angew. Chem. Int. Ed.,* **2011**, *50*, 7238; l) J. L. Dempsey, B. S. Brunschwig, J. R. Winkler, H. B. Gray, *Acc. Chem. Res.,* **2009**, *42*, 1995; m) T. R. Cook, D. K. Dogutan, S. Y. Reece, Y. Surendranath, T. S. Teets, D. G. Nocera, *Chem. Rev.,* **2010**, *110*, 6474; n) M. G. Walter, E.

L. Warren, J. R. McKone, S. W. Boettcher, Q. Mi, E. A. Santori, N. S. Lewis, *Chem. Rev.,* **2010**, *110*, 6446; o) S. Losse, J. G. Vos, S. Rau, *Coord. Chem. Rev.,* **2010**, *254*, 2492.

17. a) R. Cui, H. Huang, Z. Yin, D. Gao, J.-J. Zhu, *Biosens. Bioelectron.,* **2008**, *23*, 1666; b) J. L. uñoz-Muñoz, F. Garcia-Molina, J. Berna, P. A. Garcia-Ruiz, R. Varon, J. Tudela, J. N. Rodriguez-Lopez, F. Garcia-Canovas, *Biochim. Biophys. Acta, Proteins Proteomics,* **2012**, *1824*, 647; c) J. Peng, L.-N. Feng, K. Zhang, X.-H. Li, L.-P. Jiang, J.-J. Zhu, *Chem. Eur. J.,* **2012**, *18*, 5261.
18. a) N. Song, C. J. Gagliardi, R. A. Binstead, M.-T. Zhang, H. Thorp, T. J. Meyer, *J. Am. Chem. Soc.,* **2012**, *134*, 18538; b) M. M. Walczak, D. A. Dryer, D. D. Jacobson, M. G. Foss, N. T. Flynn, *J. Chem. Educ.,* **1997**, *74*, 1195.
19. a) L. F. Warren, *Inorg. Chem.,* **1977**, *16*, 2814; b) S. M. Peng, C. T. Chen, D. S. Liaw, C. I. Chen, Y. Wang, *Inorg. Chim. Acta,* **1985**, *101*, L31; c) Y. Konno, N. Matsushita, *Bull. Chem. Soc. Jpn.,* **2006**, *79*, 1046; d) T. Bugarcic, A. Habtemariam, R. J. Deeth, F. P. A. Fabbiani, S. Parsons, P. J. Sadler, *Inorg. Chem.,* **2009**, *48*, 9444; e) M. Kapovsky, C. Dares, E. S. Dodsworth, R. A. Begum, V. Raco, A. B. P. Lever, *Inorg. Chem.,* **2012**, *52*, 169.
20. a) G. M. Roberts, C. A. Williams, J. D. Young, S. Ullrich, M. J. Paterson, V. G. Stavros, *J. Am. Chem. Soc.,* **2012**, *134*, 12578; b) R. Montero, A. P. Conde, V. Ovejas, R. Martinez, F. Castano, A. Longarte, *J. Chem. Phys.,* **2011**, *135*, 054308; c) G. A. King, T. A. A. Oliver, M. N. R. Ashfold, *J. Chem. Phys.,* **2010**, *132*, 214307.
21. a) K. Ujike, N. Akai, S. Kudoh, M. Nakata, *J. Mol. Struct.,* **2005**, *735-736*, 335; b) K. Ujike, S. Kudoh, M. Nakata, *Chem. Phys. Lett.,* **2004**, *396*, 288.
22. a) Y. Bing, L. Qiuye, I. Hideo, K. Tetsuya, Y. Jinhua, *Sci. Technol. Adv. Mater.,* **2011**, *12*, 034401; b) D. Wang, T. Kako, J. Ye, *J. Phys. Chem. C,* **2009**, *113*, 3785; c) D. Chen, J. Ye, *Chem. Mater.,* **2009**, *21*, 2327.
23. M. Cossi, G. Scalmani, N. Rega, V. Barone, *J. Chem. Phys.,* **2002**, *117*, 43.
24. A. K. Rappe, C. J. Casewit, K. S. Colwell, W. A. Goddard, W. A. Skiff, *J. Am. Chem. Soc.,* **1992**, *114*, 10024.
25. a) R. D. Bauernschmitt, R. Ahlrichs, *Chem. Phys. Lett.,* **1996**, *256*, 454; b) A. Dreuw, M. Head-Gordon, *Chem. Rev.,* **2005**, *105*, 4009.

26. H. Iikura, T. Tsuneda, T. Yanai, K. Hirao, *J. Chem. Phys.,* **2001**, *115*, 3540.
27. M. J. Frisch, G. W. Trucks, H. B. Schlegel, G. E. Scuseria, M. A. Robb, J. R. Cheeseman, G. Scalmani, V. Barone, B. Mennucci, G. A. Petersson, H. Nakatsuji, M. Caricato, X. Li, H. P. Hratchian, A. F. Izmaylov, J. Bloino, G. Zheng, J. L. Sonnenberg, M. Hada, M. Ehara, K. Toyota, R. Fukuda, J. Hasegawa, M. Ishida, T. Nakajima, Y. Honda, O. Kitao, H. Nakai, T. Vreven, J. A. Montgomery, J. E. Peralta, F. Ogliaro, M. Bearpark, J. J. Heyd, E. Brothers, K. N. Kudin, V. N. Staroverov, R. Kobayashi, J. Normand, K. Raghavachari, A. Rendell, J. C. Burant, S. S. Iyengar, J. Tomasi, M. Cossi, N. Rega, J. M. Millam, M. Klene, J. E. Knox, J. B. Cross, V. Bakken, C. Adamo, J. Jaramillo, R. Gomperts, R. E. Stratmann, O. Yazyev, A. J. Austin, R. Cammi, C. Pomelli, J. W. Ochterski, R. L. Martin, K. Morokuma, V. G. Zakrzewski, G. A. Voth, P. Salvador, J. J. Dannenberg, S. Dapprich, A. D. Daniels, Ö. Farkas, J. B. Foresman, J. V. Ortiz, J. Cioslowski, D. J. Fox, Gaussian 09, Revision B.01. Wallingford CT, 2009.
28. R. L. Martin, *J. Chem. Phys.,* **2003**, *118*, 4775.
29. O. Kahn, *Molecular Magnetism*. Willey-VCH, New York, 1993, 380 pp.
30. G. R. Fulmer, A. J. M. Miller, N. H. Sherden, H. E. Gottlieb, A. Nudelman, B. M. Stoltz, J. E. Bercaw, K. I. Goldberg, *Organometallics,* **2010**, *29*, 2176.
31. M. C. Burla, R. Caliandro, M. Camalli, B. Carrozzini, G. L. Cascarano, L. De Caro, C. Giacovazzo, G. Polidori, R. Spagna, *J. Appl. Crystallogr.,* **2005**, *38*, 381.
32. CrystalStructure 3.8.2, Crystal Structure Analysis Package; Rigaku and Rigaku/MSC: The Woodlands, TX, 2000−2006.
33. G. Sheldrick, SHELX-97 Program for Crystal Structure Solution and the Refinement of Crystal Structures, Institüt für Anorganische Chemie der Universität Göttingen, Tammanstrasse 4, D-3400 Göttingen, Germany, 1997.
34. A. Czapik, M. Gdaniec, *Acta Crystallogr. Sect. C: Cryst. Struct. Commun.,* **2010**, *C66*, o198.
35. a) I. L. Eremenko, M. A. Kiskin, I. G. Fomina, A. A. Sidorov, G. G. Aleksandrov V. N. Ikorskii, Y. G. Shvedenkov, Y. V. Rakitin, V. M. Novotortsev, *J. Cluster Sci.,* **2005**, *16*, 331; b) T. B. Mikhailova, A. E. Malkov, A. A. Sidorov, I. G. Fomina, G. G. Aleksandrov, I.

F. Golvaneva, V. M. Dem'yanovich, V. M. Novotortsev, V. N. Ikorskii, I. L. Eremenko, *Zh. Neorg. Khim.,* **2002**, *47*, 1829.

36. A. Czapik, M. Gdaniec, *Acta Crystallogr. Sect. C: Cryst. Struct. Commun.,* **2010**, *C66*, o198.
37. a) Y. Bing, L. Qiuye, I. Hideo, K. Tetsuya, Y. Jinhua, *Sci. Technol. Adv. Mater.,* **2011**, *12*, 034401; b) D. Wang, T. Kako, J. Ye, *J. Phys. Chem. C,* **2009**, *113*, 3785; c) D. Chen, J. Ye, *Chem. Mater.,* **2009**, *21*, 2327.
38. a) B. Milliken, L. Borer, J. Russell, M. Bilich, M. M. Olmstead, *Inorg. Chim. Acta,* **2003**, *348*, 212; b) H. Y. Cheng, S. M. Peng, *Inorg. Chim. Acta,* **1990**, *169*, 23.
39. N. P. Loveless, K. C. Brown, R. H. Horrocks, *J. Org. Chem.,* **1981**, *46*, 1182.
40. S. I. Gorelsky, E. S. Dodsworth, A. B. P. Lever, A. A. Vlcek, *Coord. Chem. Rev.,* **1998**, *174*, 469.
41. J. Piera, J.-E. Bäckvall, *Angew. Chem. Int. Ed.,* **2008**, *47*, 3506.
42. The ^{1}H NMR sample of Figure 21a was prepared by the treatment of three equivalents of Opda and $[Fe^{II}(H_2O)_6](ClO_4)_2$, and ten equivalents of HQ in THF. Then, after stirring the mixture for 5 min, the THF was evaporated and the mixture was extracted using degassed DMSO-d_6. The Opdas coordinated to Fe^{II} ion were replaced by DMSO-d_6 solvent molecules, probably because of the stronger coordinating property and excess amounts of DMSO-d_6 compared with Opda (see also Reference 43).
43. a) A. P. White, K. N. Robertson, T. S. Cameron, B. V. Liengme, D. B. Leznoff, S. Trudel, M. A. S. Aquino, *Can. J. Chem.,* **2007**, *85*, 372; b) A. Müller, H. Bögge, U. Schimanski, M. Penk, K. Nieradzik, M. Dartmann, E. Krickemeyer, J. Schimanski, C. Römer, M. Römer, H. Dornfeld, U. Wienböker, W. Hellmann, M. Zimmermann, *Monatsh. Chem.,* **1989**, *120*, 367; c) R. M. Silva, C. Gwengo, S. V. Lindeman, M. D. Smith, G. J. Long, F. Grandjean, J. R. Gardinier, *Inorg. Chem.,* **2008**, *47*, 7233.

Chapter 6

Photocatalytic Hydrogen Evolution from MeOH by *o*-Aminophenol, *o*-Aminophenolate, and Its Fe(II) Complex at Room Temperature

Abstract

Exposing *o*-aminophenol (ApH_2) and deprotonated *o*-aminophenolate (ApH^-) in MeOH to photoirradiation (289 ± 10 nm) at room temperature for 5 h resulted in the formation of 4.1 (external quantum yield, Φ_{H2} = 2.9%) and 5.2 eq. H_2 (Φ_{H2} = 3.7%) per ApH_2 and ApH^-, respectively, under concomitant formation of HCHO. In addition, the complexation of Fe(II) with ApH^- afforded *trans*-[$Fe^{II}(ApH)_2(MeOH)_2$] (**1**), which also exhibited photochemical activity, generating 6.7 eq. H_2 (Φ_{H2} = 4.8%) per **1**. Photoirradiation of **1** in MeOH for 24 h at 350 ± 10 nm generated 0.48 eq. of H_2 (Φ_{H2} = 0.019%) per **1**, suggesting that complex **1** enables the photochemical dehydrogenation of MeOH using longer-wavelength light. Mechanistic investigations using MeOH-d_3 or 2-methylpropane-2-thiol revealed the photo-induced formation of hydrogen radicals. These photochemical reactions represent the first example of MeOH dehydrogenation at room temperature, catalyzed by organophotocatalysts (ApH_2 and ApH^-) and the Fe(II) complex (**1**).

6-1. Introduction

Molecular hydrogen (H_2) is one of the most promising energy sources of the future.[1] As gaseous H_2 is difficult to handle and store, hydrogen storage materials have been the subject of intensive investigation in recent years.[2] Among a number of materials, methanol (MeOH) has been one of the most fascinating hydrogen carriers,[3] which is used in fuel cells[4] due to its high gravimetric H_2 content (12.6 wt% H_2). Since the generation of H_2 from MeOH is an endothermic reaction, both dehydrogenation catalysts and high temperatures (T = 200-300 °C) are usually required for this reaction to proceed,[5] and several heterogeneous[5] and homogeneous[6,7] catalyst systems have been investigated in this context.[8] For example, Beller *et al*. reported that the use of [Ru^{II}(H)Cl(PNP)] (PNP = $HN(C_2H_4P\textit{i}\text{-}Pr_2)_2$) and the non-precious metal complex [Fe^{II}(H)(BH_4)(PNP)] allow a decrease of the undesirably high reaction temperatures to 90 °C for the dehydrogenation of MeOH.[6] In the proposed reaction mechanisms, the tridentate PNP ligand abstracts the hydroxyl proton of MeOH in the presence of a base. After the proton abstraction, the hydride is transferred from the α-carbon of the resulting MeO^- moiety to the metal.[6a] Another example was reported by Grützmacher *et al*., who demonstrated the dehydrogenation of MeOH catalyzed by a [Ru^{II}(H)(1,4-bis(5H-dibenzo [a,d]cyclohepten-5-yl)-1,4-diazabuta-1,3-diene)]$^-$ complex at 90 °C.[7] The proposed reaction mechanism involves ligand-centered evolution of H_2 from the starting state, followed by proton and hydride extraction from MeOH. The key steps in these cases are electron and proton transfers from MeOH to both metal and ligand sites.[8]

Even though intensive investigations have been carried out, options to lower the temperature of the MeOH dehydrogenation and the development of non-precious metal-based catalysts still remain limited. Among several possibilities, photochemical reactions represent a promising strategy to lower the reaction temperature.[9,10] Some heterogeneous photocatalysts represent relatively high efficiencies in the H_2 production ($\leq \Phi_{H2}$ = 32.5%[9a]) in the presence of MeOH (Table 1).[9] Conversely, only a small number of homogeneous molecular catalysts have been

developed despite the advantages of homogenous system in terms of its designability and diversity:[10] Saito *et al*. reported the dehydrogenation of MeOH and the concomitant generation of catalytic amounts of H_2 by using Rh, Pd, and Ir-based precious metal catalysts at 64-65 °C,[10a,10b] whereas values of Φ_{H2} were not estimated in these systems. These pioneering studies motivated us to develop homogeneous photocatalysts for the dehydrogenation of MeOH at ambient temperature.[10a,10b] However, even though these studies made substantial progress, some challenges remained unsolved.

Table 1. Quantum yields (Φ and Φ_{H2}) of previously reported catalysts for the photochemical dehydrogenation of MeOH

Catalysts	Φ (%)[a]	Φ_{H2} (%)[b]	Solution	λ (nm)	T (°C)	Ref
$KCa_2Nb_{2.97}Rh_{0.03}O_{10}$	65	32.5	19 vol% H_2O/MeOH	300	–[c]	9a
	0.0054	0.0027	19 vol% H_2O/MeOH	410	–[c]	9a
La, Cr-codoped $SrTiO_3$:Pt	25.6	12.8	19 vol% H_2O/MeOH	425	–[c]	9b
$SrTiO_3$:Rh(2%)	13.3	6.65	10 vol% H_2O/MeOH	420	–[c]	9c
$CaFe_4O_4/MgFe_2O_4$	10.1	5.05	15 vol% H_2O/MeOH	>420	–[c]	9d
Ta_3N_5:Pt	6	3	20 vol% H_2O/MeOH	>420	–[c]	9e
Pt(0.1 wt%)/$SrTiO_3$:Rh(1%)	5.2	2.6	10 vol% H_2O/MeOH	420	–[c]	9f
$RbPb_2Nb_3O_{10}$:Pt	5	2.5	17 vol% H_2O/MeOH	420-500	–[c]	9g
$SrSnO_3$:Pt(0.5 wt.%)	4.6	2.3	14 vol% H_2O/MeOH	300	–[c]	9h
Graphite oxide	2.7	1.35	20 vol% H_2O/MeOH	UV	–[c]	9i
$PbBi_2Nb_2O_9$:Pt(1 wt%)	0.95	0.475	15 vol% H_2O/MeOH	>420	–[c]	9j
Pt (0.4 wt%)/$(Sr_{0.95}$-$Cr_{0.05})TiO_3$	0.86	0.43	19 vol% H_2O/MeOH	420.4	–[c]	9k
Ta_3N_5:Pt(3.0% w/w)	0.1	0.05	10 vol% H_2O/MeOH	>420	–[c]	9l
cis-$Rh_2Cl_2(CO)_2(dpm)_2$[d]	–[c]	–[c]	10 vol% Acetone/MeOH	–[c]	64	10a
$Pd_2Cl_2(dpm)_2$[d]	–[c]	–[c]	10 vol% Acetone/MeOH	–[c]	64	10a
$Et_4N[IrH(SnCl_3)_5]$	–[c]	–[c]	MeOH	–[c]	65	10b
$RuH_2(N_2)(PPh_3)_3$	–[c]	–[c]	MeOH with NaOH[e]	–[c]	150	10c
$RuH_2(PPh_3)_3$	–[c]	–[c]	MeOH with NaOH[e]	–[c]	150	10c

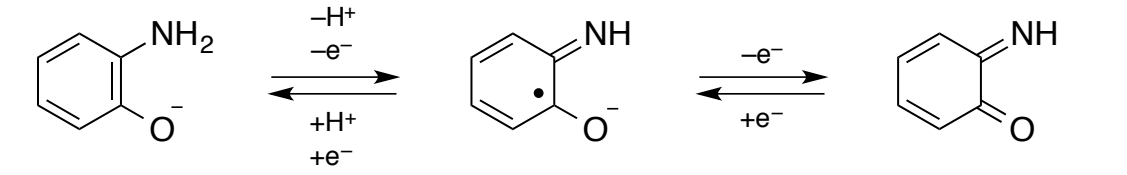
[a] Quantum yields (Φ) were estimated based on the number of electrons. [b] Quantum yields (Φ_{H2}) were estimated based on the amount of evolved H_2. [c] Not mentioned. [d] dpm = bis(diphenylphosphino) methane. [e] [NaOH] = 1 M.

The previous chapter was demonstrated that $[Fe^{II}(opda)_3]^{2+}$ (opda = *o*-phenylenediamine) can photochemically generate H_2 in tetrahydrofuran.[11] In this reaction, opda does not only act as a chelating ligand *via* the two amino groups, but also as a multi-electron and proton-pooling site for the photochemical generation of H_2 at ambient temperature. It was proposed that H_2 is released as a result of the photochemical activation of the N–H bonds in the amino moieties of opda, accompanied by an oxidation to afford the oxidized *semi*-benzoquinodiimine or *o*-benzoquinodiimine species.

In contrast to the homoleptic coordination of opda *via* two amino groups, the corresponding *o*-aminophenolato ligand (ApH^-) displays a heteroleptic coordination pattern *via* one amino and the deprotonated hydroxyl group, which should facilitate the transfer of two electrons and one proton (Scheme 1).[12,13] Pino *et al*. have reported photochemical reactions and the associated mechanism for *o*-aminophenol (ApH_2) in the gas phase, including a $^1\pi$-π^* excited state, a $^1\pi$-π^*/$^1\pi$-σ^* conical intersection, and the homolytic cleavage of the O–H bond that generates hydrogen radicals.[14] This characteristic reactivity, which operates at the picosecond timescale in the gas phase at 65-90 °C, has recently been labeled "excited state hydrogen detachment (ESHD)". However, there is a considerable gap between the ESHD of aromatic amines and alcohols and the photochemical hydrogen evolution reaction (PHER) of $[Fe^{II}(opda)_3]^{2+}$, because the generation of H_2 has not yet been reported in the ESHD system.

Recently, successful examples on the elucidation of electron- and proton-transfer properties of the transition metal complexes of ApH^-, together with the characterization of isq^- complexes have been reported, and these studies are currently under extensive investigation as models for non-heme-type iron dioxygenase.[12,13] In contrast to these sophisticated examples for the reactivity of ApH_2 derivatives, which proceed under the exclusion of light, examples on photochemical reactions still remain elusive. Here, this chapter demonstrates the photochemical dehydrogenation of MeOH at room temperature catalyzed by ApH_2, ApH^-, and *trans*-$[Fe^{II}(ApH)_2(MeOH)_2]$ (**1**), together with the mechanism for the photochemical generation of hydrogen radicals.

Scheme 1. Electron- and proton-transfer properties of ApH^-.



o-aminophenolate (ApH^-) | *o*-iminosemiquinonate (ISQ^-) | *o*-iminobenzoquinone (IBQ)

6-2. Experimental Section

General Procedures. Unless noted otherwise, all synthetic operations and measurements were carried out under an atmosphere of N_2 using Schlenk-line techniques. $Fe^{II}(ClO_4)_2 \cdot 6H_2O$, $Cu^{II}(OAc)_2$ (OAc = acetate), HCO_2H, acetic acid (AcOH), ammonium acetate (NH_4OAc), acetyl acetone, calcium oxide (CaO), and H_2SO_4 were purchased from Wako Pure Chemical Industries. Dehydrated MeOH, dichloromethane (CH_2Cl_2), and MeOH-d_4 were purchased from Kanto Chemical Co. Inc. Tetra-*n*-butylammonium hydroxide (TBAOH) in MeOH (37%), which was used after the removal of MeOH, an aqueous solution of HCHO (37%), 2-methylpropane-2-thiol (*t*-BuSH), di-*tert*-butyl disulfide (*t*-Bu_2S_2), 3-carbamyl-1-methyl pyridinium chloride (NADCl), and ApH_2 were purchased from Tokyo Chemical Industry Co. Ltd. Prior to use, ApH_2 was washed with CH_2Cl_2 and dried *in vacuo* for several minutes, while *t*-BuSH was used after stirring with CaO for 12 h, followed by distillation. MeOH-d_3 was purchased from Sigma-Aldrich. 2-Aminophenoxazine-3-one (APX) was prepared according to a reported procedure.[27] All solvents that were used under anaerobic conditions were thoroughly degassed by at least five freeze-pump-thaw cycles immediately prior to use. **Caution!** Although we did not experience any difficulties with perchlorate salts, these should be regarded as potentially explosive, and therefore handled with utmost care.

***trans*-$[Fe^{II}(ApH)_2(MeOH)_2]$ (1).** A colorless MeOH solution (5 mL) of ApH_2 (144 mg, 1.31 mmol) and TBAOH (340 mg, 1.31 mmol) was slowly deposited onto an aqua-blue MeOH (5 mL) solution of $Fe^{II}(ClO_4)_2 \cdot 6H_2O$ (240 mg, 0.661 mmol) under an atmosphere of N_2. After leaving the solution to stand at 3 °C for a period of 5 d, colorless crystals of **1**, suitable for X-ray crystallographic analysis, were obtained. Crystalline **1** was isolated by filtration, washed with MeOH (2 × 4 mL), and dried *in vacuo* (yield: 59%). Crystals of **1** were found to be highly hygroscopic, and always contained small amounts of water. Anal. Found: C, 49.49; H, 6.08; N, 8.27. Calc. for $C_{14}H_{20.4}FeN_2O_{4.2}$ (**1** + 0.2 H_2O): C, 49.49; H, 6.05; N, 8.24.

***trans*-[Cu^{II}(ApH)$_2$(H_2O)] (2).** A colorless MeOH (10 mL) solution of ApH_2 (200 mg, 2.0 mmol) was added to 20 mL of a blue aqueous solution of $Cu^{II}(OAc)_2$ (100 mg, 1.0 mmol), resulting in the formation of an aqua-blue suspension after stirring the reaction mixture for 5 min. Complex **2** was isolated as an aqua-blue powder by filtration, washed with MeOH (3 × 3 mL) and Et_2O (2 × 3 mL), before being dried *in vacuo* (yield: 83%). Anal. Found: C, 48.13; H, 4.75; N, 9.17. Calc. for $C_{12}H_{14}CuN_2O_3$ (**2**): C, 48.40; H, 4.74; N, 9.41. Single crystals, suitable for X-ray crystallographic analysis, were obtained by layering an aqueous solution of ApH_2 onto an aqueous solution of $Cu^{II}(OAc)_2$.

Equipment for the Photochemical Hydrogen Evolution Reactions. A 200 W Hg-Xe lamp (LC8, Hamamatsu Photonics) with a quartz light guide (ϕ5 L9588) was used as a light source. For photoirradiation at 289 ± 10 nm, a 289 nm band pass filter (BPF) was used, while a 350 nm BPF (03 type filter) was used for irradiation at 350 ± 10 nm. For photoirradiation at 460 ± 10 nm, a 100 W Xe lamp (LAX-103, Asahi Spectra Co. Ltd.) with a quartz light guide (ϕ5 × 1000L UD0030), a VIS-type mirror module, and a 460 nm BPF were used. The intensity of the light was measured using a power meter (NOVA, Ophir optronics Ltd.) and a thermopile sensor (3A, Ophir optronics Ltd.). The released quantities of H_2, HD, and D_2 were measured using a gas chromatograph (GC, Shimadzu GC-2014), equipped with a 2 m column packed with either MS5A at 70 °C using Ar carrier gas or 8% KOH alumina at 77 K using He carrier gas, respectively.

Photochemical Hydrogen Evolution Reaction (PHER) with ApH_2 in MeOH. A handmade Schlenk flask-equipped quartz vessel (V = 115 mL) was charged with 1 mL of a methanolic ApH_2 solution that was prepared by dissolving ApH_2 (4.36 mg, 0.04 mmol) in MeOH (20 mL). Subsequently, the solution was exposed to photoirradiation in a water bath at room temperature. Gas samples (0.3 mL) were collected from the headspace of the vessel using a gas-tight syringe (Tokyo Garasu Kikai Co. Ltd.) and analyzed by GC (MS5A column).

PHER with ApH^- in MeOH. The quartz vessel was charged with 1 mL of a methanolic ApH^- solution that was prepared by dissolving ApH_2 (4.36 mg, 0.04 mmol) and TBAOH (10.4 mg, 0.04 mmol) in MeOH (20 mL). Subsequently, the solution was exposed to photoirradiation in a water bath at room temperature. Gas samples (0.3 mL) were collected from the headspace of the vessel using a gas-tight syringe and analyzed by GC, similar to the aforementioned procedure.

PHER with 1 in MeOH. Crystals of **1** were filtered and washed with MeOH (2 × 4 mL), before being dissolved in MeOH (4 mL) to afford a saturated pale-orange MeOH solution of **1**. Subsequently, 1 mL of this solution was transferred into the quartz vessel. The reaction and analysis were carried out as described above.

Analysis of HCHO in PHER Solutions.[16] An aqueous solution of AcOH (100 mL, 2.26 M) was prepared by dissolving 12.9 mL of AcOH (226 mmol) in water under an atmosphere of air. Subsequently, an aqueous solution of NH_4OAc (200 mL, 2.25 M) was prepared by dissolving NH_4OAc (34.68 g, 450 mmol) in water (200 mL). An AcOH/NH_4OAc buffer solution was prepared by combining 8 mL of the aqueous AcOH solution with 200 mL of the aqueous NH_4OAc solution. An aqueous solution (1000 mL) of acetyl acetone and ethanol was prepared by dissolving 7 mL of acetyl acetone and 14 mL of ethanol in water (979 mL). Methanolic standard solutions of HCHO (0, 1, 5, and 10 mM) were prepared by diluting a methanolic HCHO solution (37%) with appropriate amounts of dehydrated MeOH. A mixture of the methanolic standard solutions of HCHO (0.1 mL), the AcOH/NH_4OAc buffer solution (2.0 mL), and the aqueous acetyl acetone solution (2.0 mL) was heated to 60 °C for 15 min. Then, the solution was cooled to room temperature, and 20 μL of the reaction mixture were analyzed by high-performance liquid chromatography (HPLC), using a Synergi 4u Hydro-RP80A column (Phenomenex) and H_2O/MeCN (*v*/*v* = 85/15) at a flow rate of 1.0 mL/min. The targeted 3,5-diacetyl-1,4-dihydro-2,6-lutidine, which was generated from HCHO, was detected at 370

nm, and the calibration curves gave the apparent linearity, a quantitative analysis of the compound in the PHER solutions should be possible (Figure 5a). In order to estimate the amount of HCHO produced in the PHER solutions, 0.1 mL of the corresponding reaction mixtures were used instead of standard solutions.

Analysis of HCO_2H in PHER Solutions. Methanolic standard solutions of HCO_2H (0, 0.5, 1, 2, and 4 mM) were prepared from diluting formic acid with MeOH in water under an atmosphere of air. 500 μL of each solution were treated with 5 μL of H_2SO_4 at room temperature and stirred for 15 min. These HCO_2H standard solutions were analyzed by HPLC using a Synergi 4u Hydro-RP80A column (Phenomenex) and H_2O/MeCN (*v*/*v* = 95/5) at a flow rate of 1.0 mL/min. Quantities of HCO_2H were calculated based on the detected methyl formate at 210 nm, and the calibration curves gave the apparent linearity, a quantitative analysis of the compound in the PHER solutions should be possible (Figure 5b). In order to estimate the amount of HCO_2H produced in the PHER solutions, 500 μL of the corresponding reaction mixture were used instead of standard solutions.

PHER with 1 in MeOH-d_3. All reactions and analyses were carried out as described above, except that **1** was dissolved in MeOH-d_3, and that an 8% KOH alumina column was used for the GC analysis. The H_2 standards were detected at 5.0 (*p*-H_2) and 6.3 min (*o*-H_2) (Figure 11a). D_2 gas was generated from the reaction of MeOH-d_4 with sodium metal, and the corresponding peaks were detected at 7.8 (*p*-D_2) and 8.4 min (*o*-D_2) (Figure 11b). HD gas was generated from the reaction of a MeOH/MeOH-d_4 (*v*/*v* = 1/1) mixture with sodium metal, and the corresponding signals for HD were detected at 6.4 min (Figure 11c). Since pure HD gas was unobtainable, the calibration and quantitative estimation of generated HD could not be carried out.

Photochemical Reactions using ApH_2 and 1 in the Presence of Scavengers. All reactions were carried out as described above for the PHER procedures, except for using a quartz NMR

tube as the reaction vessel and MeOH-d_4 as the solvent. ApH_2 or **1** was dissolved in degassed MeOH-d_4 (ApH_2: 2 mM; **1**: 1 mM) with *t*-BuSH or NADCl (2 mM), before the solutions were analyzed by ^{1}H NMR spectroscopy prior and posterior to photochemical reactions.

External Quantum Yield (Φ_{H2}) Calculations. MeOH solutions of ApH_2, ApH^-, and **1** were irradiated at λ = 289 ± 10 nm or 350 ± 10 nm. The amount of hydrogen evolved in the subsequent 5 h was used to calculate the external quantum yields (Φ_{H2}) according to the following equations:

$$\Phi_{H2} = \frac{N_{H2}}{N_P} \qquad \text{eq. 1}$$

$$N_P = \frac{E_I}{E_P} R \qquad \text{eq. 2}$$

$$N_{H2} = M_{H2} N_A \qquad \text{eq. 3}$$

$$E_I = I t \qquad \text{eq. 4}$$

$$E_P = h \frac{c}{\lambda} \qquad \text{eq. 5}$$

$$R = 1 - 10^{-A} \qquad \text{eq. 6}$$

wherein, N_{H2}, N_p, E_I, E_p, R, M_{H2}, N_A, I, t, h, c, and A refer to the number of the evolved H_2 molecules, the number of absorbed photons, the energy of the irradiation source, the energy of the irradiation photon, the proportion of the catalyst that is absorbing light, the mol number of the evolved H_2, the Avogadro constant, the optical intensity of the light, the irradiation time, the Planck constant, the speed of light in vacuum, and the absorbance of the catalyst in MeOH. The absorbance throughout the photoreaction was assumed to be constant at an optical length of 1.0 cm: ApH_2 (5.72 at λ = 289 nm), ApH^- (5.39 at λ = 289 nm), and **1** (7.76 at λ = 289 nm, 1.15 at λ = 350 nm).

Physical Measurements. ^{1}H NMR (500 MHz) spectra were measured on a JEOL EX-500 spectrometer. Elemental analyses were carried out on a Perkin-Elmer 2400 II CHN analyzer. UV-vis-NIR spectra (200-3300 nm) in solution or in the solid state (KBr pellets) were recorded on a Hitachi U-4100 spectrophotometer at 296 K. HPLC measurements were carried out on a Shimadzu LC-20AT liquid chromatograph, equipped with an SPD-20A UV-vis detector. Emission spectra were recorded on a Horiba fluoromax using MeOH solutions of ApH_2 and **1** at 296 K.

Crystallographic Data Collection and Structure Refinement. Single-crystal X-ray diffraction patterns were recorded on a Rigaku VariMax with Saturn equipment (**1**), or on a Rigaku AFC-7R diffractometer, equipped with a Mercury CCD area detector (**2**). In both cases, graphite-monochromated Mo-Kα radiation (λ = 0.71069 Å) was used. Single crystals of suitable size and quality were selected under paraffin oil or silicon grease, and mounted onto MicroMounts (MiTeGen), and cooled to 93 (**1**) or 200 K (**2**) by an N_2 flow-type temperature controller. Molecular structures were solved by direct methods (SIR2004),[17] which allowed the successful location of all non-hydrogen atoms within the unit cell. All calculations were carried out using the CrystalStructure software package,[18] except for refinement calculations, which were carried out using SHELXL-97.[19] A summary of the crystallographic data for **1** and **2** is shown in Table 2. Full crystallographic details were deposited at the Cambridge Crystallographic Data Centre (CCDC) as supplementary publications CCDC-1062112 (**1**) and CCDC-1418535 (**2**).

Table 2. Crystallographic data for **1** and **2**

	1	**2**
Formula	$C_{14}H_{20}FeN_2O_4$	$C_{12}H_{14}CuN_2O_3$
fw	336.17	297.80
Crystal size (mm^3)	0.40 × 0.19 × 0.13	0.20 × 0.12 × 0.02
Crystal system	monoclinic	triclinic
Space group	$P2_1/c$ (No. 14)	P-1 (No. 2)
a (Å)	8.889(9)	9.666(4)
b (Å)	5.114(5)	9.702(4)
c (Å)	16.29(2)	12.945(5)
α (°)	90	82.884(13)
β (°)	100.40(2)	80.779(14)
γ (°)	90	89.707(18)
V ($Å^3$)	728.4(12)	1189.0(8)
T (K)	93	200
Z	2	4
D_{calc} (g cm^{-3})	1.533	1.664
F (000)	352.00	612.00
μ(Mo Kα) (cm^{-1})	10.513	18.381
Measured reflections	3873	6102
Unique reflections	1604	4900
Refined parameters	16.54	326
GOF on F^2	1.194	1.240
R_{int}	0.0468	0.0410
R_1 [a]	0.0576	0.0633
wR_2 [b] (all data)	0.1559	0.1685

[a] $R_1 = \Sigma||F_o| - |F_c||/\Sigma|F_o|$. [b] $wR_2 = \{[\Sigma w(F_o^2 - F_c^2)^2]/[\Sigma w(F_o^2)^2]\}^{1/2}$.

6-3. Results and Discussion

6-3-1. Photochemical Hydrogen Evolution Reactions from ApH_2 and ApH^-

Figure 1 shows the UV-vis-NIR spectra of ApH_2 (2.00 mM) and ApH^- (2.00 mM), which were generated *in situ* by the treatment of ApH_2 with one equivalent of TBAOH. For both ApH_2 and ApH^-, two absorptions were observed at λ_{max} (ε / M^{-1} cm^{-1}) = 230 (6,260) and 285 nm (3,020), as well as at 230 (5,540) and 288 nm (2,630), respectively (Table 3). These bands were assigned to two π-π* transitions,[14,20] and the observed similarity of the spectral profiles indicates a negligible effect of the deprotonation of ApH_2 on the π-π* transitions.

Both MeOH solution of ApH_2 and ApH^- did not exhibit any signs of gas evolution under the exclusion of light. In contrast, the photoirradiation (289 ± 10 nm; 3.2 mW Hg-Xe lamp) of a MeOH solution of ApH_2 for 5 h induced the evolution of gas, and the GC analysis of a gaseous sample taken from the headspace of the reaction vessel allowed the detection of H_2 (Figure 2). After 5 h of photoirradiation (t_{irr} = 5 h), 4.1 eq. of H_2 per molecule of ApH_2 (Φ_{H2} = 2.9%) were

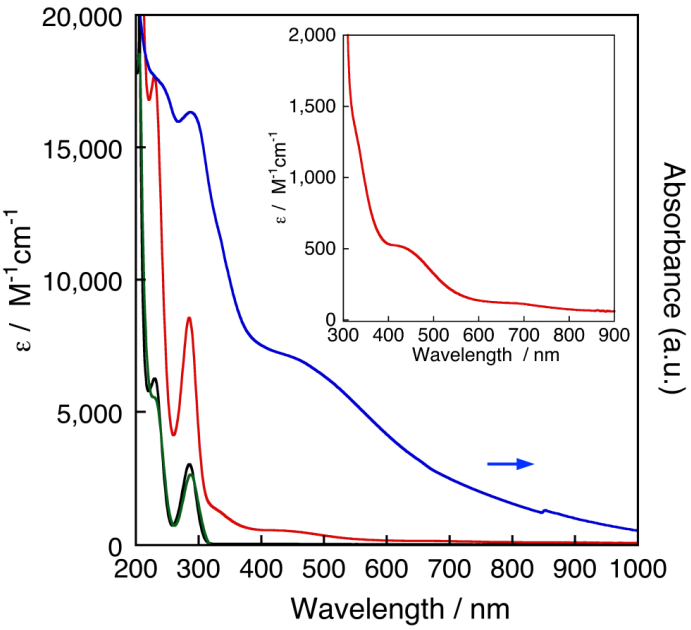


Figure 1. UV-vis-NIR spectra of ApH_2, ApH^-, and **1** in MeOH. [ApH_2 (black line)] = [ApH^- (green line)] = 2 mM; [**1** (red line)] = 1.35 mM. The ApH^- was generated *in situ* by the treatment of ApH_2 with TBAOH. The solid-state spectrum of **1** (KBr disk, blue line) is shown for comparison. The inset shows a magnification (300-900 nm) of the solution spectrum of **1**.

Table 3. Summary of the UV-vis-NIR spectroscopic data for ApH_2, ApH^-, **1**, and **2** in MeOH solution and in the solid state.

	State	λ / nm (ε / M^{-1} cm^{-1})				
ApH_2	Solution	230 (6,260)	285 (3,020)			
ApH^-	Solution	230 (5,540)	288 (2,630)			
1	Solid[a]	235[sh]	287	335[sh]	450[sh]	750[sh]
1	Solution	230 (17,690)	285 (8,550)	335 (1,210)[sh]	450 (480)[sh]	680 (118)[sh]
2	Solid[a]	235[sh]	293	340		
2	Solution	227 (17,400)	283 (8,800)	335 (440)[sh]	450 (130)[sh]	607 (80)

[a] KBr disk. [sh] Shoulder peak.

obtained (Figure 3, Table 4), while up to 6.5 eq. H_2 per molecule of ApH_2 were obtained after prolonged photoirradiation (t_{irr} = 24 h; Figure 4), suggesting that the reaction is not stoichiometric, but a catalytic. The deprotonated ApH^- form also exhibits similar PHER activity (Φ_{H2} = 3.7%) upon the irradiation at 289 ± 10 nm (Figures 3 and 4 and Table 4). Control reactions, using neat MeOH under the same conditions, did not show any PHER activity (Figure 3). Considering these PHER results and the aforementioned absorption spectra, it seems feasible to assume that the π-π* excitation on ApH_2 and ApH^- initiates the PHERs.

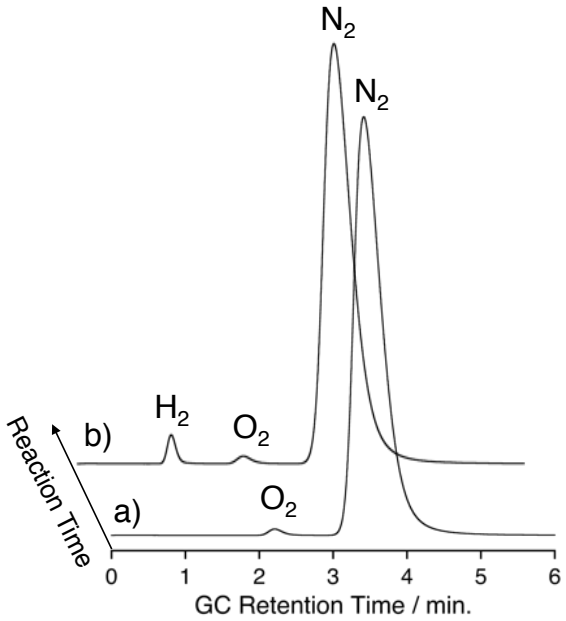


Figure 2. GC analysis for PHERs (λ = 289 ± 10 nm; 3.2 mW) of ApH_2 in MeOH (2 mM) after a) 0 h and b) 5 h.

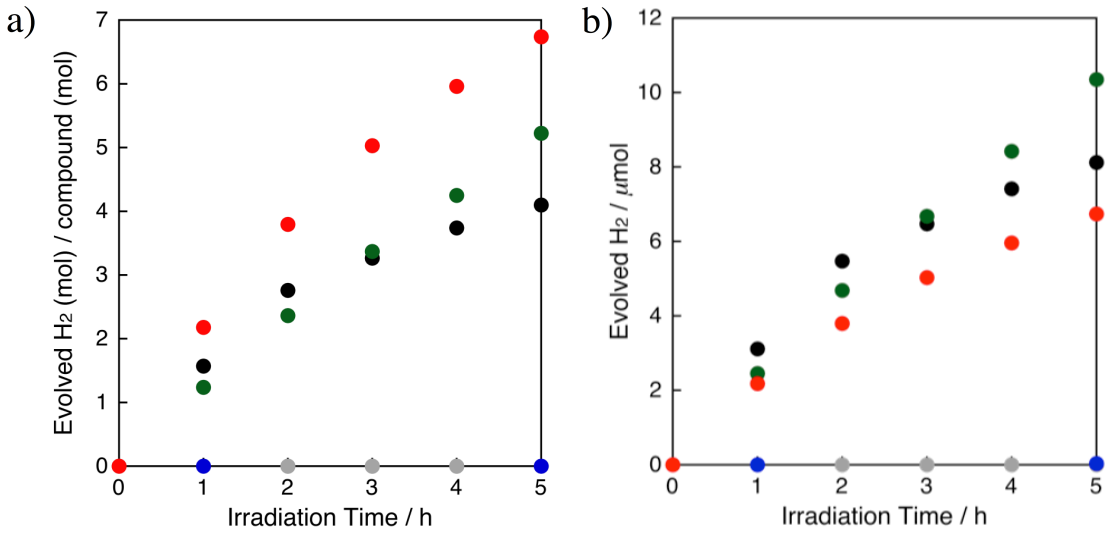


Figure 3. H_2 evolution from MeOH solutions of ApH_2, ApH^-, and **1** ($\lambda = 289 \pm 10$ nm, 3.2 mW). a) Evolution of H_2 (mol) per compound (mol) and b) evolution of H_2 (μmol) as a function of PHER time for MeOH solutions of ApH_2 (2 mM; black circles), ApH^- (2 mM; green circles), **1** (1 mM; red circles), and $Fe^{II}(ClO_4)_2 \cdot 6H_2O$ (1 mM; blue circles), together with pure MeOH (gray circles).

Table 4. PHER products for ApH_2, ApH^-, and **1** in MeOH.[a]

Compound	λ_{ex} (nm)	t_{irr} (h)	eq. per compound			Φ_{H2} (%)
			H_2	HCHO[b]	HCO_2H[c]	
ApH_2	289 ± 10	5	4.1	3.3	N. D.[d]	2.9[e]
ApH^-	289 ± 10	5	5.2	4.1	N. D.[d]	3.7[e]
1	289 ± 10	5	6.7	6.8	N. D.[d]	4.8[e]
ApH_2	289 ± 10	24	6.5	4.9	0.7	
ApH^-	289 ± 10	24	14.1	14.5	0.7	
1	289 ± 10	24	14.9	10.2	0.96	
ApH_2	350 ± 10	24	N. D.[d]	N. D.[d]	N. D.[d]	
ApH^-	350 ± 10	24	N. D.[d]	N. D.[d]	N. D.[d]	
1	350 ± 10	24	0.48[f]	0.99[f]	N. D.[d]	0.019[e]

[a] $[ApH_2] = [ApH^-] = 2$ mM; [**1**] = 1 mM. [b] Detected as 3,5-diacetyl-1,4-dihydro-2,6-lutidine. [c] Detected as methyl formate. [d] Not detected. [e] External quantum yields are estimated based on the amount of evolved H_2 at $t_{irr} = 5$ h. [f] Possibly associated with an increased experimental error, due to the small amount of product generated.

In general, oxidation of MeOH should afford oxidized species such as formaldehyde (HCHO),[10] formic acid (HCO_2H),[10] and CO_2.[6] After PHER of ApH_2 (t_{irr} = 5 h), HPLC analysis revealed that 3.3 eq. of HCHO per molecule of ApH_2 were generated (Table 4 and Figure 5a), corroborating a photochemical dehydrogenation of MeOH. Furthermore, prolonged PHER (t_{irr} = 24 h) afforded a small amount of HCO_2H in addition to H_2 and HCHO (Table 4 and Figure 5b). This reaction thus represents the first example of an organophotocatalyst promoting the photochemical dehydrogenation of MeOH to generate H_2. In particular, the external quantum

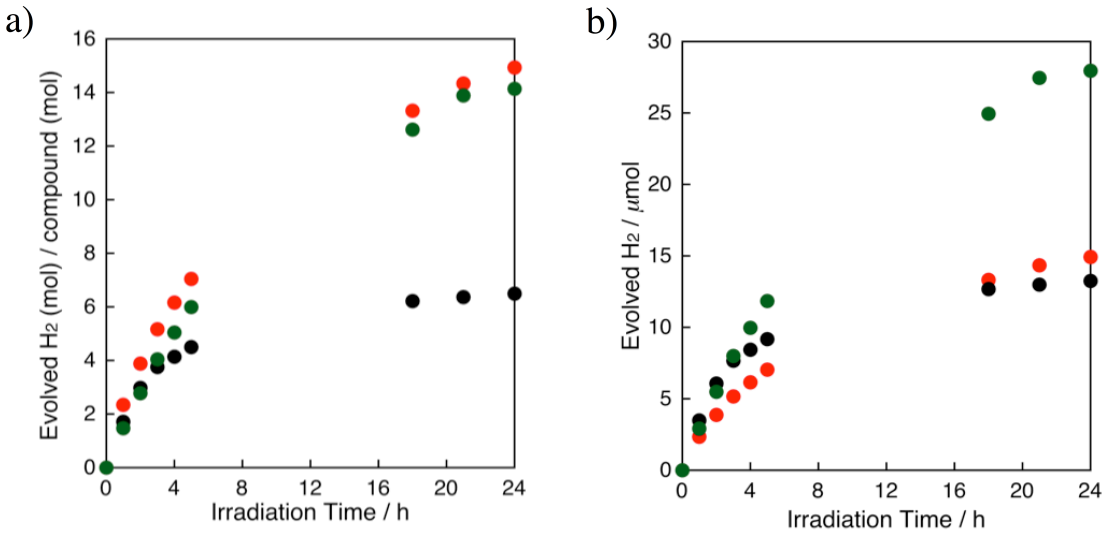


Figure 4. Evolution of a) H_2 (mol) per compound (mol), and b) H_2 (μmol) as a function of PHER time (λ = 289 ± 10 nm; 3.2 mW) of MeOH solutions of ApH_2 (2 mM; black circles), ApH^- (2 mM; green circles), and **1** (1 mM; red circles).

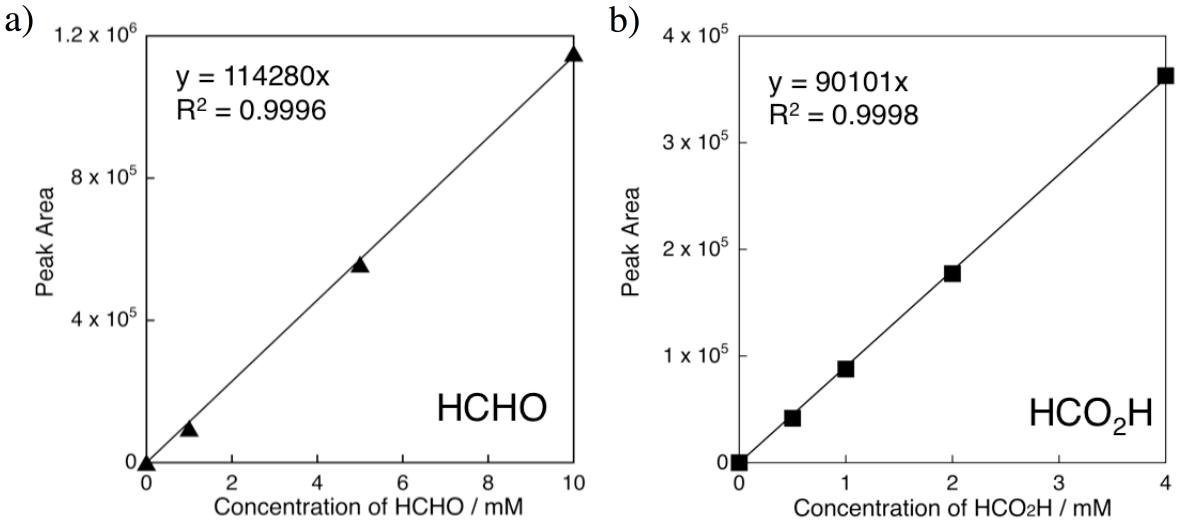


Figure 5. HPLC calibration curves for a) HCHO and b) HCO_2H.

yields (ApH_2: Φ_{H2} = 2.9; ApH^-: Φ_{H2} = 3.7%) are comparable to those of previously reported photocatalysts (Table 1).[9e-9h]

6-3-2. PHER from *trans*-[$Fe^{II}(ApH)_2(MeOH)_2$] (1)

Mixing two equivalents of ApH_2 and TBAOH with $Fe^{II}(ClO_4)_2 \cdot 6H_2O$ in MeOH under an atmosphere of N_2 afforded colorless crystals of **1**. The molecular structure of **1** is shown in Figure 6, and selected bond distances are summarized in the Table 5. The structure of **1** is characterized by a pseudo-octahedral Fe atom, which is located on an inversion center, and two bidentate NO ligands that occupy the equatorial positions, while two monodentate O ligands reside on the apical positions. The two chelating ligands adopt *trans* geometry, most likely to reduce steric repulsion.[22] The assignment of the two chelating ligands requires great care, as these could be present as either ApH^-, ISQ^-, or IBQ (Scheme 1).[12,13] In complex **1**, the observed C–N and C–O bond distances of 1.461(5) and 1.342(5) Å, respectively, suggest a single bond character for these bonds.[11,13,23] Moreover, the observed C–C bond distances of 1.385-1.417(6) Å within the six-membered ring suggest high levels of aromaticity. The ApH_2 contains one hydroxyl and two amino protons, which can be deprotonated by TBAOH (1

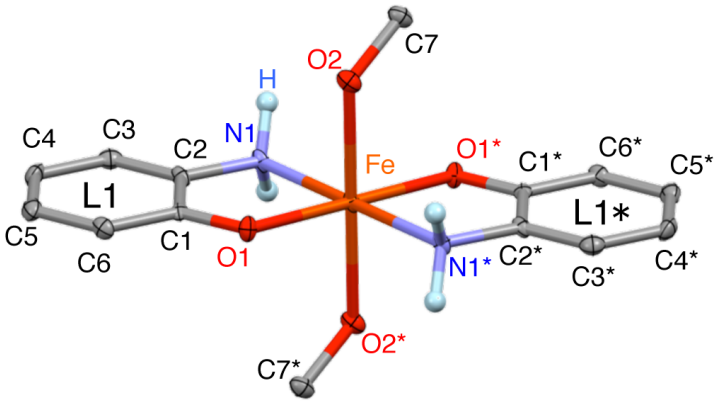
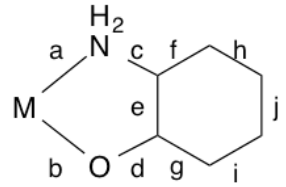


Figure 6. Molecular structure of **1**. Atomic displacement parameters are set at 50% probability; color code: Fe = orange, O = red, N = light blue, and C = dark gray; ball-and-stick plots for N-bound hydrogen atoms (aqua), while all other hydrogen atoms are omitted for clarity. C1/C1*, C2/C2*, C3/C3*, C4/C4*, C5/C5*, C6/C6*, C7/C7*, N1/N1*, N2/N2*, O1/O1*, and O2/O2* denote pairs of crystallographically equivalent atoms related by the symmetry operation 2–*x*, –*y*, 2–*z*.

eq.) to give monoanionic $C_6H_4NOH_2^-$, and previous reports on Fe(II) complexes of ApH^- have shown that it is possible to deprotonate the hydroxyl proton in ApH_2 selectively.[13] As the Fe–O1 (2.048(3) Å) and Fe–N1 (2.214(4) Å) bond distances in **1** are comparable with those in these examples (Fe–O: 1.931-1.994(2) Å; Fe–N: 2.212-2.299(7) Å),[13] the structure of the chelating ligands is consistent with that of ApH^-. Furthermore, the selective deprotonation of the hydroxyl proton was consistent with typical pK_a values for aromatic amines (*e.g.* pK_a aniline = 30.6)[24] and alcohols (*e.g.* pK_a phenol =18.0).[25] The observed Fe–O2 bond distance (2.229(3) Å) is comparable to those of typical Fe^{II}–HOMe bonds (2.205(16) Å),[26] while it is substantially longer than typical Fe^{II}–OMe bonds (1.782(3) Å).[27] Accordingly, the axial ligands should be MeOH ligands. Moreover, the Fe–N1, Fe–O2, and Fe–O1 bond distances of 2.214(4), 2.229(3), and 2.048(3) Å, respectively, suggest the presence of a *high-spin* Fe^{II} center.[13]

Table 5. Selected bond distances (Å) for **1** and **2**, as well as for previously reported ApH_2.



M = Fe^{II} (**1**) and Cu^{II} (**2**)

		Bond distances [Å]				
		a	b	c	d	e
1	L1	2.214(4)	2.048(3)	1.461(5)	1.342(5)	1.417(6)
2	L1	2.011(3)	1.940(3)	1.448(5)	1.329(4)	1.413(4)
	L2	2.013(3)	1.939(3)	1.454(5)	1.342(4)	1.408(6)
	L3	1.999(3)	1.939(3)	1.455(5)	1.335(4)	1.404(5)
	L4	2.015(3)	1.946(3)	1.450(5)	1.339(4)	1.402(5)
ApH_2[a]				1.413(1)	1.366(2)	1.410(2)
		f	g	h	i	j
1	L1	1.385(7)	1.401(5)	1.390(6)	1.394(7)	1.408(6)
2	L1	1.376(5)	1.402(5)	1.384(5)	1.391(5)	1.393(5)
	L2	1.384(5)	1.397(5)	1.381(5)	1.381(5)	1.397(6)
	L3	1.379(5)	1.408(6)	1.399(6)	1.390(5)	1.371(7)
	L4	1.389(5)	1.404(6)	1.393(6)	1.389(5)	1.388(5)
ApH_2[a]		1.397(2)	1.389(2)	1.398(2)	1.400(2)	1.397(2)

[a] Ref. 21.

These observations, in their entirety, suggest that complex **1** adopts a structure that is consistent with *trans*-[$Fe^{II}(ApH)_2(MeOH)_2$].

It should be noted that the Fe–N1 bond distance (2.214(4) Å) in **1** is similar to those in [$Fe^{II}(opda)_3$](ClO_4)$_2$ (2.204-2.234(2) Å), whereas the dihedral angle between the O1–Fe1–N1 and O1–C1–C2–N1 planes in **1** (1.06 °) is relatively small compared to those in [$Fe^{II}(opda)_3$](ClO_4)$_2$ (35.90, 38.17, and 44.15 °).[11] The high levels of planarity in the five-membered rings that contain the Fe^{II} center in **1** is indicative for the presence of interactions between the d-orbitals of Fe^{II} and the π-orbitals of the ApH^- moieties *via* the p-orbitals on the O atom(s).[13a] It is noteworthy that the observed differences with respect to the dihedral angles induce a substantially different coordination environment for the amino groups in **1** relative to those in [$Fe^{II}(opda)_3$](ClO_4)$_2$.[11]

Mixing two equivalents of a methanolic solution of ApH_2 with an aqueous solution of $Cu^{II}(OAc)_2$ under an atmosphere of N_2 resulted in the formation of **2** as an aqua-blue solid. The unit cell of **2** contains two crystallographically independent mononuclear units, **A** and **B** (Figures 7a and 7b). In these, the Cu atoms adopt square-pyramidal coordination geometry, wherein the two bidentate NO ligands occupy the equatorial positions, while one O atom resides

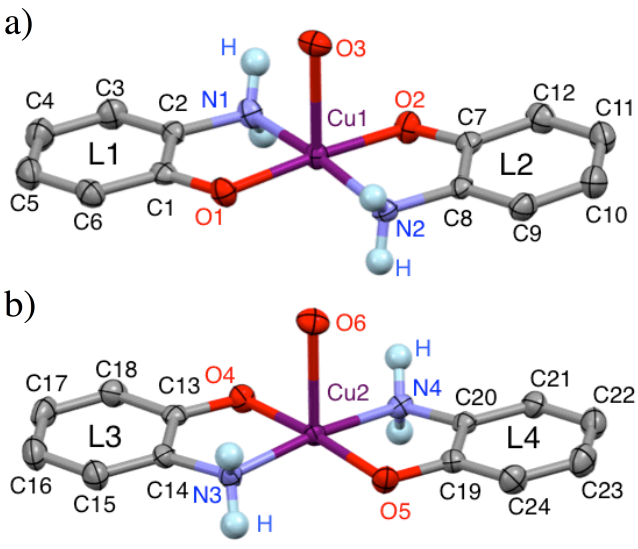


Figure 7. Molecular structures of the crystallographically independent units a) **A** and b) **B** in **2** with atomic displacement parameters set at 50% probability; color code: Cu = purple, O = red, N = light blue, and C = dark gray; ball-and-stick plots for N-bound hydrogen atoms (aqua), while all other hydrogen atoms are omitted for clarity.

on the apical position. The structures of **A** and **B** are almost identical, except for their chirality around the Cu center. The C–N (1.448-1.455(5) Å) and C–O (1.329-1.342(4) Å) bond distances in the four bidentate NO ligands indicate a single bond character for these bonds, and the C–C bond distances in the six-membered rings (1.371-1.413(7) Å) suggest high levels of aromaticity. As in the case of **1**, these results suggest that the ligands in **2** adopt a structure that is consistent with ApH^-.[11,13,23] As the Cu–O (**A**: Cu1–O3 = 2.431(3) Å, **B**: Cu2–O6 = 2.424(3) Å) bond distances are consistent with those of previously reported Cu^{II}–OH_2 bonds (2.475(10) Å) in *e.g. cis*-[Cu^{II}(L-isoleucinato)$_2$(H_2O)],[28] the apical ligand in **2** should be assigned to H_2O, leading to the formulation of **2** as *trans*-[Cu^{II}(ApH)$_2$(H_2O)]. The difference in coordination number between **1** and **2** should be attributed to the different degree of electron repulsion around the metal center of Fe^{II} (d^6) and Cu^{II} (d^9). As in the case of **1**, the observed dihedral angles of 0.19, 0.93, 10.42, and 11.76 ° between the O–Cu–N and O–C–C–N planes in ApH^- in **2** indicate interactions between the d-orbitals on Cu^{II} and the π-orbitals on the ApH^- moieties. Although antibacterial activity has been demonstrated for ApH^- complexes of Cu(II), their detailed structures have not yet been reported.[29] Thus, complex **2** represents the first example of a structurally resolved ApH^- complex of Cu(II).

The UV-vis-NIR spectra of **1** (1.35 mM) in MeOH, as well as that of solid **1** (KBr disk) are shown in Figure 1. For **1**, four absorption bands were observed at λ_{max} (ε / M^{-1} cm^{-1}) = 230 (17,690), 285 (8,550), 335 (1,210), 460 (480), and 680 (118) nm. The two absorption bands at 230 and 285 nm, with relatively large molar extinction coefficients, are similar to those of ApH_2 and ApH^-, and were therefore assigned to the transitions involving ApH^--centered π-π*.[14] The two bands at 335 and 460 nm, which were not observed for ApH_2 and ApH^-, could be tentatively assigned to charge transfer (CT) transitions between Fe(II) and the ApH^- ligands,[13c] while the d-d transitions of the Fe(II) center appeared as a shoulder band at 680 nm (118 M^{-1} cm^{-1}). In the solid state, the absorption bands of **1** appeared at 235, 287, 335, 450, and 750 nm, similar to those of the MeOH solution, suggesting comparable structures in solution and in the solid state.

As metal ions have been known to interact with ApH^- and perturb its properties, the

UV-vis-NIR spectrum of **2** in solution (1.00 mM in MeOH) exhibited five absorption bands at λ_{max} (ε / M^{-1} cm^{-1}) = 227 (17,400), 283 (8,800), 335 (440), 450 (130), and 607 (80) nm (Table 3 and Figure 8). The two absorption bands at 227 and 283 nm with large molar extinction coefficients are similar to those of **1**, ApH_2, and ApH^-, and were accordingly assigned to transitions involving ApH^--centered π-π*. Conversely, the three bands at 335, 460, and 607 nm, which were not observed for ApH^- and ApH_2, should be assigned to CT transitions between Cu(II) and the ApH^- ligands (335 and 460 nm), as well as to Cu-centered d-d transitions (607 nm).

No time-dependent spectral change was observed for **1** (Figure 9a), whereas the spectral profile of **2** gradually changed over the course of 20 h under an atmosphere of N_2 (Figure 9b), resulting in the emergence of an absorption band at 427 nm. The absorption maximum of this band was identical to that of APX, thus indicating the formation of APX from **2** in MeOH. This notion is supported by previous reports on APX analogues such as actinomycin D, which can be synthesized from the appropriate ApH_2 precursors by phenoxazine synthase-catalyzed oxidative deprotonation.[30] Furthermore, Nishinaga and co-workers reported the Co^{II}(salen)-catalyzed (salen = *N*,*N*'-bis(salicylidene)ethylenediamine) formation of APX from ApH_2, and proposed a

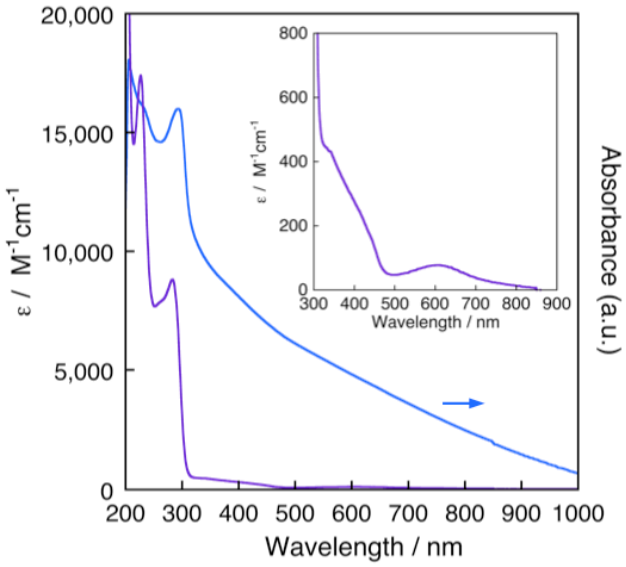


Figure 8. UV-vis-NIR spectra of **2** in MeOH (1.00 mM; purple line) and in the solid state (KBr disk; blue line) under an atmosphere of N_2. The inset shows a magnification (300-900 nm) for the solution spectrum.

nucleophilic attack from the amino group of ApH_2 to the Co^{II}-bound IBQ intermediate as the initial step of the reaction, followed by a multistep oxidative deprotonation and the formation of a C–O bond.[31] Another previous report rationalized the formation of APX from **2** on the basis of the generation of a Cu-bound IBQ intermediate (Scheme 2). As the reduction potential of Cu^{II} is in general more positive than that of Fe^{II}, the different reactivity of **1** relative to **2** might be related to the increased electron-accepting capacity of Cu^{II} in **2** relative to that of Fe^{II} in **1**. These results suggest a remarkable influence of the metal center on the electron-donating ability of the ApH^- ligand. As the Cu complex proved to be unstable in MeOH, no PHER was carried out on this complex.

Figure 3 shows the amount of evolved H_2 as the result of the photoirradiation (289 ± 10 nm; 3.2 mW Hg-Xe lamp; t_{irr} = 5 h) of a MeOH solution of **1** as red circles. The MeOH solution of **1** also showed PHER activity, resulting in the formation of 6.7 (t_{irr} = 5 h) and 14.9 (t_{irr} = 24 h) eq. of H_2 per molecule of **1**, respectively (Figure 4). Prolonged PHER (t_{irr} = 24 h) afforded a small amount of HCO_2H in addition to H_2 and HCHO (Table 4), while no detectable amounts of CO_2 were generated. In contrast, control reactions under the same conditions, using a MeOH solution of $Fe^{II}(ClO_4)_2 \cdot 6H_2O$ did not show any PHER activity (Figure 3). For the PHER of

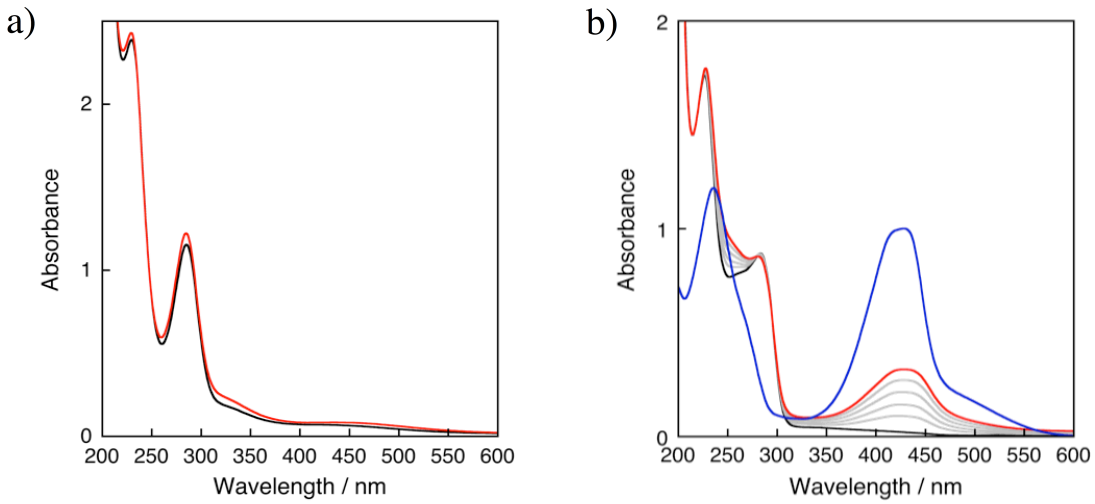
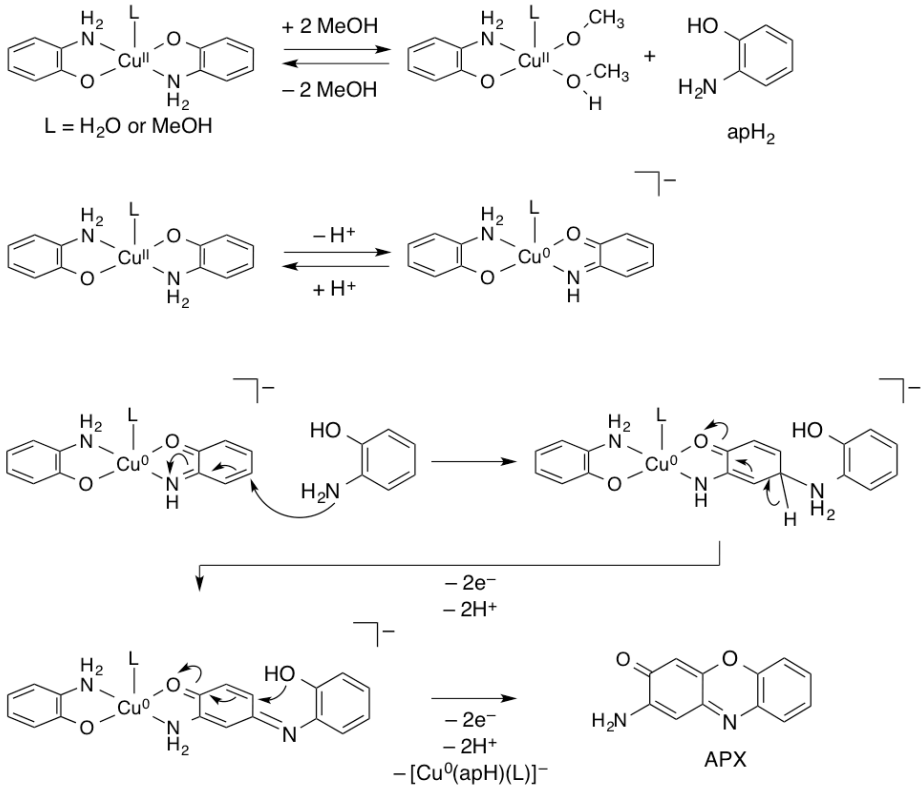


Figure 9. UV-vis spectra of a) **1** (t = 0 h; black line) and **1** (t = 20 h; red line) (1.35 mM), as well as of b) **2** (t = 0 h; black line), **2** (t = 4, 8, 12, and 16 h; gray line), and **2** (t = 20 h; red line) (1.00 mM) in MeOH under an atmosphere of N_2. The UV-vis spectrum of APX (1 mM; blue line) is shown for comparison.

Scheme 2. A Plausible mechanism for the formation of APX from **2**.[31]



solution of **1**, a Φ_{H2} value of 4.8% (t_{irr} = 5 h) was estimated. Considering these PHER results and the aforementioned absorption spectra, it seems feasible to suggest that the photo-excitation of the ApH^- ligand moiety in **1** initiates the PHER. Interestingly, the photocatalytic activity on ApH^- was not suppressed even after the complexation with the Fe^{II} center, implying the possibility to tune reactivity of the system *via* structural design.

In order to determine the excitation that initiates the PHER of **1** in MeOH, we examined the correlation between PHER performance and the wavelength of the irradiation source. Exposing a MeOH solution of **1** to photoirradiation at 460 ± 10 nm ($\varepsilon_{460\,nm}$ = 483 M^{-1} cm^{-1}, t_{irr} = 24 h), did not generate any H_2. However, upon exposing a MeOH solution of **1** to photoirradiation at 350 ± 10 nm (21.8 mW, $\varepsilon_{350\,nm}$ = 932 M^{-1} cm^{-1}, t_{irr} = 24 h) PHER resulted in the formation of 0.48 eq. of H_2, and a Φ_{H2} value of 0.019% was estimated (Figure 10). Although the Φ_{H2} value for irradiation at 350 ± 10 nm (0.019%) is lower than that at 289 ± 10 nm (4.8%), these results imply that PHER may be driven by lower-energy light sources, given a suitable combination of ApH^--type ligands with metal ions.

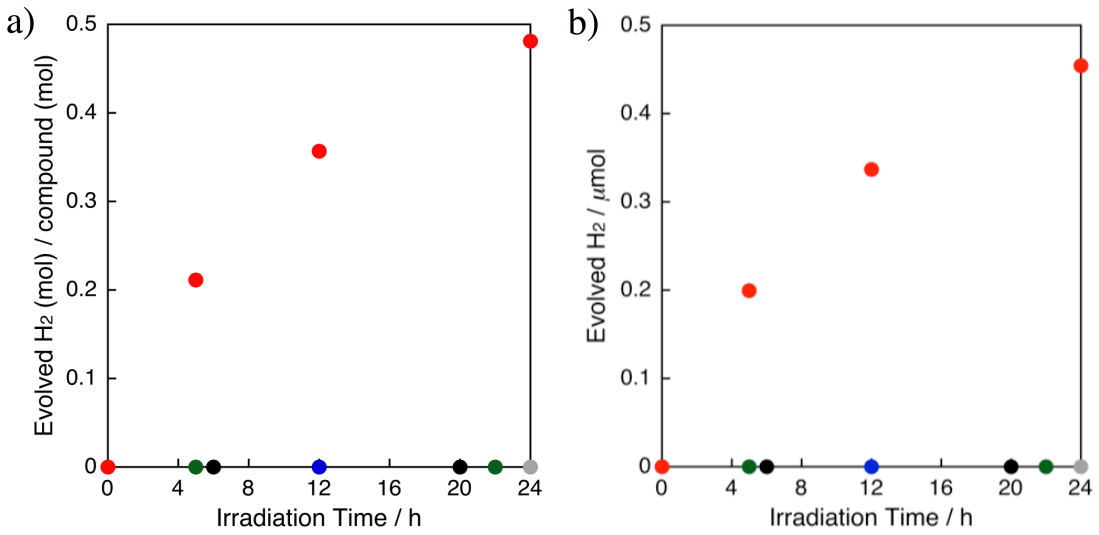


Figure 10. H_2 evolution from MeOH solution of **1** (λ = 350 ± 10 nm, 21.8 mW). Evolution of a) H_2 (mol) per compound (mol) and b) H_2 (μmol) as a function of PHER time for MeOH solutions of ApH_2 (2 mM; black circles), ApH^- (2 mM; green circles), **1** (1 mM; red circles), and $Fe^{II}(ClO_4)_2 \cdot 6H_2O$ (1 mM; blue circles), together with pure MeOH (gray circles).

6-3-3. A Reaction Mechanism for the Dehydrogenation of Methanol Catalyzed by ApH_2, ApH^-, and 1

To shed light on the fundamental PHER mechanism operative in MeOH solutions of ApH_2, ApH^-, and **1**, we wanted to identify the source of H_2. In this context, it is pertinent to distinguish proton and electron sources according to: (i) the hydroxyl and methyl protons of MeOH, (ii) the aromatic protons of ApH_2, ApH^-, and ApH^- in **1**, and (iii) the amino protons of ApH_2, ApH^-, and ApH^- in **1**. Taking the amount of photochemically generated H_2 (Table 4) and the formation of HCHO and HCO_2H into account, it seems plausible to consider (i) as the probable source of the evolved H_2. In order to experimentally confirm this hypothesis, PHERs were carried out in MeOH-d_3, and the evolved gas was subsequently analyzed by GC at 77 K (Figure 11). For H_2, D_2, and HD standards, retention times of 5.0 (p-H_2), 6.3 (o-H_2), 7.8 (p-D_2), 8.4 (o-D_2), and 6.4 min (HD) were observed (Figures 11a-11c). Photoirradiation of ApH_2 in MeOH-d_3 at 289 ± 10 nm afforded gas samples that exhibited a single peak with a retention time of 6.4 min (Figure 11d), suggesting the selective formation of HD under such PHER conditions.

Clearly, the D atom in the evolved HD originates from an α-hydrogen of MeOH-d_3, thus suggesting a C–H (D) bond cleavage during PHER. The PHER of ApH^- and **1** (Figures 11e and 11f), as well as the photoirradiation of a MeOH-d_3 solution of **1** at 350 ± 10 nm (Figure 11g) furnished samples that displayed similar HD peaks in the GC analysis. These results confirm that the PHER of MeOH solutions of ApH_2, ApH^-, and **1** generate H_2 from MeOH.

As ApH_2 and ApH^- can promote one-proton and two-electrons transfers, it is not surprising that these can generate electron(s), hydrogen radical(s), or a hydride (Scheme 1). In order to get a better mechanistic insight into the observed PHERs, photochemical reactions were carried

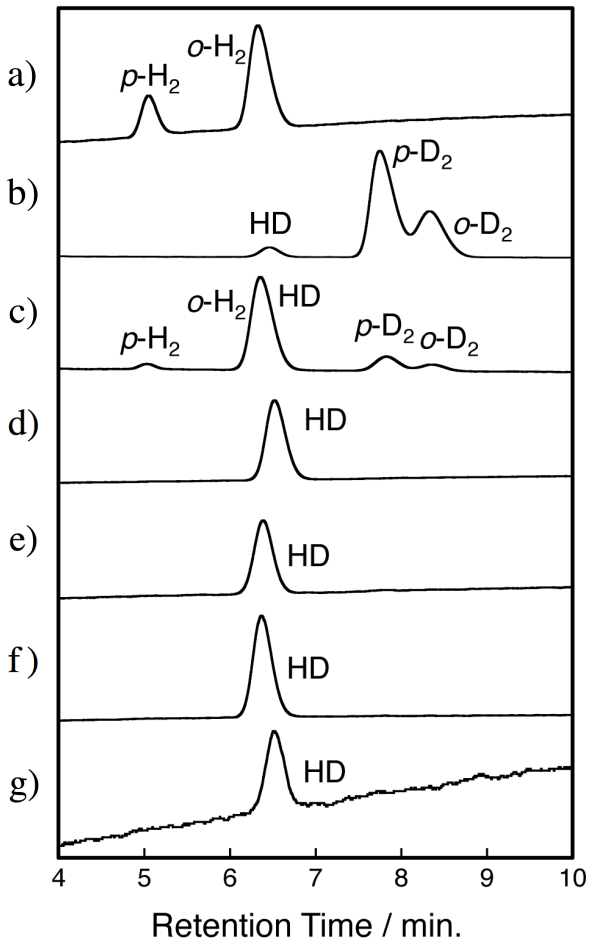


Figure 11. GC analysis of H_2, D_2, and HD standards and gas samples from PHERs. GC profiles of a) H_2, b) D_2 and HD generated by treatment of MeOH-d_4 (99.8%) with sodium metal, c) HD, H_2 and D_2 generated by the treatment of a mixed MeOH/MeOH-d_4 solution (v/v = 1/1) with sodium metal, gas samples obtained from MeOH-d_3 (99.5%) solutions of d) ApH_2, e) ApH^-, and f) **1** after photoirradiation at λ = 289 ± 10 nm (3.2 mW, t_{irr} = 24 h), and g) **1** after photoirradiation at λ = 350 ± 10 nm (21.8 mW, t_{irr} = 24 h); GC conditions: 8% KOH alumina column; T = 77 K.

out in the presence of *t*-BuSH, which is able to act as a hydrogen radical scavenger due to the relatively low bond dissociation energy of the S–H bond, resulting in the formation of *t*-Bu_2S_2.[32]

The ^{1}H NMR spectrum of *t*-BuSH prior to photoirradiation at $\lambda = 289 \pm 10$ nm ($t_{irr} = 24$ h) in MeOH-d_4 is shown in Figure 12a. A singlet peak was observed at $\delta = 1.40$ ppm, which was assigned to the protons of the *t*-Bu group, while no considerable change in the spectrum was

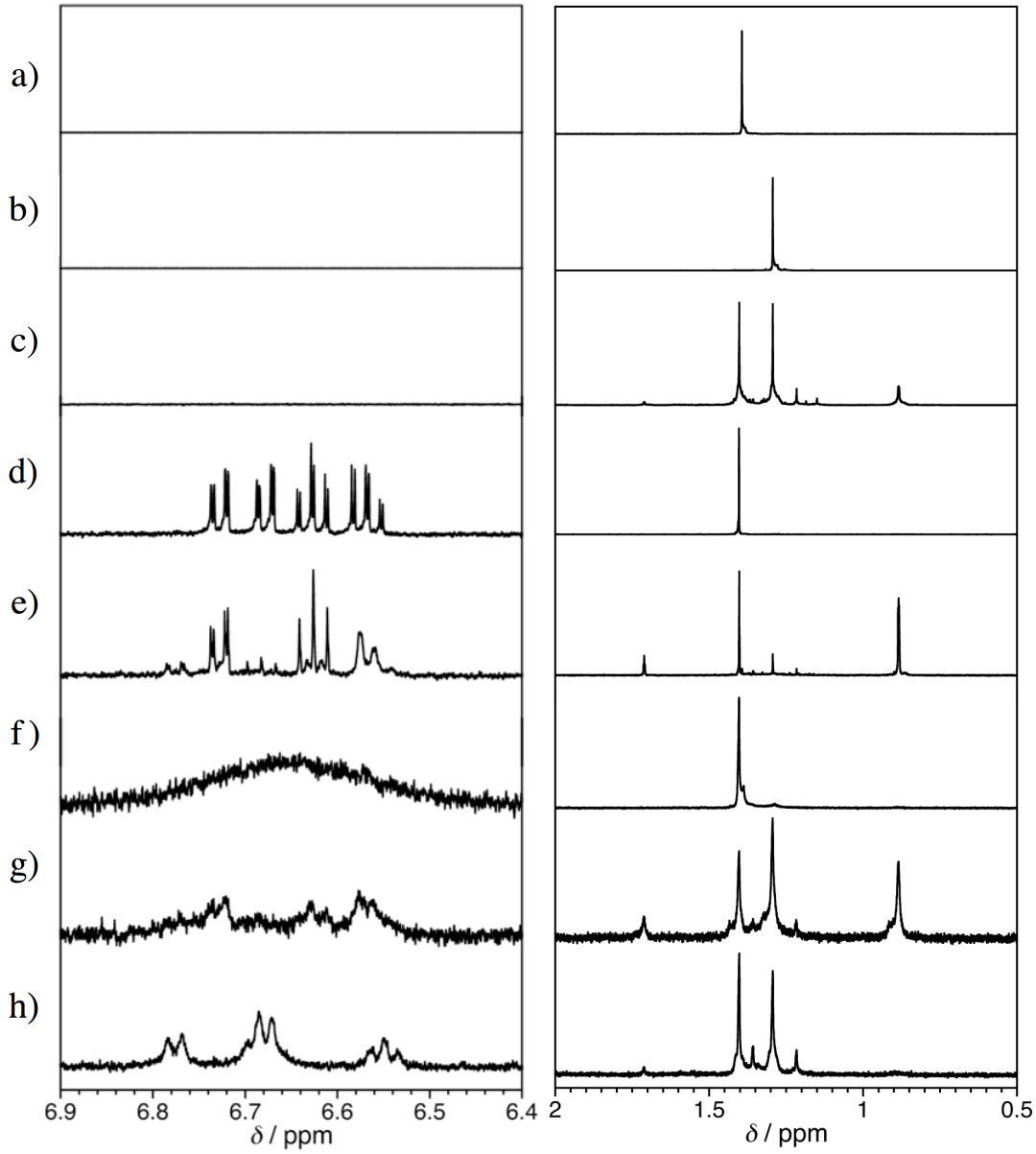


Figure 12. ^{1}H NMR spectra (MeOH-d_4) in the aromatic (left) and aliphatic (right) regions of a) *t*-BuSH, b) *t*-Bu_2S_2, c) *t*-Bu_2S_2 after photoirradiation at $\lambda = 289 \pm 10$ nm ($t_{irr} = 5$ h), d) *t*-BuSH with ApH_2, e) *t*-BuSH with ApH_2 after photoirradiation at $\lambda = 289 \pm 10$ nm ($t_{irr} = 5$ h), f) *t*-BuSH with **1**, g) *t*-BuSH with **1** after photoirradiation at $\lambda = 289 \pm 10$ nm ($t_{irr} = 5$ h), and h) *t*-BuSH with **1** after photoirradiation at $\lambda = 350 \pm 10$ nm ($t_{irr} = 24$ h).

observed after photoirradiation (Figure 13), which is consistent with the absence of an absorption around λ = 289 nm (Figure 14a). The ^{1}H NMR and UV-vis spectra of *t*-Bu_2S_2 in MeOH-d_4 and MeOH are shown in Figures 12b and 14b, respectively. In MeOH-d_4, the ^{1}H NMR spectrum of *t*-Bu_2S_2 exhibits a singlet resonance at δ = 1.29 ppm, while the UV-vis spectrum shows an absorption around λ = 289 nm in MeOH. After photoirradiation of a MeOH-d_4 solution of *t*-Bu_2S_2 at λ = 289 ± 10 nm (t_{irr} = 5 h), major singlet peaks emerged at δ = 1.71, 1.40, 1.29, and 0.88 ppm together with several minor peaks, thus demonstrating the photochemical reactivity of *t*-Bu_2S_2 (Figure 12c). These resonances are therefore indicative of the *in situ* formation of *t*-Bu_2S_2 and its photochemically decomposed products.

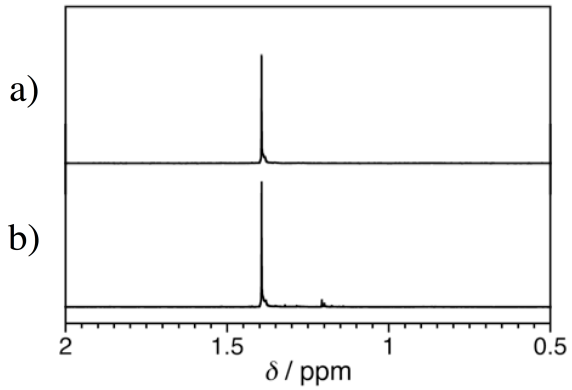


Figure 13. ^{1}H NMR spectrum of *t*-BuSH (2 mM) in MeOH-d_4 a) prior and b) posterior photoirradiation at λ = 289 ± 10 nm (t_{irr} = 24 h).

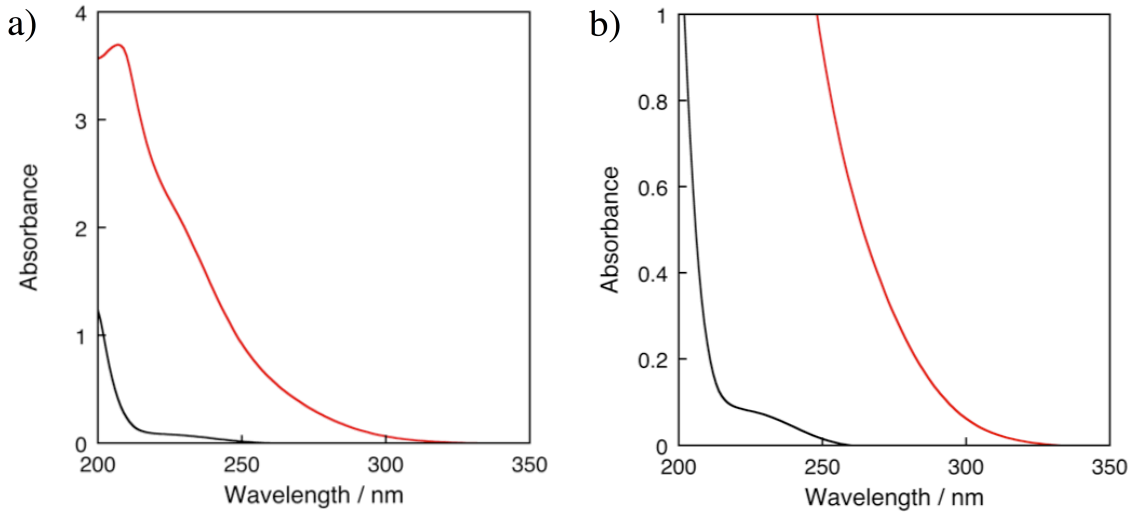


Figure 14. a) UV-vis spectra of *t*-BuSH (20 mM; black line) and *t*-Bu_2S_2 (20 mM; red line) in MeOH, and b) magnification of the spectra (absorbance = 0-1).

The ^{1}H NMR spectrum of a mixture of *t*-BuSH and ApH_2 in MeOH-d_4 (Figure 12d) displays a peak at δ = 1.40 ppm, which is comparable to the resonances of pure *t*-BuSH in MeOH-d_4 (Figure 12a), thus suggesting negligible interaction between ApH_2 and *t*-BuSH in the ground state. After photoirradiation of this solution at λ = 289 ± 10 nm (t_{irr} = 5 h), new singlet peaks emerged at δ = 1.71, 1.29, 1.22, and 0.88 ppm (Figure 12e). The new peaks are identical to those obtained for photoreacted *t*-Bu_2S_2 (Figure 12c), suggesting the formation of *t*-Bu_2S_2 during the photoreaction of ApH_2 and *t*-BuSH.

Similar experiments were also carried out for **1**, but the ^{1}H NMR spectrum of *t*-BuSH in the presence of **1** (Figures 12a and 12f) did not indicate any significant interaction between *t*-BuSH and paramagnetic **1** in the ground state. After photoirradiation of this solution at λ = 289 ± 10 nm (t_{irr} = 5 h), new singlet peaks were observed at δ = 1.71, 1.29, 1.22, and 0.88 ppm (Figure 12g). These peaks are comparable to those of the photoirradiation product obtained from *t*-BuSH and ApH_2 (Figure 12e), and these results thus suggest the formation of *t*-Bu_2S_2 from *t*-BuSH in the presence of **1**.

At this point it should be beneficial to consider possible formation mechanisms for the formation of *t*-Bu_2S_2 from *t*-BuSH. One possibility is the oxidation of *t*-BuSH by ApH_2 in the excited state, while another is the generation of hydrogen radicals from photoirradiated ApH_2,

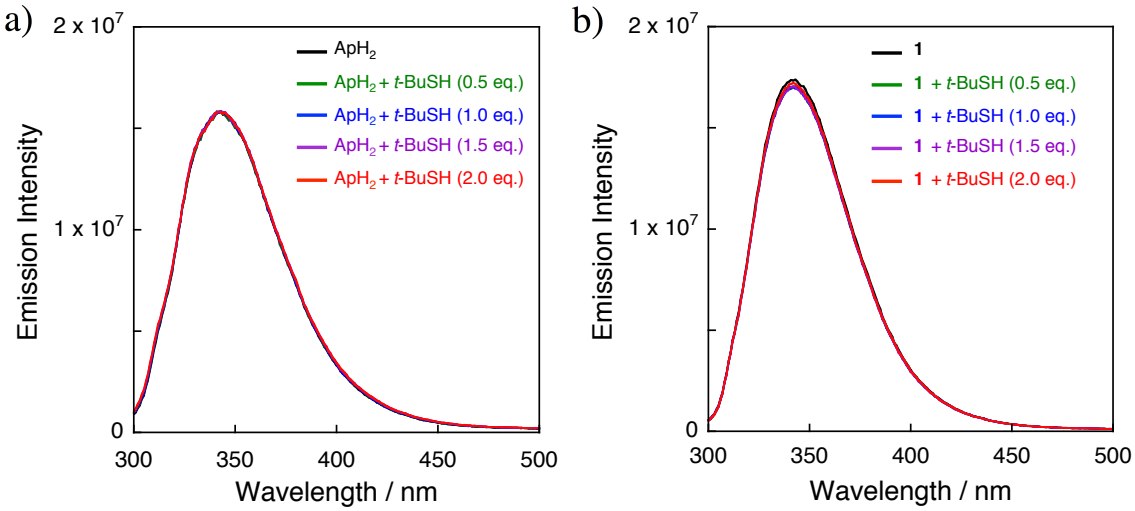


Figure 15. Emission spectra of a) ApH_2 (0.02 mM; black line) and b) **1** (0.01 mM; black line) excited at λ = 285 nm, together with those after addition of 0.5 eq. (green line), 1.0 eq. (blue line), 1.5 eq. (purple line), and 2.0 eq. (red line) of *t*-BuSH in MeOH under an atmosphere of N_2.

followed by the abstraction of a hydrogen radical from *t*-BuSH. Upon excitation at λ = 285 nm in MeOH, ApH_2 exhibits an emission peak at 342 nm (Figure 15a). This emission was tentatively assigned to the $^1\pi$-π^* excited state, which was not quenched by *t*-BuSH. Therefore, the generation of a hydrogen radical from an alternative excited path represents a more likely mechanism compared to an electron transfer *via* the $^1\pi$-π^* excited state. Similar to the case of ApH_2, the emission peak of **1** in MeOH was not influenced by the presence of *t*-BuSH upon excitation at λ = 285 nm (Figure 15b). This result suggests that PHER of **1** does not include the oxidation of *t*-BuSH by the excited state of **1**, but the generation of a hydrogen radical from **1**.

Furthermore, the characteristic singlet peak for *t*-Bu_2S_2 at δ = 1.29 was observed after photoirradiation of **1** at λ = 350 ± 10 nm (t_{irr} = 24 h; Figure 12h). These results suggest that the pathway for the generation of hydrogen radials is also included in the excitation of **1** at λ = 350 ± 10 nm, similarly to the excitation of **1** and ApH_2 at λ = 289 ± 10 nm. The photoirradiation of **1** in MeOH at λ = 350 ± 10 nm in the presence of NADCl, which is an electron or hydride

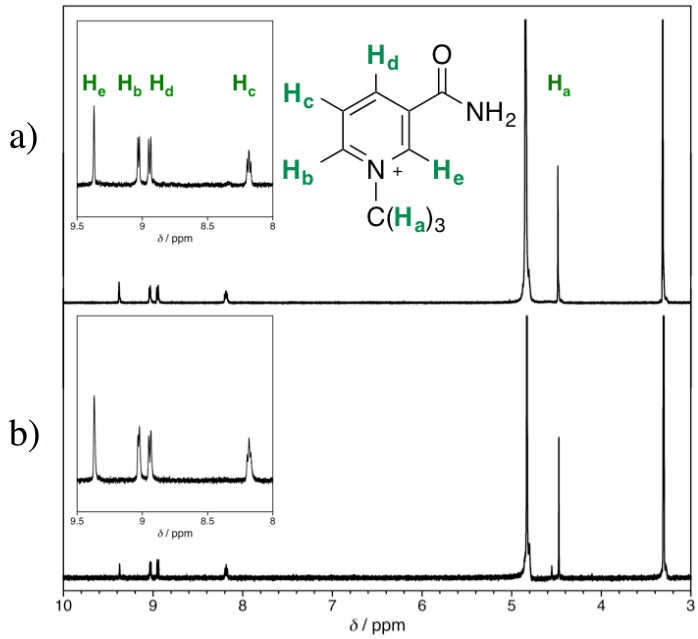
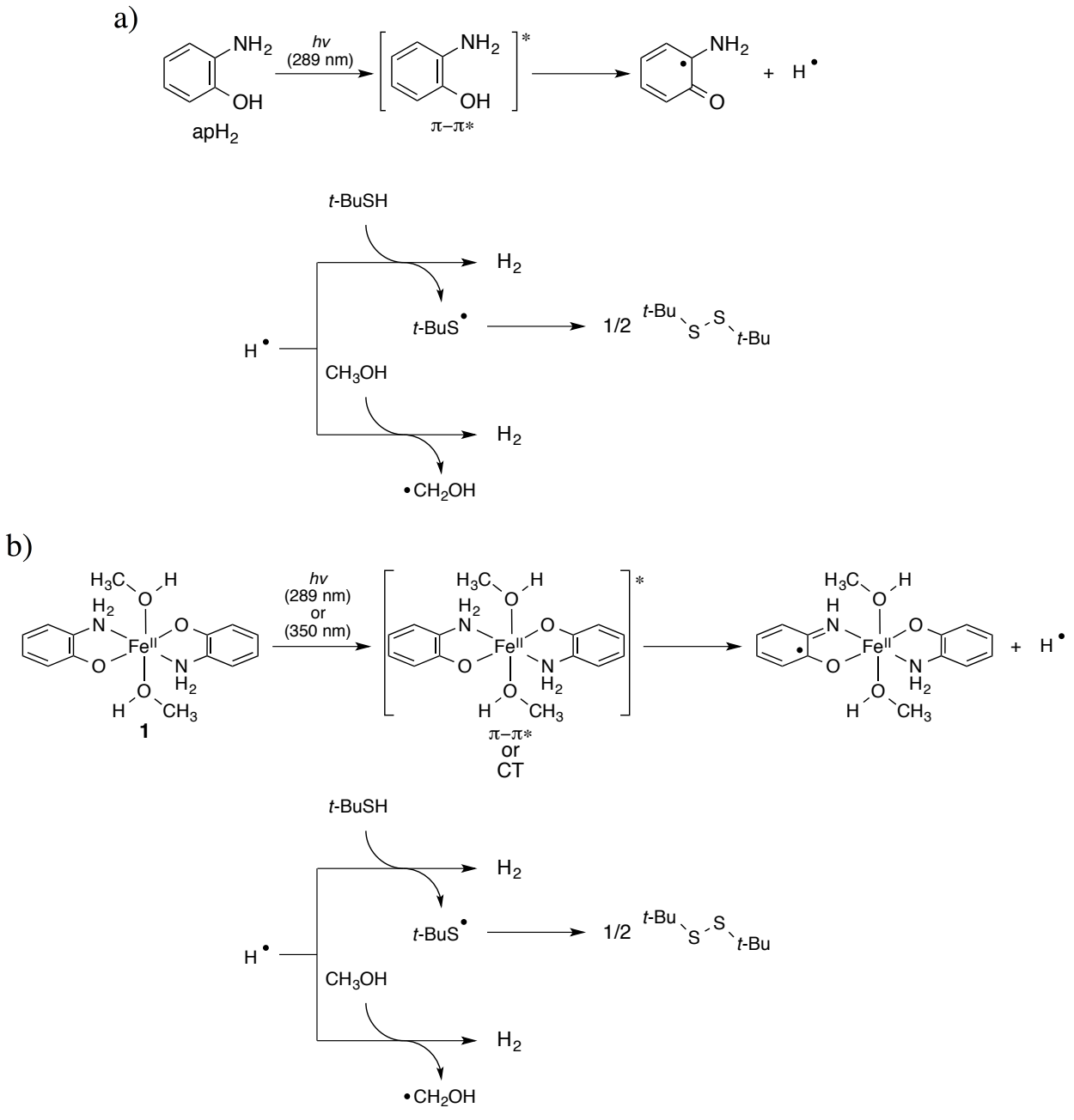


Figure 16. ^{1}H NMR spectra of **1** (1 mM) in the presence of NADCl (2 mM) in MeOH-d_4 a) prior and b) posterior to photoirradiation at λ = 350 ± 10 nm (t_{irr} = 24 h). The insets show a magnification of the 9.5-8 ppm region. The amide protons could not be detected, most likely on account of an H/D exchange between NADCl and MeOH-d_4.

scavenger,[33] revealed no considerable change in the ^{1}H NMR spectra prior and posterior to photoreaction (Figure 16). These results indicate that the photoreaction of **1** at $\lambda = 350 \pm 10$ nm does not include any electron transfer or generation of hydrides, and are thus consistent with a mechanism based on hydrogen radicals (Scheme 3).

In general, hydrogen can be generated from MeOH using an electron donor, a hydrogen radical, or a hydride. Experiments between MeOH-d_3 and sodium metal (electron donor) or

Scheme 3. Plausible mechanisms for the photochemical reaction of a) ApH_2 and b) **1** in the presence of *t*-BuSH.



$NaBH_4$ (hydride donor) showed that under these conditions, H_2 was produced selectively (eqs. 7 and 8 and Figure 17). In contrast, the formation of HD was negligible, as the *o*-H_2/*p*-H_2 peak area ratio was almost identical to that of the H_2 standard (Table 6). Hydrogen radicals have previously been reported to react with the α-hydrogen atoms of MeOH to produce H_2 and the corresponding $\cdot CH_2OH$ radical (eq. 9).[34] The $\cdot CH_2OH$ radical is moreover a good reducing agent and able to react with electron acceptors (EA) such as Fe(III) or Co(III),[34] which affords HCHO as the oxidized species of the $\cdot CH_2OH$ radical (eq. 10).

$$2CD_3OH + 2e^- \longrightarrow 2CD_3O^- + H_2 \qquad \text{eq. 7}$$

$$CD_3OH + H^- \longrightarrow CD_3O^- + H_2 \qquad \text{eq. 8}$$

$$CH_3OH + H\bullet \longrightarrow \bullet CH_2OH + H_2 \qquad \text{eq. 9}$$

$$\bullet CH_2OH + EA \longrightarrow CH_2O + H^+ + EA^- \qquad \text{eq. 10}$$

For ApH_2, proton- and electron-transfer properties should be expected, and ApH_2 should thus be able to donate electrons, hydrides, and/or hydrogen radicals. The ability to photochemically generate hydrogen radicals, which originate from the hydroxyl protons, has already been reported for ApH_2.[14] As previously discussed, it was confirmed that PHERs of MeOH-d_3 solutions of ApH_2, ApH^-, and **1** selectively generate HD (Figure 11), which suggests a selective abstraction of the α-hydrogen atoms from MeOH. Actually, the generation of hydrogen

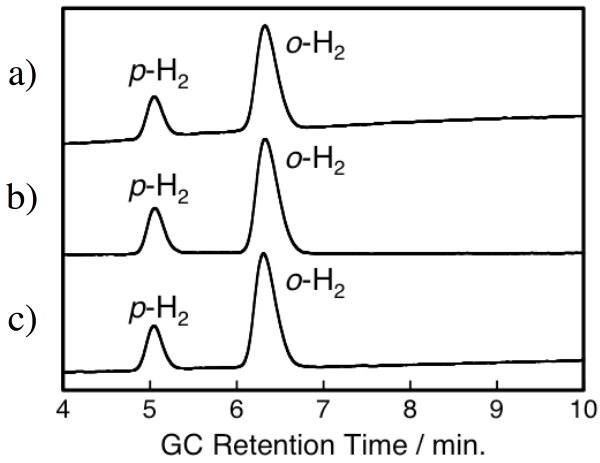


Figure 17. Gas chromatograms for standards: a) H_2, b) H_2 generated by treatment of CD_3OH (99.5%) with sodium metal, and c) H_2 generated by the treatment of CD_3OH (99.5%) with $NaBH_4$.

Table 6. GC peak area for H_2 obtained from the treatment of MeOH-d_3 with sodium metal, and from the treatment of MeOH-d_3 with $NaBH_4$.

H_2 source	Area for *p*-H_2 × 10^3	Area for *o*-H_2 × 10^3	*o*-H_2 / *p*-H_2
Standard H_2	2.23	7.56	3.39
MeOH-d_3 + Na	2.47	8.16	3.30
MeOH-d_3 + $NaBH_4$	2.33	7.81	3.35

radicals was confirmed in the photochemical reactions of ApH_2 and **1** in the presence of the scavengers (Figure 12). Consequently, all PHERs should be initiated by the generation of a hydrogen radical.

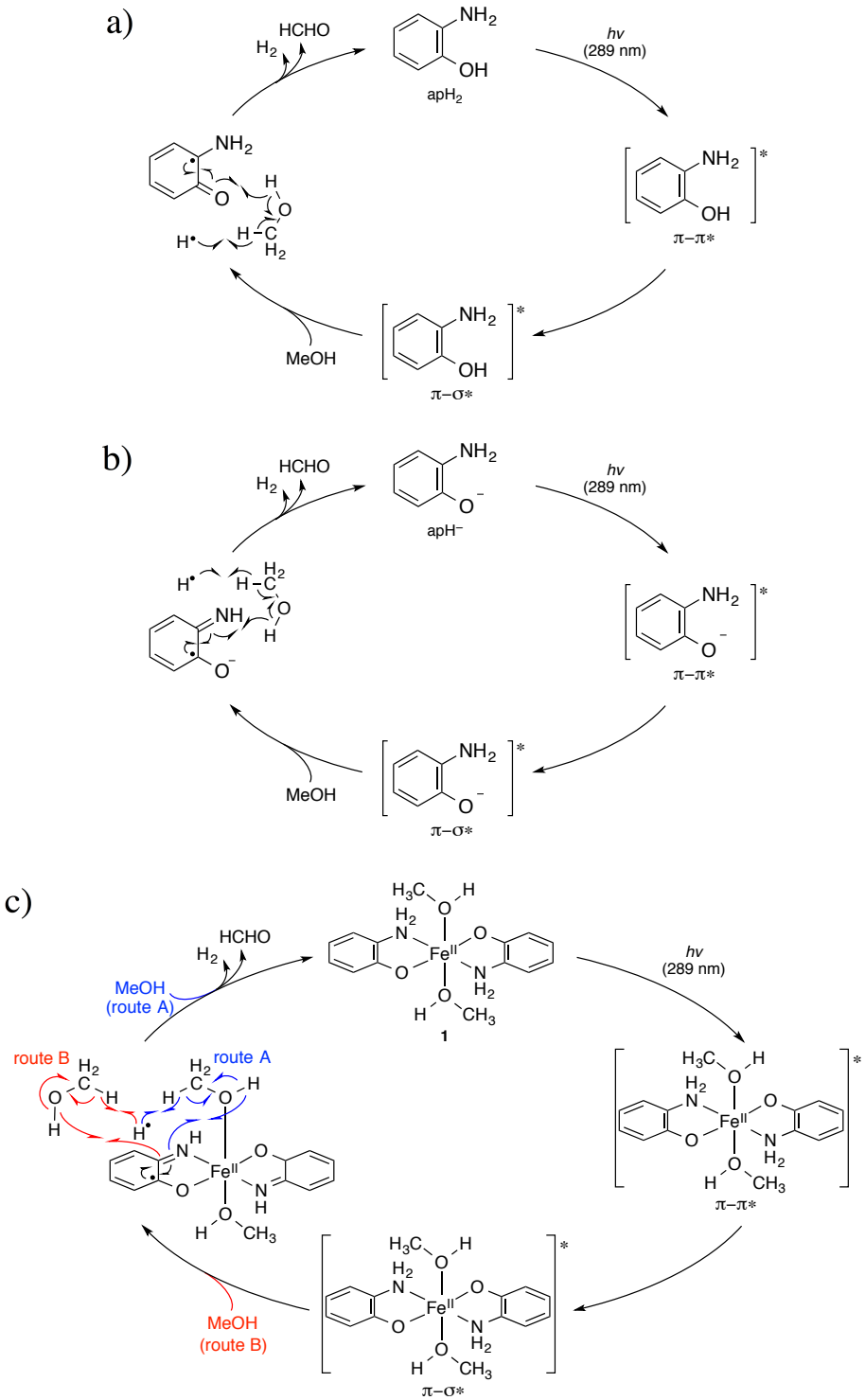
Scheme 4a shows a plausible mechanism for the PHER involving ApH_2. It seems reasonable to assume that PHER (λ = 289 ± 10 nm) proceeds *via* the initial photochemical generation of hydrogen radicals from the hydroxyl moieties of ApH_2. Subsequently, H_2 and HCHO should be formed by the selective abstraction of α-hydrogen atoms from MeOH (Figure 11). The additional oxidation product HCO_2H would then be generated from the dehydrogenation of HCHO and co-existing water.

In the case of ApH^-, a hydroxyl proton is not present, and therefore, O–H bond cleavage in ApH^- should not occur during PHER. Previous studies on aromatic amines, such as aniline and opda, revealed characteristic photoreactions, which are initiated by the π-π* excitation through the 3s Rydberg states of the nitrogen atom in the amino group.[35] Eventually, the N–H σ-bonds in these amino moieties are photochemically activated to generate hydrogen radicals *via* the π-π*/π-σ* conical intersection in these reactions, which is similar to the case of ApH_2.[36] The formation of a hydrogen radical and ISQ^- may be possible from the homolytic cleavage of an N–H bond in the π-σ* exited state from a π-π* excitation (Scheme 4b), and subsequent reactions indicate the generation of H_2 and HCHO, similar to the case of ApH_2.

Furthermore, complex **1**, containing ApH^- ligands, should also generate hydrogen radicals by the homolysis of an N–H bond in the ApH^- moiety under photoirradiation conditions (λ = 289 ± 10 nm; Scheme 4c). In the plausible mechanism for **1**, either the MeOH molecule coordinated to the Fe(II) center or that not directly bound to the Fe(II) center or both may be included in the

reaction as described in routes A and B. Remarkably, the complexation of ApH^- with Fe(II) does not inhibit its PHER activity. It should also be noted here that the PHER proceeding *via* excitations including π-π* transitions show higher Φ_{H2} values (4.8%) relative to CT excitations (0.019%).

Scheme 4. Plausible PHER mechanisms. Reaction cycles catalyzed by a) ApH_2, b) ApH^-, and c) **1** upon irradiation at $\lambda = 289 \pm 10$ nm.



6-4. Conclusions

This chapter demonstrated the first examples for the photocatalytic dehydrogenation of MeOH at room temperature, using ApH_2, ApH^-, and an Fe(II) complex of ApH^- (**1**) as photocatalysts. The PHERs, which are initiated by the π-π* excitations of the ApH^- moieties in ApH_2, ApH^-, and **1**, include the formation of hydrogen radicals and ultimately result in the dehydrogenation of MeOH. Although these photochemical reactions still require mostly UV light, the PHER activity and the comparable Φ_{H2} values of ApH_2 and ApH^- promises potential for these compounds as a new organophotocatalyst platform. Furthermore, complex **1** demonstrated a comparable photochemical reactivity and Φ_{H2} value with respect to ApH^-, despite of the presence of a paramagnetic Fe(II) center. The PHER activity upon photoexcitation of the CT band of **1** suggested that the complexation between Fe^{II} and ApH^- allows access to unprecedented photoreactivity that is able to realize the photochemical generation of H_2 at longer wavelengths relative to ApH_2 and ApH^-. The central issues to be addressed in the immediate future are improvements of the catalytic activity and the use of visible light as a driving force, by using various combinations of metal ions with ApH^--type ligands and extended π-systems.

6-5. Notes and References

1. a) N. Armaroli, V. Balzani, *Angew. Chem. Int. Ed.,* **2007**, *46*, 52; b) P. Du, R. Eisenberg, *Energy Environ. Sci.,* **2012**, *5*, 6012; c) A. J. Esswein, D. G. Nocera, *Chem. Rev.,* **2007**, *107*, 4022; d) G. J. Kubas, *Chem. Rev.,* **2007**, *107*, 4152; e) N. S. Lewis, D. G. Nocera, *Proc. Natl. Acad. Sci. U. S. A.,* **2006**, *103*, 15729; f) S. R. Reece, J. A. Hamel, K. Sung, T. D. Jarvi, A. J. Esswein, J. J. H. Pijpers, D. G. Nocera, *Science*, **2011**, *334*, 645.
2. a) U. Eberle, M. Felderhoff, F. Schüth, *Angew. Chem. Int. Ed.,* **2009**, *48*, 6608; b) L. Schlapbach, A. Zuttel, *Nature*, **2001**, *414*, 353; c) M. P. Suh, H. J. Park, T. K. Prasad, D.-W. Lim, *Chem. Rev.,* **2011**, *112*, 782.
3. a) M. A. Peña, J. P. Gómez, J. L. G. Fierro, *Appl. Catal., A: Gen.,* **1996**, *144*, 7; b) J. F. Haw, W. Song, D. M. Marcus, J. B. Nicholas, *Acc. Chem. Res.*, **2003**, *36*, 317: c) R. M. Navarro, M. A. Peña, J. L. G. Fierro, *Chem. Rev.,* **2007**, *107*, 3952; d) J. D. Holladay, J. Hu, D. L. King, Y. Wang, *Catal. Today*, **2009**, *139*, 244; e) J. D. Holladay, J. Hu, D. L. King, Y. Wang, *Catal. Today*, **2009**, *139*, 244; f) N. L. Rosi, J. Eckert, M. Eddaoudi, D. T. Vodak, J. Kim, M. O'Keeffe, O. M. Yaghi, *Science,* **2003**, *300*, 1127.
4. a) J. N. Tiwari, R. N. Tiwari, G. Singh, K. S. Kim, *Nano Energy*, **2013**, *2*, 553; b) R. B. Biniwale, S. Rayalu, S. Devotta, M. Ichikawa, *Hydrogen Energy*, **2008**, *33*, 360; c) V. Neburchilov, J. Martin, H. Wang, J. Zhang, *J. Power Sources*, **2007**, *169*, 221; d) H. Liu, C. Song, L. Zhang, J. Zhang, H. Wang, D. P. Wilkinson, *J. Power Sources*, **2006**, *155*, 95.
5. S. Sá, H. Silva, L. Brandão, J. M. Sousa, A. Mendes, *Appl. Catal. B: Environ.,* **2010**, *99*, 43.
6. a) M. Nielsen, E. Alberico, W. Baumann, H.-J. Drexler, H. Junge, S. Gladiali, M. Beller, *Nature*, **2013**, *495*, 85; b) E. Alberico, P. Sponholz, C. Cordes, M. Nielsen, H.-J. Drexler, W. Baumann, H. Junge, M. Beller, *Angew. Chem. Int. Ed.,* **2013**, *52*, 14162.
7. R. E. Rodríguez-Lugo, M. Trincado, M. Vogt, F. Tewes, G. Santiso-Quinones, H.

Grützmacher, *Nat. Chem.,* **2013**, *5*, 342.

8. M. Trincado, D. Banerjee, H. Grützmacher, *Energy Environ. Sci.,* **2014**, *7*, 2464.
9. a) Y. Okamoto, S. Ida, J. Hyodo, H. Hagiwara, T. Ishihara, *J. Am. Chem. Soc*., **2011**, *133*, 18034; b) S. Ouyang, H. Tong, N. Umezawa, J. Cao, P. Li, Y. Bi, Y. Zhang, J. Ye, *J. Am. Chem. Soc*., **2012**, *134*, 1974; c) S. Okunaka, H. Tokudome, R. Abe, *J. Mater. Chem. A*, **2015**, *3*, 14794; d) H. G. Kim, P. H. Borse, J. S. Jang, E. D. Jeong, O.-S. Jung, Y. J. Suh, J. S. Lee, *Chem. Commun*., **2009**, 5889; e) M. Hara, G. Hitoki, T. Takata, J. N. Kondo, H. Kobayashi, K. Domen, *Catal. Today*, **2003**, *78*, 555; f) R. Konta, T. Ishii, H. Kato, A. Kudo, *J. Phys. Chem. B*, **2004**, *108*, 8992; g) J. Yoshimura, Y. Ebina, J. Kondo, K. Domen, A. Tanaka, *J. Phys. Chem*., **1993**, *97*, 1970; h) D. Chen, J. Ye, *Chem. Mater*., **2007**, *19*, 4585; i) T.-F. Yeh, J.-M. Syu, C. Cheng, T.-H. Chang, H. Teng, *Adv. Funct. Mater*., **2010**, *20*, 2255; j) H. G. Kim, D. W. Hwang, J. S. Lee, *J. Am. Chem. Soc*., **2004**, *126*, 8912; k) D. Wang, J. Ye, T. Kako, T. Kimura, *J. Phys. Chem. B*, **2006**, *110*, 15824; l) G. Hitoki, A. Ishikawa, T. Takata, J. N. Kondo, M. Hara, K. Domen, *Chem. Lett*., **2002**, *31*, 736.
10. a) H. Yamamoto, S. Shinoda, Y. Saito, *J. Mol. Catal*., **1985**, *30*, 259; b) K. Makita, K. Nomura, Y. Saito, *J. Mol. Catal*., **1994**, *89*, 143; c) D. Morton, D. J. Cole-Hamilton, *J. Chem. Soc., Chem. Commun*., **1988**, 1154.
11. T. Matsumoto, H.-C. Chang, M. Wakizaka, S. Ueno, A. Kobayashi, A. Nakayama, T. Taketsugu, M. Kato, *J. Am. Chem. Soc*., **2013**, *135*, 8646.
12. M. M. Bittner, S. V. Lindeman, A. T. Fiedler, *J. Am. Chem. Soc*., **2012**, *134*, 5460.
13. a) M. M. Bittner, D. Kraus, S. V. Lindeman, C. V. Popescu, A. T. Fiedler, *Chem. Eur. J*., **2013**, *19*, 9686; b) B. Chakraborty, T. K. Paine, *Angew. Chem. Int. Ed*., **2013**, *52*, 920; c) B. Chakraborty, S. Bhunya, A. Paul, T. K. Paine, *Inorg. Chem*., **2014**, *53*, 4899; d) S. Banerjee, P. Halder, T. K. Paine, *Z. Anorg. Allg. Chem*., **2014**, *640*, 1168.
14. M. C. Capello, M. Broquier, S.-I. Ishiuchi, W. Y. Sohn, M. Fujii, C. Dedonder-Lardeux, C. Jouvet, G. A. Pino, *J. Phys. Chem. A*, **2014**, *640*, 1168.
15. T. Horváth, J. Kaizer, G. Speier, *J. Mol. Catal. A: Chem*., **2004**, *215*, 9.

16. a) P. Sritharathikhun, M. Oshima, S. Motomizu, *Talanta*, **2005**, *67*, 1014; b) T. Nash, *Biochem. J.*, **1953**, *55*, 416; c) A. Hantzsch, *Ber. Dtsch. Chem. Ges.*, **1881**, *14*, 1637.
17. M. C. Burla, R. Caliandro, M. Camalli, B. Carrozzini, G. L. Cascarano, L. De Caro, C. Giacovazzo, G. Polidori, R. Spagna, *J. Appl. Crystallogr.*, **2005**, *38*, 381.
18. CrystalStructure 3.8.2, Crystal Structure Analysis Package; Rigaku and Rigaku/MSC: The Woodlands, TX, 2000−2006.
19. G. Sheldrick, SHELX-97 Program for crystal structure solution and the refinement of crystal structures, Institut für Anorganische Chemie der Universität Göttingen, Tammanstrasse 4, D-3400 Göttingen, Germany, 1997.
20. Assignments were supported by DFT calculations at the B3LYP/6-31G(d) level of theory, using Gaussian 03.
21. F. H. Allen, V. J. Hoy, J. A. K. Howard, V. R. Thalladi, G. R. Desiraju, C. C. Wilson, G. J. Mclntyre, *J. Am. Chem. Soc.*, **1997**, *119*, 3477.
22. R. Becker, J. Weiß, M. Winter, K. Merz, R. A. Fischer, *J. Organomet. Chem.*, **2001**, *630*, 253.
23. M. F. Reynolds, M. Costas, M. Ito, D.-H. Jo, A. A. Tipton, A. K. Whiting, L. Que Jr., *J. Biol. Inorg. Chem.*, **2003**, *8*, 263.
24. F. G. Bordwell, D. J. Algrim, *J. Am. Chem. Soc.*, **1988**, *110*, 2964.
25. F. G. Bordwell, R. J. McCallum, W. N. Olmstead, *J. Org. Chem.*, **1984**, *49*, 1424.
26. C. Cairns, S. M. Nelson, M. G. B. Drew, *J. Chem. Soc., Dalton Trans.*, **1981**, 1965.
27. R. T. Jonas, T. D. P. Stack, *J. Am. Chem. Soc.*, **1997**, *119*, 8566.
28. C. M. Weeks, A. Cooper, D. A. Norton, *Acta Crystallogr. Sect. B*, **1969**, *25*, 443.
29. a) N. V. Loginova, T. V. Koval'chuk, R. A. Zheldakova, N. P. Osipovich, V. L. Sorokin, G. I. Polozov, G. A. Ksendzova, G. K. Glushonok, A. A. Chernyavskaya, O. I. Shadyro, *Bioorg. Med. Chem. Lett.*, **2006**, *16*, 5403; b) N. V. Loginova, T. V. Koval'chuk, N. P. Osipovich, G. I. Polozov, V. L. Sorokin, A. A. Chernyavskaya, O. I. Shadyro, *Polyhedron*, **2008**, *27*, 985; c) N. V. Loginova, A. T. Gres, G. I. Polozov, T. V. Koval'chuk, N. P. Osipovich, R. A. Zheldakova, Y. V. Faletrov, I. S. Strakha, I. I.

Azarko, *Polyhedron*, **2011**, *30*, 2581.

30. U. Hollstein, *Chem. Rev.*, **1974**, *74*, 625.
31. K. Maruyama, T. Moriguchi, T. Mashino, A. Nishinaga, *Chem. Lett.*, **1996**, *25*, 819.
32. T. Büttner, J. Geier, G. Frison, J. Harmer, C. Calle, A. Schweiger, H. Schönberg, H. Grützmacher, *Science*, **2005**, *307*, 235.
33. a) J. Zielonka, A. Marcinek, J. Adamus, J. Gębicki, *J. Phys. Chem. A*, **2003**, *107*, 9860; b) Y. Matsubara, K. Koga, A. Kobayashi, H. Konno, K. Sakamoto, T. Morimoto, O. Ishitani, *J. Am. Chem. Soc.*, **2010**, *132*, 10547.
34. D. D. Campano, E. R. Kantrowitz, M. Z. Hoffman, M. S. Weinberg, *J. Phys. Chem.*, **1974**, *78*, 686.
35. a) G. M. Roberts, G. A. Williams, J. D. Young, S. Ullrich, M. J. Paterson, V. G. Stavros, *J. Am. Chem. Soc.*, **2012**, *134*, 12578; b) R. Montero, Á. P. Conde, V. Ovejas, R. Martínez, F. Castaño, A. Longarte, *J. Chem. Phys.*, **2011**, *135*, 054308; c) G. A. King, T. A. A. Oliver, M. N. R. Ashfold, *J. Chem. Phys.*, **2010**, *132*, 214307.
36. a) K. Ujike, S. Kudoh, M. Nakata, *Chem. Phys. Lett.*, **2004**, *396*, 288; b) K. Ujike, N. Akai, S. Kudoh, M. Nakata, *J. Mol. Struct.*, **2005**, *735-736*, 335.

Future Perspectives

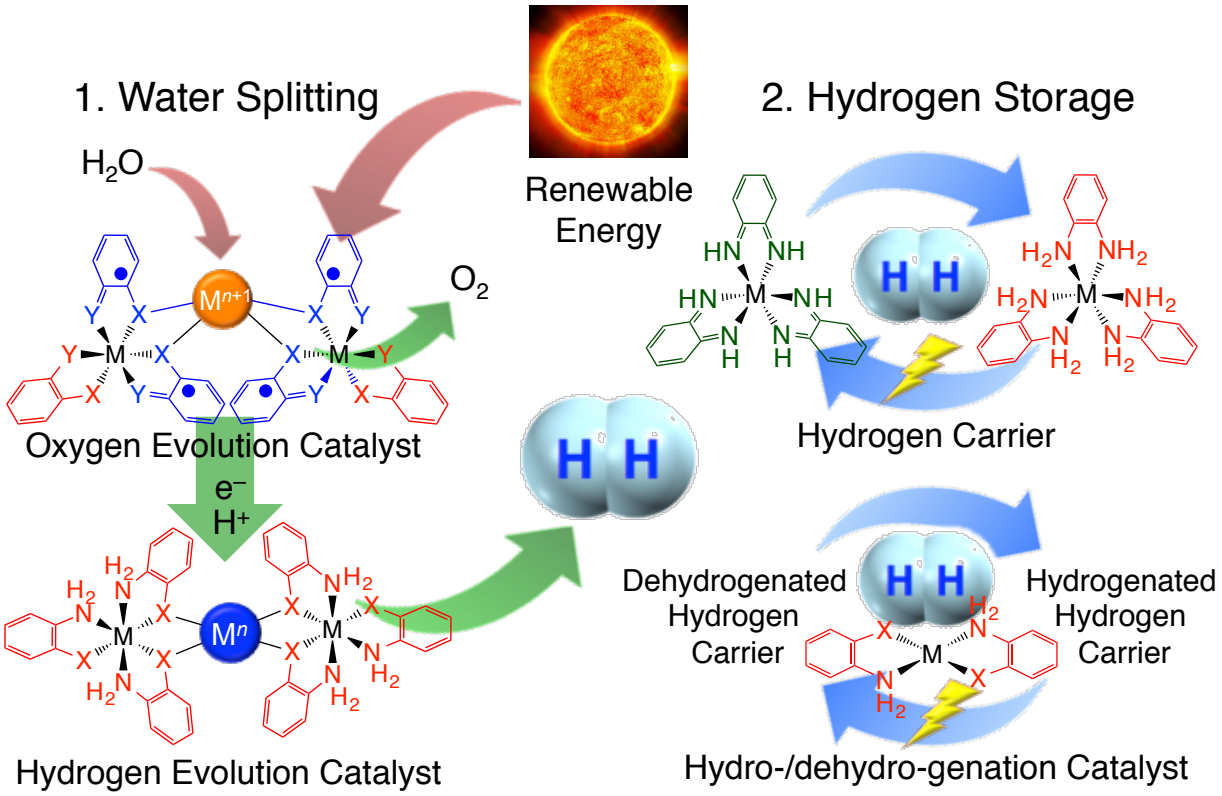
Chapter 2-4 described coordination of RMLs to several guest metal ions together with metal- or ligand-centered redox reactions of the homo and heteroleptic MLs. It was found that the combination of the RMLs with a guest metal ions led to the formation of the supramolecular structures, such as 1:1 complex, 2:1 complex, 1-D coordination polymer, and 2-D henycomb-like structure. Moreover, it was revealed that coordination of RMLs to guest metal ions modulate not only redox potentials but also the number of transferred electrons as well as redox centers in RML complexes. Theses results elucidate details on the interactions between RMLs and guest metal ions to establish the design principles for creating multi-electron transfer system.

In addition, Chapter 5-6 described PHERs by Fe complexes with the electron- and proton-transfer ligands such as Opda and ApH_2. It is found that the electron- and proton-transfer activity of ligands allow to proceed two typs of PHERs, which is the evolution of hydrogen from ligands or from the hydrogen carrier *i.e.* MeOH. These results demonstrated PHER activities of non-precious metal complexes as a electron- and proton-pooling site at ambient temperatures.

Water-derived hydrogen that has been generated catalytically with the use of renewable energy sources represents one of the most desirable chemical energy sources for the future.[8] Therefore, the developments of water splitting catalysts to produce hydrogen, as well as the complementary hydrogen-storage materials to store the furnished hydrogen safely with high efficiency, represent desirable research targets.

In future study, the creations of catalysts and materials are investigated based on the electron- and proton-transfer activity on their redox-active ligands. It is expected that the properties of theses redox-active ligands, (i) activate ligand-centered multi-electron and -proton transfer, and (ii) construct reaction fields for the formation of hydrogen from the ligands, are further developed by complexation and assembling the ligands using non-precious metals.

Chart 1. Hydrogen production and storage using redox-active ligands as electron- and proton -pooling sites.



Initially, water splitting will be realized by the use of two types of RML assemblies (Chart 1). One RML assembly will have strong electron-accepting properties, and will thus be able to capture and activate water molecules on the guest metal site. Then, RMLs will accept electrons and protons from water molecules to generate molecular oxygen. The second RML assembly will exhibit electron- and proton-transfer activity, *i.e.* accept electrons and protons, which are supplied from the oxygen-evolution RML assembly. Subsequently, hydrogen will be generated from the ligands in the RML assembly, preferably by using renewable energy sources.

In a second step, hydrogen will be stored either in materials consisting of metal complexes that contain electron- and proton-transfer active ligands, or in organic hydrogen carriers. Chemical hydrogen absorption is carried out on electron- and proton-deficient ligands in the metal complex, prior to hydrogen being generated from electron- and proton-rich ligands *via* photochemical excitation. In addition, dehydrogenation and hydrogenation reactions of

hydrogen carriers will be catalyzed by metal complex with electron- and proton-transfer active ligands.

It is expected that the judicious combination of electron- and proton-transfer activity and photochemical reactivity, will lead to new catalysts and materials that exhibit high activities for electron- and proton-transfer as well as progression of new chemistry for electron- and proton-transfer.

List of Publications

Chapter 2 Takeshi Matsumoto, Masanori Wakizaka, Hirokazu Yano, Atsushi Kobayashi, Ho-Chol Chang, Masako Kato

Coordination site–Dependent Cation Binding and Multi–responsible Redox Properties of Janus–Head Metalloligand, $[Mo^{V}(1,2\text{-mercaptophenolato})_3]^-$

Dalton Trans., **2012**, *41*, 8303-8315. (*Front Cover*)

Chapter 3 Masanori Wakizaka, Takeshi Matsumoto, Atsushi Kobayashi, Masako Kato, Ho-Chol Chang

Interactions Between the Trianionic *Ligand*-centred Redox-active Metalloligand $[Cr^{III}(perfluorocatecholato)_3]^{3-}$ and Guest Metal Ions

Dalton Trans., **2015**, *44*, 14304-14314.

Chapter 4 Masanori Wakizaka, Takeshi Matsumoto, Atsushi Kobayashi, Masako Kato, Ho-Chol Chang

Guest Metal Ion Binding by Heteroleptic Site of Ligand-centered Redox-active Metalloligand $[Cr^{III}(2\text{-mercaptophenolato})_3]^{3-}$

to be submitted.

Chapter 5 Takeshi Matsumoto, Ho-Chol Chang, Masanori Wakizaka, Sho Ueno, Atsushi Kobayashi, Akira Nakayama, Tetsuya Taketsugu, M. Kato

Nonprecious-Metal-Assisted Photochemical Hydrogen Production from *ortho*-Phenylenediamine

J. Am. Chem. Soc., **2013**, *135*, 8646-8654. (*Front Cover*)

Chapter 6 Masanori Wakizaka, Ryota Tanaka, Takeshi Matsumoto, Akane Usui, Atsushi Kobayashi, Masako Kato, Ho-Chol Chang

Photocatalytic Hydrogen Evolution from MeOH by *o*-Aminophenol, *o*-Aminophenolate, and Its Fe(II) Complex at Room Temperature

submitted to Nat. Commun.

Other Publications

1. Takeshi Matsumoto, Hirokazu Yano, Masanori Wakizaka, Atsushi Kobayashi, Masako Kato, Ho-Chol Chang

Syntheses and Structures of Molybdenum-oxo Complexes Prepared by the Reactions of $[Mo^{II}_2(OAc)_4]$ with *tert*-Butyl- or Bromo-substituted Catechols

Bull. Chem. Soc. Jpn., **2015**, *88*, 74-83.

2. Shota Yamada, Takeshi Matsumoto, Masanori Wakizaka, Ho-Chol Chang

Highly Polar Solvent-induced Disproportionation of a Cationic Pt(II)-Diimine Complex Containing an *o*-Semiquinonato

Dalton Trans., **2016**, in press.

List of Presentations

Oral Presentations

1. Masanori Wakizaka, Ryota Tanaka, Akane Usui, Atsushi Kobayashi, Masako Kato, Takeshi Matsumoto, Ho-Chol Chang

   Photochemical Dehydrogenation of Methanol Catalyzed by Bis-(2-aminophenolato) Fe(II) Complex at Room Temperature

   The 96th Chemical Society of Japan Annual Meeting, 3D6-33, Kyotanabe, March 2016.

2. Masanori Wakizaka, Atsushi Kobayashi, Masako Kato, Takeshi Matsumoto, Ho-Chol Chang

   The Design of Molecule-based Assemblies Having Multi-electron Transfer Activity Based on Redox-active Metalloligands

   The 65th Conference of Japanese Society of Coordination Chemistry, 1Fb-11, Nara, September 2015.

3. Masanori Wakizaka, Atsushi Kobayashi, Masako Kato, Takeshi Matsumoto, Ho-Chol Chang

   Study on Multi-electron Oxidation Reaction Using Redox-active Metalloligand with Electron-withdrawing Groups

   The 64th Conference of Japanese Society of Coordination Chemistry, 1Fc-03, Tokyo, September 2014.

4. Masanori Wakizaka, Ryota Tanaka, Akane Usui, Atsushi Kobayashi, Masako Kato, Ho-Chol Chang

   Photochemical Reactions of 2-Aminophenolato and *ortho*-Phenylenediamine Complexes

   The 94th Chemical Society of Japan Annual Meeting, 4F2-05, Nagoya, March 2014.

5. Masanori Wakizaka, Atsushi Kobayashi, Ho-Chol Chang, Masako Kato

   Metal Binding and Redox Properties Multi-electron Oxidation Reaction Using Redox-active Metalloligand with Electron-withdrawing Groups

   The 64th Conference of Japanese Society of Coordination Chemistry, 2Fc-19, Okinawa, November 2013.

6. Masanori Wakizaka, Takeshi Matsumoto, Akane Usui, Atsushi Kobayashi, Ho-Chol Chang, Masako Kato

   Assembly of Non-innocent-type Complex for the Design of Multi-electron Transfer Systems

   2013 Young Coordination Chemist's Association Japan Summer School, Oral Presentation 2, Sapporo, August 2013. (*Best Presentation Award*)

7. Masanori Wakizaka, Takeshi Matsumoto, Hirokazu Yano, Atsushi Kobayashi, Ho-Chol Chang, Masako Kato

   Assembly of Metal Ions by Tris(2-mercaptophonolato) Mo(V) Metalloligand

   2011 Winter Conference on Hokkaido Branch of Chemical Society of Japan, 1B-03, Sapporo, February 2011.

Poster Presentations

1. Masanori Wakizaka, Atsushi Kobayashi, Masako Kato, Takeshi Matsumoto, Ho-Chol Chang

   Electrochemical Oxidation Reaction of Redox-active Metalloligand with Electron-withdrawing Groups

   2015 Annual Meeting of Japan Society for Molecular Science, 3P083, Hiroshima, September 2014.

2. Masanori Wakizaka, Takeshi Matsumoto, Atsushi Kobayashi, Ho-Chol Chang, Masako Kato

   Binding of Metal Ions by Metalloligands with Redox-active Metal and Ligands

41st International Conference on Coordination Chemistry, ID650, Singapore, July 2014. (*Best Poster Award*)

3. Masanori Wakizaka, Takeshi Matsumoto, Atsushi Kobayashi, Masako Kato, Ho-Chol Chang
   Coordination Programming toward Multi-electron/proton Transfer
   International Symposium on Coordination Programming 2014, Tokyo, Japan, January 2014.

4. Masanori Wakizaka, Takeshi Matsumoto, Akane Usui, Atsushi Kobayashi, Ho-Chol Chang, Masako Kato
   Assembly of the Non-innocent-type Complex Modules for the New Design of Water Splitting Catalysts
   The 28th Summer Seminar of Bioinorganic Chemistry, Poster No. 22, Hitachinaka, August 2013.

5. Masanori Wakizaka, Takeshi Matsumoto, Akane Usui, Atsushi Kobayashi, Ho-Chol Chang, Masako Kato
   Construction of the Molecular Assemblies with Multi-electron Transfer Ability Using Tetrafluorocatecholato Cr(III) Complex
   The 93rd Chemical Society of Japan Annual Meeting, 2PA-091, Kusatsu, March 2013.

6. Masanori Wakizaka, Takeshi Matsumoto, Akane Usui, Sho Ueno, Atsushi Kobayashi, Ho-Chol Chang, Masako Kato
   Creation of the Non-innocent-type Metalloligands with O/S/NH_2 Coordination Atoms
   The 62nd Conference of Japanese Society of Coordination Chemistry, 1PF-28, Toyama, September 2012.

7. Masanori Wakizaka, Takeshi Matsumoto, Hirokazu Yano, Atsushi Kobayashi, Ho-Chol Chang, Masako Kato

   Coordination site-Dependent Cation Binding and Multi-responsible Redox Properties of Janus-Head Metalloligand, [Mo^{V}(1,2-mercaptophenolato)$_3$]

   12th Eurasia Conference on Chemical Sciences, S_9-PP8, Corfu, Greece, April 2012.

8. Masanori Wakizaka, Takeshi Matsumoto, Hirokazu Yano, Atsushi Kobayashi, Ho-Chol Chang, Masako Kato

   Selective Metal Ions Binding and Multi-responsiveness of the Non-innocent-type Metalloligand

   The 61st Conference of Japanese Society of Coordination Chemistry, 1PF-07, Okayama, September 2011.

9. Masanori Wakizaka, Takeshi Matsumoto, Hirokazu Yano, Atsushi Kobayashi, Ho-Chol Chang, Masako Kato

   Selective Metal Ions Binding and Multi-responsiveness of the Redox-active Metalloligand

   2011 Young Coordination Chemist's Association Japan Summer School, P-14, Kanazawa, July 2011. (*Best Poster Award*)